



## Closed Loop Wind Farm Control

### Integrated wind farm controllers

Deliverable No.	D2.5	Work Package No.	WP2	Tasks No.	2.4
Work Package Title		Wind farm flow control technologies and algorithms			
Linked Tasks Title		Integrated wind farm control			
Status		Draft			
Dissemination level		public			
Due date deliverable		2019-08-31	Submission date		2019-12-09
Deliverable version		1.1			



This project has received funding from the European Union's Horizon 2020 research and innovation programme under grant agreement No 727477

**DOCUMENT CONTRIBUTORS**

<b>Deliverable responsible</b>	Delft University of Technology
<b>Contributor</b>	<b>Organization</b>
Torben Knudsen	AAU
Maria Aparicio-Sanchez	CENER
Irene Eguinoa	CENER
Iñaki Sandua	CENER
David Astrain	CENER
Bart Doekemeijer	Delft University of Technology
Jan-Willem van Wingerden	Delft University of Technology
Ervin Bossanyi	DNV GL
Stoyan Kanev	ECN part of TNO
Rodolfo Reyes Baez	ECN part of TNO
Steffen Raach	USTUTT

<b>Reviewer</b>	<b>Organization</b>
Stefan Kern	GE Global Research
Giancarlo Potenza	Enel Green Power

## CONTENTS

<b>List of Figures</b>	<b>3</b>
<b>List of Tables</b>	<b>5</b>
<b>1 Executive summary</b>	<b>6</b>
<b>2 Introduction</b>	<b>9</b>
<b>3 On combined yaw and pitch based active wake control</b>	<b>11</b>
3.1 Introduction	11
3.2 Problem formulation	12
3.2.1 Wind farm layouts	12
3.2.2 Wind farm model	13
3.2.3 Cases of study	14
3.3 Optimization algorithm	14
3.4 Results and discussions	15
3.4.1 Sedini wind farm: Test array 1	15
3.4.2 Sedini wind farm: Test array 2	18
3.4.3 Three turbine case in full wake overlapping	20
3.5 Conclusions and future work	23
<b>4 Closed-loop model-based control using a steady-state surrogate model</b>	<b>25</b>
4.1 Combined induction control and wake steering under constant inflow conditions	25
4.1.1 Methodology and results	25
4.1.2 A continued discussion	38
4.2 Assessing the observability of the ambient conditions: robustifying the estimation of the ambient conditions in the closed-loop model-based controller	39
4.2.1 Methodology and results	39
4.2.2 A continued discussion	57
4.3 Wake steering under time-varying inflow conditions	57
4.3.1 Methodology and results	57
4.3.2 A continued discussion	85
4.4 Conclusions	85
<b>5 Combined feedback-feedforward wake redirection control</b>	<b>86</b>
5.1 Introduction	86
5.2 Methodology and results	87
5.3 Control design	106
5.3.1 Control design model	106
5.3.2 Control synthesis	107
5.4 Controller analysis	108
5.5 Conclusions and Discussion	110
<b>6 Dynamic integration of feed-forward induction control</b>	<b>112</b>
6.1 Estimation of environmental conditions	112
6.1.1 Introduction	112
6.1.2 Ambient wind speed estimation	114
6.1.3 TI estimation	115

---

6.2	Calculation of optimum derating configurations . . . . .	117
6.3	Supercontroller interface . . . . .	119
6.4	Integration . . . . .	119
6.5	Example . . . . .	120
6.5.1	Wind input . . . . .	122
6.5.2	Baseline result . . . . .	122
6.5.3	Estimation of environmental conditions . . . . .	125
6.5.4	Calculation of optimum derating configurations . . . . .	125
6.5.5	Supercontroller operational modes . . . . .	126
6.5.6	Comparison of power and DEL . . . . .	128
6.6	Conclusions and Future Work . . . . .	136
<b>7</b>	<b>Wind farm controller design and testing with LongSim . . . . .</b>	<b>140</b>
<b>8</b>	<b>Data-driven EMPC feedback wind farm control . . . . .</b>	<b>163</b>
<b>9</b>	<b>Load-minimizing active power control for wind farms . . . . .</b>	<b>164</b>
9.1	Introduction . . . . .	164
9.2	Methodology . . . . .	164
9.3	Conclusion . . . . .	179
<b>10</b>	<b>Conclusions . . . . .</b>	<b>180</b>
	<b>References . . . . .</b>	<b>181</b>



## LIST OF FIGURES

Figure 1.	Sedini wind farm layout. Plot generated with FLORIS [20] . . . . .	13
Figure 2.	Three turbines wind farm layout. . . . .	13
Figure 3.	Flow velocities [m/s] at hub height for Test array 1 of the Sedini wind farm at CYP-based maximum power wind direction (230°) and TI=0.10 . . . . .	15
Figure 4.	Test array 1 of the Sedini wind farm under yaw-based AWC and TI=0.10 . . . . .	16
Figure 5.	Test array 1 of the Sedini wind farm under pitch-based AWC and TI=0.10 . . . . .	17
Figure 6.	Test array 1 of the Sedini wind farm under CYP-based AWC and TI=0.10 . . . . .	18
Figure 7.	Flow velocities [m/s] at hub for Test array 2 of the Sedini wind farm at maximum power wind direction (237°) and TI=0.10 . . . . .	19
Figure 8.	Test array 1 of the Sedini wind farm under CYP-based AWC and TI=0.10 . . . . .	20
Figure 9.	Three turbines case at maximum power wind direction (180°) and TI=0.06 . . . . .	21
Figure 10.	Three turbine case wind farm under pitch-based AWC and TI=0.06 . . . . .	22
Figure 11.	Three turbine case wind farm under yaw-based AWC and TI=0.06 . . . . .	22
Figure 12.	Three turbine case wind farm under CYP-based AWC and TI=0.06 . . . . .	23
Figure 13.	Flow field [m/s] at turbine hub height for the generic 9-turbine wind farm in which the axial induction factors of turbines 1-6 have been optimized for maximum power capture, found to be 0.305. This leads to an effective power gain of 0.2% according to FLORIS in comparison to operation with an induction factor of 0.333. . . . .	38
Figure 14.	Model identification steps to obtain a controller design model with SOWFA. The first plot shows the yaw angle, the second plot gives the estimated wake position at a downwind distance of 3 times the rotor diameter (3D). . . . .	106
Figure 15.	Bode plot . . . . .	107
Figure 16.	Averaged model from the model identification. . . . .	108
Figure 17.	The different controllers synthesized using the obtained controller design models. A $H_{\infty}$ controller, a fixed structure PI controller and a robust controller taking all models into account. . . . .	109
Figure 18.	The different controllers synthesized using the obtained controller design models. A $H_{\infty}$ controller, a fixed structure PI controller and a robust controller taking all models into account. . . . .	109
Figure 19.	Step responses of the closed-loop controller. In the disturbed case, output disturbances are applied which can be seen in the second plot. All controllers perform well and achieve an error-free final result. . . . .	110
Figure 20.	Methodology of ambient wind conditions estimation . . . . .	113
Figure 21.	Power ( $\bar{W}$ ) distributions for all combinations of wind velocities and yaw angles (for different derating settings, TI= 8%) . . . . .	114
Figure 22.	Methodology of ambient wind speed estimation . . . . .	115
Figure 23.	Estimation of mean ambient wind speed . . . . .	116
Figure 24.	Estimation of mean ambient wind speed (zoom in on variables with valid estimates) . . . . .	116

Figure 25. Methodology of ambient TI estimation . . . . .	117
Figure 26. Estimation of ambient TI . . . . .	118
Figure 27. Methodology for the integration of supercontroller . . . . .	120
Figure 28. Farm controller block diagram . . . . .	121
Figure 29. 3x3 CL-Windcon Lay-out . . . . .	121
Figure 30. Wind speed input . . . . .	122
Figure 31. Power for all wind turbines (baseline) . . . . .	123
Figure 32. <i>RootMyb</i> for all wind turbines (baseline) . . . . .	124
Figure 33. Zoom analysis (baseline) . . . . .	124
Figure 34. Time window analysis (baseline) . . . . .	125
Figure 35. Power for all wind turbines (with supercontroller) . . . . .	130
Figure 36. <i>RootMyb</i> for all wind turbines (with supercontroller) . . . . .	130
Figure 37. WT1 Power Comparison (baseline and supercontroller) . . . . .	130
Figure 38. WT1 <i>RootMyb</i> Comparison (baseline and supercontroller) . . . . .	131
Figure 39. WT1 zoom Comparison (baseline and supercontroller) . . . . .	131
Figure 40. WT2 Power Comparison (baseline and supercontroller) . . . . .	132
Figure 41. WT2 <i>RootMyb</i> Comparison (baseline and supercontroller) . . . . .	132
Figure 42. WT2 zoom Comparison (baseline and supercontroller) . . . . .	133
Figure 43. WT3 Power Comparison (baseline and supercontroller) . . . . .	134
Figure 44. WT3 <i>RootMyb</i> Comparison (baseline and supercontroller) . . . . .	135
Figure 45. WT3 zoom Comparison (baseline and supercontroller) . . . . .	135
Figure 46. WT3 FFT Comparison (baseline and supercontroller) . . . . .	136
Figure 47. Time window comparison (baseline and supercontroller) . . . . .	137
Figure 48. General results in percentage: Power of the wind farm and Maximum DEL <i>RootMyb</i>	138

LIST OF TABLES

Table 1. Turbulence intensity and wind velocity considered in the simulation study . . . . . 14

Table 2. Controlled maximum power gain of Test array 1 for different turbulence intensity . 19

Table 3. Controlled maximum power gain of Test array 2 for different turbulence intensity . 20

Table 4. Environmental conditions for each time window . . . . . 126

Table 5. Depowering settings for wind speed 8 m/s . . . . . 127

Table 6. Depowering settings for wind speed 10 m/s . . . . . 127

Table 7. Depowering settings for wind speed 12 m/s . . . . . 127

Table 8. Derating solutions for all time windows of the FAST.Farm simulation . . . . . 128

## 1 EXECUTIVE SUMMARY

As the depletion of fossil fuels continues relentlessly, there is a shift in focus in the research community towards the optimization of renewable energy technologies. One popular field of research is *wind farm control*, in which turbines are coordinated to increase the performance of the entire wind farm. Two popular methods for wind farm control are *axial induction control* and *wake steering*. Axial induction control reduces the energy extraction of an upstream turbine to reduce the wake effects on downstream turbines. Wake steering displaces the wake downstream by purposefully misaligning the upstream turbine's rotor plane with the incoming air stream.

The European CL-Windcon project revolves around the development, integration and validation of closed-loop control solutions for current and future wind turbine power plants. The workpackage corresponding to this deliverable is concerned with wind farm controller synthesis. In previous work in this workpackage, separate wind farm control algorithms were synthesized with a single purpose in mind. These purposes included, amongst others, axial induction control for power maximization, wake redirection for power maximization, axial induction control for turbine load mitigation, and axial induction control for active power control. In the deliverable at hand, several control methods are unified to provide comprehensive, integrated control solutions that further improve the efficiency of wind farms.

Several contributions on integrated control are depicted in this work. Firstly, a detailed analysis is performed on the differences of axial induction control, wake redirection control, and the combination of the two, in pursuit of maximum energy extraction. Two wind farm layouts are investigated, being an onshore wind farm in Italy and a virtual farm with three aligned 10MW wind turbines. The control setpoints are optimized using the static surrogate model FLORIS. The potential gains as predicted by FLORIS are calculated for a range of wind directions and two turbulence levels. For the Italian wind farm, at low turbulence levels and at situations with heavy wake losses, wake redirection control shows a potential increase in energy extraction of up to 17% in power extraction, axial induction control shows a potential increase of 6%, and the combination shows a potential of 19% in FLORIS. For the three-turbine case, these gains go up to 20% for wake redirection, decrease to 3% for axial induction control, and show a combined gain of 20% in FLORIS. Future work involves updating the surrogate model, improving the optimization algorithm, investigating the controller's performance under more realistic inflow conditions and at a higher fidelity, and assessing the controller's influence on the mechanical loads on the turbines.

Secondly, in continuation of the previous contribution, a wind farm controller combining axial induction control and wake redirection control for wind farm power maximization is matured and assessed in a high-fidelity environment. For this reason, a closed-loop control framework is proposed using FLORIS that is used for continuous ambient-condition estimation and control-setpoint optimization. High-fidelity simulation results show that the surrogate model FLORIS does not predict any gains in energy yield for axial induction control, and the controller thereby exclusively employs wake steering

for power maximization. This is largely in agreement with the foregoing analysis. Furthermore, the controller was then robustified using a theoretical measure of observability, which ensures that only the parameters that can be estimated, are estimated. Finally, an integrated closed-loop control solution was proposed and tested in high-fidelity simulation using varying inflow conditions, showing an increase of 1% to 9% in energy extraction compared to greedy operation.

Thirdly, a combined feedback-feedforward controller is proposed for wake redirection control in wind farms. In this strategy, FLORIS is used to assign a set of yaw misalignment angles to each turbine to maximize the energy extraction of the farm in a feedforward approach. Due to the uncertainties commonly present in such steady-state surrogate models, the assigned yaw angles are often under- or overestimated, effectively leading to suboptimal energy extraction. A feedback control scheme is then superimposed to correct the yaw angles and thereby achieve the desired wake displacement. To this extend, a lidar is used to actively measure the wake displacement. High-fidelity simulations show a promising increase in energy extraction of up to 16.9% compared to a baseline controller for a three-by-three wind farm layout. In future work, the proposed controller should be tested for changing inflow conditions.

Fourthly, a control solution that integrates turbine derating for a multi-objective cost function that trades off mechanical loads with energy yield is presented. To do so, a loads database was constructed, which is used together with a DEL estimation method. This database was combined with a variant of the FLORIS surrogate model to provide predictions on the turbine fatigue loads and power production as a function of the inflow conditions. Furthermore, a solution was also provided for the estimation of such ambient conditions using upstream turbine measurement data, which is an essential component to any model-based wind farm control solution. The control solution was validated successfully in the medium-fidelity simulation environment *FAST.Farm*.

Fifthly, a wind farm control solution is outlined that leverages the simplified surrogate model LongSim. This controller is synthesized for the onshore wind farm in Sardini on the island of Sardinia, Italy for real-world experiments on axial induction control for power maximization. Special attention is paid towards the shift from static to dynamic control. While axial induction control has often appeared impractical for power maximization, LongSim does predict increases up to the order of 10% in energy extraction by derating several upstream turbines for conditions with large wake losses (i.e., at a low turbulence intensity and for the right wind direction). Moreover, special attention was paid towards the shift from steady control solutions to a more realistic, dynamic environment, thereby rendering the controller one of the most prominent wind farm control solutions presented in this report.

Sixthly, a concise follow-up is presented on a model-free data-driven approach for axial induction control for power maximization. It was concluded that this model-free wind farm controller proposed in previous work is not feasible. This control solution was therefore discontinued.

Seventhly, a wind farm control solution for secondary frequency regulation is outlined. This wind farm control solution leverages axial induction control to track a demanded power signal (e.g., assigned by transmission system operators) to allow the integration of energy from the wind farm with

the electricity grid. Since there is a plethora of different derating strategies in the farm, a secondary objective, fatigue load minimization, is introduced. High-fidelity simulations show that the control solution is able to track reference power signals in timescales of 1 to 10 seconds, while reducing temporal fluctuations of the rotor axial force of each turbine. Moreover, yaw-based wake steering is leveraged to maximize the possible power production in situations where the demanded power signal exceeds the currently available power. While successful, more work is necessary to fully integrate this concept of yaw-based wake steering in the active power control solution. Another future research direction is the assessment of the controller under realistic, time-varying inflow conditions.

Looking ahead, in the next workpackage of this European project, several of these control algorithms will be tested on various levels of fidelity; in high-fidelity simulation, wind tunnel experiments and/or field campaigns on an onshore wind farm in Sedini, on the island of Sardinia, Italy. This should further verify, validate and increase the trust in these control solutions.

## 2 INTRODUCTION

As the depletion of fossil fuels continues relentlessly, there is a shift in focus in the research community towards the optimization of renewable energy technologies. A popular technology that is increasingly explored in the research is *wind farm control*, in which turbines are operated in a collective fashion to increase the overall performance (e.g., energy yield or component lifetime) of the entire farm. Two popular methods for wind farm control are explored in the literature:

- *Axial induction control, or derating control.* In this control methodology, the turbines are operated to extract less energy from the flow than in greedy operation. This leaves more energy in the flow downstream, and reduces the increase in the turbulence intensity due to blade-flow interactions. Axial induction control is often used for active power control, which focuses on integration of wind energy with the electricity grid. Another popular objective for axial induction control is load mitigation and load distribution between turbines.
- *Wake steering or wake redirection control.* In this control methodology, the rotor plane is purposefully misaligned with the incoming flow to induce a lateral (yaw-based) or vertical force (tilt-based) on the incoming flow, which then induces a lateral/vertical displacement of the wake downstream. This can be used to steer wakes away from the downstream turbines. This methodology is typically used for power maximization in wind farms.

The European CL-Windcon project revolves around the development, integration and validation of closed-loop control solutions for current and future wind turbine power plants. For this purpose, the project contains three technical workpackage, along side several business-oriented, management and ethics workpackages. The three technical workpackages are:

- WP1. mathematical model development,
- WP2. controller synthesis,
- WP3. algorithm verification and validation.

This document details work performed for workpackage 2: controller synthesis. In previous work in this workpackage [2], separate wind farm control algorithms were synthesized with a single purpose in mind. These purposes included, amongst others, axial induction control for power maximization, wake redirection for power maximization, axial induction control for load mitigation, and axial induction control for active power control. In this deliverable, several control methods are unified to provide comprehensive, integrated control solutions.

The structure of the report is as follows:

- In Chapter 3, the effects of axial induction control, wake redirection control, and the combination of the two, are explored in detail. The proposed wind farm control solution pursues power maximization and therefore leverages the static surrogate model FLORIS developed by

NREL and TUDelft. The simulation studies are also performed with FLORIS, thereby assessing the upper limits of the potential of these methods.

- In Chapter 4, in continuation of Chapter 3, axial induction control is combined with wake redirection control for wind farm power maximization. Furthermore, a closed-loop control framework is proposed using FLORIS for continuous ambient-condition estimation and control-setpoint optimization. The control solution is then tested in a high-fidelity environment with time-varying inflow conditions as first of its kind.
- In Chapter 5, a feedforward-feedback wind farm controller is synthesized that employs wake redirection control for power maximization. The FLORIS model is used to determine the optimal yaw misalignment angles for power maximization in a feedforward setting. Then, due to the ubiquitous model uncertainties, a feedback loop is integrated that measures (using a lidar system) and corrects the wake displacement by further adjusting the yaw angle. The control strategy is tested in high-fidelity simulation.
- In Chapter 6, a control solution leveraging a variant on FLORIS is presented that integrates turbine derating for a multi-objective cost function that trades off mechanical loads with energy yield. This chapter also depicts how the ambient conditions, which are necessary for the control solution, can be derived from wind turbine measurement data. The control solution is then validated in a medium-fidelity simulation environment called FAST.Farm.
- In Chapter 7, a wind farm control solution is outlined that leverages the simplified surrogate model LongSim. This controller is synthesized for the onshore wind farm in Sedini on the island of Sardinia, Italy for real-world experiments on axial induction control for power maximization. Special attention is paid towards the shift from static to dynamic control.
- In Chapter 8, a concise follow-up is presented on a model-free data-driven approach for axial induction control for power maximization.
- In Chapter 9, a wind farm control solution for active power control is outlined. This controller uses axial induction control to have a wind farm produce a demanded amount of power while minimizing the fatigue loads of the turbines. Additionally, concepts of wake steering are leveraged to maximize the power production when the demanded power exceeds the available power.

Finally, the report is concluded in Chapter 10.



### 3 ON COMBINED YAW AND PITCH BASED ACTIVE WAKE CONTROL

#### 3.1 Introduction

The goal of a wind farm control strategy is twofold [12]: first, maximizing the wind farm's power production and, secondly, mitigating the associated mechanical loads acting on each wind turbine in the farm. Such loads are the result of each turbine's gravitational, inertial, and aerodynamical effects, and due to the interaction with the neighboring upstream wind turbines in the farm, i.e., the so-called *wake effects*. In order to alleviate the local loads of a single wind turbine, several control schemes have been developed in the past two decades (see for instance [46, 40], and Chapter 3 of Deliverable D2.1 for a summary). Whereas for mechanical loads due to wakes, few results have been proposed, see [42, 44, 43] for a wind farm control literature review, and [12] for a tutorial on this topic.

Some notable works on wind farm control are the following. The axial-induction-based control (AIC) approach in [5], where upstream wind turbines production is reduced by changing the axial induction factor so that the downstream turbines can generate more power. The active wake control (AWC) optimization method for weak steering of [41], in which, roughly speaking, wakes are redirected aside from downstream wind turbines, also for increasing the power production of downstream turbines. A first exploratory study on combined AIC and wake steering control methods is presented in [16], where a simple wind farm consisting of a row of six generic  $2MW$  wind turbines is considered. Finally, in the recent work of [53], the design and analysis of a wake steering controller with wind direction variability is presented for a two-turbine array using the FLOW Redirection and Induction in Steady State (FLORIS) control-oriented wake model.

Among the above wind farm control strategies, we highlight the optimization based AWC method in [41], where two classes of AWC methods are compared: pitch-based AWC, which is the pitch-based AIC described in [5]; and yaw-based AWC that consists in operating upstream turbines at yaw misalignment. For comparing the possible benefits and/or disadvantages of these two AWC methods, an optimization of the yearly power production task is assigned to the pitch-based AWC, whereas a load-based lifetime power optimization task is assigned to the yaw-based AWC<sup>1</sup>. This is a suitable comparison criteria since fatigue loads reduction is an implicit feature of derating by pitching [1]. Both AWC methods are optimized for several full-scale commercial wind farms with different layouts and turbine sizes. The conclusion is that yaw-based AWC considerably increases the power production with respect to its pitch counterpart (which is limited to wind farms with turbine distances of up to  $6D$  to  $7D$ , with  $D$  the turbine diameter) and reduce the loads on the considered wind components.

From a practical point of view, experimental validations of AWC are presented in the very recent works of [35] and [28]. In the first reference, a pitch-based AWC field test is presented, the analysis of the one year measurements under this control scheme indicates that the power production is increased. The optimization algorithm used in the strategy of [35] is implemented with the wake

<sup>1</sup> Both, pitch and yaw based AWC methods can be applied to either power optimization or power and loads optimization

model FarmFlow from ECN part of TNO. In the case of yaw-based AWC, an initial stage of a field campaign of wake steering at a commercial wind farm is presented in [28]. For two closely spaced turbines, an approximate 14% increase in energy was measured on the downstream turbine over a 10 degrees sector, with a 4% increase in energy when accounting for losses of the upstream turbine. These gains in energy are *consistent* to predictions made using the FLORIS model [20] [25].

### 3.2 Problem formulation

Motivated by the simulated and experimental benefits of the pitch-based and yaw-based AWC methods described above, as well as the benefits showed in the exploratory study of *combined* yaw and pitch (CYP) based AWC in [16], in this chapter we concentrate in further exploring the CYP-based AWC strategy on different *realistic* wind farm layouts. The performance of this strategy will be measured in terms of power production.

#### 3.2.1 Wind farm layouts

Two reference wind farms in the CL-Windcon project are considered, namely the lined three turbines case and the Sedini wind farm. These two wind farms are briefly described bellow:

##### *Sedini wind farm case*

Since field experiments are planned to be carried out in the Enel Green Power's Sedini wind farm during the second and third year of this project; it is pertinent to evaluate the performance of the CYP-based AWC strategy on this farm.

- Turbines: The turbines used in for this farm are GE1.5 s defined in Section 3.5 of deliverable CL-Windcon-D1.1-Definitions.
- Layout: The turbines are not aligned in regular rows, they are placed in an area keeping an irregular distance among the turbines, see Figure 1. This layout offers flexibility for exploring different scenarios by clustering a number of wind turbines. For instance, in Figure 1 are shown the test arrays of Sedini wind farm that are considered in this chapter; Test array 1 consisting of four turbines, while Test array 2 consists of nine turbines.  
Orographic effects are not accounted in the present study.

##### *Three turbines case*

- Turbines: The considered turbine is the DTU 10 MW , which was developed within the FP7 Project INNWIND. All its data is publicly available, allowing replication of the results. The turbine parameters can be found in [9].
- Layout: Three turbines on a line perpendicular to the predominant wind direction in full wake overlapping; see Figure 2. The spacing among the wind turbines considered here is of  $7D$ . This differs from the same case in deliverable CL-Windcon-D1.1, where the first and second turbines are on the straight line, and the last one is shifted to the right in the x-direction.

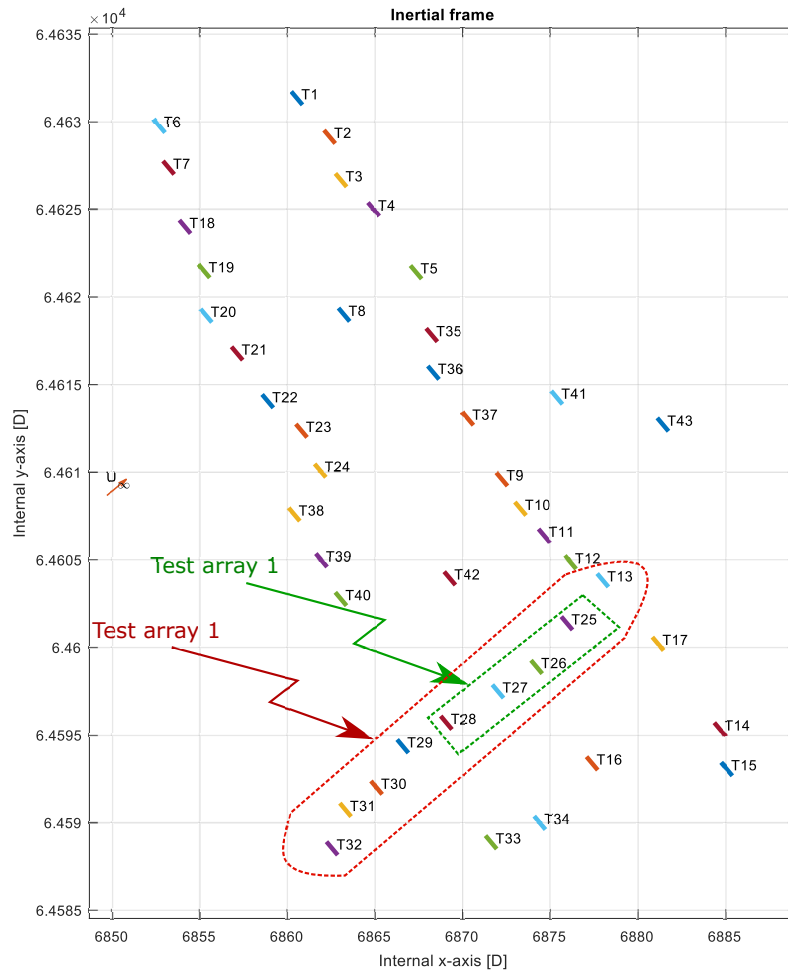


Figure 1. Sedini wind farm layout. Plot generated with FLORIS [20] .

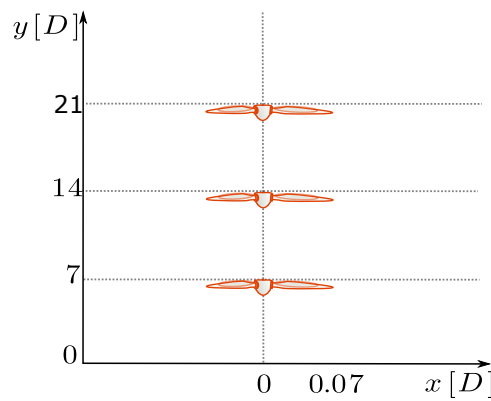


Figure 2. Three turbines wind farm layout.

### 3.2.2 Wind farm model

The present study will be performed using the Matlab version of the steady-state wind farm control oriented model FLORIS. This wind farm model has been created for real-time online wind farm

control, low-fidelity offline wind farm analysis and layout optimization purposes. For further details check Chapter 6 of Deliverable CL-Windcon-D1.2-Wind farm models and [20] .

### 3.2.3 Cases of study

The simulation will be carried on three wind farm scenarios as summarized in the following table.

**Table 1. Turbulence intensity and wind velocity considered in the simulation study**

Wind farm scenarios	Turbulence intensity (TI)		Wind speed [m/s]
Test array 1 Sedini	0.10	0.16	8
Test array 2 Sedini	0.10	0.16	8
Three turbines case	0.06	0.16	8

## 3.3 Optimization algorithm

The CYP-based ACW in the present chapter will be implemented for maximizing the wind power production. The FLORIS built in optimization algorithm will be used for finding optimal yaw and pitch angles for each wind turbine in the farm under yaw-based, pitch-based and CYP-based AWC.

---

**Algorithm 1:** FLORIS power maximization algorithm

---

```

 $x_0 \leftarrow \text{Turbine.inputdata}(\text{Yaw}, \text{Pitch}); ; \text{run FLORIS}(x_0);$ 
 $P_0 \leftarrow \sum_{i=1}^N \text{FLORIS.outputdata.power}_i(x_0) \quad N = \#\text{turbines};$ 
 $x \leftarrow \text{FLORIS.outputdata}(\text{Yaw}, \text{Pitch}); \text{flag} \leftarrow 1;$ 
while  $\text{flag} = 1$  do
     $J(x) \leftarrow P_T = - \sum_{i=1}^N \text{FLORIS.power}_i(x);$ 
     $x_{\text{opt}} \leftarrow \min_{x_{\text{lb}} \leq x \leq x_{\text{up}}} J(x);$ 
    run FLORIS( $x_{\text{opt}}$ );
     $P_T \leftarrow \sum_{i=1}^N \text{FLORIS.outputdata.power}_i(x_{\text{opt}});$ 
    if  $P_T > P_0$  then
         $x \leftarrow x_{\text{opt}}; P_0 \leftarrow P_T;$ 
    else
         $\text{flag} \leftarrow 0;$ 
        disp(Optimization was unsuccessful. Sticking to old control settings.);
    end
end

```

---

The optimization method for minimizing the cost function  $J(x)$  is based on the *fmincon* algorithm from the Matlab Optimization toolbox, which is a static nonlinear constrained gradient based optimization method. The main disadvantage of this is that the minimum might not be global, but local

due to the imposed constraints. Nevertheless, for the present exploratory study, with a steady-state wind farm model, it is enough<sup>2</sup>.

### 3.4 Results and discussions

In this section the results of the application of CYP-based AWC on the wind farm scenarios described in Table 1 are presented and compared with the standard yaw-based and pitch-based AWC methods.

#### 3.4.1 Sedini wind farm: Test array 1

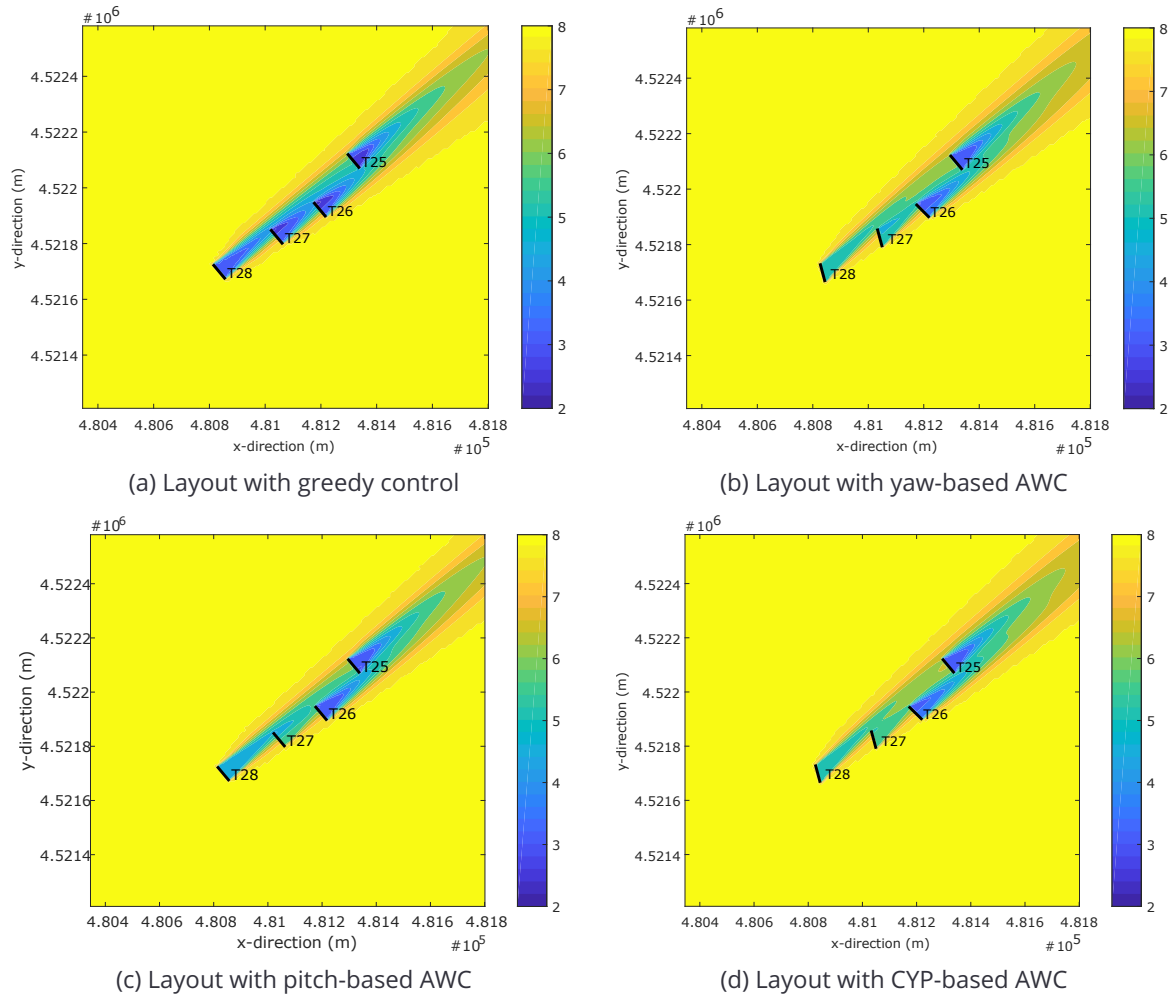


**Figure 3. Flow velocities [m/s] at hub height for Test array 1 of the Sedini wind farm at CYP-based maximum power wind direction ( $230^\circ$ ) and  $TI=0.10$**

The velocity flow performance of the Sedini wind farm Test array 1 is shown in Figure 3 for the three aforementioned control configurations. It can be observed in Figure 3(a) that due to Turbines T26, T27 and T28 are almost aligned on a straight line, there is wake overlapping that causes the downstream turbine T26 to have velocity flow region of very small magnitude. In the case of Turbine T25, the downstream smallest magnitude reduction of the velocity flow is only partial because this turbine

<sup>2</sup>Further studies consist in implementing the CYP-based AWC scheme with the optimization method in [41] on FLORIS or FarmFlow wind farm models.

is out of the aforementioned straight line.

The performance of the same test array but under the yaw-based AWC strategy is shown in Figure 3(b). It is clear that, due to yaw-misalignment, the downstream velocity flow performance for turbines T26 and T25 is considerably improved in magnitude with respect to previous case. This implies an expected increase of the whole Test array 1 power production.

On the other hand, Figure 3(c) shows the velocity flow behavior of the Test array 1 but under pitch-based AWC. Qualitatively speaking, the performance is also improved with respect to the greedy strategy in Figure 3(a), but worse than 3(b) in terms of velocity flow magnitude. Therefore, the expected power production is smaller than the one under yaw-based AWC.

Finally, in Figure 3(d), the CYP-based AWC strategy is evaluated. By inspection it is clear that with this strategy, the Test array 1 has the best velocity flow performance. The magnitude of downstream velocity flow of turbine T28 is similar to the one under both, yaw-based and pitch-based AWC methods. Notice that the downstream velocity flow of turbine T26 is considerably higher than in the other control configurations. This in turn implies that turbine T25 is expected to produce the most power only under CYP-based AWC, since its yaw angle is kept fixed in all control modes.

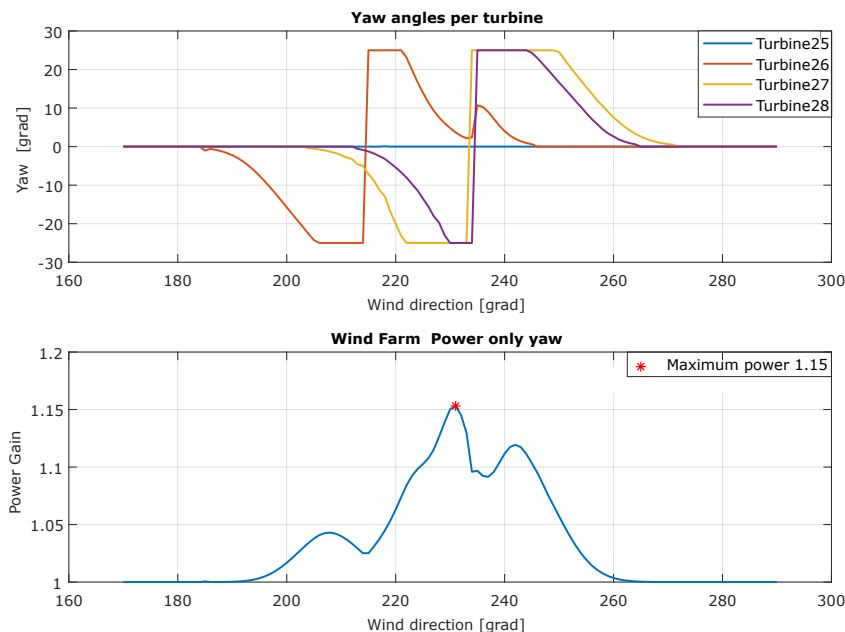


**Figure 4. Test array 1 of the Sedini wind farm under yaw-based AWC and  $TI=0.10$**

All the above conclusions are confirmed quantitatively in the following figures, modulus FLORIS farm model results. Figure 4 shows each turbine yaw angle (upper plot), and total wind farm power production gain (bottom plot) under yaw-based AWC. The maximum power production occurs around wind direction  $230^\circ$ , with an increase of 15% with respect to the conventional greedy scheme. The main disadvantage of yaw-based AWC is the occurrence of abrupt yaw angles changes as it can be observed on the top plot of Figure 4. In fact, turbines T26, T27 and T28 experience *fast* yaw angle changes at certain wind directions. It can also be observed that turbine T25 is practically in greedy mode. Similar conclusions with respect to the power improvement of yaw misalignment were ob-

tained in [40], where an analysis with the FarmFlow model of ECN part of TNO were carried out, and validated in [45] with different methods from data.

The performance of pitch-based AWC is shown in Figure 5 in terms of pitch angles (top plot) and power gain (bottom plot). In this case, there is an increase of power production of 5%, with respect to the greedy strategy. Indeed, it can be seen in Figure 5 that wind turbine T25 is in greedy configuration, while the upstream wind turbines T26, T27 and T28 are pitching, for maximizing the total power production. Despite the smaller power production gain of pitch-based AWC with respect to the yaw-based counterpart, this possesses the extra benefit of pitch-based controllers of loads mitigation, as explained in [5, 40]. Interestingly, the maximum power production occurs at  $234^\circ$ , that is, in the neighborhood of the maximum power production direction with yaw-based AWC. This already suggest a possible production improvement by combining both AWC approaches.

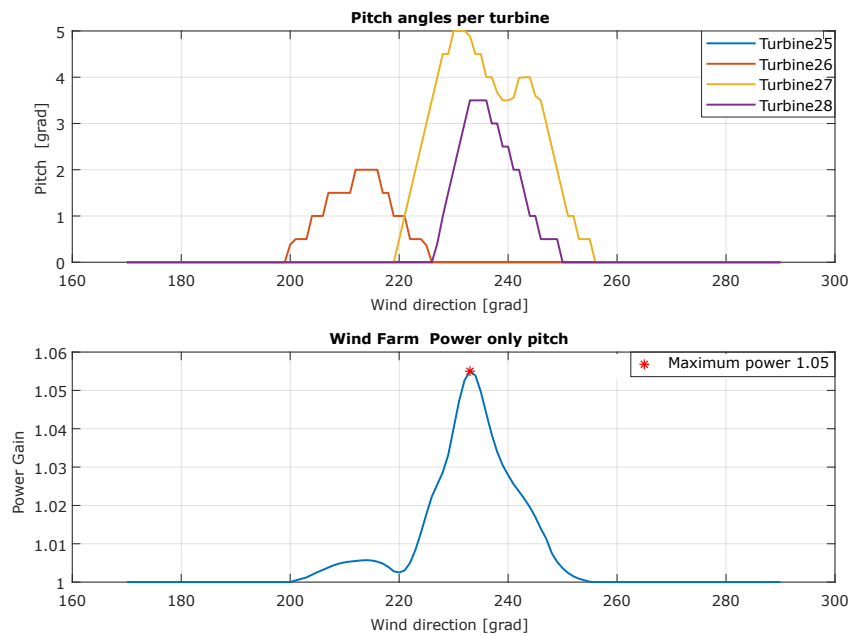


**Figure 5. Test array 1 of the Sedini wind farm under pitch-based AWC and  $TI=0.10$**

The farm behavior of the Test array 1 under CYP-based AWC is shown in Figure 6; the top plot contains each turbine's yaw angle for different wind directions, the middle plot shows each turbine's pitch angle in the same wind directions interval, and the bottom plot shows the power production gain performance of the test array under the three different AWC methods discussed in this work.

From Figure 6, it is clear that the CYP-based AWC scheme has the highest maximum power gain (16.31%) with respect to the yaw-based (15.31%) and pitch based (5.5%) strategies, thanks to the simultaneous yawing and pitching. In this case, the maximum power production occurs at the wind direction  $236^\circ$ , which is approximately the average of the maximum power direction of the other two AWC methods. The resulting power gain performance with CYP-based AWC is superior not only at the maximum power direction, but over the whole wind direction interval under consideration. Also notice that the power gain decrease at  $233^\circ$  of the yaw-based strategy in Figure 4 is compensated by

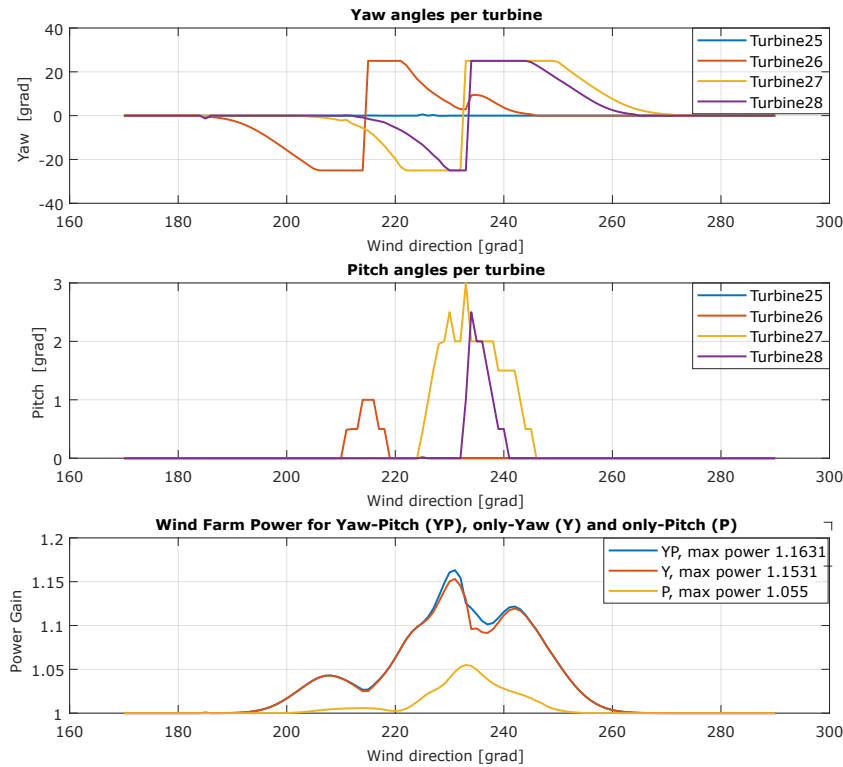


**Figure 6. Test array 1 of the Sedini wind farm under CYP-based AWC and  $TI=0.10$**

the pitching action in the CYP-based method, see bottom plot of Figure 6.

Also notice that each wind turbine's yaw angle performance under CYP-based AWC is quite close to the yaw angles performance under only yaw-based AWC (see top plot of Figure 4); with small variations around the bounds of the wind direction interval in consideration. This is not the case for the wind turbines pitch angles under CYP-based AWC and its pitch-based counterpart. In fact, the only pitch angle that is saturated to its upper bound under the CYP-based scheme is the one from wind turbine T27; whereas in the pitch-based method, wind turbines T26, T27 and T28 reach the pitch angle upper bound at different wind directions, see Figure 5.

As expected, wind turbine T25 under CYP-based is kept in greedy mode in all the considered wind directions.

The simulations results for turbulence intensity  $TI=0.16$  in the Test array 1 of the Sedini wind farm exhibit a similar performance as the above case with  $TI=0.10$ . For this reason, velocity flow, angles actions and power plots are not presented. Instead, the maximum power gain results are summarized in Table 2. The same conclusions hold, and CYP-based AWC is the scheme that shows the best power production gain result. Moreover, the power gain results from one turbulence intensity to the other differ by a factor of 0.858 in average under all control methods.

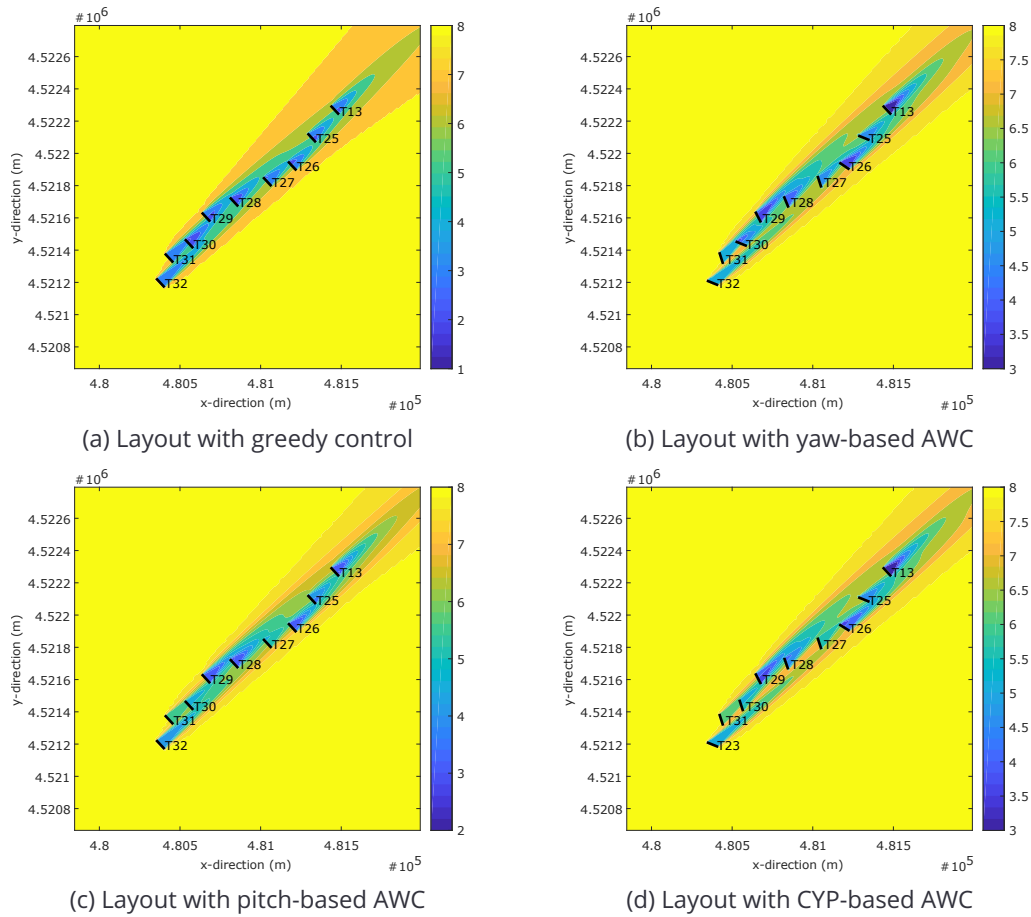
### 3.4.2 Sedini wind farm: Test array 2

Now the Test array 2 of the Sedini wind farm (see Figure 1) is considered. The clustered turbines are distributed on a zigzag-like pattern so that full overlapping is avoided.



**Table 2. Controlled maximum power gain of Test array 1 for different turbulence intensity**

Turbulence intensity (TI)	Maximum power gain		
	Yaw-based	Pitch-based	CYP-based
0.10	1.1531	1.055	1.1631
0.16	1.003	1.001	1.004

**Figure 7. Flow velocities [m/s] at hub for Test array 2 of the Sedini wind farm at maximum power wind direction ( $237^\circ$ ) and  $TI=0.10$** 

Similar to the Test array 1, it is possible to see in Figure 7 that the last downstream wind turbine T13 is kept under greedy control in all AWC strategies. It is also appreciated that the wake losses are the lowest under CYP control, with yaw-based AWC in second place, pitch-based in third place, and the greedy control in last place as expected.

The performance of each turbine's yaw and pitch angles along an interval of wind directions are shown in the top and middle plots of Figure 8; whereas the power gain behavior on the same interval of wind directions is shown in the bottom plot.

As expected from the previous velocity flow analysis, it is clear that the power production gain of the Test array 2 under CYP-based AWC (19.18%) is higher than with the yaw-based (16.71%) and pitch-

based (6.43%) AWC counterparts. Notice that in the neighborhood of maximum power production wind direction ( $227^\circ$ ), the yaw and pitch angles have different values are simultaneously active.

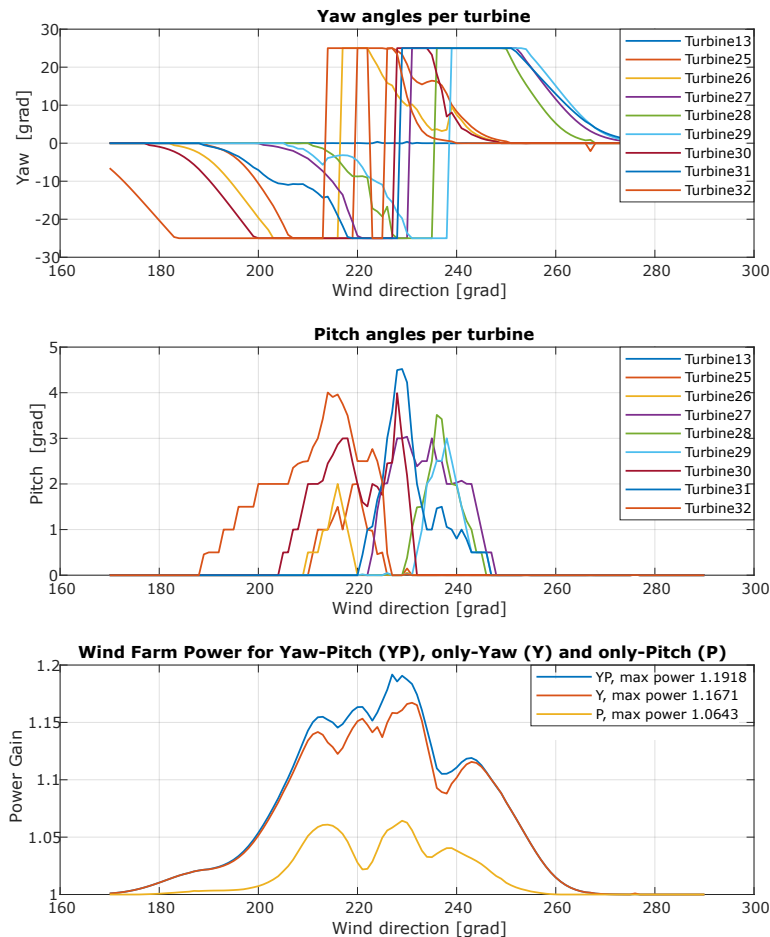


**Figure 8. Test array 1 of the Sedini wind farm under CYP-based AWC and TI=0.10**

Similar to the Test array 1, Table 3 contains the maximum power gain under the three AWC methods that considered in this chapter, for two different turbulence intensity values. The power gains from the first turbulence intensity to the other differ by a factor of around 0.9717, in average.

**Table 3. Controlled maximum power gain of Test array 2 for different turbulence intensity**

Turbulence intensity (TI)	Maximum power gain		
	Yaw-based	Pitch-based	CYP-based
0.06	1.1671	1.0643	1.1918
0.16	1.132	1.047	1.146

### 3.4.3 Three turbine case in full wake overlapping

This section studies on the three turbine layout of Figure 2.

This case is particularly interesting for studying the effect of CYP-based AWC due to the maximum farm power production occurs exactly at the wind direction ( $180^\circ$ ) in which the three turbines are in

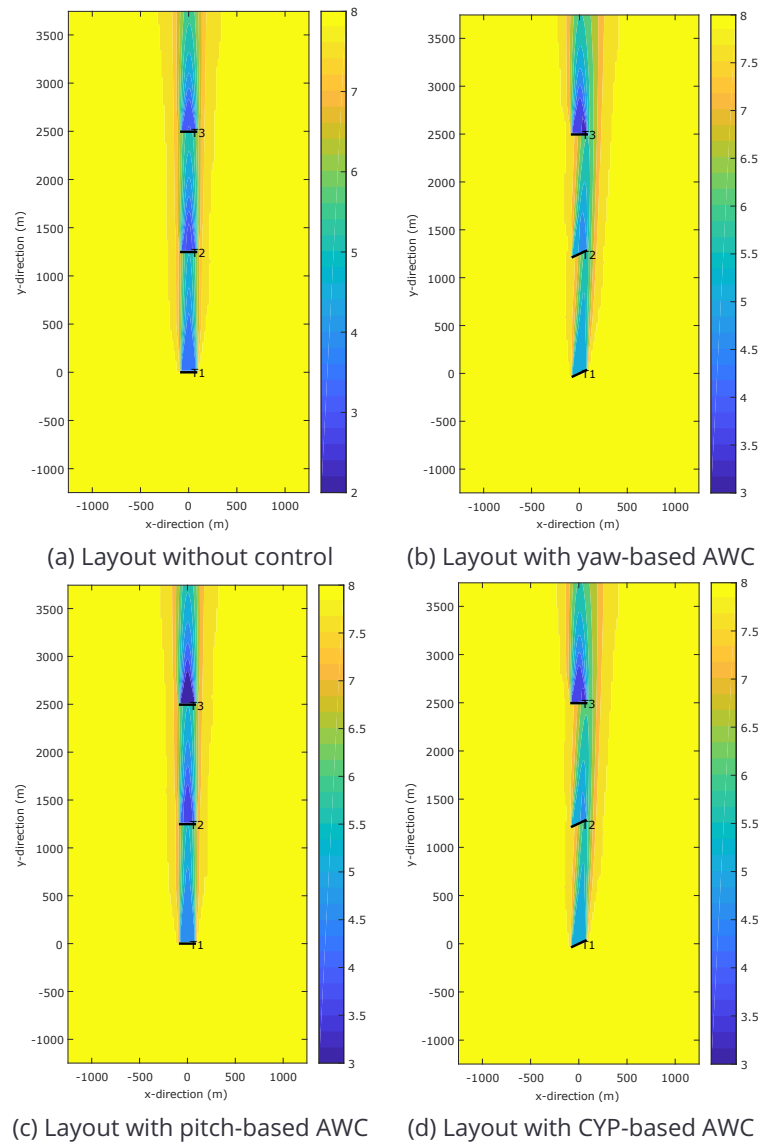


**Figure 9. Three turbines case at maximum power wind direction (180°) and TI=0.06**

full wake overlapping. The velocity flow performance a maximum power gain production for each of the control methods used in this chapter is shown in Figure 9, where a turbulence intensity of 0.06 has been considered.

It can be seen that pitch-based control (Figure 9(b)) improves the wake effects from turbine T1 to turbine T2, but for the rest is close to the wakes effects with greedy control (Figure 9(a)). Indeed, it is shown in the bottom plot of Figure 10 that the power gain increase is of 3%, which is much smaller compared to the other Sedini cases (see Table 2 and Table 3). This is because the maximum power production occurs exactly at the direction in which all turbines are in full wake overlapping. As in the previous simulation examples, the last downstream wind turbine is in greedy control configuration, while the the other two are pitching.

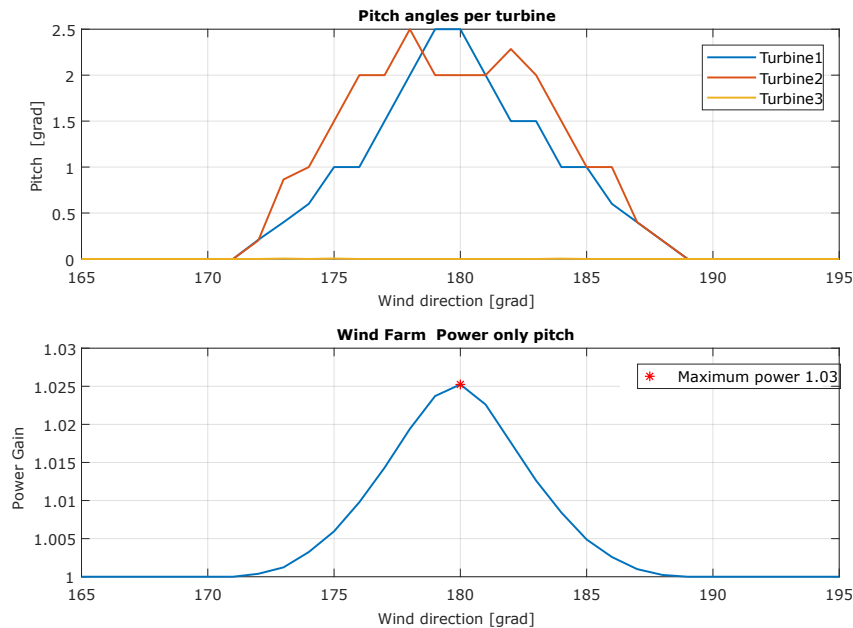


**Figure 10. Three turbine case wind farm under pitch-based AWC and TI=0.06**

On the other hand, the velocity field under yaw-based (Figure 9(c)) and CYP-based (Figure 9(d)) has clearly lower wake effects with respect to the pitch-based AWC strategy. Nevertheless, it is not clear with which of these two AWC the velocity field has the best performance. In order to clarify it, consider the power gain curves in Figure 11 and Figure 12. As expected, the CYP-based strategy has a bigger increase, 20.42%, in power production gain than the yaw-based method, 20.35%; but there is not much difference.

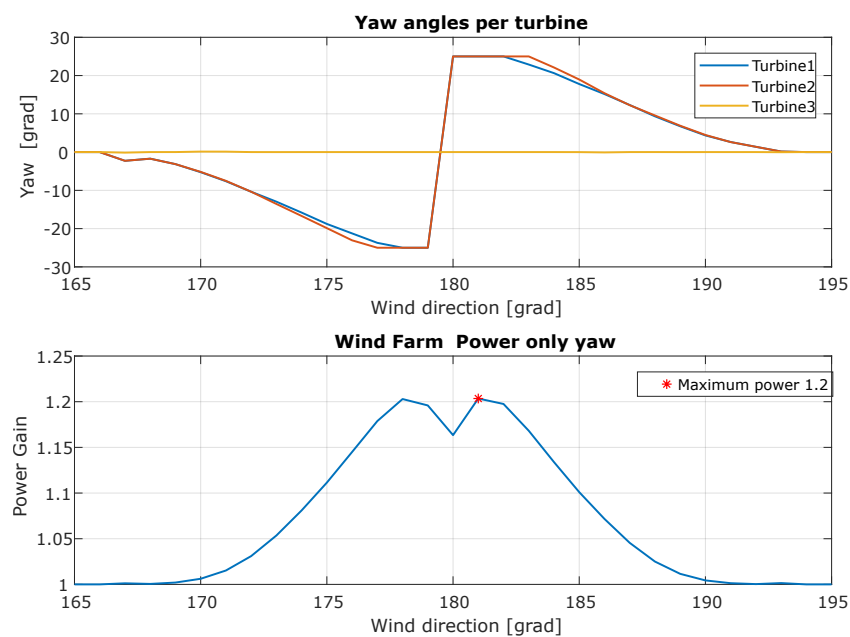


**Figure 11. Three turbine case wind farm under yaw-based AWC and TI=0.06**

Again, the last downstream turbine T3 is in greedy configuration, while the other two are yawing. Notice that the yawing behavior of turbines T1 and T2 is almost synchronized; see Figure 9.

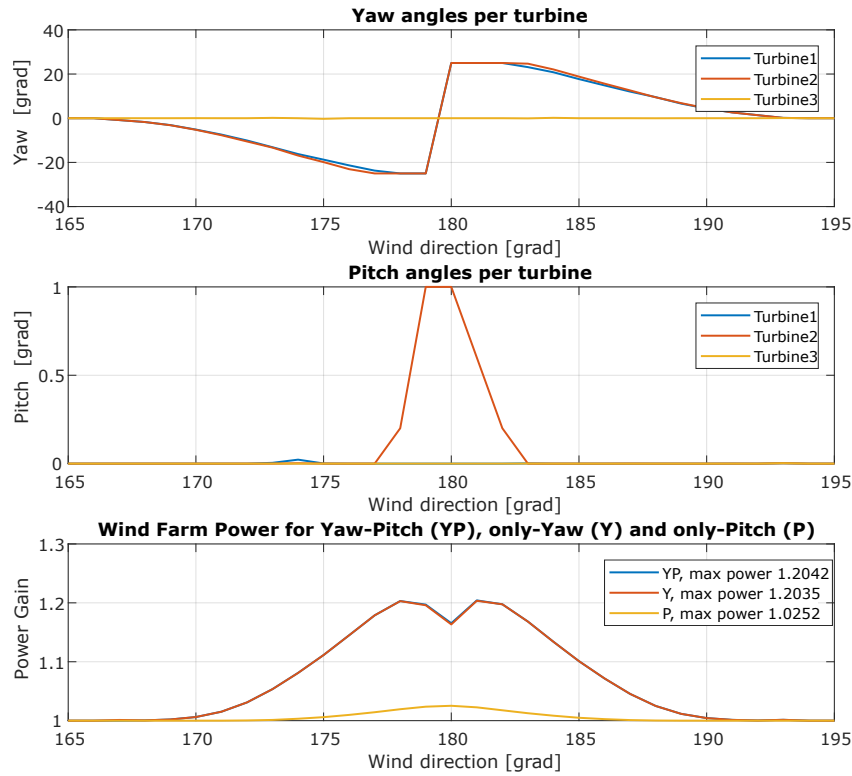


**Figure 12. Three turbine case wind farm under CYP-based AWC and TI=0.06**

There is a power gain loss around wind direction  $180^0$  in the bottom plot of Figure 11. Despite the CYP-based scheme has a small power gain increase, the power gain loss of the yaw-based AWC is not compensated by yawing and pitching simultaneously, the bottom plot of Figure 12. The main reason is that, as it is shown in the middle plot in the same figure, only turbine T2 is pitching and only in a small region of wind directions. Therefore, it follows that under yaw-based and CYP-based AWC approaches, this wind farm produces almost the same power production increase, but CYP may still be more beneficial in terms of loading.

### 3.5 Conclusions and future work

In this chapter a combined yaw and pitch based active wake control strategy has been evaluated on realistic wind farm layouts using the steady-state wind farm model FLORIS.

The study shows that a CYP-based AWC strategy can take the benefits of the individual yaw-based and pitch based AWC methods. That is, the power gain increase of yaw-based AWC and the potential load mitigation property of the pitch-based method. Even under the full wake overlapping case, the CYP-based strategy showed that pitching can improve the power gain performance over the only yaw-based.

There is a big room for improvements and future research. First, the optimization algorithm used here should be replaced by one that can overcome the problem of local minimum; this may result, for instance in the three turbine case, in extra pitching actions that increase the power gain. Secondly, implement the CYP-based AWC strategy on the control oriented wind farm model FarmFlow. Third, analyze the performance of the three control schemes considered in this study under variable wind speed conditions on FLORIS. A further study consist in investigating the impact of loads of the CYP-based AWC strategy.

Another possible research direction, it is the use of feedback distributed control methods for improving the optimization and adding group coordination properties to the wind farm.

## 4 CLOSED-LOOP MODEL-BASED CONTROL USING A STEADY-STATE SURROGATE MODEL

This chapter is concerned with closed-loop model-based control for combined induction control and wake steering using a steady-state surrogate model. Initial work on the framework is described in Section 4.1, where two compromising assumptions are made – being that the wind direction is constant and assumed to be measured. Then, in Section 4.2, a theoretical analysis is performed on the observability of the ambient conditions. This approach is leveraged to decide which measurements are necessary to estimate the ambient conditions. Finally, a robust closed-loop controller is synthesized in Section 4.3, which is then tested under realistic, time-varying wind conditions. This further stress tests the concept and matures it for practical usage.

### 4.1 Combined induction control and wake steering under constant inflow conditions

A concept often explored in the literature of wind farm control has been the static derating of upstream turbines in order to increase the power yield of the wind farm. This derating occurs by changing the turbine generator torque and/or the blade pitch angles. While often promising in simplified simulation studies, this wind farm control concept has led to mixed results in high-fidelity simulation [4] and scaled experiments [17] in terms of increasing the power production of the wind farm. A more fitting goal for induction control is load mitigation and electricity grid frequency regulation (grid integration) [14], which are not further discussed in this chapter. In contrast to induction control, the concept of wake redirection by purposeful misalignment of the rotor plane with the inflow has been convincingly promising in the literature of wind farm control in terms of increasing the power yield of wind farms. Wake redirection typically refers to a yaw misalignment, but a tilt misalignment is theoretically possible too [6]. Numerous high-fidelity simulations [33], scaled experiments [17] and full-scale experiments [29] have shown significant improvements in power yield compared to greedy operation for yaw-based wake redirection control.

#### 4.1.1 Methodology and results

In this section, a closed-loop model-based control framework is proposed. In this framework, a simplified surrogate model of the wind farm is used twofold. The first use of the surrogate model is to estimate the ambient conditions through a model inversion approach. Thus, we answer the question “what ambient conditions produced the turbine signals that we currently measure in our wind farm?”. Secondly, we use the surrogate model to optimize the control setpoints, such as to increase the power yield of the wind farm. Thus, we answer the question “what turbine yaw angles lead to the highest amount of energy extraction?”

The remainder of this section shows the corresponding publication for the American Control Conference (ACC), which took place in Philadelphia, Pennsylvania, U.S., on July 10-12, 2019. This paper was accepted as a tutorial paper on the topic of wind farm control [24].

# A tutorial on the synthesis and validation of a closed-loop wind farm controller using a steady-state surrogate model

Bart M Doekemeijer<sup>†</sup>, Paul A Fleming<sup>‡</sup> and Jan-Willem van Wingerden<sup>†</sup>

**Abstract**—In wind farms, wake interaction leads to losses in power capture and accelerated structural degradation when compared to freestanding turbines. One method to reduce wake losses is by misaligning the rotor with the incoming flow using its yaw actuator, thereby laterally deflecting the wake away from downstream turbines. However, this demands an accurate and computationally tractable model of the wind farm dynamics. This problem calls for a closed-loop solution. This tutorial paper fills the scientific gap by demonstrating the full closed-loop controller synthesis cycle using a steady-state surrogate model. Furthermore, a novel, computationally efficient and modular communication interface is presented that enables researchers to straight-forwardly test their control algorithms in large-eddy simulations. High-fidelity simulations of a 9-turbine farm show a power production increase of up to 11% using the proposed closed-loop controller compared to traditional, greedy wind farm operation.

## I. INTRODUCTION

As wind turbines extract energy from the air stream, a slower, more turbulent flow trails behind their rotors, called the “wake”. In wind farms, wake interaction leads to losses in power capture and accelerated structural degradation when compared to freestanding turbines (e.g., [1]). For example, for the Lillgrund offshore wind farm, wake losses have been estimated at 23% in the literature [2]. The area of wind farm control aims to minimize these wake losses by intelligently operating the turbines in the farm. A popular method to reduce wake losses in the literature is by misaligning the rotor planes with the incoming flow using their yaw actuators, thereby laterally deflecting the wake away from downstream turbines [3]. This methodology is called “wake redirection control” or “yaw control”. However, an accurate model of the wind farm is a prerequisite to accurately determine the optimal misalignment angles of the turbines [4].<sup>1</sup>

The concept of wake redirection control has been demonstrated successfully in a number of situations in the literature. Among others, [7], [8] demonstrated the concept in high-fidelity simulation. Furthermore, [9], [10] demonstrated the

concept of wake redirection control in wind tunnel experiments, and [11], [12] even tested the concept situationally in full-scale field experiments. However, all these experiments followed an open-loop approach, in which the information flows as demonstrated in Fig. 1.

However, due to the lack of information and the complicated dynamics at a range of spatial and temporal scales inside the wind farm, accurate control cannot be achieved without feedback [4]. More precisely, the surrogate models used in the framework of Fig. 1 are only accurate in particular situations, and do not suffice for all the conditions relevant throughout the annual operation of the wind farm. Hence, a closed-loop framework is preferred, in which information flows as demonstrated in Fig. 2. In this closed-loop control setting, measurements are used in a real-time optimization framework to determine the next control policy. Here, a simplified surrogate model of the wind farm is calibrated in real-time using noisy measurements from wind farm. These measurements may originate from, e.g., sensors inside the wind turbine, measurement towers, or lidar systems [13]. After calibration, the surrogate model should more accurately capture the current dynamics inside the wind farm. Then, a model-based optimization algorithm employs this surrogate model to find the optimal control settings for each turbine, where optimality is defined according to the respective control objective. The frequency at which the closed-loop controller operates depends on the surrogate model, the frequency at which measurements are available, the computational hardware, and the algorithms internal to the wind farm controller (the adaptation and optimization algorithm, respectively).

To synthesize a closed-loop controller, a number of key steps are taken, as displayed in Fig. 3. These steps are, in logical order:

- 1) Surrogate model selection: the closed-loop framework of Fig. 2 requires an accurate yet computationally tractable mathematical model of the dynamics inside the wind farm that are relevant for control. This can be either a steady-state model of the wind farm which predicts the time-averaged effects of a control policy on the power output of the wind farm (e.g., [7], [10], [14], [15]), but can also be a dynamic model which predicts the second-to-second flow and wind turbine dynamics (e.g., [8], [16]–[19]). The surrogate model for the closed-loop controller in this work is described in Section II.

<sup>†</sup>Bart Doekemeijer and Jan-Willem van Wingerden are with the Delft Center for Systems and Control (DCSC), Faculty of Materials, Mechanical, and Maritime Engineering (3mE), Delft University of Technology, The Netherlands b.m.doekemeijer@tudelft.nl, j.w.vanwingerden@tudelft.nl

<sup>‡</sup>Paul Fleming is with the National Renewable Energy Laboratory (NREL), Golden, Colorado, United States of America paul.fleming@nrel.gov

<sup>1</sup>There is research towards model-free methods for wind farm optimization (e.g., [5], [6]), but the time delays involved in wake propagation pose a real challenge to such methods. This is not further explored here, and the interested reader is referred to Boersma et al. [4].



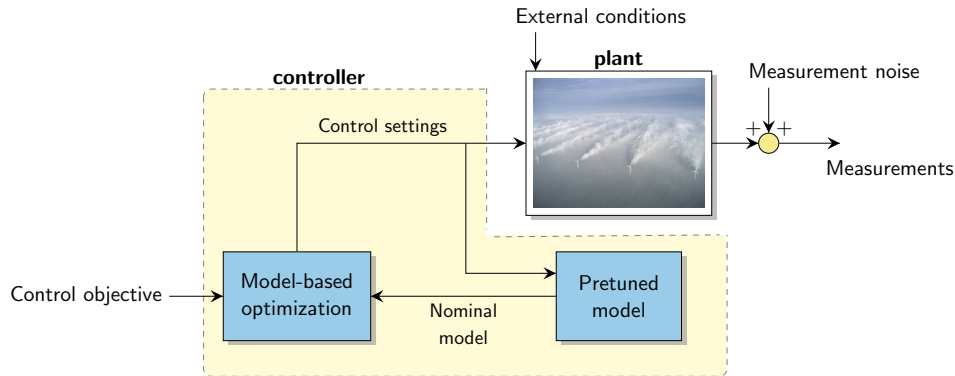


Fig. 1. The open-loop control framework, in which a pretuned surrogate model is used to determine an optimal control policy, according to the assigned control objective (e.g., power maximization, power reference signal tracking).

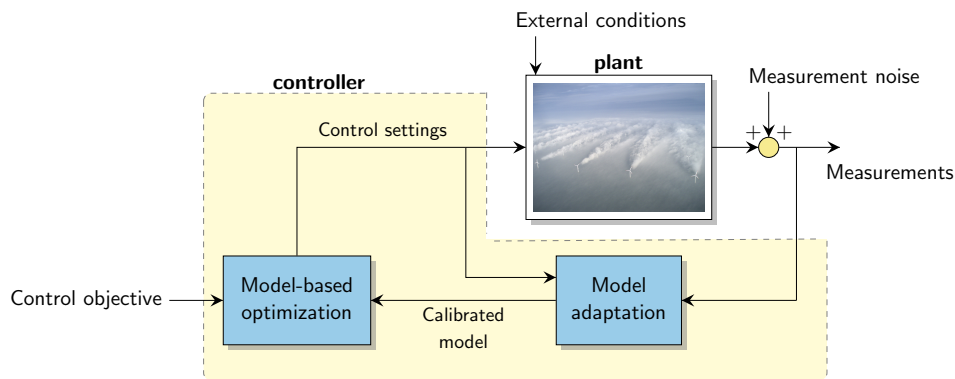


Fig. 2. The closed-loop control framework, in which measurements are used in real-time to calibrate a surrogate model. This surrogate model is then used to determine an optimal control policy, according to the assigned control objective (e.g., power maximization, power reference signal tracking).



Fig. 3. Flowchart for closed-loop controller synthesis

2) Surrogate model calibration through high-fidelity simulation: typically, surrogate wind farm models contain a number of tuning parameters which are dependent on the wind turbines and wind farm topology modeled. To push the accuracy of the surrogate model, the tuning parameters are optimized through high-fidelity simulation prior to controller algorithm design. Typically, quantities of interest to fit the surrogate model for are the turbine power capture, as this often has an important role in the optimization objective of the wind farm controller, and possibly flow dynamics at particular locations, as these may have an important contribution for the real-time calibration algorithm in the closed-loop controller (e.g., as in [20]). A priori (offline)

calibration with high-fidelity data is advantageous compared to calibration with experimental data, in the sense that measurement errors are not an issue. Furthermore, the full three-dimensional flow field is available at any point in time. In this work, the high-fidelity simulation model will be described in Section III, after which offline model calibration will be discussed in Section IV.

3) Surrogate model validation through high-fidelity simulation: Once the model has been calibrated, it's accuracy should be validated to ensure the model parameters have not been over-fit for the calibration dataset. If successful, the next step is model validation with experimental data. Model validation through

simulation will be the topic of Section IV.

- 4) Surrogate model (calibration and) validation with experimental data: after offline model calibration, the surrogate model should be validated, ideally with field data of the wind farm for which the closed-loop controller is synthesized. For example, Schreiber and Bottasso [21] and Annoni et al. [22] have demonstrated this validation procedure for simplified steady-state surrogate models. This step is considered to be out of the scope of this paper for the presented case study.

- 5) Online estimation & optimization algorithm design: Once the surrogate model is validated, the controller is to be synthesized. As shown in Fig. 2, the closed-loop controller consists of two components: an estimation algorithm which adapts the surrogate model to the current conditions inside the farm in real time, and an optimization algorithm that determines the optimal control policy of the wind turbines for the conditions at hand.

Literature on online estimation for wind farm surrogate models is scarce. Fortunately, additional sensing equipment in the wind farm such as lidar systems are becoming increasingly popular in the literature (e.g., [13], [23]). This additional information may be used on the turbine level for load reduction, but can additionally be used on the wind farm level for real-time surrogate model calibration. However, currently, the step of estimation has conveniently been ignored in most of the literature on wind farm control (e.g., [8], [24], [25]), yielding an open-loop control solution. In some cases, a simplified state estimation algorithm has been applied for dynamic surrogate models, such as a linear Kalman filter (e.g., [17], [26]). More recently, there have been positive developments in the field of real-time model adaptation, using more sophisticated estimation algorithms that attempt to balance accuracy with computational efficiency (e.g., [27], [28]).

In terms of optimization, for steady-state surrogate models, a gradient-based or nonlinear optimization algorithm is typically employed to determine the optimal steady-state control settings for the wind farm (e.g., [7], [29], [30]). For dynamic surrogate models, typically predictive control methods are followed to yield an optimal control policy, which typically is a time-varying solution (e.g., [24], [31], [32]). Model-based estimation and optimization will be the topic of Section V.

- 6) Controller verification through high-fidelity simulation: before deploying the controller in the field, it should be tested in high-fidelity simulation to ensure robustness and to provide an insight of the potential gains. Another important factor to investigate is the change in loads on the turbine structure due to the

new control policy. In simulation, identical inflows can be simulated, allowing one-to-one comparisons of the controller with the baseline situation. While many controllers in the literature have been tested in simulation, they were typically assessed in idealistic conditions, using simplified models [4]. There are only a handful of closed-loop control algorithms that were tested in a high-fidelity wind farm simulation (e.g., [8], [33]–[35]). An important contribution of this work is the facilitation of a communication infrastructure that enables researchers to test their control algorithms more easily in a high-fidelity environment. Controller verification through simulation is the topic of Section VI.

- 7) Controller validation through field experiments: finally, the wind farm controller should be deployed in the field. The literature on this topic has been very limited (e.g., [11], [12]). Generally, it may be difficult to reliably measure the gains of the closed-loop control algorithm compared to greedy control, as the ambient conditions vary continuously. Due to measurement uncertainty, the need for additional sensors and processing equipment, and the changing atmospheric conditions, controller validation through field experiments is significantly more complicated than in simulation, yet very necessary. Controller validation through field experiments is out of the scope of this work.

Even though the flowchart is drawn linearly in Fig. 3, one has to note that it is often necessary to go through multiple iterations of simulation, algorithm development, and experimental validation, before satisfactory wind farm control performance has been realized.

Most of the literature on wind farm control has focused on only one component of the closed-loop controller synthesis for wind farms. Typically, this is either the surrogate model or the optimization algorithm. Furthermore, these solutions are typically only tested in a simplified simulation environment, and therefore the usefulness of these control solutions remains uncertain. To address this scientific gap in the literature, the main contributions of this paper are:

- the explanation and demonstration of the full closed-loop controller synthesis cycle for wind farms using a steady-state surrogate model of the dominant wind farm dynamics,
- the development of an open-source, open-access communication interface that enables researchers to straightforwardly test their control algorithms (developed in Python, MATLAB, or a similar language) with the high-fidelity large-eddy simulator SOWFA [36],
- providing a benchmark/example simulation case in which a closed-loop wind farm control algorithm relying on a simplified surrogate model is tested in high-fidelity simulation [37].

The structure of the paper is as follows. First, a steady-state surrogate model of the wind farm is outlined in Section II. A high-fidelity simulation model used for model calibration, validation, and controller verification is discussed in Section III. Then, the surrogate model is calibrated and validated through high-fidelity simulation in Section IV. Further, a closed-loop controller is synthesized using this surrogate model in Section V. Finally, controller verification through high-fidelity simulation is the topic of Section VI. The paper is concluded in Section VII.

## II. SURROGATE MODEL

The surrogate model used in this work combines a single wake model for wake redirection and turbine derating based on [10] with a wake deficit summation model [38], a turbine-induced turbulence model [39], and a turbulence summation model [40] from the literature. The focus in this section is on the single wake model, as it is the most insightful for the remainder of this paper. This surrogate model is selected for its strong theoretical origin, its performance when compared to experimental data from wind tunnel testing [10] and experimental data from the field [22], and for the fact that it has fewer tuning parameters than some comparable models (e.g., [7]). Note that this surrogate model is interchangeably called the “FLO Redirection and Induction in Steady-state” (FLORIS) model in this paper, and has also been published in the public domain under the same name [22], [41].

In short, the near-wake zone is modeled as a linearly converging cone with its base at the turbine rotor, and its tip located at distance  $x_0$  downstream. Here,  $x_0$  is calculated by

$$\frac{x_0}{D} = \frac{\cos(\gamma) \cdot [1 + \sqrt{1 - C_T}]}{\sqrt{2} \cdot (\alpha \cdot I_{\text{rotor}} + \beta \cdot [1 - \sqrt{1 - C_T}])}, \quad (1)$$

with  $D$  the rotor diameter,  $\gamma$  the yaw misalignment angle of the rotor with the incoming flow,  $C_T$  the non-dimensional thrust coefficient,  $I_{\text{rotor}}$  the turbulence intensity at the rotor of the turbine, and  $\alpha$  and  $\beta$  tuning parameters. A schematic overview of the wake model is given in Fig. 4.

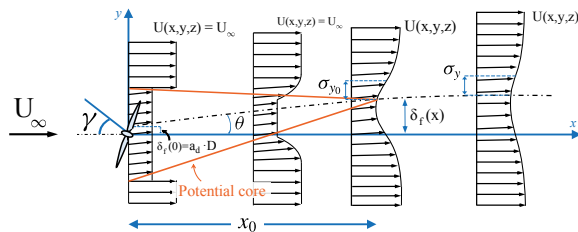


Fig. 4. A schematic drawing of the single wake model, taken and modified from [10].

At the onset of the near wake and in the far wake region, the wake deficit follows the shape of a two-dimensional

Gaussian distribution, according to

$$\frac{U(x, y, z)}{U_\infty} = 1 - \left( 1 - \sqrt{1 - \frac{\sigma_{y0}\sigma_{z0}}{\sigma_y\sigma_z} C_T} \right) \times \exp\left( \frac{(y - \delta_f)^2}{2\sigma_y^2} + \frac{z^2}{2\sigma_z^2} \right), \quad (2)$$

where  $U_\infty$  is the wind speed far upstream of the turbine,  $\sigma$  is the standard deviation in the specified direction, and  $(x, y, z)$  is the Euclidian space with its origin at the turbine hub,  $x$  aligned with the wind direction and  $z$  being positive upwards. The Gaussian-shaped wake is centralized around the centerline. The centerline is displaced in  $y$ -direction from the  $x$ -axis by distance  $\delta_f$  due to a yaw misalignment and the rotor rotation, calculated as

$$\delta_f = \delta_r(x) + \tan(\theta) x_0 + \frac{\theta}{5.2} \cdot \left( C_0^2 - 3e^{1/12} C_0 + 3e^{1/3} \right) \times \sqrt{\frac{\sigma_{y0}\sigma_{z0}}{k_y \cdot k_z \cdot C_T}} \cdot \ln \left[ \frac{(1.6 + \sqrt{C_T})(1.6S_\sigma - \sqrt{C_T})}{(1.6 - \sqrt{C_T})(1.6S_\sigma + \sqrt{C_T})} \right]. \quad (3)$$

Here,  $\theta$  is the initial deflection angle, calculated as

$$\theta \approx \frac{0.3\gamma}{\cos \gamma} \left( 1 - \sqrt{1 - C_T \cos \gamma} \right). \quad (4)$$

Furthermore,  $C_0 = 1 - \sqrt{1 - C_T}$ ,  $k_y$  and  $k_z$  are linear wake expansion coefficients similar to that in Jensen [14], and  $S_\sigma$  is defined as  $S_\sigma = \sqrt{(\sigma_y\sigma_z)/(\sigma_{y0}\sigma_{z0})}$ , with  $\sigma_y$  and  $\sigma_z$  the standard deviations of the Gaussian in the  $y$ - and  $z$ -direction, respectively. These are calculated as

$$\sigma_y = \sigma_{y0} + (x - x_0)k_y, \quad \text{with} \quad \sigma_{y0} = \frac{D}{2\sqrt{2}} \cos \gamma, \quad (5)$$

$$\sigma_z = \sigma_{z0} + (x - x_0)k_z, \quad \text{with} \quad \sigma_{z0} = \frac{D}{2\sqrt{2}}. \quad (6)$$

The wake expansion coefficients are a function of  $I_{\text{rotor}}$ , as

$$k_y = k_z = k_a \cdot I_{\text{rotor}} + k_b, \quad (7)$$

with  $k_a$  and  $k_b$  tuning parameters. Further,  $\delta_r$  is the wake deflection induced by the rotation of the blades, approximated using a linear function following the idea of Gebraad et al. [7], by  $\delta_r = a_d \cdot D + b_d \cdot x$ , with  $a_d$  and  $b_d$  tuning parameters.

Finally, the time-averaged power capture of a turbine is calculated by combining the effects of all wakes impinging this turbine's rotor following Katic [38] and actuator disk theory. The interested reader is referred to related literature [10], [22] for more information.

## III. HIGH-FIDELITY MODEL

In this work, the Simulator fOr Wind Farm Applications (SOWFA), a high-fidelity simulation model from the U.S. National Renewable Energy Laboratory (NREL), is used for model calibration, model validation and controller verification [36], [42].

### A. SOWFA

SOWFA is a large-eddy simulation model that incorporates a rotating actuator disk implementation of wind turbines, and solves the three-dimensional, filtered, unsteady Navier-Stokes equations over a finite temporal and spatial mesh, accounting for Coriolis and geostrophic forcing terms. Large-eddy simulation models such as SOWFA resolve larger scale flow dynamics directly, and employ a subgrid-scale model for smaller eddy dynamics. SOWFA has been used on multiple occasions for surrogate model calibration (e.g., [7], [19], [43]), model validation, and wind farm controller verification (e.g., [28], [33], [34], [43]).

### B. Wind farm controller interface

In order to test controllers in a closed-loop setting, measurement data and control settings need to be passed between SOWFA and an external wind farm controller periodically throughout the simulation. As most wind farm control algorithms from the literature are implemented in Python or MATLAB, and SOWFA operates in C, coupling these pieces of software is not straight-forward. For this reason, an important contribution of this work is the development of an interface that allows researchers to test their control algorithms with SOWFA without making significant modifications to their code.

The open-source software zeroMQ [44] was implemented in SOWFA as a message passing interface to an external wind farm controller and published in the public domain [42]. Using this interface, one can straight-forwardly expand their wind farm controller implemented in a programming language of choice (supporting zeroMQ) to receive measurement data from SOWFA, and return control settings. Note that SOWFA and the wind farm controller are run in parallel, and can even operate on different computers, platforms, and networks – as long as a (network-based) connection can be made. Currently, the TCP protocol is used for communication.

The order of operations in a typical wind farm simulation using the ZeroMQ interface is shown in Fig. 5. In this case, MATLAB is used as an example in which the wind farm control algorithm is implemented. Note that SOWFA and MATLAB are run in parallel, rather than in serial. After initialization, each waits for the other to perform its computations, and thus only one of the two is really performing computations at any point in time. Hence, the idea is to have SOWFA and MATLAB share the same computational cores to minimize the time that cores spend idling. Communication through ZeroMQ happens twice each discrete timestep of the simulation – once to transmit measurements to MATLAB, and once to receive control settings from MATLAB.

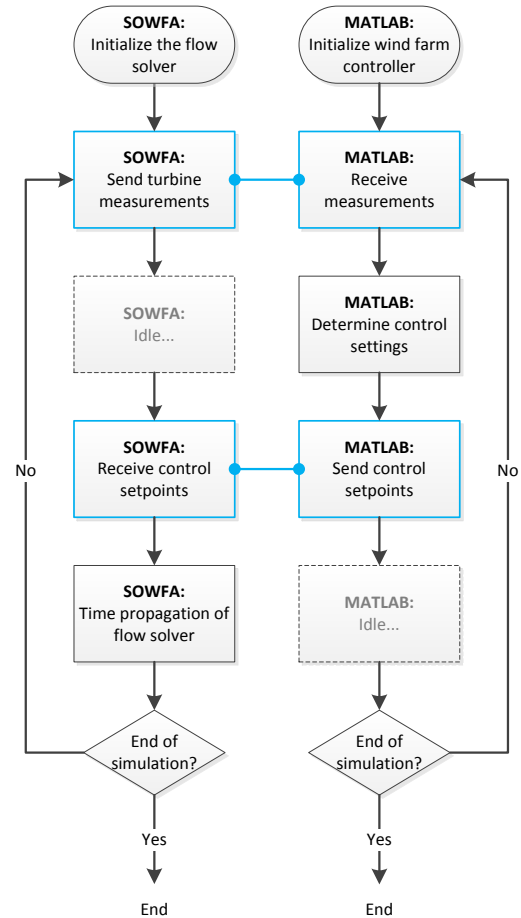


Fig. 5. This figure shows a flowchart of the order of operations in a SOWFA simulation which is coupled to a closed-loop wind farm controller (in this case: implemented in MATLAB).

## IV. MODEL CALIBRATION & VALIDATION THROUGH HIGH-FIDELITY SIMULATION

The model presented in Section II has a number of tuning parameters that may vary with, e.g., the wind farm topology and wind turbine types. Specifically, some of the literature of Section II is based on wind tunnel experiments, in which flow behavior is known to deviate from the actual large-scale wind farms. For this reason, the parameters  $\alpha$ ,  $\beta$ ,  $k_a$ ,  $k_b$ ,  $a_b$  and  $b_d$  are tuned to high-fidelity, true-scale wind farm simulation data in this section, prior to control algorithm design.

We perform a set of single-turbine simulations in SOWFA to calibrate the surrogate model with. This set contains:

- Two types of inflow: one set with uniform inflow and one set with turbulent inflow,
  - each consisting of a set of simulations with yaw angles ranging from  $-30^\circ$  to  $30^\circ$  with a collective blade pitch angle of  $0^\circ$ ,

- and another set of simulations with a turbine yaw angle of  $0^\circ$  and the collective blade pitch angle varying from  $1^\circ$  to  $4^\circ$ .

This covers both wake deflection and turbine derating for typical turbine operation. The NREL 5MW turbine is used [45]. Using this data, the model is now calibrated offline as follows.

#### A. Calibration methodology

- 1) A spatially and temporally averaged vertical inflow profile is extracted from the high-fidelity dataset. The same inflow profile is used in the surrogate model through a linear spline interpolation. An example is given in Fig. 6.

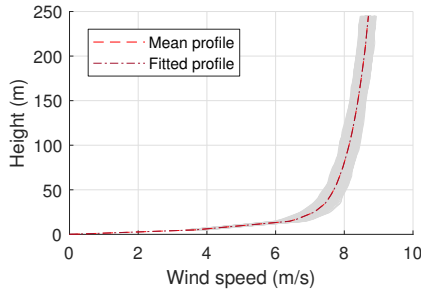


Fig. 6. Inflow comparison. In gray are all vertical profiles along the spatial domain, upon which a single mean profile is fit using spline interpolation.

- 2) The flow field from the high-fidelity simulation is time-averaged over a 10-minute window to average local fluctuations. This fits the scope of what the surrogate model intends to reproduce.
- 3) This time-averaged flow field is sliced at  $3D$ ,  $5D$ ,  $7D$  and  $10D$  downstream, and measurements are sampled over a rectangular grid at each downstream location. An example is shown in Fig. 7 for one of the simulations with uniform inflow.
- 4) A cost function is set-up, where the root-mean-squared error between the flow measurements from SOWFA and that predicted by the surrogate model is minimized for arguments  $\Psi = [\alpha \ \beta \ k_a \ k_b \ a_d \ b_d]$ , as:

$$\Psi_{\text{opt}} = \arg \min_{\Psi} \sum_i (U_{\text{SOWFA}}^i - U_{\text{FLORIS}}(\Psi)), \quad (8)$$

where  $i$  covers the full set of single-turbine simulations. The control settings and ambient conditions varying with  $i$  are neglected in notation here.

An important remark is that, in a more elaborate study, one would have to include the combined effect of turbine derating and wake redirection. Furthermore, a wider range of turbulent inflows should be considered, at various turbulence intensities and various mean wind speeds. Also, it is important to consider the interaction for multiple turbine wakes. However, this is outside of the scope of this work.

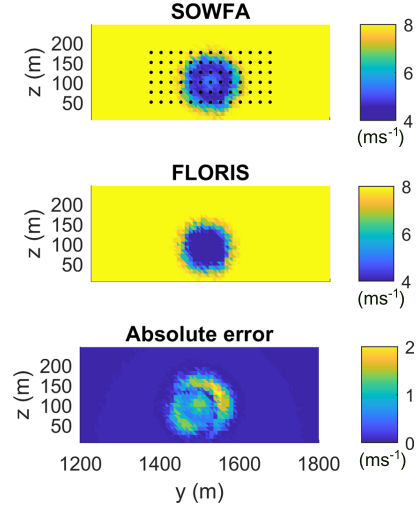


Fig. 7. Wake comparison at 5D downstream. The black dots in the top subplot show the locations of the measurements that will be used to calibrate the surrogate model with SOWFA.

#### B. Calibration results

The model described in Section II has been implemented in MATLAB, and made available to the public [41]. A constrained genetic algorithm optimization approach is used to solve the problem of Eq. 8 in an efficient, parallelized manner, taking approximately 20 CPU-hours. The optimized parameters  $\Psi_{\text{opt}}$  are displayed in Table I. The lower and upper bounds on the parameter optimization space are chosen as to stay within the same order of magnitude as the nominal values presented in the literature [10], in order to limit overfitting and parameter divergence.

TABLE I  
OPTIMAL PARAMETERS  $\Psi_{\text{OPT}}$  FOR THE SURROGATE MODEL AFTER CALIBRATION USING HIGH-FIDELITY SIMULATION DATA

Variable	Lower bound	Upper bound	Optimal value
$\alpha$	$5.80 \cdot 10^{-1}$	9.28	3.16
$\beta$	$3.85 \cdot 10^{-2}$	$6.16 \cdot 10^{-1}$	$3.28 \cdot 10^{-1}$
$k_a$	$9.59 \cdot 10^{-2}$	$1.53 \cdot 10^0$	$1.74 \cdot 10^{-1}$
$k_b$	$9.25 \cdot 10^{-4}$	$1.48 \cdot 10^{-2}$	$9.69 \cdot 10^{-4}$
$a_d$	-1.00	1.00	$-1.34 \cdot 10^{-3}$
$b_d$	$-4.00 \cdot 10^{-2}$	$-2.50 \cdot 10^{-3}$	$-2.68 \cdot 10^{-3}$

Inspecting Table I, it is seen that most of the optimized values lay between their lower and upper bound. This is a good sign, as the opposite situation may indicate overfitting and parameter divergence.

#### C. Validation results

To ensure that the model calibration procedure was successful, the calibrated model is compared with a high-fidelity simulation dataset of a 9-turbine wind farm in which arbitrary yaw angles are applied to the turbines. The model has not been fit for wake interaction, and hence this is an interesting



case to inspect. The yaw angles are derived from a Gaussian distribution, yielding

$$\vec{\gamma} = [2.9^\circ, 32.1^\circ, 12.6^\circ, -20.3^\circ, 16.1^\circ, \\ -14.4^\circ, -1.9^\circ, -21.6^\circ, 29.4^\circ].$$

Note that the pitch angles are kept constant at  $0^\circ$  in this validation case, since it is unlikely that they will be exploited for wind-farm-wide power maximization in the to-be-synthesized optimization algorithm [43]. The time-averaged horizontal plane is shown in Fig. 8. Furthermore, the time-averaged wake deficits at different distances downstream are displayed in Fig. 9. From these figures, a good fit can be seen

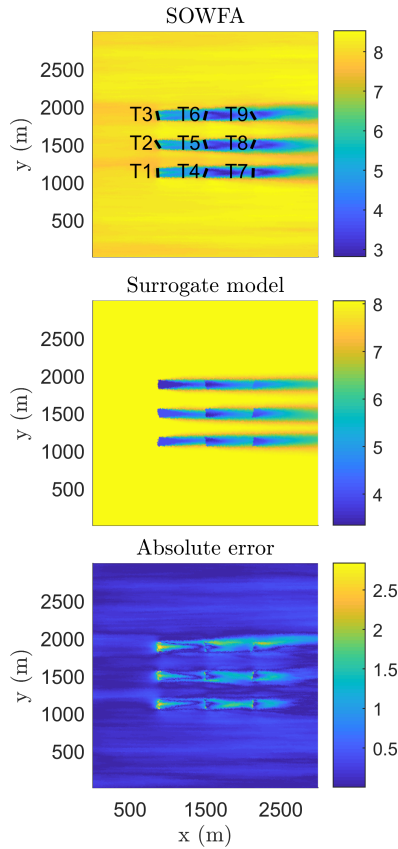


Fig. 8. Validation of the surrogate model with SOWFA: time-averaged flow field at turbine hub height. Units are  $\text{ms}^{-1}$ .

in the far-wake regions and in the single-turbine wakes. As more wakes interact, the fit gets worse, as the model has not been calibrated for this situation. Furthermore, the calibrated model parameters  $\Psi_{\text{opt}}$  have improved the model compared to the nominal model parameters from the literature  $\Psi_0$ , especially for the near-wake and far-downstream region.

The power predicted from the surrogate model is compared to the power from SOWFA in Fig. 10. One can see that the trends are adequately captured in the surrogate model. Though, it slightly underestimates the power capture in most

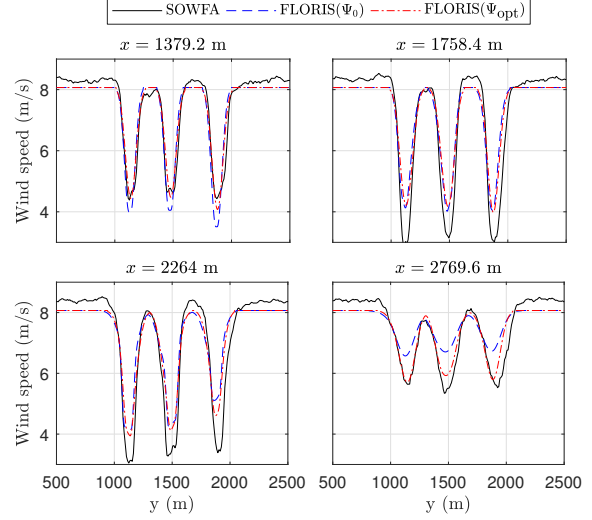


Fig. 9. Validation of the surrogate model with SOWFA: wind speed at hub height at different distances downstream

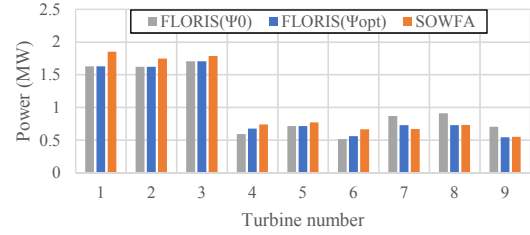


Fig. 10. Validation of the surrogate model with SOWFA: time-averaged power capture per turbine

situations. Furthermore, the calibrated parameters  $\Psi_{\text{opt}}$  show improved performance compared to  $\Psi_0$ .

In conclusion, the surrogate model can accurately capture the wake and power of this 9-turbine wind farm. However, it is still to be seen whether the surrogate model can capture more difficult situations such as deep-wake effects and partial overlap situations such as described in [46]. This should be addressed in future work.

## V. CLOSED-LOOP CONTROLLER SYNTHESIS

The turbine control settings inside the wind farm are optimized using the surrogate model from Section II in a closed-loop setting. The model was calibrated on 10-minute average data in Section IV. In the proposed closed-loop controller, the control settings of the turbines are optimized every 10 minutes. The controller consists of two components: an estimator and an optimizer, each described next.

### A. Estimation

In this work, online estimation is limited to the ambient conditions: the freestream wind direction, turbulence intensity and mean wind speed. A single-shot estimation of all three ambient parameters using only turbine power measurements would most likely result in parameter divergence and overfitting. For example, in a two-turbine case, one can almost always bring the cost function to zero by choosing a certain (wrong) wind direction and wind speed.

To avoid overfitting, firstly the wind direction is assumed to be estimated for each turbine individually following the approach of [47]. Secondly, the wind speed and turbulence intensity are collectively estimated on a farm-wide level by minimizing a weighted root-mean-squared error of the measured and predicted turbine power signals of each turbine, putting a higher weight on the upstream turbines, as

$$\Xi_{\text{opt}} = \arg \min_{\Xi} \sum_i^{N_t} w_i (P_i^{\text{SOWFA}} - P_i^{\text{FLORIS}}(\Xi)). \quad (9)$$

Here,  $N_t$  indicates the number of turbines,  $w_i$  is a weighing term, and  $\Xi = [I_\infty, U_\infty]$  is to be estimated.

### B. Optimization

The wind direction is known to have a significant impact on the optimal yaw angles inside the wind farm [30]. The approach used to estimate the wind direction was derived from [47]. In the corresponding paper, a standard deviation in wind direction estimation of  $6^\circ$  was given for  $U_\infty = 8$  m/s. Hence, a robust optimization approach is followed. In this case, we use the approach from Rott et al. [30], in which the yaw angles are optimized for a probability distribution of wind directions, rather than one deterministic wind direction. The optimization is formulated as follows,

$$\vec{\gamma}_{\text{opt}} = \arg \max_{\vec{\gamma}} \int_{-\pi}^{\pi} \rho(\phi) \sum_i^{N_t} P_i^{\text{FLORIS}}(\gamma_i), \quad (10)$$

with  $\vec{\gamma} = [\gamma_1 \ \gamma_2 \ \dots \ \gamma_{N_t}]$ ,  $N_t$  the number of turbines, and  $\rho$  a probability distribution of variable  $\phi$ , the wind direction. Basically, the yaw angles are now optimal if they provide consistent performance for a range of wind directions in proximity of the mean wind direction. For a solution to exist within a reasonable computational time, the probability distribution is discretized at 5 points, as demonstrated in Fig. 11. Thus, for one function evaluation, the surrogate

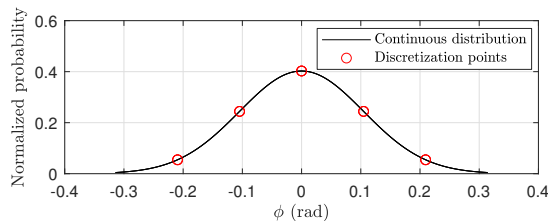


Fig. 11. Robust optimization

model is simulated five times, each with a different wind direction. In the example case of Fig. 11, this would be  $\phi = -0.21$  rad,  $\phi = -0.10$  rad,  $\phi = 0$  rad,  $\phi = 0.10$  rad, and  $\phi = 0.21$  rad. The resulting farm-wide power capture for each of these five simulations are summed, weighted according to their respective probability. The objective is to maximize this weighted sum. Note that in terms of measurement uncertainty, the standard deviation of  $\rho$  goes down with the square root of the number of individual sensors. In this case, the number of individual sensors is equal to  $N_t$ , as each turbine is assumed to provide a unique measurement of (what is assumed to be) the same quantity.

## VI. SIMULATION RESULTS

The 9-turbine wind farm from Fig. 8 is used to test the closed-loop controller described in Section V. The turbines are initialized at a greedy control setting, where  $\gamma_i = 0^\circ \forall i$ . Then every 600 s, the controller determines the optimal yaw angles, constrained with  $-25^\circ \leq \gamma_i \leq 25^\circ \forall i$  to threshold the increase in structural loads due to a yaw misalignment.<sup>2</sup>

### A. Open-loop controller

In the first case, an open-loop (OL) controller is synthesized where a single set of time-invariant ambient conditions  $\Xi$  is assumed. Specifically,  $\Xi$  contains the freestream wind direction  $\phi$ , the turbulence intensity  $I_\infty$  and the mean ambient wind speed  $U_\infty$ , respectively. The true ambient conditions are  $\Xi_{\text{true}} = [0.0^\circ \ 6.0\% \ 8.0 \text{ ms}^{-1}]$ . In the open-loop case, we simulate the situation of a model mismatch by assuming  $\Xi = [10.0^\circ \ 1.0\% \ 6.5 \text{ ms}^{-1}]$ . Additionally, in the OL controller, the probability distribution  $\rho$  in Eq. 10 is assumed to have a zero standard deviation. The optimal control settings for the OL controller are displayed in Table II.

TABLE II  
OPTIMAL CONTROL POLICY USING OPEN-LOOP CONTROL

Time [s]	$\vec{\gamma}_{\text{opt},1:2} [^\circ]$	$\vec{\gamma}_{\text{opt},3} [^\circ]$	$\vec{\gamma}_{\text{opt},4} [^\circ]$	$\vec{\gamma}_{\text{opt},5:6} [^\circ]$	$\vec{\gamma}_{\text{opt},7:9} [^\circ]$
0	0.0	0.0	0.0	0.0	0.0
600	-9.6	-10.9	-12.0	-11.0	0.0
1200	-9.6	-10.9	-12.0	-11.0	0.0
1800	-9.6	-10.9	-12.0	-11.0	0.0

As this is a steady-state, open-loop controller, the optimal yaw angles are time-invariant throughout the simulation.

### B. Closed-loop controller

In the second case, two closed-loop (CL) controllers are synthesized, in which the past 300 s of measurements are time-averaged and used to estimate the ambient conditions  $\Xi$ . The weights  $w_i$  in Eq. 9 are set to be 3 for upstream turbines  $w_{1,2,3} = 3$ , the weights are  $w_{4,5,6} = 2$  for the first row of downstream turbines, and  $w_{7,8,9} = 1$  for the most downstream turbines. Basically, it is assumed that the confidence is

<sup>2</sup>Note that pitch angles were also optimized by the controller, but were found to be zero in all cases.

highest with the unwaked turbines, and the model fit is progressively worse with more wake interactions.

The two closed-loop controllers differ in their optimization approach. The standard deviation of  $\rho$  in Eq. 10 is assumed to be  $0^\circ$  for the deterministic CL controller, and  $\frac{6}{\sqrt{9}} = 2^\circ$  for the robust CL controller, as there are nine turbines providing a unique measurement of (what is assumed to be) the same quantity. The resulting control policy for the robust CL controller is shown in Table III.

TABLE III

OPTIMAL CONTROL POLICY USING CLOSED-LOOP CONTROL AND A ROBUST OPTIMIZATION METHODOLOGY

Time [s]	$\Xi_{\text{opt}} [^\circ, \%, \text{ms}^{-1}]$	$\tilde{\gamma}_{\text{opt},1:3} [^\circ]$	$\tilde{\gamma}_{\text{opt},4:6} [^\circ]$	$\tilde{\gamma}_{\text{opt},7:9} [^\circ]$
0	N/A	0.0	0.0	0.0
600	$\begin{bmatrix} 2.3 & 6.0 & 8.16 \end{bmatrix}$	-24.4	-23.3	0.0
1200	$\begin{bmatrix} -3.7 & 7.6 & 8.15 \end{bmatrix}$	19.6	18.3	0.0
1800	$\begin{bmatrix} 1.1 & 6.9 & 8.15 \end{bmatrix}$	24.5	18.7	0.0

The optimal yaw angles provided by the robust CL controller vary with time, due to the changing atmospheric conditions  $\Xi$ . Note that there is some switching behavior at  $t = 1200$  s in the optimal yaw angles due to the change in sign of the estimated wind direction. While the robust optimization approach should account for this [30], it is expected that the standard deviation for  $\rho$  in the optimization was too low. This should be investigated in future work. The time-averaged flow field in SOWFA under the closed-loop control policy for  $t = 900$  s to  $t = 1200$  s is shown in Fig. 12.

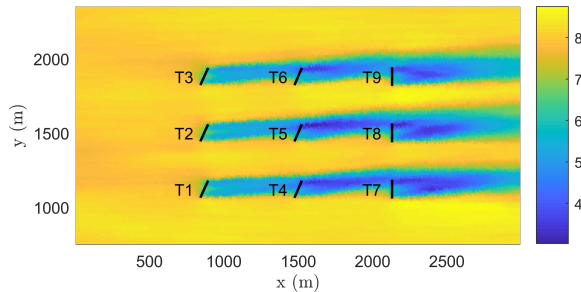


Fig. 12. Time-averaged wind speed in  $\text{ms}^{-1}$  at the horizontal flow slice at  $z = 90$  m (hub-height) for  $t = 900$  to  $t = 1200$  s.

### C. Comparison

The performance of the open-loop and closed-loop controllers is shown in Table IV. In this table,  $\tilde{\gamma}_{\text{opt,CL}}^{\text{det}}$  and  $\tilde{\gamma}_{\text{opt,CL}}^{\text{rob}}$  are the sets of optimal yaw angles obtained in closed-loop by optimizing with a standard deviation for the ambient wind direction  $\rho$  in Eq. 10 of  $0^\circ$  and  $2^\circ$ , respectively. One can see that both the OL and the CL controllers improve the farm-wide power capture compared to a greedy control approach. However, the CL controllers consistently outperform the OL controller, with a situational wind-farm-wide power increase of approximately 3% for the OL controller compared to greedy wind farm operation, and between 7% and 11% for

TABLE IV

COMPARISON OF GREEDY CASE, OPEN-LOOP CONTROLLER CASE, AND THE CLOSED-LOOP CONTROLLERS CASES

Time window	$\gamma = \tilde{\gamma}_{\text{greedy}}$	$\gamma = \tilde{\gamma}_{\text{opt,OL}}^{\text{det}}$	$\gamma = \tilde{\gamma}_{\text{opt,CL}}^{\text{det}}$	$\gamma = \tilde{\gamma}_{\text{opt,CL}}^{\text{rob}}$
0-600 s	10.71 MW	10.71 MW	10.71 MW	10.71 MW
600-900 s	9.78 MW	9.71 MW	9.29 MW	9.40 MW
900-1200 s	9.49 MW	9.80 MW	10.44 MW	10.49 MW
1200-1500 s	9.54 MW	9.78 MW	10.50 MW	10.45 MW
1500-1800 s	9.64 MW	9.92 MW	10.32 MW	10.34 MW
0-2000 s	10.07 MW	10.21 MW	10.40 MW	10.45 MW

the CL controllers. This is due to the fact that the surrogate model more accurately captures the current conditions inside the farm for the CL controllers. The only loss compared to greedy control is for  $t = 600 - 900$  s, in which the effect of yawing the upstream turbines has not yet resulted in a weaker wake on the downstream rotors. Furthermore, the robust optimization approach leads to slightly better performance when compared to an approach in which the wind direction is assumed to be deterministic.

The loss in power capture at  $t = 600 - 900$  s can be more explained using Fig. 13. In this figure, the power signals are time-averaged with a moving average filter (non-causal low-pass filter) with a time window of 50 s for both past and future data, to provide more insight. As turbines 1 and 4 are purposely misaligned with the incoming flow at 600 s, they see a loss in power capture shortly after 600 s. While this generates weaker wakes behind turbines 1 and 4, it takes some time for these weaker wakes to propagate to turbines 4 and 7 downstream. Once that happens, a significant gain can be seen (especially for turbine 7, around 800 s). Furthermore, a similar effect can be seen at 1200 s, since wind turbines 1 and 4 are now yawed towards the opposite direction. This leads to a temporary increase in power capture, as the turbines pass  $\gamma = 0^\circ$ , but eventually also to a decrease due to the stronger wakes generated downstream. After the flow settles, there is again a constant gain in overall power capture compared to the greedy control case.

### D. Discussion

While the closed-loop controllers presented in this section yield a significant increase in wind-farm-wide power production compared to traditional, greedy operation, an important remark should be made. Namely, the controllers have been simulated under idealistic ambient conditions. While the large-eddy SOWFA simulation is of significantly higher fidelity than the surrogate model, the inflow in SOWFA still only has one mean wind direction, wind speed, and turbulence intensity. As the control settings are optimized at a frequency of every 10 minutes, this may or may not be fast enough in a more realistic setting where ambient conditions slowly vary with time. The actuation frequency necessary for wind farm control remains an open question in the research [4]. Because of this, the fidelity necessary for surrogate models also remains an open



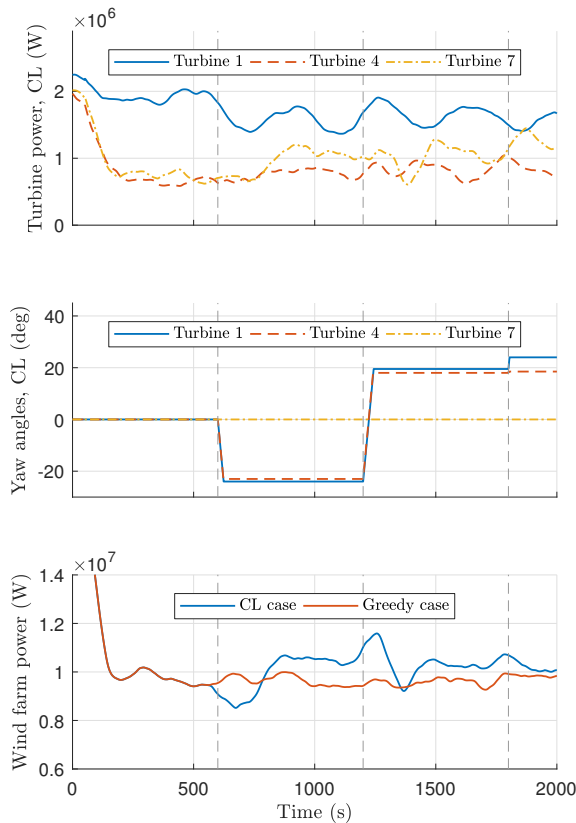


Fig. 13. Timeseries of the power capture and turbine yaw angles for the robust closed-loop wind farm simulation. The first and third subplot show moving averages of the turbine resp. wind farm power capture, averaged by a time window of 50 s in both the past and future data. The yaw angles are updated according to the controller at a rate of 600 s, starting from the traditional greedy control strategy at 0 s.

question, and a wide range of steady-state and dynamical models is investigated in the literature. The study of SCADA data, experimental testing and high-fidelity, large-eddy simulations coupled with mesoscale models should further provide guidance in answering these questions. This is out of the scope of this work.

#### E. Wind farm controller interface

An important contribution of this work is the open-source communication interface developed for the verification of wind farm control algorithms in a high-fidelity environment. For the simulations presented in this section, the computational time required by the ZeroMQ communication was found to be on the order of  $1 \cdot 10^{-3}$  s for sending a single message (set of measurements or control settings) in either direction. This is negligible compared to the computational cost of SOWFA, which is in the order of  $10^1$  s per timestep for this parallelized 80-core case.

## VII. CONCLUSIONS

This paper demonstrated the synthesis cycle of a closed-loop wind farm controller using a steady-state surrogate model. The surrogate model was first calibrated and validated using high-fidelity simulations, after which the controller was tested in a high-fidelity 9-turbine wind farm simulation. To facilitate the testing of wind farm controllers written in MATLAB or Python in a high-fidelity environment, a communication interface was developed for the high-fidelity simulator SOWFA. SOWFA simulations with closed-loop wind farm control showed an increase in wind farm power capture of 7% to 11% through yaw control. Furthermore, the proposed communication architecture has a negligible computational cost. While positive results were shown in the simulations presented in this work, the ambient conditions vary slowly in real wind farms. In theory, this closed-loop framework should be able to deal with such changes. This should be explored further in future work.

## ACKNOWLEDGMENT

The authors would like to thank Manon Kok for the insightful discussions on real-time model calibration of the surrogate model. This project has received funding from the European Union's Horizon 2020 research and innovation programme under grant agreement No 727477.

## SOFTWARE AVAILABILITY

All software presented in this work is open-source. The high-fidelity simulation software SOWFA is developed by NREL [42]. This software repository also includes the communication interface that exchanges information through ZeroMQ. The surrogate model presented in this work is actively being developed by the Delft University of Technology [41]. The community-driven ZeroMQ library is also available in the public domain [44]. The wind farm controller relying on the surrogate model, exchanging information through the ZeroMQ interface with SOWFA, has also been made available [37] as an example and a benchmark case.

## REFERENCES

- [1] S. Kanev, F. Savenije, and W. Engels, "Active wake control: An approach to optimize the lifetime operation of wind farms," *Wind Energy*, vol. 21, no. 7, pp. 488–501,
- [2] R. J. Barthelmie, S. C. Pryor, S. T. Frandsen, K. S. Hansen, J. G. Schepers, K. Rados, W. Schlez, A. Neubert, L. E. Jensen, and S. Neckelmann, "Quantifying the impact of wind turbine wakes on power output at offshore wind farms," *Journal of Atmospheric and Oceanic Technology*, vol. 27, no. 8, pp. 1302–1317, 2010.

- [3] P. A. Fleming, P. M. O. Gebraad, S. Lee, J. W. van Wingerden, K. Johnson, M. Churchfield, J. Michalakakis, P. Spalart, and P. Moriarty, "Simulation comparison of wake mitigation control strategies for a two-turbine case," *Wind Energy*, vol. 18, no. 12, pp. 2135–2143, 2015.
- [4] S. Boersma, B. M. Doekemeijer, P. M. O. Gebraad, P. A. Fleming, J. Annoni, A. K. Scholbrock, J. A. Frederik, and J. W. van Wingerden, "A tutorial on control-oriented modeling and control of wind farms," *American Control Conference (ACC)*, pp. 1–18, 2017.
- [5] J. R. Marden, S. D. Ruben, and L. Y. Pao, "A model-free approach to wind farm control using game theoretic methods," *IEEE Transactions on Control Systems Technology*, 2013.
- [6] M. A. Rotea, "Dynamic programming framework for wind power maximization," *IFAC Proceedings Volumes*, vol. 47, no. 3, pp. 3639–3644, 2014, 19th IFAC World Congress.
- [7] P. M. O. Gebraad, F. W. Teeuwisse, J. W. van Wingerden, P. A. Fleming, S. D. Ruben, J. R. Marden, and L. Y. Pao, "Wind plant power optimization through yaw control using a parametric model for wake effects - a cfd simulation study," *Wind Energy*, vol. 19, no. 1, pp. 95–114, 2016.
- [8] W. Munters and J. Meyers, "An optimal control framework for dynamic induction control of wind farms and their interaction with the atmospheric boundary layer," *Philosophical Transactions of the Royal Society of London A: Mathematical, Physical and Engineering Sciences*, vol. 375, no. 2091, 2017.
- [9] F. Campagnolo, V. Petrović, C. L. Bottasso, and A. Croce, "Wind tunnel testing of wake control strategies," *Proceedings of the American Control Conference (ACC)*, pp. 513–518, 2016.
- [10] M. Bastankhah and F. Porté-Agel, "Experimental and theoretical study of wind turbine wakes in yawed conditions," *Journal of Fluid Mechanics*, vol. 806, pp. 506–541, 2016.
- [11] P. A. Fleming, J. Annoni, J. J. Shah, L. Wang, S. Ananthan, Z. Zhang, K. Hutchings, P. Wang, W. Chen, and L. Chen, "Field test of wake steering at an offshore wind farm," *Wind Energy Science*, vol. 2, no. 1, pp. 229–239, 2017.
- [12] P. A. Fleming, J. Annoni, A. K. Scholbrock, E. Quon, S. Dana, S. Schreck, S. Raach, F. Haizmann, and D. Schlipf, "Full-scale field test of wake steering," *Journal of Physics: Conference Series*, vol. 854, no. 1, 2017.
- [13] A. Scholbrock, P. Fleming, D. Schlipf, A. Wright, K. Johnson, and N. Wang, "Lidar-enhanced wind turbine control: Past, present, and future," in *2016 American Control Conference (ACC)*, 2016, pp. 1399–1406.
- [14] N. O. Jensen, "A note on wind generator interaction," Tech. Rep. RISØ-M-2411, 1983.
- [15] J. F. Ainslie, "Calculating the flowfield in the wake of wind turbines," *Journal of Wind Engineering and Industrial Aerodynamics*, vol. 27, no. 1, pp. 213–224, 1988.
- [16] M. Soleimanzadeh, R. Wisniewski, and A. Brand, "State-space representation of the wind flow model in wind farms," *Wind Energy*, vol. 17, no. 4, pp. 627–639, 2014.
- [17] P. M. O. Gebraad, P. A. Fleming, and J. W. van Wingerden, "Wind turbine wake estimation and control using FLORIDyn, a control-oriented dynamic wind plant model," *American Control Conference (ACC)*, pp. 1702–1708, 2015.
- [18] J. Annoni, P. M. O. Gebraad, and P. Seiler, "Wind farm flow modeling using an input-output reduced-order model," *American Control Conference (ACC)*, pp. 506–512, 2016.
- [19] S. Boersma, B. M. Doekemeijer, M. Vali, J. Meyers, and J. W. van Wingerden, "A control-oriented dynamic wind farm model: Wfsim," *Wind Energy Science Discussions*, vol. 2017, pp. 1–34, 2017.
- [20] C. L. Bottasso and J. Schreiber, "Online model updating by a wake detector for wind farm control," *American Control Conference (ACC)*, 2018.
- [21] J. Schreiber, E. M. Nanos, F. Campagnolo, and C. L. Bottasso, "Verification and calibration of a reduced order wind farm model by wind tunnel experiments," *Journal of Physics: Conference Series*, vol. 854, no. 1, 2017.
- [22] J. Annoni, P. Fleming, A. Scholbrock, J. Roadman, S. Dana, C. Adcock, F. Porté-Agel, S. Raach, F. Haizmann, and D. Schlipf, "Analysis of control-oriented wake modeling tools using lidar field results," *Wind Energy Science Discussions*, vol. 2018, pp. 1–17, 2018.
- [23] A. Rettenmeier, D. Schlipf, I. Wrth, and P. W. Cheng, "Power performance measurements of the nrel cart-2 wind turbine using a nacelle-based lidar scanner," vol. 31, pp. 2029–2034, Oct. 2014.
- [24] J. P. Goit and J. Meyers, "Optimal control of energy extraction in wind-farm boundary layers," *Journal of Fluid Mechanics*, vol. 768, pp. 5–50, 2015.
- [25] M. Vali, V. Petrović, S. Boersma, J. W. Van Wingerden, and M. Kühn, "Adjoint-based model predictive control of wind farms: Beyond the quasi steady-state power maximization," *IFAC World Congress*, vol. 50, no. 1, pp. 4510–4515, 2017.
- [26] G. V. Iungo, C. Santoni-Ortiz, M. Abkar, F. Porté-Agel, M. A. Rotea, and S. Leonardi, "Data-driven reduced order model for prediction of wind turbine wakes," *Journal of Physics: Conference Series*, vol. 625, no. 1, 2015.
- [27] C. R. Shapiro, P. Bauweraerts, J. Meyers, C. Meneveau, and D. F. Gayme, "Model-based receding horizon control of wind farms for secondary frequency regulation," *Wind Energy*, vol. 20, no. 7, pp. 1261–1275, 2017, we.2093.
- [28] B. Doekemeijer, S. Boersma, L. Y. Pao, T. Knudsen, and J. W. van Wingerden, "Online model calibration for a simplified les model in pursuit of real-time

- closed-loop wind farm control,” *Wind Energy Science Discussions*, vol. 2018, pp. 1–30, 2018.
- [29] J. J. Thomas, P. M. O. Gebraad, and A. Ning, “Improving the floris wind plant model for compatibility with gradient-based optimization,” *Wind Engineering*, vol. 41, no. 5, pp. 313–329, 2017.
- [30] A. Rott, B. M. Doekemeijer, J. Seifert, J. W. van Wingerden, and M. Kühn, “Robust active wake control in consideration of wind direction variability and uncertainty,” *Wind Energy Science Discussions*, vol. 2018, pp. 1–22, 2018.
- [31] M. Soleimanzadeh, R. Wisniewski, and S. Kanev, “An optimization framework for load and power distribution in wind farms,” *Journal of Wind Engineering and Industrial Aerodynamics*, vol. 107-108, pp. 256–262, 2012.
- [32] S. Siniscalchi-Minna, F. D. Bianchi, and C. Ocampo-Martinez, “Predictive control of wind farms based on lexicographic minimizers for power reserve maximization,” *American Control Conference (ACC)*, 2018.
- [33] P. M. O. Gebraad and J. W. van Wingerden, “Maximum power-point tracking control for wind farms,” *Wind Energy*, vol. 18, no. 3, pp. 429–447, 2015.
- [34] J. W. Van Wingerden, L. Y. Pao, J. Aho, and P. A. Fleming, “Active power control of waked wind farms,” *IFAC World Congress*, pp. 4570–4577, 2017.
- [35] S. Boersma, B. M. Doekemeijer, S. Siniscalchi-Minna, and J. W. van Wingerden, “A constrained wind farm controller providing secondary frequency regulation: An les study,” *Renewable Energy Journal*, 2018, Under review.
- [36] M. J. Churchfield, S. Lee, J. Michalakes, and P. J. Moriarty, “A numerical study of the effects of atmospheric and wake turbulence on wind turbine dynamics,” *Journal of Turbulence*, vol. 13, no. 14, pp. 1–32, 2012.
- [37] B. M. Doekemeijer, *A MATLAB-based implementation of the ZeroMQ closed-loop wind farm controller for SOWFA relying on the FLORIS model*, English, <https://github.com/Bartdoekemeijer/zeromqServer-FLORIS/tree/ACC2019>, 2018.
- [38] I. Katic, J. Højstrup, and N. Jensen, “A simple model for cluster efficiency,” in *EWEC’86. Proceedings. Vol. 1*, W. Palz and E. Sesto, Eds. A. Raguzzi, 1987, pp. 407–410.
- [39] A. Crespo and J. Hernandez, “Turbulence characteristics in wind-turbine wakes,” *Journal of Wind Engineering and Industrial Aerodynamics*, vol. 61, no. 1, pp. 71–85, 1996.
- [40] A. Niayifar and F. Porté-Agel, “Analytical modeling of wind farms: A new approach for power prediction,” *Energies*, vol. 9, no. 741, 2016.
- [41] B. M. Doekemeijer and R. Storm, *FLORISSE\_M Github repository*, English, [https://github.com/TUDELFT-DataDrivenControl/FLORISSE\\_M](https://github.com/TUDELFT-DataDrivenControl/FLORISSE_M), 2018.
- [42] National Renewable Energy Laboratory (NREL), *SOWFA Github repository*, English, <https://github.com/NREL/SOWFA>, 2018.
- [43] J. Annoni, P. M. O. Gebraad, A. K. Scholbrock, P. A. Fleming, and J. W. van Wingerden, “Analysis of axial-induction-based wind plant control using an engineering and a high-order wind plant model,” *Wind Energy*, vol. 19, no. 6, pp. 1135–1150, 2016.
- [44] Community-driven, *ZeroMQ Github repository*, English, <https://github.com/zeromq/libzmq>, 2018.
- [45] J. M. Jonkman and M. L. Buhl, “FAST v6.0 user’s guide,” English, National Renewable Energy Laboratory (NREL), Technical Report, 2005.
- [46] L. A. Martínez-Tossas, J. Annoni, P. A. Fleming, and M. J. Churchfield, “The aerodynamics of the curled wake: A simplified model in view of flow control,” *Wind Energy Science Discussions*, vol. 2018, pp. 1–17, 2018.
- [47] M. Bertele, C. L. Bottasso, S. Cacciola, F. Daher Adegas, and S. Delpont, “Wind inflow observation from load harmonics,” *Wind Energy Science*, vol. 2, no. 2, pp. 615–640, 2017.

#### 4.1.2 A continued discussion

Looking at the paper presented in Section 4.1.1, it is noted that the optimization algorithm leads to non-derated operation, even though the possibility of derating is incorporated into the optimization. This means that, according to the FLORIS model, there is no benefit in turbine derating (induction control) for power maximization. This agrees with previous findings in the literature [4, 17].

We can solidify this hypothesis by optimizing the induction settings of the turbines inside FLORIS for an arbitrary wind farm. Take a generic 9-turbine wind farm of NREL 5MW turbines represented as static actuator disks. A greedy control approach in which all induction factors are  $1/3$  is negligibly worse than an optimized set of induction control settings. Specifically, optimization of this particular case leads to all turbines besides the most downstream ones to be set at an induction factor of 0.305, leading to a hypothesized power gain of 0.2% over greedy control for the whole wind farm. The wind farm and flowfield are displayed in Fig. 13.

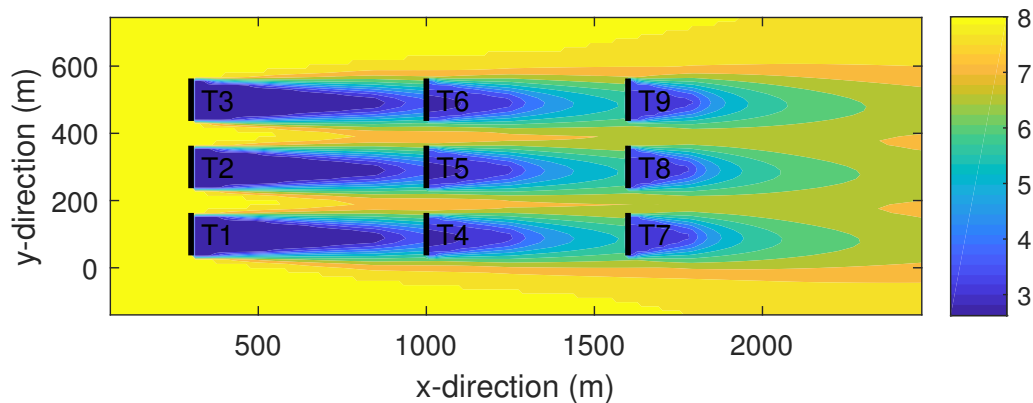


**Figure 13. Flow field [m/s] at turbine hub height for the generic 9-turbine wind farm in which the axial induction factors of turbines 1-6 have been optimized for maximum power capture, found to be 0.305. This leads to an effective power gain of 0.2% according to FLORIS in comparison to operation with an induction factor of 0.333.**

Further, if the actuator disk models are replaced with  $C_p$ - $C_t$  tables generated by a BEM code such as OpenFAST, then no gain can be achieved at all, and the optimal pitch angles are equal to the fine pitch angles [23].

Further, the controller does assign yaw misalignments to the turbines that shed a wake on other downstream turbines. This wake redirection leads to a notable power increase of approximately 7% to 11%. This shows good agreement with what is seen in literature; namely, a significant power yield can be obtained by purposely yawing a subset of the wind turbines away from the mean inflow direction with 10 – 25 degrees, leading to gains in power yield in the order of 5 – 15%.

Further, note that the simulations presented in Section 4.1.1 are of the NREL 5MW turbine. Similar situations focusing on wake redirection control only<sup>3</sup> can be found in [22], which was also previously discussed in deliverable D2.3 of the CL-Windcon project. The success of wake redirection control

<sup>3</sup>Though, results are most probably identical to combined induction-redirection control since FLORIS predicts no gains in power capture through turbine derating

is closely related to the predicted losses of an upstream turbine due to yaw misalignment, and the amount of wake deflection that can be achieved for a particular misalignment angle. Note that, in this work, the turbine power measurements are used to estimate the ambient conditions. However, these measurements do not always contain sufficient information to uniquely reconstruct the ambient conditions. A theoretical study on the observability of the ambient conditions will be presented in the next section.

## **4.2 Assessing the observability of the ambient conditions: robustifying the estimation of the ambient conditions in the closed-loop model-based controller**

The previous section outlined a wind farm control solution in which the ambient conditions are estimated continuously using a model-based approach. In this manner, three parameters are estimated, namely the freestream wind direction, the wind speed, and the turbulence intensity. However, these parameters can not always be estimated. More specifically, the estimability of these parameters highly depends on the measurements available, their uncertainty, and the current conditions inside the wind farm. This section proposes a theoretical measure that gives a strong indication which parameters can be estimated with the sensors available. In Section 4.2.1, a scientific publication is outlined that presents the method and showcases it in simulation. Secondly, a brief discussion is presented in Section 4.2.2.

### **4.2.1 Methodology and results**

In Section 4.1, a control algorithm was outlined in which the ambient conditions were estimated following a model inversion approach. In this article, both the wind speed and turbulence intensity were estimated using the turbine power measurements, and the wind direction was estimated following the method proposed by [11]. However, in reality, the inflow parameters can only be estimated in certain scenarios. For example, if the wind was coming from a direction which leads to no wake interaction, the turbine power measurements would be independent of the turbulence intensity, and hence it would not be possible to estimate this parameter. The question of observability is immensely important in robustifying wind farm control algorithms. This section outlines a theoretical approach in establishing a measure of observability, which aids in deciding what parameters to estimate with the sensors at hand.

The work presented in this section was submitted to the Wind Energy journal for review in July 2019. The authors hope the article is available for the public in early-mid 2020.

Received: Added at production | Revised: Added at production | Accepted: Added at production

DOI: xxx/xxxx

## ARTICLE TYPE

# Observability of the ambient conditions in model-based estimation for wind farm control: a focus on static models

Bart Doekemeijer\* | Jan-Willem van Wingerden

<sup>1</sup> Delft Center for Systems and Control, Delft University of Technology, Mekelweg 2, 2628 CD, Delft, The Netherlands

## Correspondence

\*Bart Doekemeijer, Email:  
B.M.Doekemeijer@tudelft.nl

## Summary

Wind farm control (WFC) algorithms rely on an estimate of the ambient wind speed, wind direction and turbulence intensity in the determination of the optimal control setpoints. However, the measurements available in a commercial wind farm do not always carry sufficient information to estimate these atmospheric quantities. In this paper, a novel measure ("observability") is introduced that quantifies how well the ambient conditions can be estimated with the measurements at hand through a model inversion approach. The usefulness of this measure is shown through several case studies. These case studies show the strong need for wind direction measurements for WFC. Further, generally, more wake interaction leads to a higher observability. Also, turbine power measurements provide no additional information compared to local wind speed measurements, implying that power measurements are superfluous. Irregular farm layouts result in a higher observability due to the increase in unique wake interaction. The findings in this paper can be used in WFC to predict which ambient quantities can (theoretically) be estimated. This will ensure that the ambient condition estimation problem is well conditioned, thereby improving the performance of WFC algorithms over the complete envelope of wind farm operation.

## KEYWORDS:

closed-loop wind farm control, ambient condition estimation, observability, estimability, floris

## 1 | INTRODUCTION

The European Wind Energy Association (EWEA) predicts the amount of installed wind energy to increase from 106 GW in 2012 to 735 GW in 2050, which at that point should provide for about 50% of the European Unions electricity demand.<sup>1</sup> The success of wind energy largely relies on its financial competitiveness with other renewable and non-renewable sources. Control plays an invaluable role in this matter. In the past, the focus of control research has been on wind turbine control. Recently, the interest has largely shifted towards wind farm control (WFC), in which multiple turbines inside a wind farm are coordinated together to improve their combined energy yield.<sup>2</sup> WFC addresses the issue of wakes, which are slower and more turbulent pockets of air that form behind a wind turbine as energy is extracted. Wake formation has led up to an estimated 23% loss in the annual energy yield of the Lillgrund offshore wind farm at the coast of Sweden compared to an idealized situation without wake formation.<sup>3</sup> The underlying concept of WFC is to influence the wake such that it has a smaller impact on downstream turbines. A popular approach in the literature is yaw-based wake steering, in which the wake position is shifted laterally by purposely operating an upstream turbine at a yaw misalignment. Recent studies have shown the potential of yaw-based wake steering for wind farm power maximization in high-fidelity simulation<sup>4</sup> and real-world experiments<sup>5,6</sup>. These publications suggest an increase in the annual energy yield in the order of one percent, and situational increases of up to twenty percent.

The amount of yaw misalignment that maximizes the energy yield is highly dependent on the wind direction, wind speed, and turbulence intensity of the incoming wind field<sup>3</sup>. As these atmospheric conditions constantly change, so do the optimal yaw angles. Typically, a simplified



("surrogate") model of the flow and turbine dynamics is leveraged to calculate the optimal yaw angles.<sup>14</sup> However, due to the complicated flow behavior at a range of temporal and spatial scales, no surrogate model exists that is accurate for all the different atmospheric conditions a wind farm may encounter. For this reason, closed-loop control solutions are becoming increasingly popular in the literature<sup>2</sup>. The underlying idea of this closed-loop control framework is that the surrogate wind farm model is continuously adapted such that it accurately and consistently predicts the wind farm dynamics.

The closed-loop WFC framework is shown in Figure 1. This framework consists of three components, namely 1) a surrogate wind farm model, 2) a model adaptation algorithm, and 3) a control setpoint optimization algorithm. Surrogate wind farm models can typically be separated into static and dynamic models. These model types attempt to predict the minute-averaged and the second-to-second flow and turbine behavior, respectively. The purpose of the model adaptation algorithm is to modify parameters inside the surrogate model such that it can accurately predict the wake interactions inside the wind farm, which includes the freestream wind speed and wind direction. Finally, an optimization algorithm is necessary to determine an optimal control policy such that a particular wind farm objective is achieved, e.g., maximization of the wind farm power production. The focus in this article is on the model adaptation algorithm; the interested reader is referred to the survey by Boersma et al.<sup>2</sup> for more information on surrogate models and optimization algorithms.

The body of literature on real-time model adaptation for WFC is scarce. Most WFC literature has focused on setpoint optimization and model development.<sup>2</sup> This goes paired with the fact that most WFC algorithms in the literature have been tested under quasi-steady ambient conditions, meaning that the mean wind speed, wind direction and turbulence intensity were time invariant. This holds for both numerical simulations<sup>4</sup> and real-world scaled experiments<sup>5,7</sup>. This limits the applicability of such algorithms, as the experiments do not sufficiently represent the real-world fluctuations in the atmosphere.

A handful of articles in the literature is concerned with the estimation of atmospheric conditions and model adaptation for WFC. Annoni et al.<sup>8</sup> proposed a model-free algorithm to estimate the wind direction inside a wind farm using the wind vane measurements of different turbines and obtaining a consensus on the most probable value. Doekemeijer et al.<sup>9</sup> proposed a method to estimate the freestream conditions by a model inversion approach using the time-averaged turbine power measurements and a static surrogate model assuming the wind direction is known, which is comparable to the idea coined by Gebraad et al.<sup>4</sup>. Furthermore, Gebraad et al.<sup>10</sup> synthesized a Kalman filter for their dynamic surrogate model, which uses the turbine power measurements to estimate the flow field inside the wind farm. The adapted surrogate model was able to accurately predict the wind farm dynamics, though the wind direction was constant and assumed to be known. Similarly, Doekemeijer et al.<sup>11</sup> used a dynamic surrogate model with an Ensemble Kalman filter to estimate the flow field and turbulence intensity using turbine power measurements. High-fidelity simulations showed that the algorithm was able to successfully reconstruct the dynamic wind field for a 2-turbine and a 9-turbine wind farm. However, also in this work, the wind direction was assumed known. Further, Shapiro et al.<sup>12</sup> synthesized and evaluated a WFC solution assuming a constant wind direction. Besides the estimation of the ambient conditions, Bottasso and Schreiber<sup>13</sup> attempt to estimate several model tuning parameters to improve the accuracy of the surrogate model.

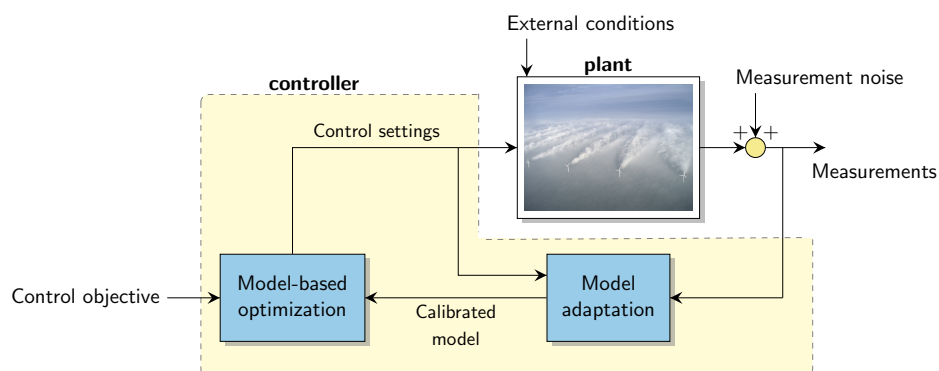


**FIGURE 1** The closed-loop framework for model-based wind farm control. In this framework, measurements from each turbine in the wind farm (e.g., turbine power signals, wind vane measurements) are used to adapt a simplified model of the wind farm to better represent the current wind farm dynamics. Typically, the freestream wind speed and wind direction are among the estimated quantities. This adapted surrogate model is then used to optimize the control settings of each turbine to increase the power capture of the wind farm. Finally, these setpoints are transmitted to the real-world turbines and the cycle repeats itself.

All aforementioned work, apart from that of Annoni et al.<sup>8</sup>, is tested under quasi-steady ambient conditions in simulation, thereby significantly limiting their applicability. In essence, these methods combine a set of measurements with some sort of surrogate or consensus model that relate one measurement to another. These methods are fundamentally limited due to the fact that only a finite amount of information is measured. One can easily think of situations in which the ambient conditions cannot be derived from the available measurements. Such a situation would be considered “unobservable” or “unestimatable”. Thus, before one may attempt to estimate the ambient conditions, one should consider whether the situation is observable in the first place. However, to the best of the authors’ knowledge, there is no literature on the observability for ambient condition estimation. This paper aims to fill this scientific gap, and the contributions of this article are:

- Proposing a formal definition for a mathematical measure (henceforth referred to as “observability”) that quantifies how well the ambient conditions (i.e., wind direction, wind speed, turbulence intensity) can be reconstructed from the measurements available in the wind farm.
- Comparing the effect of different wind farm topologies and sensor configurations on the observability for a large range of ambient conditions that a wind farm may encounter during operation.
- Performing theoretical case studies with wind farms with DTU 10MW wind turbines.

This article is organized as follows. The surrogate model used in this work is presented in Section 2. The issue of estimation and a novel quantitative measure of observability is presented in Section 3. Simulation results are shown in Section 4, and the article is concluded in Section 5.

## 2 | SURROGATE MODEL: FLORIS

The surrogate model used in this work is referred to as the “FLOw Redirection and Induction in Steady-state” (FLORIS) model<sup>14</sup>. This model predicts the time-averaged power capture of each turbine and the time-averaged three-dimensional flow field for a wind farm under a specified set of inflow conditions. The timescale of FLORIS is on the order of minutes. A schematic overview of the types of inputs and outputs to the FLORIS model is shown in Figure 2. Fundamentally, FLORIS combines several submodels from the literature. The main components of FLORIS used in this article are described in the remainder of this section.

Firstly, FLORIS includes the single-turbine wake model from Bastankhah and Porté-Agel<sup>15</sup>, which predicts the time-averaged three-dimensional wind field behind a turbine. Secondly, the turbine-induced turbulence is calculated using an empirical function proposed by Crespo and Hernández<sup>16</sup>. Thirdly, the wind field under multiple overlapping wakes is calculated through a sum-of-squared-deficits law as proposed by Katic et al.<sup>17</sup>. Fourthly, the power production of each turbine is calculated using the rotor-effective wind speed and the nondimensional power coefficient  $C_P$ , as

$$P_i = \frac{1}{2} \rho A_D U_i^3 C_P(U_i, \gamma_i), \quad (1)$$

where  $\rho$  is the air density,  $A_D$  is the rotor swept area,  $U_i$  is the spatially averaged inflow wind speed at turbine  $i$ , and  $\gamma_i$  is the yaw angle of the turbine relative to the incoming wind. The nondimensional power and thrust coefficients,  $C_P$  and  $C_T$ , can be derived using actuator disk theory for aligned inflow ( $\gamma_i = 0$ ). Alternatively, the nondimensional power and thrust coefficients can be calculated using an aero-elastic turbine simulation model for various wind speeds (and yaw misalignment angles) such as OpenFAST<sup>18</sup> or Bladed. A common expression modeling the effect of a yaw misalignment on the turbine power production is<sup>4</sup>

$$C_P(U_i, \gamma_i) = C_P(U_i, 0) \cdot \cos^\kappa(\gamma_i), \quad (2)$$

where  $\kappa$  has a value of 1.4 – 2.0, depending on the wind turbine.

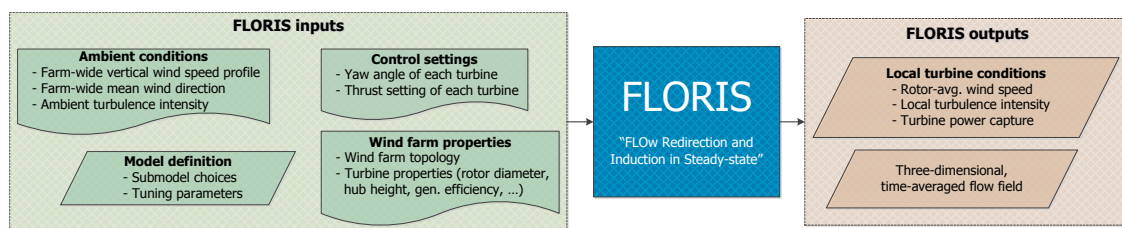


**FIGURE 2** The flow of information for the surrogate model “FLORIS”. The left four blocks represent the various model inputs, and the right two blocks represent the model outputs. Typically, the control settings and wind farm properties are known and are time invariant. However, the ambient conditions are time variant, and the tuning parameters that provide the best results are uncertain.



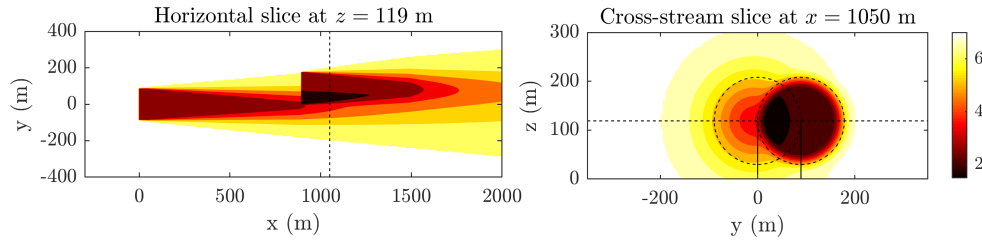


**FIGURE 3** Simulation results for a wind farm with two DTU 10MW wind turbines using FLORIS. The figure shows a horizontal flowfield and a cross-stream slice of the flow-field. The Gaussian nature of the wakes is clearly seen.

The results of an arbitrary wind farm simulation with two 10MW turbines<sup>19</sup> is shown in Figure 3. The computational cost for a single FLORIS run is 10 m s to 1 s, depending on the number of turbines in the wind farm. FLORIS has shown a good match with results from high-fidelity simulations<sup>9</sup>, wind tunnel experiments<sup>20</sup>, and field tests<sup>6,21</sup>. Furthermore, the variant presented in this article has fewer tuning parameters than a comparable model proposed in<sup>4</sup>. For a more detailed, mathematical description of the model, the reader is referred to its related literature. Note that the results that will be presented in this article are not limited to FLORIS, and can straight-forwardly be reproduced with other static surrogate models.

### 3 | METHODOLOGY: INTRODUCING A MEASURE OF OBSERVABILITY

The model adaptation solution of a WFC algorithm is not guaranteed to result in satisfactory performance. There has to be sufficient information in the wind farm measurements to uniquely determine the ambient conditions. Hence, an observability analysis is essential before the implementation of such a control algorithm. However, there is no clear definition on “observability” when it comes to (control methods relying on) a static wind farm model. Therefore, in this section, a mathematical definition of “observability” is introduced for the control framework presented in Figure 1.

#### 3.1 | Cost function in estimation

Generally, a simplistic, heuristic approach is used to determine the prevailing ambient conditions inside the wind farm. However, the reliability of such methods vary, the literature on them is scarce, and these methods are limited in their accuracy. Rather, in this work, a surrogate wind farm model is leveraged in a sensor fusion approach for the estimation of the ambient conditions.

In this work, the freestream wind speed, wind direction and turbulence intensity are estimated using the readily available measurements of each turbine. For example, consider a cost function that minimizes the error with the time-averaged power measurements of each turbine, as

$$J_1(\hat{\phi}, \hat{U}_\infty, \hat{I}_\infty) = \frac{1}{N_T} \sum_{i=1}^{N_T} \left( P_i^{\text{measured}} - \hat{P}_i^{\text{FLORIS}}(\hat{\phi}, \hat{U}_\infty, \hat{I}_\infty) \right)^2, \quad (3)$$

with  $N_T$  the number of turbines, and  $\hat{\phi}$ ,  $\hat{U}_\infty$  and  $\hat{I}_\infty$  being the freestream wind direction, wind speed and turbulence intensity as evaluated in FLORIS, respectively. Using this cost function for model adaptation, the idea is that values for  $\hat{\phi}$ ,  $\hat{U}_\infty$  and  $\hat{I}_\infty$  are found such that the error between the measured turbine power signals and what is predicted by FLORIS for these conditions is minimized. The cost function shown in Equation 3 was used for model adaptation in Doekemeijer et al.<sup>9</sup> assuming  $\phi$  was known a priori, which allowed the successful estimation of  $U_\infty$  and  $I_\infty$ . However, only using the turbine power measurements may lead to situations in which the true ambient conditions cannot be reconstructed accurately. For example, consider the case in which all turbines inside the wind farm are operating in above-rated conditions. All turbines are then generating their rated power, and one cannot distinguish different above-rated wind speeds from one another. To resolve this issue, one can include the wind speed estimates from a local turbine wind speed estimator<sup>22,23</sup> in the cost function. This term is denoted by  $J_2$ , given as

$$J_2(\hat{\phi}, \hat{U}_\infty, \hat{I}_\infty) = \frac{1}{N_T} \sum_{i=1}^{N_T} \left( U_i^{\text{measured}} - \hat{U}_i^{\text{FLORIS}}(\hat{\phi}, \hat{U}_\infty, \hat{I}_\infty) \right)^2, \quad (4)$$

where  $U_i^{\text{measured}}$  is the measurement of the local wind speed estimator of turbine  $i$ , and  $\hat{U}_i^{\text{FLORIS}}$  is what FLORIS predicts the local wind speed to be at turbine  $i$  for the hypothesized wind conditions  $\hat{\phi}$ ,  $\hat{U}_\infty$  and  $\hat{I}_\infty$ . Note that the inflow wind speed at a turbine in FLORIS, denoted by  $\hat{U}_i$ , is the freestream-equivalent wind speed at that turbine under zero yaw misalignment. Thus, the effects of a yaw misalignment of turbine  $i$  are not accounted for in this signal. However, in practice, a typical local turbine wind speed estimator provides a freestream-equivalent wind speed using the turbine power signal under the assumption of zero yaw misalignment. To account for the situation in which a turbine is misaligned with the

flow, one can model  $\hat{U}_i^{\text{FLORIS}}$  as

$$\hat{U}_i^{\text{FLORIS}}(\gamma_i) = \hat{U}_i^{\text{FLORIS,unyawed}} \cdot \sqrt[3]{\cos^{\kappa}(\gamma_i)}, \quad (5)$$

in order to match the signal definition from the local wind speed estimator,  $U_i^{\text{measured}}$ . Finally, one can combine  $J_1$  and  $J_2$  into cost function  $J_{12}$ , as

$$J_{12} = \lambda_P J_1 + \lambda_U J_2, \quad (6)$$

where  $\lambda_P$  and  $\lambda_U$  are weighing terms. Using the cost function defined in Equation 6, difficult situations may arise when trying to estimate  $\phi$ ,  $U_\infty$  and  $I_\infty$ . For example, if there is no wake interaction, one cannot estimate the freestream turbulence intensity, as the effects of  $I_\infty$  have no correlation with (i.e., impact on) the measured signals. Moreover, issues may arise concerning the estimation of  $\phi$ , as demonstrated in Figure 4. In this situation,  $\hat{\phi} = 6.0^\circ$  and  $\hat{\phi} = -3.6^\circ$  yield almost identical values for  $\hat{U}_{1,2}^{\text{FLORIS}}$  and  $\hat{P}_{1,2}^{\text{FLORIS}}$ , thereby making it impossible to distinguish these two situations using the measurements available.

To address the latter issue, local wind direction estimates of each turbine are included in the cost function, e.g., using the filtered wind vane measurements.<sup>24</sup> This term is modeled as  $J_3$ , given by

$$J_3(\phi) = \frac{1}{N_T} \sum_{i=1}^{N_T} (\phi_i^{\text{measured}} - \hat{\phi})^2, \quad (7)$$

where  $\phi_i^{\text{measured}}$  is the filtered wind vane measurement of turbine  $i$ , and  $\hat{\phi}$  is the hypothesized wind direction in FLORIS. The complete cost function  $J$  is now defined as

$$J(\hat{\phi}, \hat{U}_\infty, \hat{I}_\infty) = \frac{1}{N_T} \sum_{i=1}^{N_T} \left( \underbrace{\lambda_P (P_i^{\text{measured}} - \hat{P}_i^{\text{FLORIS}}(\hat{\phi}, \hat{U}_\infty, \hat{I}_\infty))^2}_{\text{Contribution of local power measurements}} + \underbrace{\lambda_U (U_i^{\text{measured}} - \hat{U}_i^{\text{FLORIS}}(\hat{\phi}, \hat{U}_\infty, \hat{I}_\infty))^2}_{\text{Contribution of local wind speed estimates}} + \underbrace{\lambda_\phi (\phi_i^{\text{measured}} - \hat{\phi})^2}_{\text{Contr. of local wind direction (vane) estimates}} \right), \quad (8)$$

with  $\lambda_\phi$  a weighing term for the local wind direction estimates. This weighing term is to be chosen according to the relative measurement noise and bias in the wind vane measurements, and could vary per turbine. The to-be-estimated quantities are  $\phi$ ,  $U_\infty$  and  $I_\infty$ . Each of the three components includes a squared term to quadratically penalize mismatches between the surrogate model and sensor measurements. The situation of Figure 4 becomes increasingly better conditioned as the contribution of the wind vane measurements increases, as visualized in Figure 5.

Thus, it is clear that local wind speed measurements (to deal with above-rated wind speeds), wind direction measurements (to deal with situations as exemplified in Figure 4), and wake interaction (to enable correlation between  $I_\infty$  and the measurements) are required to promote observability of the freestream conditions over the full range of operation. When multiple minima exist at a notable distance from the true solution (in the example case of Figures 4 and 5 this would be  $\|\Delta\phi\| \gg 0$ , with  $\hat{\phi} = \phi + \Delta\phi$ ), the ambient conditions cannot be reliably estimated, and the situation becomes “unobservable”.<sup>1</sup>

However, while it is clear that particular situations are unobservable, a quantitative measure is still required to determine the degree of unobservability. For example, is the situation in Figure 5 with  $\lambda_\phi = 1.0$  “observable enough” to uniquely determine the ambient conditions? To answer such questions, a quantitative measure of unobservability for static models is introduced in the next section.

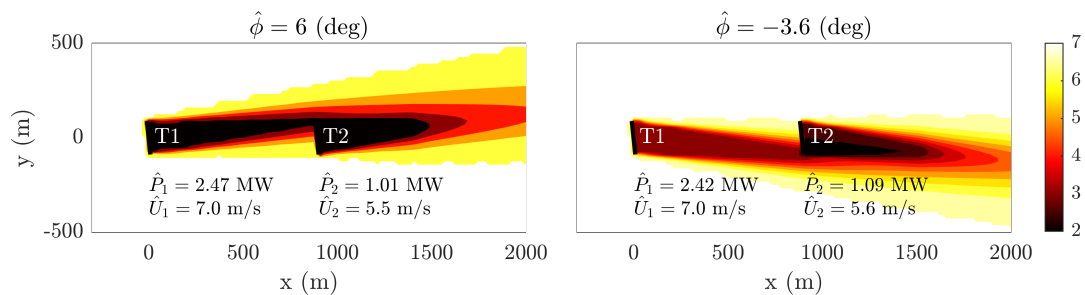


**FIGURE 4** The issue of symmetry exemplified on a two-turbine wind farm for the estimation of  $\phi$ . The definitions are that  $\phi = 0^\circ$  when the air moves from west to east (left to right), and is counter-clockwise positive. The colorbar depicts wind speed in  $\text{m s}^{-1}$ . In this plot, it is seen that  $\hat{\phi} = 6^\circ$  and  $\hat{\phi} = -3.6^\circ$  yield almost identical turbine power signals and local wind speeds, thus making them indistinguishable in the cost function of Equation 6. This leads to an unobservable situation.

<sup>1</sup>Note that observability has a different notion in the field of control engineering for dynamical systems. In this article, an equivalent definition is defined for the static problem outlined in this section.

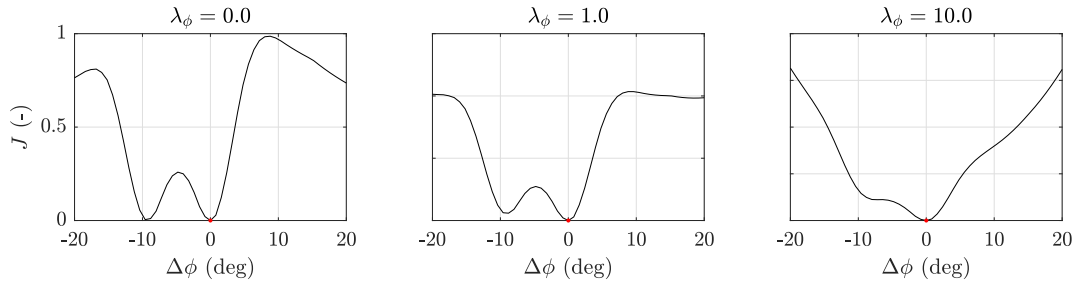


**FIGURE 5** The issue of exclusively using power measurements in the cost function  $J$  (Equation 8), exemplified on the two-turbine case of Figure 4. In all subplots,  $\lambda_P = 10^{-12}$  and  $\lambda_U = 0$  (In this example case,  $\lambda_U = 0$  as it carries the same information as the power signals do. This statement will be proven in Section 4.1.1). In the left figure,  $\lambda_\phi = 0$ , and thus exclusively power measurements are used. This leads to a critical point at  $\Delta\phi = -9.6^\circ$  which has negligible cost, and thus this point cannot be distinguished from the actual point  $\Delta\phi = 0^\circ$ , with  $\hat{\phi} = \phi + \Delta\phi$ , leading to unobservability. This refers back to the situation shown in Figure 4. By including wind vane measurements ( $\lambda_\phi > 0$ ), the cost function is better conditioned to uniquely estimate  $\phi$ . Note that  $\lambda_\phi$  should be chosen in accordance with the vane's measurement reliability.

### 3.2 | A quantitative measure for unobservability

With the cost function defined, a quantitative measure on the degree of observability of a particular situation is defined. With “situation”, we imply a particular wind farm layout, the true ambient conditions, and a specific choice of the regularization terms  $\lambda_P$ ,  $\lambda_U$  and  $\lambda_\phi$ . The main contribution of this paper is the introduction of such a mathematical notion for observability. The observability of a particular situation  $\mathcal{O}$  is defined as

$$\mathcal{O} = \min(\mathcal{M}), \quad (9)$$

$$\text{where } \mathcal{M}(\hat{\phi}, \hat{U}_\infty, \hat{I}_\infty) = \begin{cases} \infty & \text{if } \|\Delta\phi\| < b_\phi \text{ AND } \|\Delta U_\infty\| < b_U \text{ AND } \|\Delta I_\infty\| < b_I, \\ \frac{J(\hat{\phi}, \hat{U}_\infty, \hat{I}_\infty)}{k_\phi(\Delta\phi)^2 + k_U(\Delta U_\infty)^2 + k_I(\Delta I_\infty)^2} & \text{otherwise,} \end{cases} \quad (10)$$

with  $J$  as defined in Equation 8,  $k_\phi$ ,  $k_U$  and  $k_I$  denoting normalization terms, and  $b_\phi$ ,  $b_U$  and  $b_I$  being thresholds. Further,  $\Delta\phi = \phi - \hat{\phi}$ ,  $\Delta U_\infty = U_\infty - \hat{U}_\infty$ , and  $\Delta I_\infty = I_\infty - \hat{I}_\infty$  denote the difference between the true and hypothesized ambient conditions, respectively. In the remainder of this section, the working principle will be explained.

The function  $\mathcal{M}$  is defined such that critical points (low cost  $J$ , far away from the true solution) have a low value (less observable – hard to tell apart from the true solution), while situations in which the cost  $J$  is high yields a high value (more observable – easier to distinguish from the true solution). Furthermore, the threshold terms are present to ensure that any value estimated close enough to the true optimum does not “endanger” the observability. A more elaborate discussion on these thresholds can be found in Appendix A.

Figure 6 demonstrates how the observability  $\mathcal{O}$  is calculated for the example situation discussed in Section 3.1. The function  $\mathcal{M}$  is derived from the cost function  $\mathcal{J}$  following Equation 10. The cost function has two minima: one at  $\Delta\phi = -9.6^\circ$  and one at  $\Delta\phi = 0^\circ$ , indicating that there are two hypothetical wind directions that produce near-identical turbine power signals. This leads to a low observability.

Note that the measured quantities in  $J$  are taken as the values from the surrogate model (FLORIS) with the true ambient conditions, thus assuming a perfect model of the system. In reality, this will not hold and the work herein presents an idealized case (theoretical upper bound) of observability.

Finally, with a measure for observability defined, we can determine and analyze the observability of a particular wind farm for a certain wind direction, wind speed and turbulence intensity. The process is as follows.

1. Firstly, measurement values are generated by evaluating FLORIS for the true ambient conditions. For example, continuing the example 2-turbine wind farm of Section 3.1, the observability for this wind farm is investigated at a true freestream wind speed of  $7.0 \text{ m s}^{-1}$ , a freestream wind direction of  $6^\circ$ , and a turbulence intensity of 6.5%. Referring back to Figure 4, our measurements would be:

$$\mathbf{p}^{\text{measured}} = \mathbf{p}^{\text{FLORIS}}(\phi = 6^\circ, U_\infty = 7.0 \text{ m s}^{-1}, I_\infty = 0.065) = [2.47 \cdot 10^6, 1.01 \cdot 10^6], \quad (11)$$

$$\mathbf{U}^{\text{measured}} = \mathbf{U}^{\text{FLORIS}}(\phi = 6^\circ, U_\infty = 7.0 \text{ m s}^{-1}, I_\infty = 0.065) = [7.0, 5.5], \quad (12)$$

$$\phi^{\text{measured}} = [6.0, 6.0] \quad (13)$$

The measurement vectors contain two entries, for turbine 1 and 2, respectively. In this simulation, the turbines are assumed to be aligned with the inflow wind direction;  $\gamma_{1,2} = 0$ .

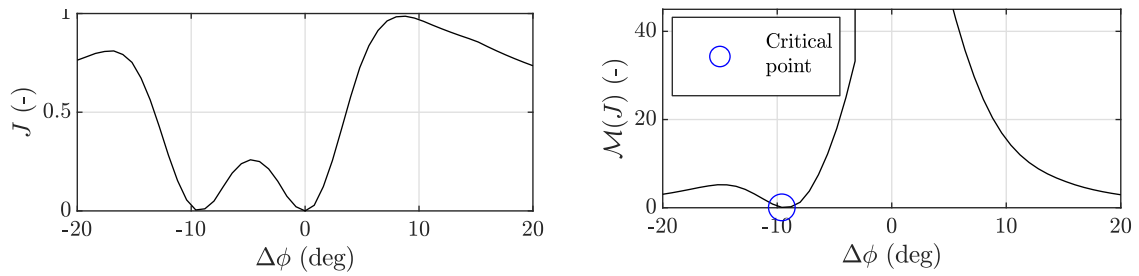


**FIGURE 6** A visualization of how the degree of observability  $\mathcal{O}$  is calculated. This is a continuation of the example shown in Figures 4 and 5. Firstly, the cost function  $J$  (left plot) is converted to a measure  $\mathcal{M}$  (right plot) which penalizes a low cost far away from the true solution (the true solution being  $\Delta\phi = 0$ ). Secondly, the degree of observability  $\mathcal{O}$  is the minimum value of  $\mathcal{M}$ . In this example,  $\mathcal{O}$  is small due to  $J \approx 0$  at  $\Delta\phi = -9.6^\circ$  (referring back to  $\hat{\phi} = 6^\circ$  and  $\hat{\phi} = -3.6^\circ$ ), and the situation is thus poorly observable. This agrees with the qualitative discussion from Section 3.1.

- Secondly, with this set of measurements, the cost function  $J$  of Equation 8 is calculated for a range of hypothetical (tested) ambient conditions. For this example, the model adaptation algorithm is limited to the estimation of  $U_\infty$  and  $\phi$ . The (two-dimensional) cost function is evaluated over the following ranges:

$$\Delta\phi = [-20.0 \ -19.2 \ -18.4 \ \dots \ 19.2 \ 20.0], \text{ with } \phi = 6^\circ + \Delta\phi, \quad (14)$$

$$\Delta U_\infty = [-1.50 \ -1.25 \ -1.0 \ \dots \ 1.25 \ 1.50], \text{ with } U_\infty = 7.0 \text{ m s}^{-1} + \Delta U_\infty, \quad (15)$$

$$\Delta I_\infty = [0.0], \text{ with } I_\infty = 0.065 + \Delta I_\infty. \quad (16)$$

If  $I_\infty$  is additionally to be estimated, the (three-dimensional) cost function is also evaluated over the following range for  $\Delta I_\infty$ :

$$\Delta I_\infty = [-0.06 \ -0.03 \ 0.0 \ 0.03 \ 0.06], \text{ with } I_\infty = 0.065 + \Delta I_\infty. \quad (17)$$

Furthermore, the turbine yaw angles are fixed in the inertial frame and assumed to be known a priori in the cost function evaluations. Thus, if the cost function is evaluated for  $\Delta\phi = 10^\circ$ , then  $\hat{\gamma}_{1,2} = -10^\circ$ .

- A two-dimensional (for  $\Delta I_\infty = 0$ ) or three-dimensional (for  $\Delta I_\infty = [-0.06 \ \dots \ 0.06]$ ) cost matrix is obtained following Equation 8, from which  $\mathcal{M}$  is calculated following Equation 10. The degree of observability  $\mathcal{O}$  is the minimum value of  $\mathcal{M}$ , being a positive real number.

The degree of observability  $\mathcal{O}$  can be calculated for a range of true wind directions following the process described above, and displayed in a single picture. The results of such an observability analysis assuming only power measurements are available ( $\lambda_P = 1$ ,  $\lambda_U = 0$  and  $\lambda_\phi = 0$ ) are shown in Figure 7 for a 6-turbine wind farm. Note that  $\lambda_U$  and  $\lambda_\phi$  are zero to provide insight into the results. In a practical wind farm control implementation, one would opt for  $\lambda_U > 0$  and  $\lambda_\phi > 0$ , if these measurements are available.

Each of the two radial plots shown in Figure 7 represents the degrees of observability for 61 different wind directions. There is one degree of observability defined for each true wind direction, plotted as a particular color across the polar axis. This thus indicates the estimability of  $\phi$  and  $U_\infty$  for this true wind direction. For each of the 61 true wind directions, a two-dimensional cost function  $\mathcal{M}$  was calculated over the variables  $\Delta\phi = [-20, -19.2, -18.4, \dots, 20.0]$  deg and  $\Delta U_\infty = [-1.50, -1.25, -1.00, \dots, 1.50]$  m s<sup>-1</sup>. Then,  $\mathcal{O}$  was taken to be the lowest value of  $\mathcal{M}$ , being the degree of observability for this true wind direction, true wind speed, true turbulence intensity, wind farm layout, and with  $\phi$  and  $U_\infty$  being the to-be-estimated parameters. We refer to this as the degree of observability for this particular "situation".

Figure 7 clearly shows that the  $\phi$  and  $U_\infty$  can only be estimated for a narrow range of true wind directions when only power measurements are available. This makes sense, since there is only wake interaction for a small range of wind directions. Without wake interaction, one cannot distinguish, for example, between the case where all turbines operate under a yaw misalignment and a higher inflow wind speed, from the case where all turbines operate without a yaw misalignment and a lower inflow wind speed. Furthermore, an interesting difference between the observability plot for a true wind speed of 6.5 m s<sup>-1</sup> and 9.0 m s<sup>-1</sup> is the degree of observability at the true wind directions of 90° and 270°. This is due to the fact that the downstream turbines operate below cut-in wind speed for the 6.5 m s<sup>-1</sup> case at these wind directions due to the close spacing and the wake effects. As these downstream turbines do not generate any power, their signals hold little information. For the 9.0 m s<sup>-1</sup> case, all turbines operate above cut-in wind speed, and thus these power signals contain more information about the flow.

The methodology presented in this section becomes more interesting when considering more complicated farm layouts, various combinations of wind vane and wind speed measurements, and the inclusion of turbulence intensity estimation. This is the focus of the next section.

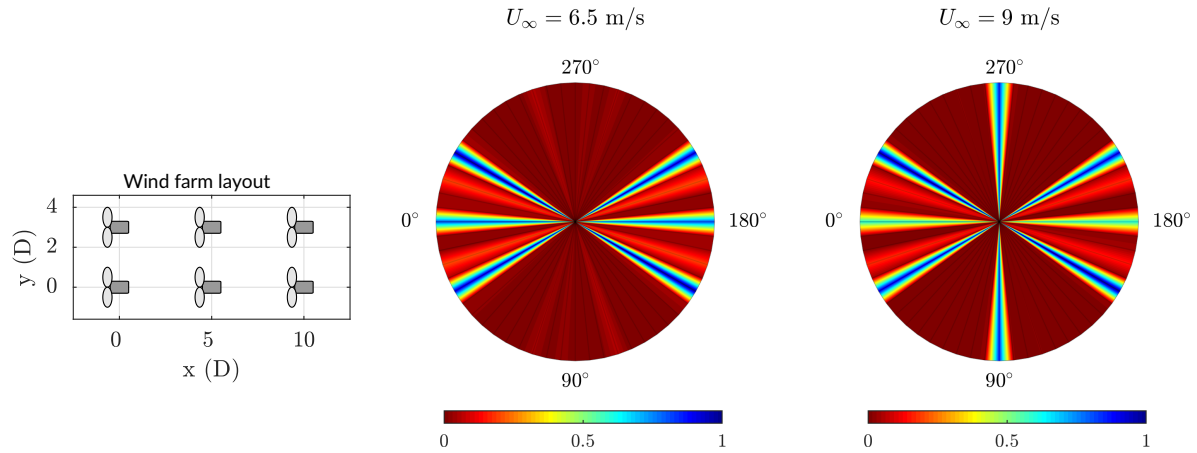


**FIGURE 7** Observability plots for the 6-turbine wind farm over a range of true wind directions (from 0 to 360 deg, plotted in 61 discrete points along the polar axis), and two true wind speeds ( $6.5 \text{ m s}^{-1}$  and  $9.0 \text{ m s}^{-1}$ ). The true turbulence intensity is assumed to be known in the estimation problem, thus  $J(\phi, U_\infty, I_\infty) = J(\phi, U_\infty)$  and  $\Delta I_\infty = 0$ , where the estimability of  $\phi$  and  $U_\infty$  is assessed. Thus for each of the  $61 \times 2$  situations (a situation is defined as a particular true wind direction and wind speed for this 6-turbine layout), the steps described earlier this section are followed. The results are normalized to a scale of 0 to 1, with 0 being unobservable, and 1 being to the best observable situation.

#### 4 | A COMPREHENSIVE OBSERVABILITY ANALYSIS FOR 3 WIND FARM LAYOUTS

The observability of the ambient conditions is investigated in this section for three different wind farm layouts, namely, two symmetrical wind farms and one asymmetrical wind farm. The layouts are shown in Figure 8. The asymmetrical 8-turbine wind farm is an interesting configuration, as there is more unique wake interaction situations in this layout. This reduces the issues with symmetry previously demonstrated in Figure 4 compared to symmetrical wind farm layouts.

For each topology, the observability is calculated for  $61 \times 4 \times 4 = 976$  situations, namely for 61 wind directions  $\phi = [0, 6, 12, \dots, 354] \text{ deg}$ , 4 levels of turbulence intensity  $I_\infty = [0.065, 0.095, 0.125, 0.155]$ , and 4 wind speeds  $U_\infty = [6.5, 9.0, 11.4, 14.5] \text{ m s}^{-1}$ , of which the latter wind speed is above rated. Thus, for each of these 976 conditions, a multidimensional cost function is set-up and the most critical situation is determined following Equation 10, upon which the observability for this situation is calculated using Equation 9. The parameters therein are shown in Table A1.

This section is separated in two parts. In Section 4.1, the observability of the various situations is assessed under the assumption that the freestream turbulence intensity is known a priori. This simplifies the estimation problem and requires less information to be extracted from the measurements at hand. However, neglecting the estimation of  $I_\infty$  would severely impact the accuracy of the surrogate model in a practical wind farm control algorithm. Hence, the observability with the inclusion of  $I_\infty$  is presented in Section 4.2.

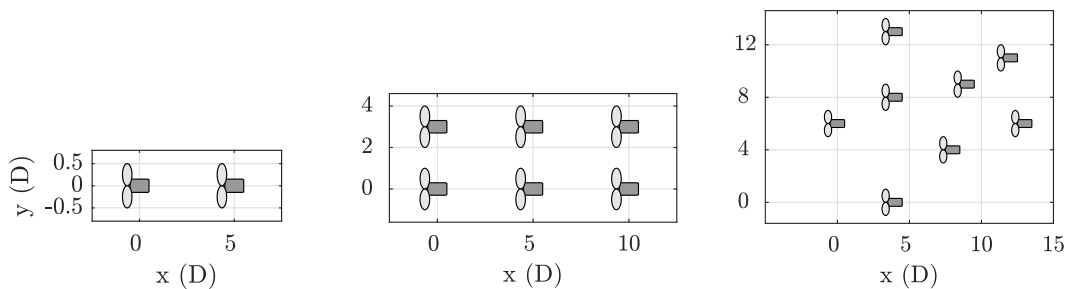


**FIGURE 8** The three wind farm layouts used in a comprehensive observability analysis to demonstrate the working principles of the algorithm presented in Section 3. The turbines are DTU 10MW turbines<sup>19</sup> with a rotor diameter  $D$  of 178.3 m and a hub-height of 119 m.

#### 4.1 | Estimating $\phi$ and $U_\infty$ under perfect knowledge of $I_\infty$

First, the observability of various situations under the assumption that the turbulence intensity is known,  $\hat{I}_\infty = I_\infty$ , is looked into. The range over which each particular cost function is calculated is  $\Delta\phi = [-20, -19.2, -18.4, \dots, 20.0]$  deg and  $\Delta U_\infty = [-1.50, -1.25, -1.00, \dots, 1.50]$  m s<sup>-1</sup>. The discretization of these parameters were tuned for convergence; such that the solutions no longer notably change at a higher precision. The range of these parameters are chosen to resemble the typical prior knowledge one has about the true ambient conditions in such an estimation problem.

##### 4.1.1 | Redundancy in the cost function: power and wind speed estimates

One important notion in the cost function shown in Equation 8 is that the local wind speed estimates and the turbine power signals carry duplicate information. Specifically, as the local wind speed estimators rely on the turbine power signal, the turbine power measurements theoretically add no information to the cost function that is not already included in the wind speed estimator signals. To validate this, an observability analysis is performed for the 6-turbine wind farm under  $\lambda_\phi = 0$  and various values for  $\lambda_P$  and  $\lambda_U$ . The results are shown in Figure 9.

From this figure, one can immediately see that situations in which all turbines are in above-rated operation are unobservable when  $\lambda_U = 0$  (top-right subplot). This subplot shows some observability when the turbulence intensity is low and the wake interactions are deep, such that one or multiple downstream turbines are operating below rated conditions. Furthermore, turbine power measurements do not add anything to the observability compared to the wind speed estimates. Note that the observability plots are not identical for below-rated conditions as power is cubically related to the wind speed,  $P_i \propto U_i^3$ , and thus the observability is spread slightly differently within the radial plots. Though, the trends are identical. Hence, in the remainder of this work,  $\lambda_P = 0$ .

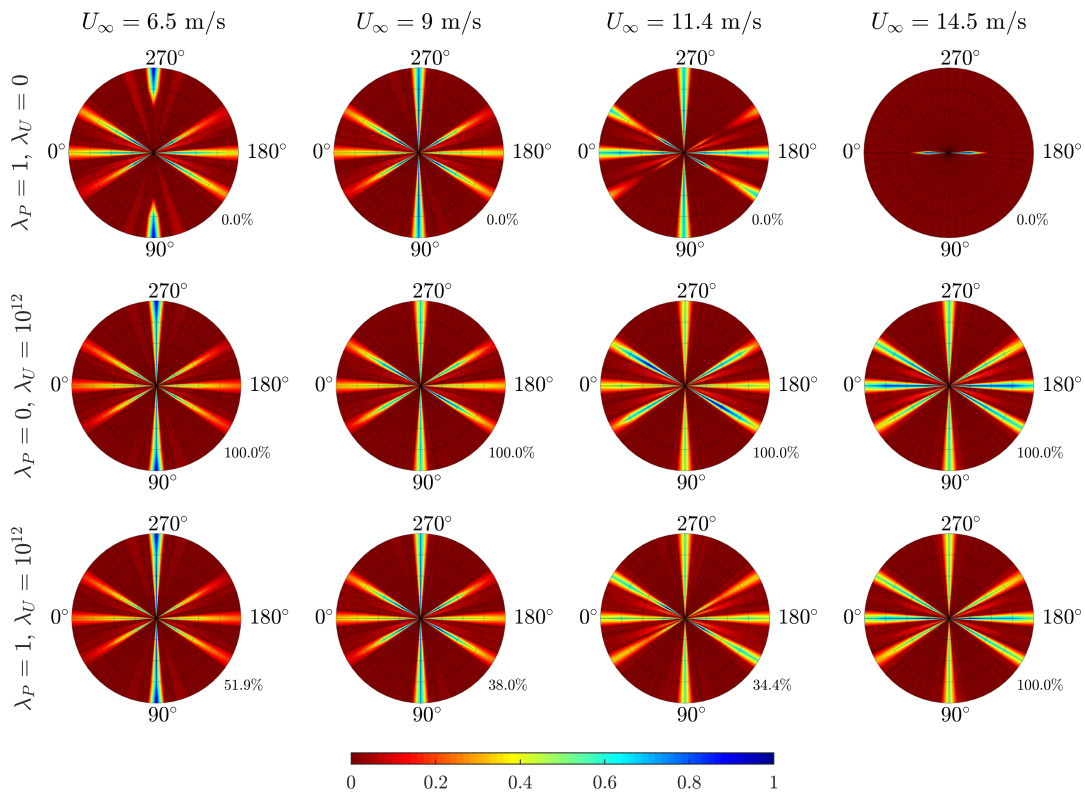


**FIGURE 9** The observability for a range of wind speeds, wind directions and turbulence intensities under the assumption that  $I_\infty$  is known, with  $\lambda_\phi = 0$ . The observability in each radial plot is normalized with respect to its highest value. The percentage on the bottom-right corner of each radial plot indicates to what degree the local wind speed measurements contribute to the observability. It can be seen that the power measurements provide no additional information compared to wind speed estimates, and no information at all above rated wind speeds (top-right subplot).

#### 4.1.2 | Using exclusively wind speed estimator measurements ( $\lambda_P = 0$ , $\lambda_U = 1$ , $\lambda_\phi = 0$ )

Here, the situation with solely wind speed measurements available is investigated;  $\lambda_P = \lambda_\phi = 0$  and  $\lambda_U = 1$ . This is comparable to the estimation framework applied in previous work<sup>9</sup>, in which wind vane measurements were not assumed to be available. This is a particularly difficult problem, as previous results from Section 3 suggest. In the remainder of this section, all three wind farm layouts will be addressed. The observability roses are shown in Figure 10.

A number of observations can be made from Figure 10. Firstly, for the two-turbine wind farm, it is clear that the wind direction and wind speed can only be estimated accurately for a narrow range of wind directions – specifically, in which there is sufficient wake interaction. Theoretically, the  $U_\infty$  can always be reconstructed from the wind speed estimate of the upstream turbine, and the upstream turbine can be distinguished if there is wake interaction: it is the turbine with the highest power signal. The wind direction can then be estimated by looking at the quantity of wake losses at the downstream turbine. However, this may lead to situations in which two hypothesized wind directions lead to a near-identical inflow wind speed  $U_i$ , as was seen previously in Figure 4.

Secondly, for the six-turbine wind farm, it can be seen that this topology has more wake interaction than the two-turbine wind farm, and thus has an increased observability for many situations. However, there are still situations with little to no wake interaction which are unobservable. Note that the radial plots for both the two-turbine wind farm and the six-turbine wind farm are radially symmetrical, as the topologies are also radially symmetrical.

Thirdly, for the eight-turbine wind farm, one can directly see that observability greatly increases due to many more unique wake interaction between turbines. With all topologies, generally, it is noted that a higher atmospheric turbulence leads to a lower observability. Specifically, the turbulence intensity reduces the wake interaction with downstream turbines. The results from Figure 10 show that  $\phi$  and  $U_\infty$  can only be reconstructed for particular situations, and thus care has to be taken in such estimation algorithms and related wind farm control algorithms. The next section shows the estimability of  $\phi$  and  $U_\infty$  with the inclusion of wind vane measurements.

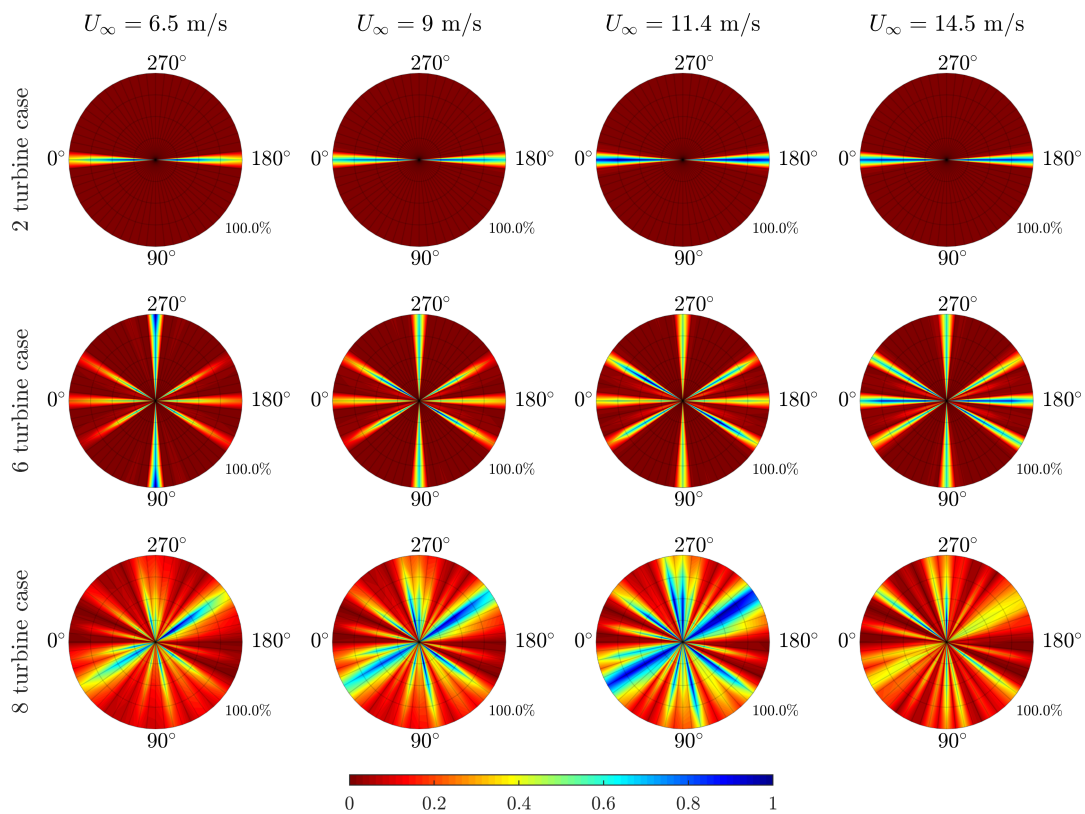


**FIGURE 10** The observability for a range of wind speeds, wind directions, and wind farm layouts under the assumption that  $I_\infty$  is known, with  $\lambda_P = \lambda_\phi = 0$ . The observability in each radial plot is normalized with respect to its highest value. The percentage on the bottom-right corner of each radial plot indicates to what degree the local wind speed measurements contribute to the observability, which in this situation is 100%.



#### 4.1.3 | Using local wind speed and wind direction estimates ( $\lambda_P = 0$ , $\lambda_U = 1$ , $\lambda_\phi = 10$ )

By including local estimates of the wind direction,  $\lambda_\phi > 0$ , one can attain observability for all situations, as shown in Figure 11. Now, one assumes both wind speed measurements and wind vane measurements to be available.

It is clear to see that all the necessary information is contained in the measurements available for the estimation of  $U_\infty$  and  $\phi$ : all situations appear observable. Observability is guaranteed due to the availability of local wind speed and wind direction measurements, which are quantities directly derived from the ambient wind speed, ambient wind direction, and the wake interactions. Note that there are some variations within the radial circle, which are both due to physical effects such as more or less wake interaction, and also due to fact that the search space of the cost function ( $\Delta\phi$ ,  $\Delta U_\infty$ ,  $\Delta I_\infty$ ) is discretized at a finite resolution.

The tools presented in this work may prove useful to find a balanced trade-off in the cost function between the contributions from various measurement sources. However, even with an accurate estimation of  $\phi$  and  $U_\infty$ , significant model discrepancies may remain. The freestream turbulence intensity  $I_\infty$  has a relatively large impact on the optimal turbine setpoints for wake steering, as it has a direct relationship to the degree of wake recovery. Hence, the estimation of  $I_\infty$  is a necessity in reliable wind farm control algorithms. In the next section, the estimation of  $I_\infty$  is incorporated into the observability analysis.

#### 4.2 | The full estimation problem: estimating $\phi$ , $U_\infty$ , and $I_\infty$

While observability for all situations was shown in Section 4.1.3, a compromising assumption was made that the freestream turbulence intensity  $I_\infty$  was known. In reality, this is not a realistic assumption, and  $I_\infty$  must be estimated together with  $U_\infty$  and  $\phi$ . The observability when estimating  $\phi$ ,  $U_\infty$  and  $I_\infty$  is shown in Figure 12, where  $\Delta I_\infty = [-0.06, -0.03, 0.0, 0.03, 0.06]$ .

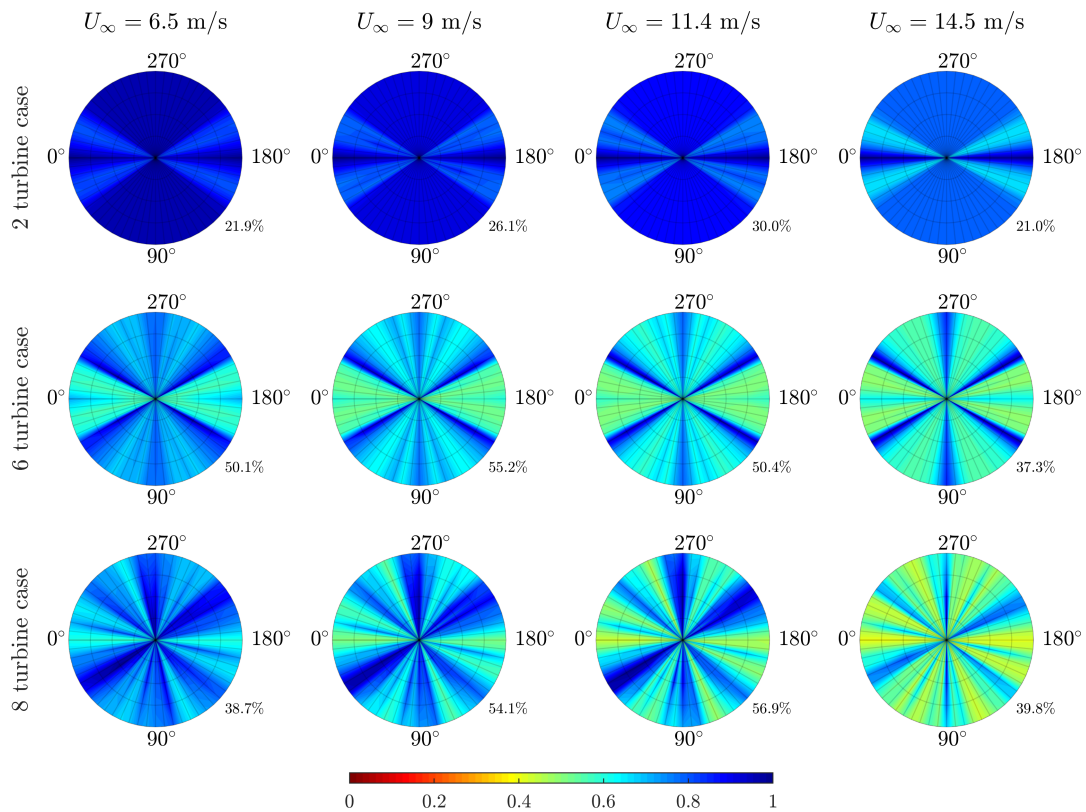


**FIGURE 11** The observability for a range of wind speeds, wind directions, and wind farm layouts under the assumption that  $I_\infty$  is known, with  $\lambda_\phi = 5 \cdot 10^6$  and  $\lambda_U = 0$ . The observability in each radial plot is normalized with respect to its highest value. The percentage on the bottom-right corner of each radial plot indicates to what degree the local wind speed measurements contribute to the observability, which provides an idea to the robustness of the solution.



Several observations can be made. Firstly, one can directly see that the observability significantly reduces for a large range of conditions compared to only the estimation of  $\phi$  and  $U_\infty$ . For the two-turbine case, observability only remains for the narrow window of wind directions in which there is wake interaction. This can be explained by the fact that the measurements provide direct information on  $\phi$  and  $U_\infty$ , while the estimation of  $I_\infty$  is enabled through inversion of the surrogate model and the usage of the local wind speed measurement at the downstream turbine. This only applies when wake interaction is present.

Secondly, observability is reduced in the 6-turbine case compared to Figure 11, yet observability remains more widespread than the two-turbine case. More wake interaction and multiple-wake interaction leads to the fact that the turbine power signals are more sensitive to the freestream turbulence, and thus yield a higher observability than the two-turbine case. Additionally, while a higher turbulence intensity leads to additional wake recovery, it also leads to wider wakes which can impact a downstream turbine where it would not for lower turbulence intensities. These two effects have an opposite effect on the observability, and hence observability does not uniformly decrease with an increase in the freestream turbulence intensity.

Thirdly, the 8-turbine wind farm has the most observable situations from the three topologies. Due to the many unique wake interactions, the solutions become relatively sensitive to the freestream turbulence intensity, and the ambient conditions can be estimated for most conditions. Though, also in this wind farm one can find several situations in which the freestream conditions cannot uniquely be reconstructed from the measurements available.

Finally, recall that these results present an idealized case, in which there is no measurement noise, and the surrogate model is used to generate the measurements, implying that the surrogate model perfectly represents reality. None of these assumptions are valid in practice, and thus the observability roses presented in this section will further diminish. Though, the results presented in this section are an essential step towards the synthesis of an algorithm that estimates the ambient conditions in a robust manner. The observability roses from Figure 12 provide a theoretical upper limit on the relative estimability of the ambient conditions  $\phi$ ,  $U_\infty$  and  $I_\infty$  from the measurements available. This can provide guidance in

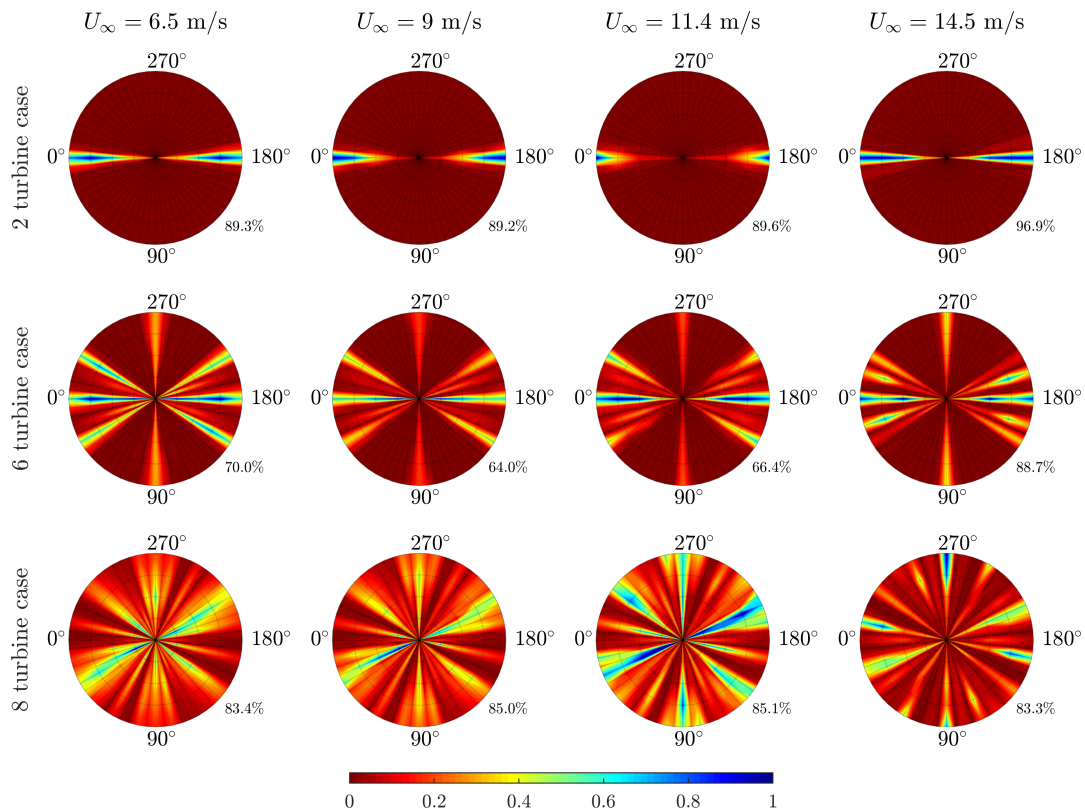


**FIGURE 12** The observability for a range of wind speeds, wind directions, and wind farm layouts with  $\lambda_U = 1$  and  $\lambda_\phi = 10$ . The observability in each radial plot is normalized with respect to its highest value. The percentage on the bottom-right corner of each radial plot indicates to what degree the local wind speed measurements contribute to the observability, which provides an idea to the robustness of the solution.

wind farm control algorithms on when to estimate certain parameters. Since  $\phi$  and  $U_\infty$  are always estimable according to Figure 11, the observability analysis presented in this section can be used to determine whether to estimate  $I_\infty$  in addition to  $U_\infty$  and  $\phi$ . If the situation is "observable enough" (which is to be selected experimentally), the measurements should contain sufficient information to reliably estimate  $I_\infty$ . If not, one can assume  $I_\infty$  to be equal to its past value (since the turbulence intensity also does not change very rapidly in the field), and exclusively estimate  $\phi$  and  $U_\infty$ . This approach is currently being explored and will be published in future work.

## 5 | CONCLUSIONS

Over the last years, the scientific community surrounding wind farm control has shown an increasing amount of interest towards the real-time estimation of the ambient conditions inside a wind farm. This ambient flow information is essential to the optimization of the turbine yaw angles for wake steering, which is currently the most popular methodology of wind farm control for power maximization. The degree of reconstructability of the ambient conditions highly depends on the measurements available and the wind farm layout. For many situations, it is clear to see that the ambient conditions cannot be estimated. However, no quantitative measure exists to represent the degree of estimability of the ambient conditions. This paper addresses this scientific gap.

The main contribution of this paper is the introduction of a novel, mathematical definition for the observability of the ambient conditions. This measure describes how well the true ambient conditions can be distinguished from hypothesized ambient conditions through a model inversion approach for a particular set of measurements. This measure of "observability" is modular and can easily be extended with other measurement sources or other surrogate models.

In several case studies, we show the usefulness of the proposed measure. Moreover, the cases show the strong need for wind direction information to be included in the estimation algorithm. Generally, situations in which there is sufficient wake interaction are observable, while situations with little to no wake interactions are unobservable. Furthermore, local turbine power measurements provide no additional information compared to local wind speed estimates, implying that power measurements can be omitted from the cost function. Also, more complicated, unstructured wind farm layouts generally result in a higher observability as there are more unique wake interactions between turbines.

In general, even with local wind speed and wind direction information, one still cannot reconstruct the full set of ambient conditions (wind speed, wind direction and turbulence intensity) for all conditions that a particular wind farm may encounter. Thus, before one may attempt to estimate the ambient conditions, one should consider whether the situation is observable in the first place. Using this information, one may condition their wind farm control algorithm to situations that are sufficiently observable. This will significantly improve the reliability of wind farm control algorithms and thereby hopefully the willingness to adopt such algorithms by the industry.

## ACKNOWLEDGMENTS

This project has received funding from the European Union's Horizon 2020 Research and Innovation Programme under Grant Agreement No 727477 as part of the CL-Windcon project. The authors would like to thank Sebastiaan Mulders for his valuable insights in writing this document.

## Financial disclosure

None reported.

## Conflict of interest

The authors declare no potential conflict of interests.



## APPENDIX

## A ADDRESSING IRREGULAR BEHAVIOR, NUMERICAL ISSUES, AND SINGULARITIES IN THE CALCULATION OF THE DEGREE OF OBSERVABILITY

Equation 10 provides a clear measure for the degree of observability of a particular situation. With this formulation, evaluated ambient conditions far away from the true ambient conditions (e.g.,  $\|\Delta\phi\| \gg 0$ ) that yield a low estimation error  $J$  are penalized heavily. Namely, the nominator is small and the denominator is large, leading to a low value of  $\mathcal{O}$ . In such a situation, it is unclear what the true ambient conditions are based on the measurements available. These situations result in a low degree of observability. Alternatively, situations with a high cost far away from the true ambient conditions result in a high degree of observability.

However, by simply dividing the cost function over the distance between the evaluated and true ambient conditions leads to undesired behaviour near the true ambient conditions (e.g.,  $\Delta\phi \approx 0$ ). For example, a singularity arises when the evaluated ambient conditions  $\hat{\phi}$ ,  $\hat{U}_\infty$  and  $\hat{I}_\infty$  are exactly the true ambient conditions  $\phi$ ,  $U_\infty$  and  $I_\infty$ , respectively. Namely, then

$$\mathcal{M}(\phi, U_\infty, I_\infty) = \frac{0}{0} = \text{undefined}.$$

Similarly, when the evaluated conditions are very close to the true conditions, it becomes difficult to envision what the function of  $\mathcal{M}$  will look like. For example, if  $J = 0$  at  $\Delta\hat{\phi} = 0.2^\circ$ , then the situation would turn out to be unobservable. This is because one cannot distinguish the true ambient condition ( $\phi = 0^\circ$ ) from a different evaluated condition ( $\hat{\phi} = 0.2^\circ$ ). Clearly, this should not yield an unobservable situation, and a situation where  $J$  is very low “close enough” to the true conditions should not negatively impact the observability of the situation. To address this issue, a “deadzone” is introduced for  $\mathcal{M}$  in proximity of the true ambient conditions. This deadzone enforces observability when the evaluated ambient conditions are “close enough” to the true ambient conditions. This can be seen as the upper formula in Equation 10, in which  $\mathcal{M} = \infty$  within the deadzone region. The effect of a deadzone is visualized in Figure A1. This deadzone resolves the issues related to singularities and numerical sensitivities.

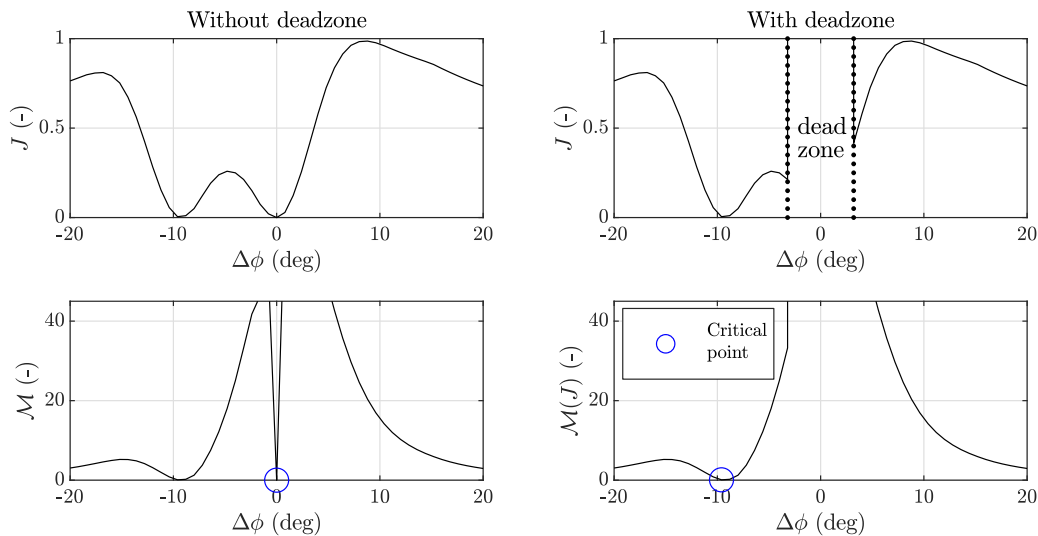


**FIGURE A1** This figure depicts the issue when  $\Delta\phi \approx 0$  for the calculation of  $\mathcal{M}$  using Equation 10. The cost function shown here refers back to the 2-turbine wind farm previously discussed in Section 3.1 with  $\lambda_\phi = \lambda_U = 0$ ). In the top-left figure,  $J$ , the mean-squared-error in turbine power signals, is plotted as a function of the hypothesized wind direction. Estimating the observability following Eq. 9 leads to a singularity point at  $\Delta\phi = 0$ , while clearly  $J = 0$  at the origin (true solution) should not lead to unobservability. This is corrected for by using a deadzone in proximity of  $\Delta\phi = 0$ , as by Eq. 10.

## References

1. European Wind Energy Association . EWEA fact sheet. 2019. <http://www.ewea.org/fileadmin/files/library/publications/statistics/Factsheets.pdf>. Accessed May 29, 2019.
2. Boersma S, Doekemeijer BM, Gebraad PMO, et al. A tutorial on control-oriented modeling and control of wind farms. *American Control Conference (ACC)* 2017: 1-18. doi: 10.23919/ACC.2017.7962923
3. Barthelmie RJ, Pryor SC, Frandsen ST, et al. Quantifying the Impact of Wind Turbine Wakes on Power Output at Offshore Wind Farms. *Journal of Atmospheric and Oceanic Technology* 2010; 27(8): 1302-1317. doi: 10.1175/2010JTECHA1398.1
4. Gebraad PMO, Teeuwisse FW, van Wingerden JW, et al. Wind plant power optimization through yaw control using a parametric model for wake effects - a CFD simulation study. *Wind Energy* 2016; 19(1): 95-114. doi: 10.1002/we.1822
5. Campagnolo F, Petrović V, Bottasso CL, Croce A. Wind tunnel testing of wake control strategies. *Proceedings of the American Control Conference (ACC)* 2016: 513-518. doi: 10.1109/ACC.2016.7524965
6. Fleming PA, Annoni J, Scholbrock AK, et al. Full-scale field test of wake steering. *Journal of Physics: Conference Series* 2017; 854(1). doi: 10.1088/1742-6596/854/1/012013
7. Campagnolo F, Petrović V, Schreiber J, Nanos EM, Croce A, Bottasso CL. Wind tunnel testing of a closed-loop wake deflection controller for wind farm power maximization. *Journal of Physics: Conference Series* 2016; 753(3). doi: 10.1088/1742-6596/753/3/032006
8. Annoni J, Bay C, Johnson K, et al. Wind direction estimation using SCADA data with consensus-based optimization. *Wind Energy Science* 2019; 4(2): 355-368. doi: 10.5194/wes-4-355-2019
9. Doekemeijer BM, Fleming PA, van Wingerden JW. A tutorial on the synthesis and validation of a closed-loop wind farm controller using a steady-state surrogate model. *American Control Conference (ACC)* 2019. Preprintdoi: 10.5281/zenodo.2556497
10. Gebraad PMO, Fleming PA, van Wingerden JW. Wind turbine wake estimation and control using FLORIDyn, a control-oriented dynamic wind plant model. *American Control Conference (ACC)* 2015: 1702-1708. doi: 10.1109/ACC.2015.7170978
11. Doekemeijer BM, Boersma S, Pao LY, Knudsen T, Wingerden vJW. Online model calibration for a simplified LES model in pursuit of real-time closed-loop wind farm control. *Wind Energy Science* 2018; 3(2): 749-765. doi: 10.5194/wes-3-749-2018
12. Shapiro CR, Meyers J, Meneveau C, Gayme DF. Dynamic wake modeling and state estimation for improved model-based receding horizon control of wind farms. *American Control Conference (ACC)* 2017: 709-716. doi: 10.23919/ACC.2017.7963036
13. Bottasso CL, Schreiber J. Online model updating by a wake detector for wind farm control. *American Control Conference (ACC)* 2018.
14. Doekemeijer BM, Storm R. FLORISSE\_M Github repository. 2019. [https://github.com/TUDELFT-DataDrivenControl/FLORISSE\\_M](https://github.com/TUDELFT-DataDrivenControl/FLORISSE_M). Accessed May 29, 2019.
15. Bastankhah M, Porté-Agel F. Experimental and theoretical study of wind turbine wakes in yawed conditions. *Journal of Fluid Mechanics* 2016; 806: 506-541. doi: 10.1017/jfm.2016.595
16. Crespo A, Hernández J. Turbulence characteristics in wind-turbine wakes. *Journal of Wind Engineering and Industrial Aerodynamics* 1996; 61(1): 71 - 85. doi: 10.1016/0167-6105(95)00033-X
17. Katic I, Hojstrup J, Jensen N. A Simple Model for Cluster Efficiency: 407-410; A. Raguzzi . 1987.
18. National Renewable Energy Laboratory (NREL) . NWTC Information Portal (OpenFAST). 2019. <https://nwtc.nrel.gov/OpenFAST>.
19. Bak C, Zahle F, Bitsche R, et al. The DTU 10-MW Reference Wind Turbine. *DTU Library* 2013. Presentation slides.
20. Schreiber J, Nanos EM, Campagnolo F, Bottasso CL. Verification and calibration of a reduced order wind farm model by wind tunnel experiments. *Journal of Physics: Conference Series* 2017; 854(1). doi: 10.1088/1742-6596/854/1/012041
21. Annoni J, Fleming P, Scholbrock A, et al. Analysis of control-oriented wake modeling tools using lidar field results. *Wind Energy Science* 2018; 3(2): 819-831. doi: 10.5194/wes-3-819-2018

- 
22. Soltani MN, Knudsen T, Svenstrup M, et al. Estimation of Rotor Effective Wind Speed: A Comparison. *IEEE Transactions on Control Systems Technology* 2013; 21(4): 1155-1167. doi: 10.1109/TCST.2013.2260751
  23. Ortega R, Mancilla-David F, Jaramillo F. A globally convergent wind speed estimator for wind turbine systems. *International Journal of Adaptive Control and Signal Processing*; 27(5): 413-425. doi: 10.1002/acs.2319
  24. Kragh K, Fleming P. *Rotor Speed Dependent Yaw Control of Wind Turbines Based on Empirical Data*; 2012

**TABLE A1** Relevant cost function parameters (left: normalization terms, right: deadzone threshold) for Eq. 9

$k_\phi$	$\frac{1}{40} \text{ deg}^{-1}$	$b_\phi$	4 deg
$k_U$	$\frac{1}{3} \text{ m}^{-1}\text{s}$	$b_U$	$0.25 \text{ ms}^{-1}$
$k_I$	$\frac{1}{0.12}$	$b_I$	0.03

#### 4.2.2 A continued discussion

When reflecting on the results presented in Section 4.2.1, it is clear to see that the observability of the ambient conditions strongly depend on not only the measurements available, but also on the actual ambient conditions, such as the wind direction. This is a chicken-and-egg problem, and you cannot determine one without the other. In practice, a threshold is to be defined below which certain ambient conditions will not be estimated.

In the next section, this theoretical measure of observability is incorporated into a closed-loop wind farm controller synthesis. The purpose of this observability check is to decide whether or not to estimate the turbulence intensity. In practice, this will lead to the following: If there is little to no wake interaction in the wind farm, the measurements are poorly correlated with the turbulence intensity. Hence, the turbulence intensity is not estimated, and only the wind direction and wind speed are estimated. Contrarily, with more wake interaction, the turbulence intensity is estimated in addition to the wind speed and wind direction. To further brings confidence to the estimated ambient conditions, and thereby to the wind farm control algorithm.

### 4.3 Wake steering under time-varying inflow conditions

With a closed-loop control framework as proposed in Section 4.1, and a theoretical measure of observability as defined in Section 4.2, an integrated solution is now proposed and tested in this section. The results of this research have been published in an article submitted to the Renewable Energy journal. This publication is outlined in Section 4.3.1. A number of important findings and a short discussion follow in Section 4.3.2.

#### 4.3.1 Methodology and results

Most wind farm control algorithms in the literature have been tested under extremely simplified conditions: typically low- to medium-fidelity simulation environments, under constant inflow conditions, and in an idealized setting where the wind farm control algorithm has full knowledge about the inflow conditions. In practice, none of these assumptions are valid, and the research field should work towards pushing the level of realism in their control validation tests. The work presented in this section showcases a closed-loop control algorithm that is built to adapt to continuously changing ambient conditions, model mismatches and uncertainties in wind turbine measurements. This algorithm is then tested in high-fidelity simulation with time-varying inflow conditions as first of its kind in the literature.

The remainder of this section shows the article in preparation for submission to the Renewable Energy journal, expecting publication in 2020.

## Closed-loop model-based wind farm control using FLORIS under time-varying inflow conditions

Bart M. Doekemeijer\*, Daan C. van der Hoek, Jan-Willem van Wingerden

*Delft University of Technology, Mekelweg 2, 2628CD, Delft, The Netherlands*

---

### Abstract

With the global growth of wind energy comes a rise in academic interest towards further improving the efficiency of wind turbines and wind farms. Wind farm control attempts to coordinate turbines to improve the collective efficiency. However, most wind farm control algorithms proposed in the literature assume a constant inflow, whereas several properties of the inflow such as its direction and speed continuously change over time in reality. Furthermore, the inflow properties are typically assumed known in the literature, which is a fundamentally compromising assumption to make. This paper presents a novel, closed-loop controller that continuously estimates the ambient conditions supported by a theoretical notion of observability, upon which it maximizes the power yield of the farm through yaw-based wake steering. This algorithm is tested in a high-fidelity simulation environment with time-varying inflow conditions on a 6-turbine wind farm. To the best of the authors' knowledge, this is the first farm control solution tested in a high-fidelity simulation with such inflow variations. Over 5000 s of simulation, a gain of 1.1% in energy yield is obtained. Paired with this improvement comes the inevitable increase in yaw actuator duty cycle and a negligible change in the blade-root out-of-plane fatigue loads. A comparable simulation subject to time-invariant inflow conditions, as typically shown in the literature, yields a gain in power yield of 8.6%. These results highlight the potential of the proposed controller, addressing most uncertainties involved in real-world wind farms. This solidifies the controller as perhaps one of the first realistic,

---

\*B. M. Doekemeijer is with the Delft Center for Systems and Control (DCSC), within the group of Data-Driven Control of prof. Van Wingerden.

*Email address:* b.m.doekemeijer@tudelft.nl (Bart M. Doekemeijer)



robust, closed-loop solutions for yaw-based wake steering.

*Keywords:* closed-loop wind farm control, time-varying inflow, wake steering, ambient condition estimation, FLORIS, large-eddy simulation

---

## 1. Introduction

In the Dutch “Klimaatakkoord” (Rijksoverheid, 2019), the Dutch government promises a reduction of carbon-dioxide emissions of 49% by 2030 compared to 1990. By 2050, the emission of greenhouse gases must have been reduced by 95% compared to the emissions in 1990. Towards this goal, the Dutch government has been installing an increasing number of wind farms. By 2030, the goal is to have 11 GW of wind energy installed off the coast of The Netherlands, accounting for 40% of the national electricity demand.

As the global installed capacity of wind energy continues to grow, so does the academic interest towards further improving the efficiency of wind turbines and wind farms. One such research field is control engineering. In the past, the focus of control engineering has been on individual wind turbine control. More recently, the focus has shifted from wind turbine towards wind farm control, in which turbines are coordinated with one another to achieve a certain collective objective.

A general distinction can be made between two strategies of wind farm control, namely *induction control* and *wake steering*. The former aims at derating upstream turbines, which purposely lowers their power capture in order to leave more wind for turbines in subsequent rows. This is accomplished through pitching the turbine blades and adjusting the generator torque, and is typically used for active power control (e.g., Shapiro et al., 2018; Boersma et al., 2019) and load mitigation strategies (e.g., Kanev et al.). The second strategy, wake steering, displaces the wake downstream by misaligning the rotor plane with the incoming flow. This is typically accomplished by assigning a yaw misalignment to the turbine. The most common objective of wake steering is power maximization. Yaw-based wake steering has shown significant potential in high-fidelity simulation (e.g. Gebraad et al., 2016) and real-world experiments (Campagnolo et al., 2016; Howland et al., 2019; Fleming et al., 2019), with typical gains in wind-farm-wide power yield of 5% to 15%. The focus of this work is on yaw-based wake steering for power maximization.

Most of the wind farm control algorithms proposed in the literature take the inflow wind field as time invariant. However, in reality, the wind field entering a wind farm changes continuously due to fluctuations in the Earth's surface heating, among others. In consequence, it is of critical importance to test farm control solutions under such time-varying inflow. Moreover, properties of the inflow such as the wind direction and wind speed are typically assumed to be prior knowledge to the wind farm control solution, which is a secondary, unrealistic, compromising assumption. Such control algorithms are considered as open-loop solutions. This lack of appropriate measurements on the inflow conditions, the related sensor uncertainties and a high complexity in modeling of the relevant wind farm dynamics leads to the urge for a closed-loop solution in wind farm control. The closed-loop model-based framework presented in this work consists of two components, being *model adaptation* and *setpoint optimization*, as depicted in Figure 1. Model adaptation consists of estimating the input parameters to a surrogate model that are currently relevant for the wind farm. This surrogate model is a simplified mathematical model of the wind farm dynamics with a low computational cost. In practice and also in this work, model adaptation typically implies the estimation of the ambient inflow condition, defined by the wind speed, wind direction, and the turbulence intensity. Secondly, the setpoint optimization leverages the adapted surrogate model to find the turbine control setpoints that maximize a certain objective. In this work, the objective is power maximization and the control setpoints are the turbine yaw angles.

The main focus in the wind farm control literature has been on surrogate model development (e.g., Gebraad et al., 2016; Bastankhah and Porté-Agel, 2016) and control setpoint optimization methods (e.g., Marden et al., 2013; Bay et al., 2018; Annoni et al., 2018). More recently, there has been an increasing amount of interest towards the estimation of the ambient conditions and dealing with the time-varying nature of wind (e.g., Annoni et al., 2019; Rott et al., 2018; Simley et al., 2019; Doekemeijer and van Wingerden, 2019). However, many of the wind farm control algorithms proposed in the literature are merely tested on simplified simulation models, from which no real conclusions can be drawn apart from a proof of concept. Furthermore, the algorithms that are tested in high-fidelity simulation and real-world experiments typically assume a constant mean inflow wind direction, wind speed, and turbulence intensity (Boersma et al., 2017). However, experiments under such steady inflow conditions insufficiently represent real-world scenarios, and thus much uncertainty remains concerning the true potential

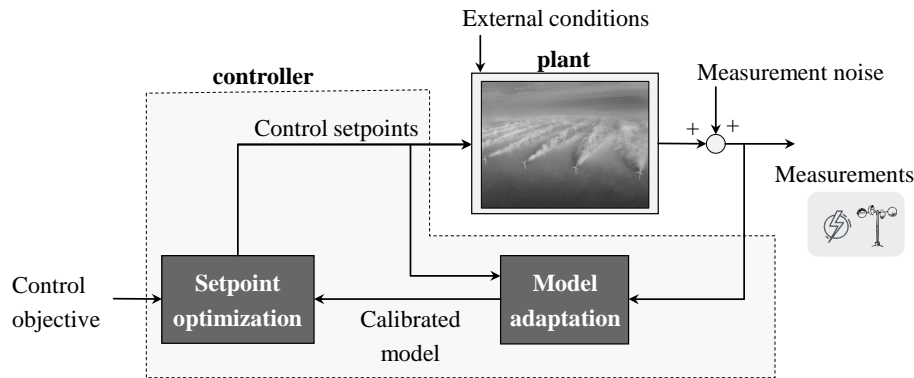


Figure 1: The closed-loop model-based wind farm control framework. A simplified surrogate model of the wind farm is used to represent the flow and turbine behavior at a low computational cost. The first step in the controller is model adaptation, implying the estimation of the inputs relevant for the current wind farm situation. Typically, this implies the estimation of the ambient conditions. Then, the turbine control setpoints are optimized using the surrogate model, which are the turbine yaw angles in this work.

of wind farm control in actual farms.

A handful of articles exist that considered time-varying inflow conditions for wind farm controller validation. Bossanyi (2019) has demonstrated a wind farm control algorithm in a low-fidelity simulation with time-varying inflow conditions. Furthermore, Ciri et al. (2017) presents a model-free control algorithm that improves the performance of turbines inside a wind farm, demonstrated through high-fidelity simulations under a time-varying inflow. However, model-free algorithms for wind farm control methods such as wake steering are fundamentally limited due to slow convergence rates combined with the inherent variability of the inflow conditions (Boersma et al., 2017).

To the best of the authors' knowledge, there is no literature on the assessment of model-based wind farm control solutions in a high-fidelity environment with time-varying inflow conditions. Addressing this scientific gap is invaluable for the practical validation and implementation of wind farm control solutions, as time-varying inflow conditions are omnipresent in real-world wind farms. The novel contributions of this article are:

1. a detailed fit of the surrogate wind farm model *FLORIS* to high-fidelity simulation data.
2. a novel, sophisticated, model-based estimation algorithm that predicts

the freestream wind direction, wind speed and turbulence intensity using readily available measurements in commercial wind farms, assisted by a theoretical measure of observability published in earlier work (Doekemeijer and van Wingerden, 2019),

3. closed-loop wind farm controller validation in high-fidelity simulation under time-varying inflow conditions,

The structure of this article is as follows. In Section 2, the surrogate model used for controller synthesis is outlined. In Section 3, the closed-loop wind farm controller is synthesized. This controller is tested in Section 4 through high-fidelity simulation under time-varying inflow conditions, among others, upon which the turbine energy yield and the turbine loads are investigated. Finally, the article is concluded in Section 5.

## 2. Surrogate model

The closed-loop control architecture outlined in Figure 1 requires a surrogate model describing the wind farm dynamics at a low computational cost. This surrogate model serves both for the model adaptation and the control setpoint optimization modules. Therefore, this model should, in an accurate fashion, predict the flow and turbine behavior as a function of the turbine control settings and the inflow wind field, while still being computationally tractable for real-time application. For this purpose, a popular, static, control-oriented surrogate model is opted for, where several model parameters are calibrated to high-fidelity simulation data.

### 2.1. Model definition

The surrogate model used in this work is the FLOW Redirection and Induction in Steady-state (FLORIS) model (Doekemeijer and Storm, 2018). FLORIS predicts the time-averaged three-dimensional flow field and turbine power capture of a wind farm for a predefined inflow. Since the surrogate model is static, the computational cost for a single model evaluation is in the order of  $10^{-2}$  to 1 s. Hence, FLORIS appears promising for the implementation in real-time control applications. The general inputs and outputs of the FLORIS model are shown in Figure 2. For a more detailed description of the model, the reader is referred to the literature (Bastankhah and Porté-Agel, 2016; Crespo and Hernández, 1996; Katic et al., 1987).

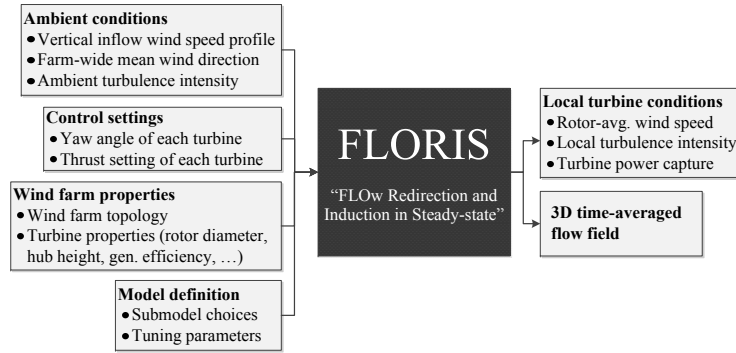


Figure 2: Flowchart of the FLORIS model. This model has four classes of inputs: the ambient conditions, the turbine control settings, the wind farm properties (e.g., layout), and a set of model parameters. FLORIS maps these inputs in a static fashion to a set of turbine outputs being the power capture and the three-dimensional flow field.

## 2.2. Model tuning prior to controller synthesis

Surrogate wind farm models typically contain many model parameters, which are chosen empirically or according to idealized theory (e.g., Gebraad et al., 2016; Bastankhah and Porté-Agel, 2016). For the surrogate model leveraged in this work, there are a total of 10 free parameters that need to be defined prior to simulation. Typically, the values of these parameters are based on theoretical studies and wind tunnel experiments (Bastankhah and Porté-Agel, 2016), but are known to vary with wind turbine type and various wind farm properties (Doekemeijer et al., 2019, e.g.). The success of the controller largely relies on the accuracy of the surrogate model. Hence, in this article, the parameters are tuned prior to controller synthesis in accordance to high-fidelity simulation data of the wind turbine and wind farm of interest. In this article, high-fidelity simulation data is generated using the large-eddy simulation tool *SOWFA*, to be described in Section 4.1.

First, the power curve of a single turbine as a function of the yaw misalignment in FLORIS is tuned. In this article, the wind farm of interest contains DTU 10MW reference wind turbines (Bak et al., 2012). Currently, FLORIS relies on a database of  $C_P$  and  $C_T$  coefficients for the 10MW turbine for a range of wind speeds ( $U_\infty$ ), yaw misalignment angles ( $\gamma$ ), turbulence intensities ( $I_\infty$ ) and derating settings, generated by an aero-elastic code using blade element-momentum theory. Based on a comparison with high-fidelity simulation data, the power coefficient is scaled by a empirically found multi-

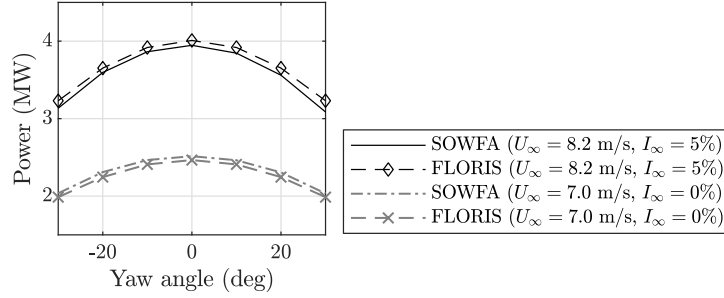


Figure 3: The power curve according to FLORIS and according to SOWFA as a function of the yaw misalignment angle. FLORIS is tuned to the data of two SOWFA simulations to guarantee a better match in power capture due to a yaw misalignment, thereby increasing the accuracy of the surrogate model.

plication factor of  $\eta(\gamma) = \frac{1.08}{\cos \gamma}$ . The result is shown in Figure 3.

Secondly, the wind profile behind a single turbine is tuned for. This is done by minimizing the error in the predicted flow fields between FLORIS and a set of 21 large-eddy simulations;

- 3 inflow conditions of a neutral atmospheric boundary layer (ABL).
  - Uniform inflow;  $U_\infty = 7.0$  m/s with  $I_\infty = 0\%$ .
  - Low-turbulence inflow;  $U_\infty = 8.0$  m/s with  $I_\infty = 6\%$ .
  - High-turbulence inflow;  $U_\infty = 8.0$  m/s with  $I_\infty = 12\%$ .
- For each inflow condition, a range of 7 yaw setpoints is assessed.
  - From  $\gamma = -30^\circ$  to  $\gamma = 30^\circ$  in steps of  $10^\circ$ .

The optimal model parameters  $\Omega^*$  are found by minimizing the root-mean-square error (RMSE) of the time-averaged flow field from SOWFA,  $U^{\text{SOWFA}} \in \mathbb{R}^{N_u}$ , and the flow field predicted by FLORIS,  $U^{\text{FLORIS}} \in \mathbb{R}^{N_u}$ , as

$$J_{\text{fit}}(\Omega) = \frac{1}{N_u} \sum_{i=1}^{N_u} w_i (U_i^{\text{FLORIS}}(\Omega) - U_i^{\text{SOWFA}})^2. \quad (1)$$

Here, the  $U$ -vectors are populated by taking  $N_u$  samples from the vertical cross-stream slices (wake profiles) at  $x = 3D$ ,  $x = 5D$ ,  $x = 7D$  and  $x = 10D$  downstream, with  $D$  the rotor diameter. Furthermore, the weighing

Table 1: Optimal model parameters after model fitting, including optimization bounds (*min* and *max*). It can be seen that none of the values are close to their optimization bounds, which suggests no overfitting has occurred.

Symbol	Relates to the...	Min	Max	Value
$k_a$	wake expansion	0.05	1.5	0.537
$k_b$	wake expansion	-0.01	0.02	-0.000848
$a_d$	wake deflection due to rotor rotation	-1.0	1.0	0.0011
$b_d$	wake deflection due to rotor rotation	-0.1	0.1	-0.0077
$\alpha$	distance of near-wake region	0.5	10.0	1.088
$\beta$	distance of near-wake region	0.03	0.60	0.222
$\tau_a$	turbine-induced turbulence	0.07	10.0	7.84
$\tau_b$	turbine-induced turbulence	0.08	10.0	4.57
$\tau_c$	turbine-induced turbulence	0.001	0.50	0.43
$\tau_d$	turbine-induced turbulence	-5.0	-0.01	-0.246

parameters are chosen as  $w_i^{3D} = 1$ ,  $w_i^{5D} = 2$ ,  $w_i^{7D} = 2$ , and  $w_i^{10D} = 1$ , respectively, to emphasize a good calibration in the flow field at  $5D$  and  $7D$  downstream, as turbines are often sited at this distance. Table 1 shows the optimized model parameters  $\Omega^*$  and the lower and upper optimization constraints. The parameters lie sufficiently far away from their extrema constraints, which suggests that the model was not overfitted.

### 2.3. Model validation

With the surrogate model calibrated for the individual turbine power curve and the single wake profile, the next step is model validation considering multiple turbines. The parameter set  $\Omega^*$  is validated using unseen data from three simulations of a three-turbine wind farm subjected to an inflow of  $U_\infty = 8.0$  m/s and  $I_\infty = 6.0\%$  in a neutral ABL. In these simulations, the first two turbines are misaligned with the inflow at  $\gamma_{1,2} = -20$  deg,  $\gamma_{1,2} = 0$  deg, and  $\gamma_{1,2} = 20$  deg, respectively, with  $\gamma_3 = 0$  deg for all three cases. This layout, inflow and operating conditions are chosen for a number of reasons. Firstly, the second turbine is set up experiences a slower, more turbulent inflow, effectively testing the wake model for inflow conditions it was not tuned for. Secondly, the third turbine operates in partially waked inflow, which is a common condition often causing significant model discrepancies in surrogate models (Martínez-Tossas et al., 2018). Thirdly, the upstream two turbines are purposely yawed in either direction to assess the model's validity under

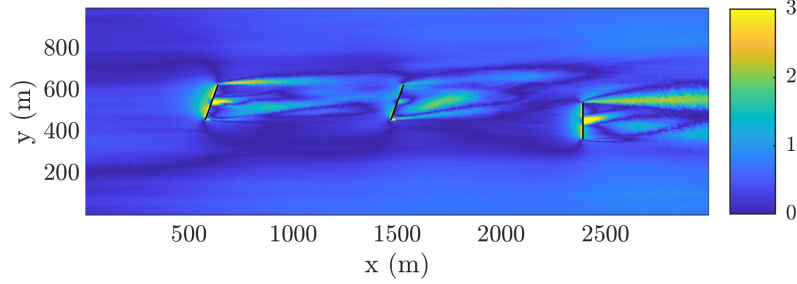


Figure 4: The absolute error between the hub-height flow field from SOWFA and as predicted by FLORIS in m/s. A great match is seen, especially in the far-wake regions and in front of the downstream turbines. Generally, the near-wake region is difficult to predict, and an accurate prediction near-wake flow is of less importance for wind farm control.

realistic wake-steering operation.

Figure 4 shows the absolute error between the hub-height flow field from SOWFA and as predicted by FLORIS for one of the three validation cases. This figure clearly shows that errors largely originate in the near-wake region, which are not particularly of interest for wind farm control. Generally, the far-wake regions and the flow in front of downstream turbines are well predicted, which should in turn lead to accurate predictions of the energy yield.

Furthermore, Figure 5 shows the cross-sectional wake profile at the turbine hub height at several streamwise distances,  $x = 1000$  m,  $x = 2000$  m and  $x = 2900$  m. Generally, the conclusions drawn from Figure 4 are confirmed. Additionally, this figure clearly shows an improvement of the parameter set  $\Omega^*$  over the default parameter choice  $\Omega^0$ .

Thus, a good match is found between FLORIS with  $\Omega^*$  and the time-averaged results from SOWFA for unseen data with multiple turbines and more complicated wake interaction. This analysis brings sufficient confidence in the surrogate model for it to be used in controller synthesis.

### 3. Controller synthesis

With the surrogate model defined, a closed-loop wind farm control solution can now be synthesized. The virtual wind farm studied in this article contains six DTU 10MW turbines sited in a 3 by 2 layout, spaced  $5D$  by  $3D$



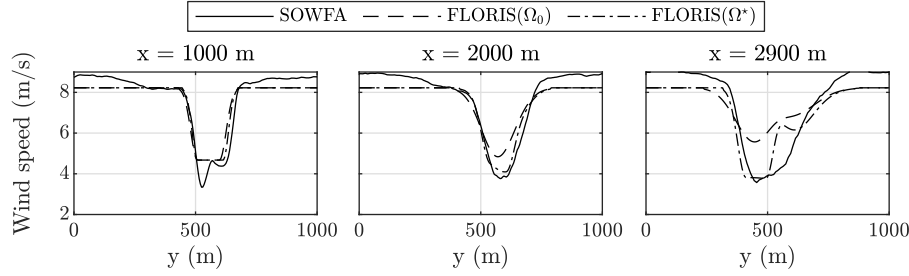


Figure 5: The wake profile at hub height for different locations downstream. An improvement is seen for the optimized set of parameters,  $\Omega^*$ , with the default parameters from the literature,  $\Omega_0$  (Bastankhah and Porté-Agel, 2016; Crespo and Hernández, 1996; Katic et al., 1987). Note that the wind speed outside of the wake appears higher in SOWFA. This is due to speed-up effects modeled in SOWFA, but neglected in FLORIS.

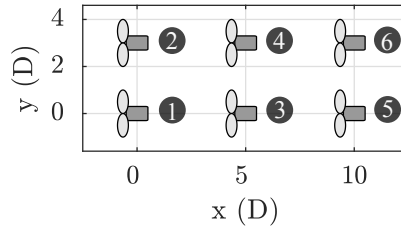


Figure 6: The six-turbine wind farm considered in this article. The turbines are DTU 10MW turbines (Bak et al., 2012), spaced  $5D$  apart longitudinally, and  $3D$  apart laterally.

apart, as shown in Figure 6. The model adaptation algorithm is described in Section 3.1. The control setpoint optimization algorithm is described in Section 3.2. An overview of the controller is given in Section 3.3.

### 3.1. Real-time model adaptation

Performance of the control solution is highly dependent on the assumed ambient conditions inside the surrogate model. As not all ambient conditions are measured (accurately) within the farm, a wind-farm-wide set of ambient conditions must be estimated before the control settings can be optimized.

In previous work (Doekemeijer et al., 2019), the wind direction was estimated using the approach of Bertelè et al. (2017), assuming blade load measurements and using blade element momentum (BEM) theory to de-

rive the turbine inflow conditions. In this work, instead, a temporally and spatially averaged freestream wind speed, wind direction and turbulence intensity are estimated using the readily available generator power and wind direction measurements of each turbine. This is achieved by minimizing the cost function

$$J_1(\Xi) = \frac{1}{N_T} \sum_{i=1}^{N_T} \lambda_P \left( P_i - \hat{P}_i(\Xi) \right)^2 + \left( \phi_i - \hat{\phi} \right)^2, \quad (2)$$

with  $N_T$  being the number of turbines,  $\lambda_P$  a weighing term assigned as  $2.0 \cdot 10^{-14}$  found empirically,  $P$  and  $\phi$  being vectors of length  $N_T$  with the time-averaged measured power and wind vane signals, respectively, and  $\hat{P}$  a vector of length  $N_T$  with the estimated power signal of each turbine according to the surrogate model. When sweeping over different hypothesized ambient conditions  $\Xi$ , the yaw angles of the turbines in FLORIS are assumed to be fixed and equal to the most recent nacelle orientation measurements. Moreover, depending on the *observability* of the situation, we either estimate three parameters or two parameters:  $\Xi = [\hat{\phi}, \hat{U}_\infty, \hat{I}_\infty]$  or  $\Xi = [\hat{\phi}, \hat{U}_\infty]$ . Observability in this sense refers to the degree of information contained within the measurements available, and whether this suffices to estimate a certain set of parameters. A more elaborate analysis concerning the observability and the choice of  $\Xi$  is performed in Doekemeijer and van Wingerden (2019), and the interested reader is referred to this work for further reference.

The relative degree of observability for the various wind directions of the 6-turbine wind farm of Figure 6 is shown in Figure 7. The top colormap shows the relative degree of observability for when  $\Xi = [\hat{\phi}, \hat{U}_\infty, \hat{I}_\infty]$  under the assumption that turbine power and wind direction measurements are available. A value of 0 implies that not all ambient conditions can be derived from the measurements, while a value of 1 refers to the best-estimatable situation. The lower colormap saturates to values of 0 and 1 exclusively, with a threshold of 0.20 found empirically.

Within the farm control solution, this saturated colormap is used to decide whether to estimate  $\Xi = [\hat{\phi}, \hat{U}_\infty, \hat{I}_\infty]$  (black zones) or to only estimate  $\Xi = [\hat{\phi}, \hat{U}_\infty]$  (white zones). If  $\Xi = [\hat{\phi}, \hat{U}_\infty]$ , the turbulence intensity is assumed to be equal to the last estimated value, and only the wind direction and wind speed estimates are updated. Performing the observability analysis with  $\Xi = [\hat{\phi}, \hat{U}_\infty]$  leads to a fully observable situation over the entire wind rose. By scheduling what parameters to estimate,  $I_\infty$  is only estimated when

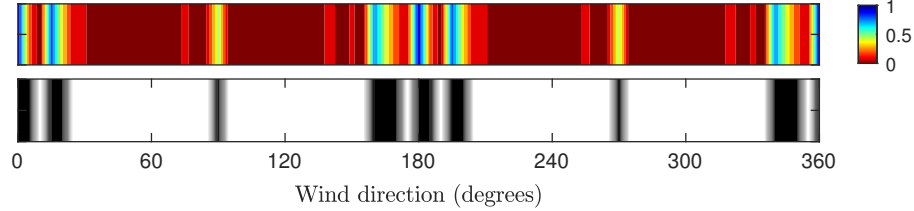


Figure 7: The observability of the situation with  $\Xi = [\hat{\phi}, \hat{U}_\infty, \hat{I}_\infty]$  and when both turbine power and wind direction measurements are available. The top colormap shows the observability on a scale of 0 (not observable) to 1 (most observable). The bottom colormap saturates to values of 0 and 1, with a threshold at 0.20. The observability is shown for the complete rose of wind directions. These plots are produced under a true TI of 6% and  $U_\infty = 8$  m/s. It is confirmed by simulation that the observability does not significantly vary over the TI and  $U_\infty$ . Within the farm control solution, the bottom colormap is used to decide whether to estimate  $\Xi = [\hat{\phi}, \hat{U}_\infty, \hat{I}_\infty]$  (black zones) or to only estimate  $\Xi = [\hat{\phi}, \hat{U}_\infty]$  (white zones).

there is sufficient information in the measurements to do so.<sup>1</sup>

### 3.2. Real-time control setpoint optimization

After estimating the ambient conditions, the turbine yaw angles are optimized and collected in a look-up table (LUT) to maximize the steady-state wind farm power production. The cost function to be minimized is

$$J_2(\gamma) = - \sum_{i=1}^{N_T} \hat{P}_i(\gamma_i). \quad (3)$$

Following this optimization, FLORIS assigns strong jumps in the yaw angle for small changes in the wind direction as to be optimal (Rott et al., 2018). These angles are therefore smoothened in post-processing using a Gaussian distribution along the wind direction with a standard deviation of  $1.5^\circ$ .<sup>2</sup> The turbines are set to not exceed a  $30^\circ$  yaw misalignment for reasons of structural loading.

<sup>1</sup>Note that Figure 7 of this paper is largely identical to Figure 7 of Doekemeijer and van Wingerden (2019), though plotted in a different fashion (linearly vs. radially).

<sup>2</sup>A more elaborate study will be necessary to determine the degree of smoothing that yields the highest energy yield. This will strongly depend on the variability of the wind and the accuracy of the surrogate model. More variability and a lower accuracy will lead to more smoothing and more conservative yaw setpoints.

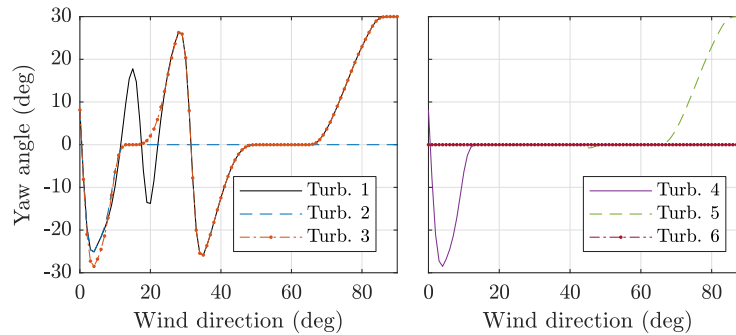


Figure 8: Optimized yaw angles as a function of wind direction for  $I_\infty = 0.07$ .

The smoothened, optimized yaw angles for the 6-turbine case with a wind speed of  $U_\infty = 8$  m/s and a low-to-medium turbulence intensity of  $I_\infty = 0.07$  are shown in Figure 8. These optimal yaw angles are largely insensitive to the wind speed in region 2 operation (Kanev, 2020). The wind direction in Figure 8 is plotted along the x-axis, where 0 deg means wind flowing from west to east, and 90 deg means wind flowing from south to north. In the 6-turbine layout, this means that turbine 1 is always upstream, and turbine 6 is always downstream. Hence, turbine 1 experiences a lot of yaw misalignment, while turbine 6 remains aligned over the entire wind range. It should be noted that, as the turbulence intensity increases, the flow recovers more quickly, wake losses diminish, and the optimal yaw misalignment angles decrease – there is less to be gained at downstream turbines.

### 3.3. An overview

The closed-loop control algorithm is synthesized by combining the estimator from Section 3.1 with the optimizer from Section 3.2. A pseudo-code is shown in Algorithm 1, where the controller generates new control setpoints every 20 seconds.

## 4. Simulation results

In this section, the controller synthesized in Section 3 is tested in high-fidelity simulation. For this purpose, a large-eddy simulation model is used. This model is described in Section 4.1. Then, two simulation cases are investigated, respectively a worst-case scenario and a best-case scenario. In

---

**Algorithm 1** Pseudo-code of the closed-loop control algorithm
 

---

```

 $k \leftarrow 0$ 
while wind farm controlled enabled do

  %% Gather time-averaged measurements
   $P \leftarrow$  SCADA measurements
   $\phi \leftarrow$  SCADA measurements

  if  $t = 20 \text{ s}, 40 \text{ s}, 60 \text{ s}, 80 \text{ s}, \dots$  then
     $k \leftarrow k + 1$ 

    %% Determine observability of situation
     $\hat{\phi}^k \leftarrow \frac{1}{N_T} (\phi_1 + \phi_2 + \dots + \phi_{N_T})$ 
     $\mathcal{O} \leftarrow \text{observability}(\hat{\phi}^k)$ 

    %% Determine ambient conditions
    if  $\mathcal{O} \geq 0.20$  then
       $[\hat{\phi}^k, \hat{U}_\infty^k, \hat{I}_\infty^k] \leftarrow \min(J_1)$ 
    else
       $\hat{I}_\infty^k \leftarrow \hat{I}_\infty^{k-1}$ 
       $[\hat{\phi}^k, \hat{U}_\infty^k] \leftarrow \min(J_1)$ 
    end if

    %% Determine optimal yaw setpoints
     $\gamma \leftarrow \text{lookupYawTable}(\hat{\phi}^k, \hat{U}_\infty^k, \hat{I}_\infty^k)$ 

  end if
end while

```

---

Table 2: Important variables for the turbines and numerical mesh in SOWFA

Variable	Value
Turbine type	DTU 10MW (Bak et al., 2012)
Rotor approximation	Actuator line ( <i>ALMAdvanced</i> )
Inter-turbine spacing	$5D \times 3D$ with $D = 178.3$ m
Domain size	$3.0 \text{ km} \times 3.0 \text{ km} \times 1.0 \text{ km}$
Cell size (base mesh)	$10 \text{ m} \times 10 \text{ m} \times 10 \text{ m}$
Cell size (refined, near rotor)	$2.5 \text{ m} \times 2.5 \text{ m} \times 2.5 \text{ m}$
Blade epsilon	5.0 m

the first case, the inflow wind direction varies significantly throughout the simulation to stress-test the control algorithm. In the second case, the inflow is time invariant and chosen to yield a situation with high wake losses. In Section 4.2, the estimation submodule is assessed based on the time-varying simulation case. Then, in Section 4.3, the optimization submodule of the controller is evaluated by looking into the energy yield of the turbines. Finally, in Section 4.4, the yaw actuator duty cycle and the structural loads on the turbine blades are investigated to get a notion of the effect of wake steering on the upstream and downstream turbines.

#### 4.1. The Simulator for Wind Farm Applications

For surrogate model validation and controller verification, the high-fidelity Simulator for Wind Farm Applications (SOWFA) model developed by the National Renewable Energy Laboratory (NREL) is used (Churchfield et al., 2012). SOWFA is a large-eddy wind farm simulation model that leverages the actuator line model to determine the forces applied by each turbine on the flow. In recent work, this high-fidelity simulator was coupled with MATLAB using a network-based communication interface (Doekemeijer et al., 2019) for straight-forward control algorithm testing. An overview of the turbine layout and numerical mesh scheme is shown in Figure 6 and Table 2.

#### 4.2. Model adaptation performance

The first component of the closed-loop controller synthesized in Section 3 is the *model adaptation* block, as shown in Figure 1. For the first simulation case, the 6-turbine wind farm experiences a wind field of which the inflow direction changes often over time, as shown in the left subplot of Figure 9. In this figure, the dashed gray lines show the true values from SOWFA, while the

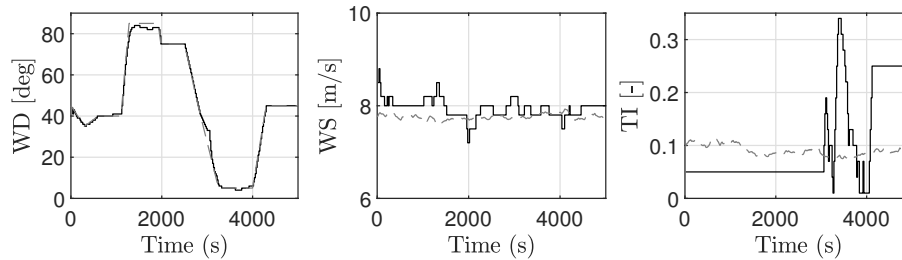


Figure 9: Overview of the estimator's performance in reconstructing the ambient conditions for the simulation with time-varying inflow. The true values are shown as gray, dashed lines. The ambient conditions estimated by the controller are shown as solid black lines. Generally, estimates are very accurate for the wind direction (WD) and wind speed (WS), while it is far less accurate for the turbulence intensity (TI).

solid black lines show the estimated values according to the controller. The true freestream wind speed is approximately 8 m/s and the true freestream turbulence intensity is around 9%.

Taking a closer look at Figure 9, it becomes clear that the wind direction (WD) and the wind speed (WS) are estimated accurately and consistently. Note that wind direction is by far the most important quantity to estimate, as the optimal yaw setpoints are most sensitive to this variable, and less so for the wind speed and turbulence intensity (Kanev, 2020). The only variable that calls for concern is the turbulence intensity. This variable is only estimated when the situation is sufficiently *observable*, as defined in Section 3.1. The wind direction often leads to the situations with little to no wake interaction, and hence the turbulence intensity is not estimated until about 3000 s into the simulation. Then, it is often estimated to be very high, up to 35%, which does not match with the physical value from SOWFA. In FLORIS, a high turbulence intensity leads it to predict very high wake recovery. An explanation for this behavior is the rapid fluctuations in the wind direction. When the inflow changes direction, an observable situation arises, and the turbulence intensity is estimated using the turbine power measurements. However, if the wakes have not yet propagated/aligned with the new inflow direction, these turbines still generate a lot of power and operate as if they are in freestream flow. The control algorithm responds to this by assigning a very high turbulence intensity to FLORIS, predicting that the wakes recover before reaching the downstream turbines – thereby effectively minimizing the error between the measurements and what is predicted by

FLORIS. Hence, one may consider this erroneous estimation of the TI as the controller attempting to account for wake propagation in a steady model. As the wakes further propagate downstream and a steady situation arises in SOWFA, which typically takes in the order of  $10^2$  s, the estimated TI should settle to more accurate values.

The flow field and turbine power signals for SOWFA and FLORIS are shown in Figure 10. As the turbine power signals are used for model adaptation, it is no surprise that the turbine power signals match very well between SOWFA and FLORIS. Notably, an interesting difference between SOWFA and FLORIS is that FLORIS predicts many situations of symmetry, in which turbines are predicted to capture an equal amount of power. In SOWFA, however, the turbulent inflow unavoidably leads to differences in power capture between turbines.

Furthermore, comparing the flow field at hub height from SOWFA with that predicted by FLORIS in Figure 10 allows us to conclude that the estimation algorithm performs very well. The controller is able to reconstruct the flow field at a high accuracy, even under significant variations in the inflow wind direction. Note that there is a significant model discrepancy between SOWFA and FLORIS, as FLORIS is a steady-state model and thus completely neglects any time dependencies. Moreover, In FLORIS, several fundamental assumptions are made on the single wake profile and the interaction between multiple wakes. Most flow estimation errors are expected to be due the absence of secondary steering effects (Martínez-Tossas et al., 2018) and time-dependent wake propagation in the surrogate model.

When investigating the situations in which the turbulence intensity was poorly estimated (e.g., for  $t = 4900$  s, recalling Figure 9) in Figure 10, one can see that this does not particularly lead to problematic situations. Actually, the flow field and the turbine power signals show a good match between FLORIS and SOWFA, even under a wrongfully high estimate of TI. Since there is little wake interaction due to the particular inflow situation at this time instant, there is insufficient information to correct the TI estimate (*unobservable*). At the same time, little wake interaction leads to little to no wake steering. Thus, these two are complementary. If wake interactions would increase due to a change in the inflow, the observability would increase, leading to more accurate TI estimations. With an accurate estimate of TI, the full potential of wake steering is leveraged. Note that, if the turbulence intensity is estimated to be too high, this would only lead to a reduction in the assigned yaw angles and in the worst-case scenario, to greedy operation.



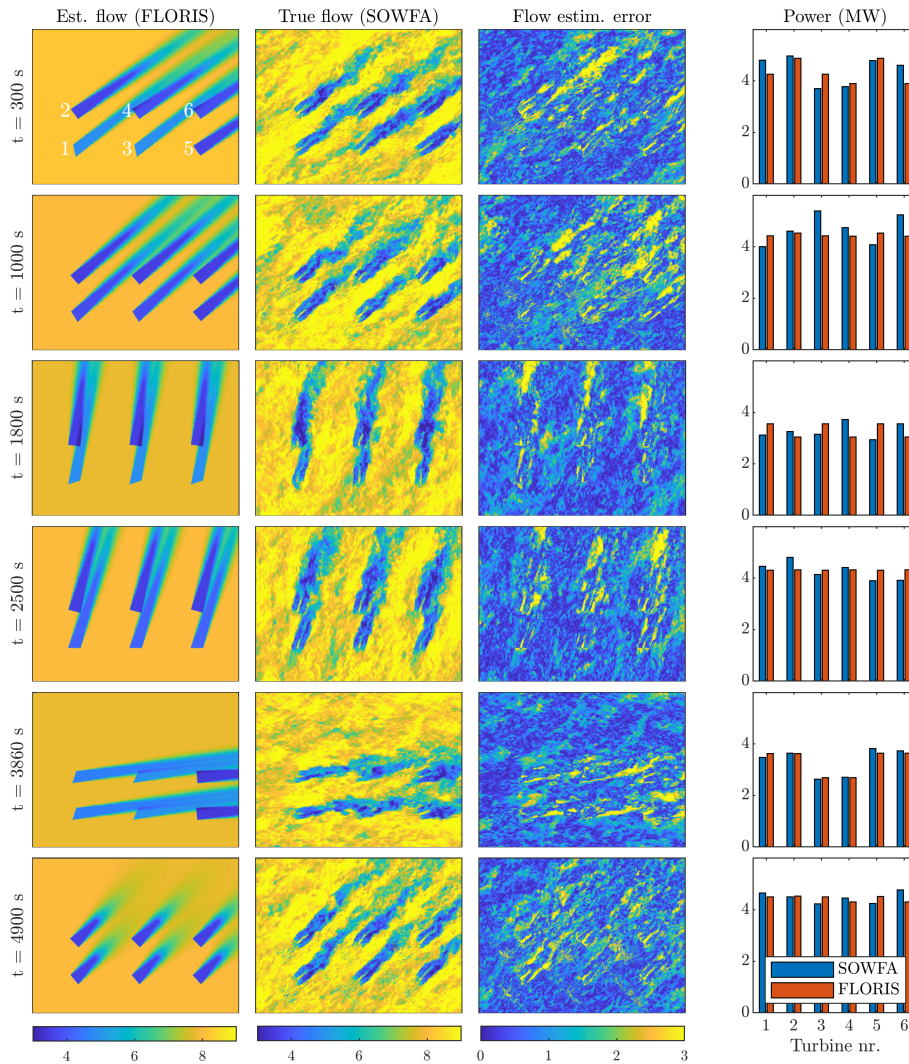


Figure 10: The estimation performance of the closed-loop controller for the simulation with time-varying inflow. The true farm's flow field and turbine power signals from SOWFA are compared to those estimated by FLORIS. This figure clearly shows that the wind farm controller accurately predicts the power signals and flow fields of SOWFA, even though there are significant model discrepancies. Most flow estimation errors are due the absence of secondary steering effects (Martínez-Tossas et al., 2018) and time-dependent wake propagation in the surrogate model.

Thus, an erroneous of the TI will, in the worst case, only lead to a suboptimal configuration of yaw angles, and not perform worse than a baseline, greedy control strategy.

#### *4.3. Setpoint optimization performance*

With the ambient conditions estimated, the second component of the closed-loop controller is setpoint optimization, as shown in Figure 1. In this work, that consists of the optimization of the turbine yaw misalignment angles to maximize the power extraction of the wind farm.

The turbine power capture from SOWFA for the case with time-varying inflow is shown in Figure 11. In this figure, the relative power capture of each turbine compared to the greedy-controlled scenario is shown averaged over the 5000 s of simulation. Since the wind changes from an inflow from left to right to an inflow from bottom to top and anywhere in between, turbines 1, 2, 3 and 5 are most often upstream, while turbines 4 and 6 are mostly downstream. Hence, wake steering induces most losses on turbines 1 and 3 by yawing these turbines, leading to significant energy gains on turbines 4 and 6. Over the total 5000 s of simulation, the energy yield is 1.1% higher with the closed-loop controller compared to the baseline case.

Note that 1.1% is lower than most values cited in the literature (Boersma et al., 2017), as those studies typically only focus on cases with significant wake losses. In this simulation, there are many situations with little to no wake interaction. Furthermore, a noticeable gain of 1.1% under the large discrepancies between FLORIS and SOWFA is a very promising (and more realistic) estimate of the true potential of wake steering.

For comparison, a second simulation is performed with a constant inflow from left to right, in which turbines 3-6 operate in waked flow. The relative power capture for this simulation is shown in Figure 12. In contrast to the first simulation case, there are consistent wake losses throughout the 5000 s of simulation, and wake steering leads to consistent gains. In total, a gain of 8.6% is found for the 6-turbine wind farm using the proposed controller. This agrees with the results typically cited in the literature (Boersma et al., 2017) for such wake-loss-heavy situations.

#### *4.4. A deeper look into the yaw actuator duty cycle and structural loads*

Wake steering shows to be very promising in increasing the energy yield of a wind farm. However, in contrast to the energy gains, the increase and uncertainty surrounding the actuator duty cycle and the structural loads on

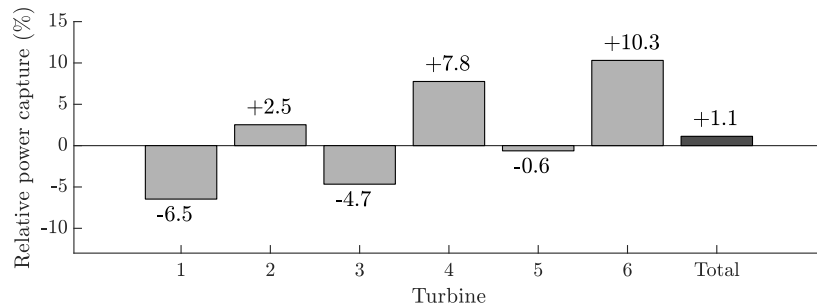


Figure 11: Relative turbine power capture compared to the case in which turbines are controlled in the traditional, greedy manner for the case with time-varying inflow. The turbines that are most often standing upstream experience most losses, as they are most often misaligned with the inflow. The largest gains are attained by the turbines that operate most often in a waked inflow. The total energy gain of the wind farm is 1.1%.

the turbines have prevented the implementation of wake steering in existing wind farms. This subsection addresses these two topics. However, more research is necessary to provide confident estimates of the change in loads on the turbines for wake steering.

#### *Yaw actuator duty cycle under wake steering*

The change in the yaw actuator duty cycle (*yaw travel*) of each turbine for the first simulation case with time-varying inflow conditions is shown in Figure 13. From this figure, it is clear to see that wake steering has a great influence on the yaw actuator duty cycle. Specifically, for the upstream turbines, an increase in yaw travel of approximately 200% is seen. Furthermore, even for the second row of turbines, an increase in yaw travel of approximately 60% is seen. This yaw travel can be related back to Figure 8, in which relatively large gradients can be seen for small changes in the wind direction. One may reduce the yaw travel by further smoothing the optimized yaw angles from Figure 8, but this may go at the loss of energy yield. In a practical controller implementation, a trade-off would have to be made according to the yaw actuator limits, the wind farm layout, and the wind rose of the wind farm.

#### *Fatigue loads on the blade roots*

The damage-equivalent loads (DELs) of the out-of-plane bending moments at the blade roots are calculated following the Palmgren Miner's rule

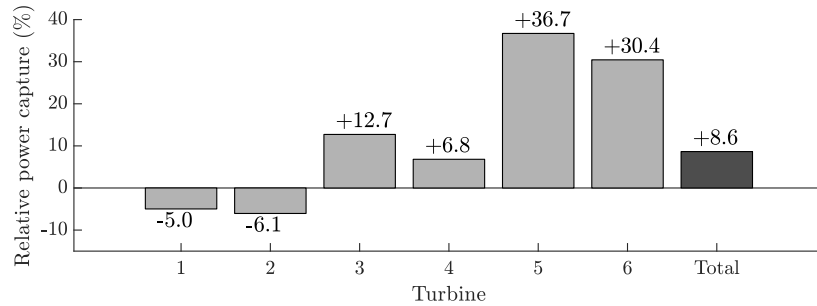


Figure 12: Relative turbine power capture compared to the case in which turbines are controlled in the traditional, greedy manner for the case with constant inflow (zero degrees, left to right in Figure 6). Turbines 1 and 2 experience most losses, as they are most often misaligned with the inflow. The largest gains are noticed on turbines 5 and 6. The total energy gain of the wind farm is 8.6%.

(Cosack, 2010), as

$$\text{DEL} = \sqrt[m]{\frac{\sum_{i=1}^n \Delta S_i^m \cdot N_i}{N_{\text{ref}}}}. \quad (4)$$

In this equation,  $m$  is the inverse of the material Wöhler slope and  $N_{\text{ref}}$  is a reference number for the total amount of cycles, taken to be 1 here,  $S_i$  is the mean load range value for a particular bin, and  $N_i$  is the number of occurrences within the bin. The load cycles are calculated following the popular rainflow counting method. Note that the blades of the DTU 10MW turbine are manufactured with a mix of glass fiber, carbon fiber, and balsa (Bak et al., 2012). Hence, the DEL values are evaluated with both  $m = 10$  (glass fiber) and with  $m = 14$  (carbon fiber), and the highest value of the two will be shown.

The DELs for the first simulation study with time-varying inflow are plotted in Figure 14. The loads between the three blades are very similar, and hence the blade-averaged DELs are shown. From this figure, it is seen that the DELs mostly decrease, apart from turbine 1, which always operates upstream and most often at a yaw misalignment. In the case of turbine 1, SOWFA predicts a relatively small increase in DEL for operating under a yaw misalignment, while predicting significant decreases in DEL for the other 5 turbines due to a less-waked inflow caused by wake steering.

The DELs for the second simulation study with constant inflow are shown in Figure 15. This figure shows the same trends as the case with time-varying

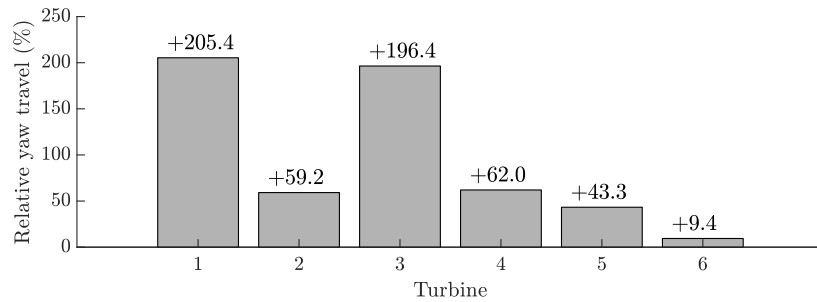


Figure 13: Relative yaw travel compared to the greedy-operated case for the simulation with time-varying inflow. A significant increase in yaw travel is noticed, especially in the most upward turbines.

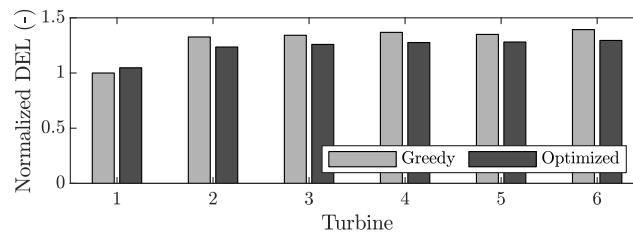


Figure 14: Damage equivalent loads for the blade root out-of-plane bending moments for the simulation case with time-varying inflow conditions, normalized with respect turbine 1 in greedy operation.

inflow. Specifically, the DELs do not noticeable change with wake steering; there is a small increase in DEL for turbine 1, and a small decrease for all other turbines.

Generally, wake steering seems to have a relatively small effect on the blade root out-of-plane bending moments in this simulation study. There is a delicate balance between the change in loads due to yawing a turbine, and due to the change in the wake profile as a result of the yawing of an upstream turbine (Mendez Reyes et al., 2019). Therefore, simulations with a higher-fidelity aero-elastic model (e.g., using OpenFAST (National Renewable Energy Laboratory (NREL), 2019)) and physical experiments are necessary to further solidify such statements.

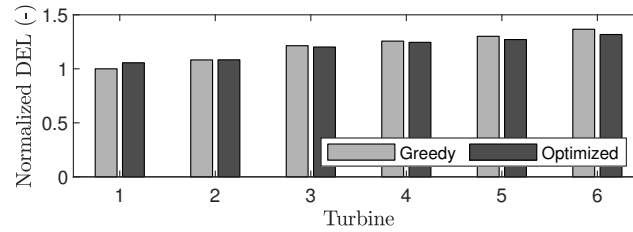


Figure 15: Damage equivalent loads for the blade root out-of-plane bending moments for the simulation case with constant inflow conditions, normalized with respect turbine 1 in greedy operation.

## 5. Conclusions

In this article, a novel, closed-loop wind farm control solution was proposed. This control solution relies on a surrogate model of the wind farm. This surrogate model is used in twofold. Firstly, it is used to estimate the ambient conditions, supported by a theoretical measure of observability to avoid the estimation of quantities about which no information is available. Secondly, the surrogate model is leveraged to optimize the turbine control setpoints for power yield maximization.

This closed-loop control solution was then tested in high-fidelity simulation under a time-varying inflow, being the first of its kind in the literature. The wind direction of the inflow in the simulation was scheduled to change often and with steep gradients to stress-test the controller. Compared to baseline operation, a total gain in energy yield of 1.1% was found for a 6-turbine wind farm. Furthermore, from an actuator duty cycle perspective, the yaw travel of the turbines increased with up to 200%. Additionally, the damage equivalent loads of the blade root out-of-plane bending moments did not change noticeably compared to the baseline controller. In a second simulation, the inflow was time-invariant and chosen to yield a wake-loss-heavy situation. In this simulation, the controller yielded a wind-farm-wide energy gain of 8.6% compared to baseline operation. This agrees very well with studies in the literature which mostly consider wind farms with time-invariant inflows (Boersma et al., 2017).

The results presented in this article highlight the potential of the proposed controller, even under time-varying inflow conditions, addressing most uncertainties involved in real-world wind farms. This solidifies the proposed control solution as perhaps one of the first realistic, robust, closed-loop

solutions for yaw-based wake steering.

## 6. Acknowledgments

The authors would like to thank Yusik Kim for his suggestions on setting up time-varying inflow simulations in SOWFA. Furthermore, the authors express their gratitude towards Sebastiaan Mulders and Joeri Frederik for providing insightful comments in presenting this work and writing the article. The work presented in this article was done as part of the European CL-Windcon (*Closed-Loop Wind Farm Control*) project. This project has received funding from the European Union's Horizon 2020 research and innovation programme under grant agreement No 727477.

## References

- Annoni, J., Bay, C., Johnson, K., Dall'Anese, E., Quon, E., Kemper, T., Fleming, P., 2019. Wind direction estimation using scada data with consensus-based optimization. *Wind Energy Science* 4, 355–368. doi:10.5194/wes-4-355-2019.
- Annoni, J., Bay, C., Taylor, T., Pao, L., Fleming, P., Johnson, K., 2018. Efficient optimization of large wind farms for real-time control, in: 2018 Annual American Control Conference (ACC), pp. 6200–6205. doi:10.23919/acc.2018.8430751.
- Annoni, J., Fleming, P., Scholbrock, A., Roadman, J., Dana, S., Adcock, C., Porte-Agel, F., Raach, S., Haizmann, F., Schlipf, D., 2018. Analysis of control-oriented wake modeling tools using lidar field results. *Wind Energy Science Discussions* 2018, 1–17. doi:10.5194/wes-2018-6.
- Bak, C., Bitsche, R., Yde, A., Kim, T., Hansen, M., Zahle, F., Gaunaa, M., Blasques, J., Døssing, M., Wedel Heinen, J.J., Behrens, T., 2012. Light rotor: The 10-mw reference wind turbine, in: Proceedings of EWEA 2012 - European Wind Energy Conference & Exhibition, European Wind Energy Association (EWEA).
- Bastankhah, M., Porté-Agel, F., 2016. Experimental and theoretical study of wind turbine wakes in yawed conditions. *Journal of Fluid Mechanics* 806, 506—541. doi:10.1017/jfm.2016.595.

- Bay, C.J., Annoni, J., Taylor, T., Pao, L., Johnson, K., 2018. Active power control for wind farms using distributed model predictive control and nearest neighbor communication, in: 2018 Annual American Control Conference (ACC), pp. 682–687. doi:10.23919/acc.2018.8431764.
- Bertelè, M., Bottasso, C.L., Cacciola, S., Daher Adegas, F., Delport, S., 2017. Wind inflow observation from load harmonics. *Wind Energy Science* 2, 615–640. doi:10.5194/wes-2-615-2017.
- Boersma, S., Doekemeijer, B., Siniscalchi-Minna, S., van Wingerden, J., 2019. A constrained wind farm controller providing secondary frequency regulation: An les study. *Renewable Energy* 134, 639 – 652. doi:https://doi.org/10.1016/j.renene.2018.11.031.
- Boersma, S., Doekemeijer, B.M., Gebraad, P.M.O., Fleming, P.A., Annoni, J., Scholbrock, A.K., Frederik, J.A., van Wingerden, J.W., 2017. A tutorial on control-oriented modeling and control of wind farms. *American Control Conference (ACC)* , 1–18doi:10.23919/acc.2017.7962923.
- Bossanyi, E., 2019. CL-Windcon D2.5: wind farm controller design and testing in LongSim. CL-Windcon deliverable repository Chapter 3, European Horizon 2020 project.
- Campagnolo, F., Petrović, V., Bottasso, C.L., Croce, A., 2016. Wind tunnel testing of wake control strategies. *Proceedings of the American Control Conference (ACC)* , 513–518.
- Churchfield, M.J., Lee, S., Michalakes, J., Moriarty, P.J., 2012. A numerical study of the effects of atmospheric and wake turbulence on wind turbine dynamics. *Journal of Turbulence* 13, 1–32. doi:10.1080/14685248.2012.668191.
- Ciri, U., Rotea, M., Santoni, C., Leonardi, S., 2017. Large-eddy simulations with extremum-seeking control for individual wind turbine power optimization. *Wind Energy* 20, 1617–1634. doi:10.1002/we.2112.
- Cosack, N., 2010. Fatigue loads monitoring with standard wind turbine signals. Ph.D. thesis. Stuttgart, Germany.



- Crespo, A., Hernández, J., 1996. Turbulence characteristics in wind-turbine wakes. *Journal of Wind Engineering and Industrial Aerodynamics* 61, 71 – 85. doi:10.1016/0167-6105(95)00033-X.
- Doekemeijer, B.M., Fleming, P.A., van Wingerden, J.W., 2019. A tutorial on the synthesis and validation of a closed-loop wind farm controller using a steady-state surrogate model. *American Control Conference (ACC)* .
- Doekemeijer, B.M., Storm, R., 2018. FLORISSE\_M Github repository. [https://github.com/TUDELFT-DataDrivenControl/FLORISSE\\_M](https://github.com/TUDELFT-DataDrivenControl/FLORISSE_M).
- Doekemeijer, B.M., van Wingerden, J.W., 2019. Observability of the ambient conditions in model-based estimation for wind farm control: a focus on static models. *Wind Energy* In review.
- Fleming, P., King, J., Dykes, K., Simley, E., Roadman, J., Scholbrock, A., Murphy, P., Lundquist, J.K., Moriarty, P., Fleming, K., van Dam, J., Bay, C., Mudafort, R., Lopez, H., Skopek, J., Scott, M., Ryan, B., Guernsey, C., Brake, D., 2019. Initial results from a field campaign of wake steering applied at a commercial wind farm – part 1. *Wind Energy Science* 4, 273–285. doi:10.5194/wes-4-273-2019.
- Gebraad, P.M.O., Teeuwisse, F.W., van Wingerden, J.W., Fleming, P.A., Ruben, S.D., Marden, J.R., Pao, L.Y., 2016. Wind plant power optimization through yaw control using a parametric model for wake effects - a cfd simulation study. *Wind Energy* 19, 95–114. doi:10.1002/we.1822.
- Howland, M.F., Lele, S.K., Dabiri, J.O., 2019. Wind farm power optimization through wake steering. *Proceedings of the National Academy of Sciences* 116, 14495–14500. doi:10.1073/pnas.1903680116.
- Kanev, S., 2020. Dynamic wake steering and its impact on wind farm power production and yaw actuator duty. *Renewable Energy* 146, 9 – 15. doi:10.1016/j.renene.2019.06.122.
- Kanev, S.K., Savenije, F.J., Engels, W.P., . Active wake control: An approach to optimize the lifetime operation of wind farms. *Wind Energy* 21, 488–501. doi:10.1002/we.2173.
- Katic, I., Højstrup, J., Jensen, N., 1987. A Simple Model for Cluster Efficiency. A. Raguzzi. pp. 407–410.

- Marden, J.R., Ruben, S.D., Pao, L.Y., 2013. A model-free approach to wind farm control using game theoretic methods. *IEEE Transactions on Control Systems Technology* .
- Martínez-Tossas, L.A., Annoni, J., Fleming, P.A., Churchfield, M.J., 2018. The aerodynamics of the curled wake: A simplified model in view of flow control. *Wind Energy Science Discussions* 2018, 1–17. doi:10.5194/wes-2018-57.
- Mendez Reyes, H., Kanev, S., Doekemeijer, B., van Wingerden, J.W., 2019. Validation of a lookup-table approach to modeling turbine fatigue loads in wind farms under active wake control. *Wind Energy Science Discussions* 2019, 1–19. doi:10.5194/wes-2019-34.
- National Renewable Energy Laboratory (NREL), 2019. NWTC Information Portal (OpenFAST). <https://nwtc.nrel.gov/OpenFAST>. Accessed July 2, 2019.
- Rijksoverheid, 2019. Klimaatakkoord. Technical Report. Rijksoverheid.
- Rott, A., Doekemeijer, B.M., Seifert, J., van Wingerden, J.W., Kühn, M., 2018. Robust active wake control in consideration of wind direction variability and uncertainty. *Wind Energy Science Discussions* 2018, 1–22. doi:10.5194/wes-2018-50.
- Shapiro, C.R., Meyers, J., Meneveau, C., Gayme, D.F., 2018. Wind farms providing secondary frequency regulation: evaluating the performance of model-based receding horizon control. *Wind Energy Science* 3, 11–24. doi:10.5194/wes-3-11-2018.
- Simley, E., Fleming, P., King, J., 2019. Design and analysis of a wake steering controller with wind direction variability. *Wind Energy Science Discussions* 2019, 1–26. doi:10.5194/wes-2019-35.

### 4.3.2 A continued discussion

The closed-loop wind farm control solution presented in Section 4.3.1 explicitly deals with time-varying ambient conditions, which are unavoidable in real-life wind farms. Which ambient conditions are estimated strongly depend on the measurements available and the current conditions inside the farm (i.e., the wind direction). A theoretical measure of observability provides a guideline for this problem, as presented in Section 4.2.

High-fidelity simulations show the performance of the control algorithm, yielding a 1.1% gain in power capture in a stress-test-like simulation set-up where the wind direction changes often and with strong jumps. Furthermore, a more classical, quasi-dynamic simulation in which the wind direction does not change over time leads to a 8.6% increase in energy extraction by the wind farm, which is in line with what is found typically in the literature. The controller does lead to a significantly higher yaw travel, and a negligible change in the turbine out-of-plane blade root fatigue loads. Overall, while a deeper look has to be taken into the increase in yaw actuation, this article takes a big step towards a realistic, robust, closed-loop wind farm control algorithm that is able to deal with the time-varying nature of wind, and the uncertainties involved in real-life wind farms.

## 4.4 Conclusions

In the remainder of this European project, closed-loop wind farm control solutions leveraging wake redirection control will be tested for wind farms with DTU 10MW turbines in high-fidelity simulation. The concepts of induction control and wake steering will also be tested on a real-life, onshore wind farm in Sedini, Italy. However, according to the results presented in this work and in existing literature, the expectation is that induction control will not lead to significant (if any) improvement in power yield, at least under the current conditions that control algorithms are assessed for. On the other hand, wake steering has a more hopeful forecast in terms of increasing the power production of the wind farm. This will be part of deliverable D3.7.

## 5 COMBINED FEEDBACK-FEEDFORWARD WAKE REDIRECTION CONTROL

### 5.1 Introduction

Currently, wind farms are operating with individual controllers at each wind turbine. In wind farm this might lead to sub-optimal operation conditions. Moreover the power yield of the wind farm might heavily decrease compared to the possible energy production the wind turbines could deliver at a certain wind speed. This is due to flow interactions in the wind farm. They cause suboptimal inflow conditions for some wind turbines in a wind farm and therefore lead to less energy production and furthermore higher structural loads. Altogether, an improvement of the flow situation in the wind farm can result in significant better operation performance. Wake redirection has been investigated to serve as a tool to optimize the flow situation in a wind farm.

In this strategy, the goal is to (partially) redirect the wake around the downstream turbines by using the yaw actuator. This changes the inflow condition for downstream turbines and lead to potentially more power extraction from the wind. First work regarding the effect of yawing a turbine on the flow can be found in [19, 34]. Although yaw effects on the flow are still not completely understood, results such as presented in [31, 54, 37] are providing more insight. They study the effect of wake redirection in high fidelity simulation and assess the ability to redirect the wake. First steady-state engineering wake model that describes wake deflection due to yaw is presented in [39]. Such types of models have appeared to be useful in wake redirection control [17, 33, 47, 30] where the objective is to find the turbine's yaw angles that maximize power production. More details are summarized in the tutorial regarding the utilization of steady-state models in control in [21]. Recently, a steady-state model has been presented in [10] whereas this farm model is based on the steady Navier-Stokes equations. This model has been incorporated in the currently online available FLOW Redirection and Induction in Steady-state (FLORIS), an optimization tool that aims to find optimal yaw settings that maximize the farm's power production <sup>4</sup>.

Applying the optimal yaw settings to the wind farm is called open-loop or feedforward control. Based on offline computations the yaw angles are set based on atmospheric conditions, like e.g. wind speed, turbulence intensity, and wind direction. The methodology improves the total power yield and the the flow situation in the wind farm and has shown promising results in various investigations. The main drawback in the methodology is the uncertainty of the steady-state wake model, and additionally, the lack of feedback of flow information.

In contrast the methodology of lidar-based wake redirection feedback control has been introduced, see [51] and [50]. A remote sensing device, a lidar system, is measuring wind speed information in the wake of the wind turbine. With the help of estimation techniques, see [50], the wake position is assessed. A wake redirection controller uses the information to set the yaw offset such that a desired wake redirection is achieved. The advantages of the approach are the adaptivity to various uncertainties, the dynamic response to changes and the possibility to compensate for disturbances

<sup>4</sup>FLORIS is online available at: [https://github.com/TUdelft-DataDrivenControl/FLORISSE\\_M](https://github.com/TUdelft-DataDrivenControl/FLORISSE_M)

like temporal cross-wind, see [48]. Drawbacks are the dependency on an additional measurement device, its measurement quality, and availability. Further the trade-off between measuring close enough to increase the bandwidth of the controller and measuring far enough to measure a wake deflection is a difficult task. Here, measuring in a distance of 2.5 to 3 times the rotor diameter has shown to result in a feasible trade-off. Furthermore, the determination of the desired wake position is still a challenge.

In the following, a combination of both approaches is presented. The general idea of the approach is to separate tasks between feedforward and feedback control to take advantage of both methodologies. Results from this approach have been submitted to Wind Energy Science Journal [Citation will be added as soon as available.](#), discussed in Deliverable 3.5, and were presented at the WESC Conference 2019 in Cork. The main aspects in this chapter are on the controller design procedures and analysis of the controllers. Furthermore, the challenges of this approach are later discussed and possible solutions are suggested. The chapter is structured as follows: First the publication is reprinted to give an introduction to the topic and to present the results obtained by the concept. Then in the second part, the controller design is described in detail and analyses are given. Finally, remarks and conclusions are stated and possible future work is described.

## 5.2 Methodology and results

The remainder of this section shows the corresponding submission to the Wind Energy Science journal which has the current status of a discussion paper, [Citation will be added as soon as available.](#)

# Feedforward-Feedback wake redirection for wind farm control

Steffen Raach<sup>1,3</sup>, Bart Doekemeijer<sup>2</sup>, Sjoerd Boersma<sup>2</sup>, Jan-Willem van Wingerden<sup>2</sup>, and Po Wen Cheng<sup>1</sup>

<sup>1</sup>Universität Stuttgart, Stuttgart Wind Energy (SWE), Allmandring 5B, 70569 Stuttgart, Germany

<sup>2</sup>TU Delft, Mekelweg 5, 2628 CD Delft, The Netherlands

<sup>3</sup>sowento GmbH, Donizettistr. 1A, 70195 Stuttgart, Germany

**Correspondence:** Steffen Raach (raach@ifb.uni-stuttgart.de)

**Abstract.** This work presents a combined feedforward-feedback wake redirection framework for wind farm control. The FLORIS wake model, a control-oriented steady-state wake model is used to calculate optimal yaw angles for a given wind farm layout and atmospheric condition. The optimal yaw angles, which maximize the total power output, are applied to the wind farm. Further, the lidar-based closed-loop wake redirection concept is used to realize a local feedback on turbine level.

5 The wake center is estimated from lidar measurements 3 D downwind of the wind turbines. The dynamical feedback controllers support the feedforward controller and reject disturbances and adapt to model uncertainties. Altogether, the total framework is presented and applied to a nine turbine wind farm test case. In a high fidelity simulation study the concept shows promising results and an increase in total energy production compared to the baseline case and the feedforward-only case.

## 1 Introduction

10 Currently, wind farms are operating with individual optimal turbine settings thus not taking wake interactions into account. This strategy is referred to as greedy wind farm control. The two main wind farm control strategies in which wake interactions are taken into account are axial induction control and wake redirection control (see Boersma et al. (2017) for an overview). In the former, the idea is to deviate the blade pitch angle and tip speed ratio from greedy settings in order to enhance farm performance. Changing these control signals alters, among others, the wind velocity deficit in the turbine's wake hence the

15 power production of downstream turbines. One of the first papers that proposes the idea of axial induction control can be found in Steinbuch et al. (1988). By now, scientific results seem to indicate that by using a currently available steady-state model to evaluate optimal axial induction settings, no power improvement on a farm level can be achieved Annoni et al. (2018). However, recent scientific results indicate that by temporally changing axial induction settings, the farms power output in the therein used wind farm simulators can be improved by using control Ciri et al. (2017); Munters and Meyers (2018).

20 Interestingly, the results in Ciri et al. (2017) seem to indicate that downstream turbine need to deviate from greedy in order to improve the farm's power production while in Munters and Meyers (2018), the control settings of the upstream turbines are temporally changing resulting in an improvement of the farm's power output indicating the necessity for more research. The second wind farm control strategy is wake redirection control and studied in this paper. In this strategy, the goal is to

(partially) curtail the wake around the downstream turbines by using yaw settings such that inflow condition for downstream turbines change and potentially more power can be extracted from the wind. Pioneers work regarding the effect of yawing a turbine on the flow can be found in Clayton and Filby (1982); Grant et al. (1997). Although yaw effects on the flow are still not completely understood, results such as presented in Fleming et al. (2014); Vollmer et al. (2016); Howland et al. (2016) are providing more insight. To the best of the authors knowledge, Jiménez et al. (2010) presents the first steady-state engineering wake model that describes wake deflection due to yaw. Such types of models have appeared to be useful in wake redirection control Campagnolo et al. (2016); Gebraad et al. (2016); Quick et al. (2017); Fleming et al. (2017b) where the objective is to find the turbine's yaw angles that maximize power production. A tutorial regarding the utilization of steady-state models in control can be found in Doekemeijer et al. (2019). A recent steady-state model has been presented in Bastankhah and Porté-Agel (2016) whereas this farm model is based on the steady Navier-Stokes equations. This model has been incorporated in the currently online available FLOW Redirection and Induction in Steady-state (FLORIS), an optimization tool that aims to find optimal yaw settings that maximize the farm's power production <sup>1</sup>.

The control paradigm when employing previously described steady-state models can be seen as open-loop (feedforward). That is, yaw settings are found using a steady-state model and are then applied to the farm. Assuming that the steady-state model describes accurately enough the farm's behaviour in yawed conditions and no changes in the atmospheric conditions occur, the open-loop control paradigm could potentially work. However, both assumptions are never completely satisfied. For example, a temporal change in wind direction, which can be seen as a disturbance, will result in non-optimal yaw settings. In this paper we therefore introduce additional local feedback controllers that steer the wakes to set point wake positions. The idea of introducing local yaw controllers to steer the wake to a desired position has been introduced before in for example Raach et al. (2017c) and successfully tested in a high-fidelity wind farm model Raach et al. (2018). In this work, both feedforward and feedback are combined in order to steer wakes in the farm to desired positions that enhance the power capture of a wind farm.

The paper is structured as follows: First the objectives of the tasks of the presented work are assessed and defined in section 2 and the total control framework is presented. The controllers are described in section 3: in section 3.1 the feedforward wake redirection methodology is presented and section 3.2 describes the feedback counterpart that supports the feedforward controller. The effectivity of the combination between feedforward and feedback control is assessed in a simulation study with a nine turbine wind farm layout in section 4. Finally, conclusions are given in section 5.

## 2 Objectives and Control Framework

### 2.1 Objectives

The main objectives of this paper are the following:

- Introduction of the feedforward+feedback wake redirection framework

<sup>1</sup>FLORIS is online available at: [https://github.com/TUDELFT-DataDrivenControl/FLORISSE\\_M](https://github.com/TUDELFT-DataDrivenControl/FLORISSE_M)

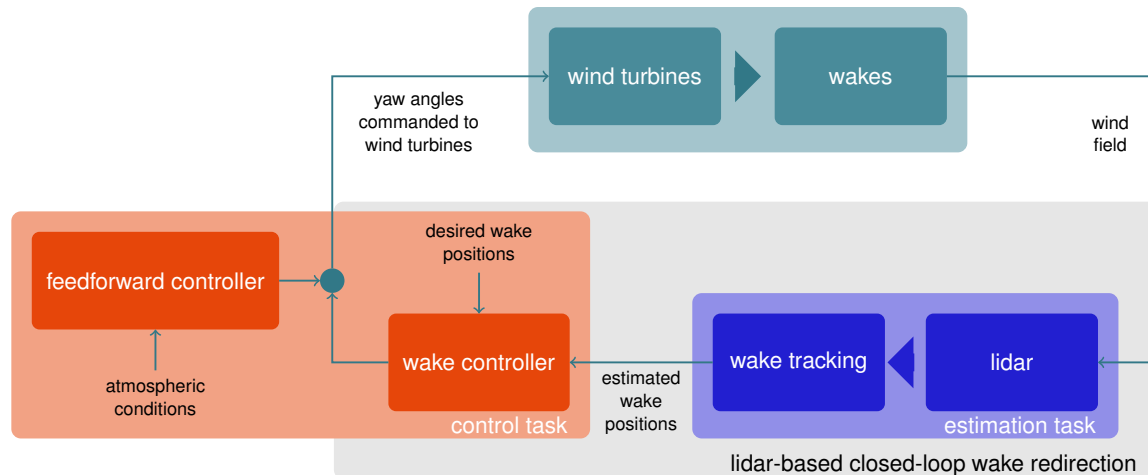


**Figure 1.** The block diagram of the general setup: feedforward-feedback wake redirection control. In the estimation task the lidar system is measuring in the wake of the wind turbine. From the measurement data the wake position is estimated. In the control task the feedforward-feedback controller use the estimated wake position as well as the atmospheric conditions of the setup to provide the yaw angle command to the wind turbine.

- Presentation of the control synthesis of the feedforward+feedback wake redirection
- Demonstration of the concept in an example case in the high-fidelity simulator SOWFA.

## 2.2 Control framework

The framework of feedforward-feedback wake redirection control consists of a feedforward part in which the optimal yaw settings are defined for given atmospheric conditions, e.g. wind speed, wind direction, and turbulence intensity. Further, the feedback controller is continuously active during operation on each wind turbine. Figure 1 depicts a block scheme of the setup. However, in order to use feedback control we need 1) measurements of the farm and 2) a controller design model. The measurements are in this work coming from modeled lidar systems, from which a wake position is estimated. In the employed simulation environment (see section 4.1), perfect lidar systems are modeled that provide estimations of the current wake position. This estimation is used by the feedback controller to reject any disturbance if present. The controller model that is necessary to design the local feedback controllers is estimated from high-fidelity simulation data using system identification techniques.



### 3 Control synthesis

#### 3.1 Control task: Feedforward wake redirection control

##### 3.1.1 Methodology

The feedforward controller contains sets of optimized yaw settings. Each set belongs to a specific atmospheric condition and contains yaw angles for each wind turbine in the farm. Each set is evaluated by solving an optimization problem that finds the optimal yaw angles that maximize the power yield of the farm given specific atmospheric conditions. A steady-state (surrogate) wake model is employed in the optimization to obtain the yaw angles.

##### 3.1.2 Surrogate wind farm model

In this work, the state-of-the-art “FLOw Redirection and Induction in Steady-state (FLORIS)” model is used, which is a modular, surrogate wind farm model used in the literature for wind farm control, wind farm topology optimization, and AEP calculations, among others.

The FLORIS model entails different submodels for single wake deficit, wake summation, and wake deflection due to yaw. In the remainder, the wake deficit and deflection submodels are largely based on the work of Bastankhah and Porté-Agel (2016), and multiple wakes are summed by using the sum-square-of-deficits rule from Katic et al. (1986). Finally, the turbine rotors are characterized using static mappings for the thrust and power coefficient, usually generated using aero-elastic simulations or more simply based on actuator disk theory. The top-view of the flow field for a 9-turbine wind farm as predicted by FLORIS is shown in Fig. 2. More information on the surrogate model and the general concept of wind farm control using steady-state

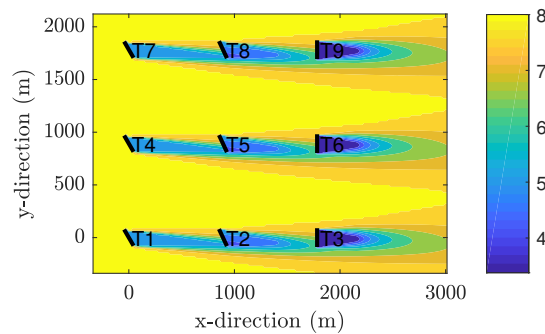


**Figure 2.** The horizontal flow field at the turbine hub height for an example 9-turbine wind farm as predicted by FLORIS

models, including the validation in a high-fidelity simulation environment, can be found in Doekemeijer et al. (2019).

### 3.1.3 Challenges with feedforward wake redirection control

Since the algorithm largely relies on a surrogate model to determine an optimal set of yaw angles, the model's accuracy is very important. Due to the complicated aero- and structural dynamics inside a wind farm, synthesizing such a surrogate model is not straight forward. Assumptions on flow, simplifications in energy extraction, and assuming symmetry in the wake simplify the calculations, however, always introduce uncertainties.

## 3.2 Control task: Feedback wake redirection control

### 3.2.1 Methodology

Closed-loop wake redirection control has been introduced first in Raach et al. (2016) further developed in Raach et al. (2017b). Different control design approaches have been studied in Raach et al. (2017c) and Raach et al. (2017a). So far, the methodology had two main tasks: ensuring the tracking such that the wake is steered to the desired position and adapting to uncertainties and disturbances. In the context of this work, the tasks will be shared, the feedforward controller is responsible to realize the tracking performance and the feedback controller adapts to various uncertainties and does the small adjustments. Therefore, the tuning of the feedback controller differs from previous work because of the different requirements and responsibilities of the controllers.

In this paper, feedback controllers are added to the framework in order to account for undesired wake position deviations. In a perfect setup, wake positions correspond exactly to the optimized yaw settings and hence result in maximum energy yield. These ideal wake positions are referred to as demanded wake positions (see Fig. 1). However, due to for example disturbances, the real wake positions can deviate from the optimal ones and consequently no maximum power production can be ensured. The feedback controller receives wake position deviations (i.e., the difference between demanded and estimated wake position) and evaluates yaw angle deviations accordingly such that the difference between demanded and estimated wake position will be steered to zero. These yaw angle deviations are added to the yaw settings from the feedforward controller, as can be seen in Fig. 1. The design of a feedback controller employs a dynamical model. This model is obtained by running experiments in the simulation model (see section 4.1) and using model identification techniques.

### 3.2.2 Wake position estimation

Since the feedback controller directly relies on a correct estimate of the wake position, the wake position estimation is a crucial part. A downwind facing lidar system is assumed at each wind turbine to measure the wind speed in the wake of the wind turbine. It is assumed that the lidar system can measure the wind speed at a distance of 3 D downstream of the wind turbine. Previous work has shown the feasibility of this assumption, however, challenges remain in realizing it in the field, see Raach et al. (2017b); Fleming et al. (2017a); Annoni et al. (2018).

In this work, a pattern fitting wind field reconstruction methodology is used which assumes a specific shape of the wake. For the wake in a distance of 3 D downwind of a wind turbine it is assumed that the wake can be described as a sum of Gaussian

functions. The basis function

$$\Lambda_j(y_j) = p_{1,j} \exp\left(\frac{-(y_j - p_{2,j})^2}{(2 \cdot p_{3,j})^2}\right) \quad (1)$$

is used with  $y$  the position vector and the three free parameters  $p_{1,j} \dots p_{3,j}$  which describe the wake deficit, the width of the wake and the  $y$  offset of the wake.

5 For the estimation a sum of several basis functions are combined to

$$\Psi = \sum_j \Lambda_j(y_j), \quad (2)$$

which gives more flexibility in estimating the wake. Furthermore, this assumption also enables to detect overlapping wakes. The resulting wake position is obtained by the weighted mean position of all  $N$  considered basis functions

$$y_{\text{res}} = \frac{1}{N} \sum_{j=1}^N \frac{p_{1,j}}{\sum_q p_{1,q}} y_j \quad (3)$$

10 In the estimation step the lidar measurements are used and fitted to the assumed wake pattern as described in detail in Raach et al. (2017b). Because of the layout a maximum of two overlapping wakes may appear. Furthermore the influence of the wake of a wind turbine at a distance of  $10D$  can be neglected. Therefore the choice of two basis functions ( $N = 2$ ) is valid because the wake is measured far downstream and not directly behind the turbine where the shape is not Gaussian. At controller sample time the free parameters are estimated by fitting the measurement data to the wake pattern.

15 To realize the pattern fitting, the lidar measurement principle needs to be included in the fitting. A lidar remotely measures the wind speed at a defined measurement point by evaluating the back-scattered laser light. However, the measurement principle is a volume averaging around the desired measurement point. The assumption of point measurements is made for describing the measure equation for the pattern fitting. Thus, the lidar measurement at point  $[x_i, y_i, z_i]$  can be written as

$$v_{\text{los},i} = \frac{1}{f_i} (x_i u_i + y_i v_i + z_i w_i) \quad (4)$$

20 with the three dimensional flow vector  $[u_i, v_i, w_i]$  at the measurement point and the focal length  $f_i = \sqrt{x_i^2 + y_i^2 + z_i^2}$ . The wind field model for the wake tracking is defined with the wake pattern of Eq. (2) to

$$\begin{bmatrix} u \\ v \\ w \end{bmatrix}_i = \begin{bmatrix} \Psi \\ 0 \\ 0 \end{bmatrix}. \quad (5)$$

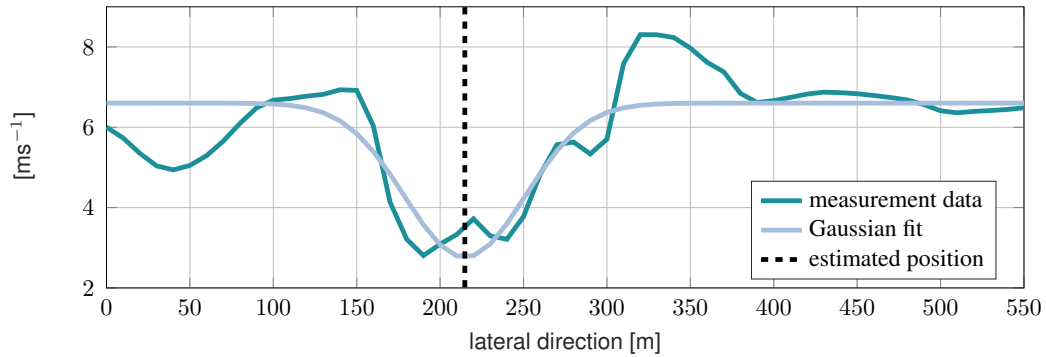


**Figure 3.** An example wake fit to the lidar measurement data using the wake pattern function of Eq. (2) and the wake fitting methods of described in Eq. (6)

Hence, the wake tracking is realized by finding the best parameter representation of the following minimization problem

$$\min \begin{bmatrix} (v_{\text{los},1} - v_{\text{los,measured},1})^2 \\ \vdots \\ (v_{\text{los},m} - v_{\text{los,measured},m})^2 \end{bmatrix} \quad (6)$$

with  $m$  lidar measurements  $v_{\text{los,measured}}$ . Figure 3 visualizes the fitting of measurement data at hub height at a downwind distance of  $3D$  downwind of the wind turbine. This results in a continuously updated wake position estimation signal which is used in the controller to calculate the desired yaw actions.

The wake tracking method is then applied to all turbines in the case study, however, with constant inflow conditions. In order to get a better understanding of the wakes and the wake tracking a snapshots of all wind turbine wakes and the estimations are presented. Furthermore, the yaw angles are plotted which are applied in a feedforward approach. The results of the wake tracking are later used in the model identification procedure to obtain controller design models. Figure 4 presents the flow measurements at several downwind distances and the obtained wake position estimation result. With the previously described precursor the experiment of an open loop step response is repeated. Lidar wake tracking gives an interesting insight in the wake dynamics and the redirection of it at the turbulent case. Figure 5 presents the result of the wake tracking of the turbulent case of the step response simulation. The signal is also plotted being filtered with a phase free filter to visualize the redirection.

### 3.2.3 Feedback controller design

As previously described, the feedback controller in the combined feedforward-feedback setup mainly has the task to adapt to disturbances and model uncertainties. The feedforward controller is responsible for the main proposition of the yaw command and the feedback controller only rejects disturbances and uncertainties. This approach is also known as the 2 DOF controller

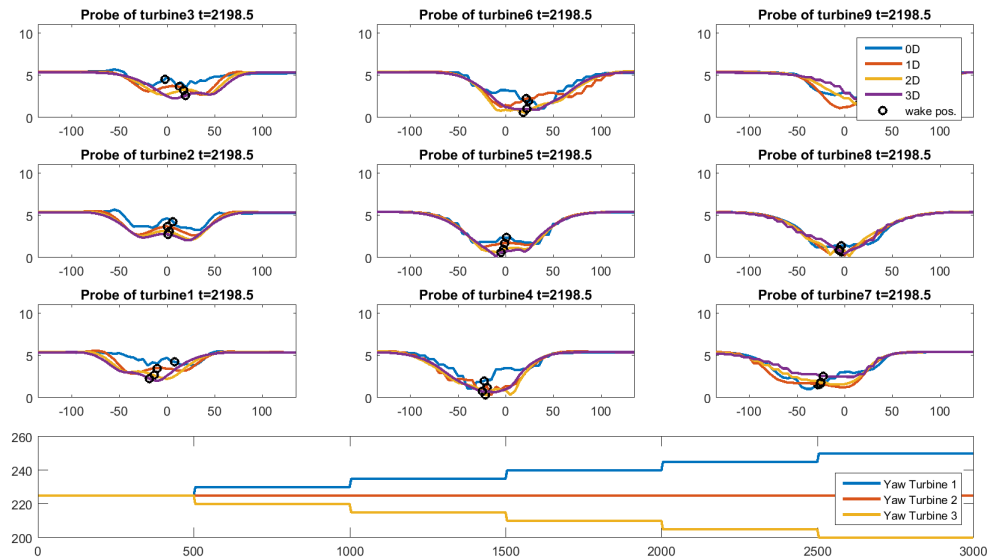


**Figure 4.** Snapshot of an open-loop experiment in SOWFA, where different yaw setpoints are applied to the first row of the  $3 \times 3$  wind farm layout. The wake is measured at different downwind distances and estimated using the presented wake tracking approach at each distance.

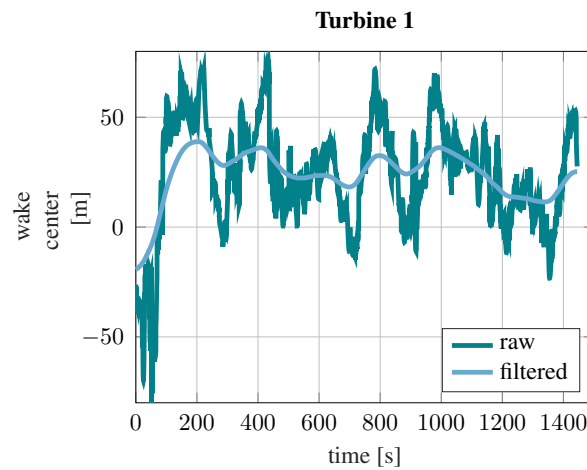


**Figure 5.** Raw time result of the wake tracking of turbine 1 at a position of  $2.5D$  downstream with the turbulent atmospheric conditions of the example case. To evaluate the wake redirection the result is filtered with a phase free filter. This shows the feasibility to estimate the wake position in more realistic turbulent conditions.

design approach. It allows the the feedback controller to be tuned much softer and robust than in the feedback only case where the feedback is also responsible to guarantee a satisfying tracking performance.

Previous work has investigated different controller synthesizes, like an internal model controller, an  $\mathcal{H}_\infty$  controller, and a robust  $\mathcal{H}_\infty$  controller. Those controller have resulted in higher order controllers due to the used synthesis methodologies. In this work, the methodology of structured  $\mathcal{H}_\infty$  controller design is applied, which is implemented in the Robust Control Toolbox of Matlab, see Apkarian and Noll (2006).

Important performance criteria to design and evaluate the feedback controller are the output sensitivity  $\mathcal{S}$ , the complementary sensitivity  $\mathcal{T}$  and the controller sensitivity  $\mathcal{U}$ . They quantify the influence of the disturbances or references to the output or the controller. With a given plant model  $G$  and the controller  $K$ , the performance criteria can be evaluated. More precisely, according to Skogestad and Postlethwaite (2005), the sensitivity  $\mathcal{S}$  gives the closed-loop transfer function from an output disturbance to the system output, the complementary sensitivity  $\mathcal{T}$  is the closed-loop transfer function from the reference to the output and is further the complement of  $\mathcal{S}$ , and  $-\mathcal{U}$  is the transfer function from the disturbance to the control signal. Thus,

$$\mathcal{S} = \frac{1}{1 + GK}, \quad (7)$$

$$\mathcal{T} = \frac{GK}{1 + GK}, \text{ and} \quad (8)$$

$$\mathcal{U} = \frac{K}{1 + GK}. \quad (9)$$

The fixed structure  $\mathcal{H}_\infty$  controller synthesis uses the performance weights and a given control structure  $K$ , e.g. a proportional controller, and solves the mixed sensitivity problem

$$\begin{aligned} \min_K \quad & \kappa \\ \text{s.t.} \quad & \left\| \begin{array}{c} W_S \mathcal{S} \\ W_T \mathcal{T} \\ W_U \mathcal{U} \end{array} \right\|_\infty \leq \kappa, \end{aligned} \quad (10)$$

where

$$\left\| \begin{array}{c} W_S \mathcal{S} \\ W_T \mathcal{T} \\ W_U \mathcal{U} \end{array} \right\|_\infty = \left\| \begin{array}{c} W_S(1 + GK)^{-1} \\ W_T GK(1 + GK)^{-1} \\ W_U K(1 + GK)^{-1} \end{array} \right\|_\infty, \quad (11)$$

with  $\kappa$  the bound on the  $\mathcal{H}_\infty$  norm and the weights  $W_S(s)$ ,  $W_T(s)$ , and  $W_U(s)$ , respectively. for the given control structure  $K$  and its free parameter (e.g. the proportional gain). For the closed-loop wake redirection control, a proportional-integral controller structure (PI controller) is used because the integral part adjusts well to model uncertainties and guarantees a zero offset. As mentioned, in contrast to previous feedback-only controllers, for the combined feedback-feedforward approach the

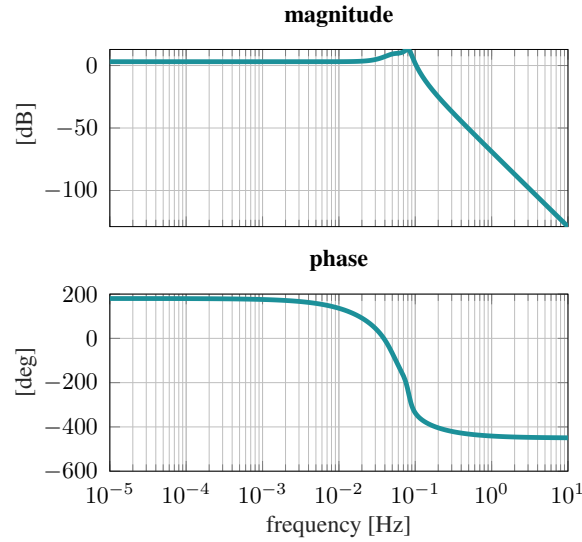


**Figure 6.** The obtained controller design model that was derived from step responses of SOWFA.

feedback controller can be synthesized with a smaller bandwidth. In the following the design process is described. First, a controller design model is derived, then the controller is synthesized using the fixed-structure approach.

The controller design model is derived from open-loop experiments. Different yaw setpoints are set and the flow data is measured with the lidar wake position estimation. Figure 4 shows a snapshot of the wake tracking for the model identification.

- 5 From these results a transfer function is estimated that gives the same step response than the estimated wake position from the simulation data. Figure 6 shows the Bode plot of the obtained controller design model.

As a next step, the fixed structure controller synthesis is formed by the performance weights  $W_S(s)$ , and  $W_U(s)$ , respectively, as follows:

$$W_S(s) = \frac{s/M + \omega_B}{s + \omega_B A} \quad (12)$$

$$10 \quad W_U(s) = \frac{R^2(s^2 + 1/2\sqrt{2}\omega_d s + \omega_d^2)}{10(s^2 + 25\sqrt{2}\omega_d s + (R\omega_d)^2)} \quad (13)$$

with  $w_B = 0.02$ ,  $A = 10^{-7}$ ,  $M = 2$ ,  $\omega_d = 0.005$ , and  $R = 20$ . This setup ensures a good disturbance rejection for low frequencies and no controller action on high frequencies. In the following section, the controller and its resulting sensitivities are analyzed.

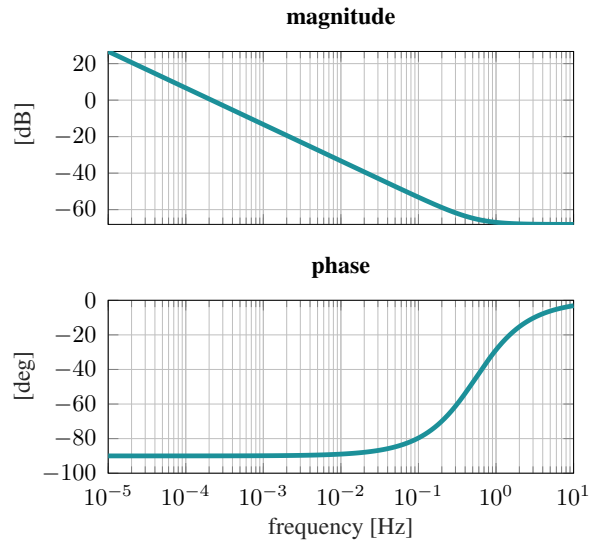


**Figure 7.** The derived fixed structure PI controller is analyzed in the Bode plot.

### 3.2.4 Controller analysis

The derived controller is shown in the Bode plot in Figure 7. The controller has the following parameter,  $K_p = 3.94 \cdot 10^{-4}$ , and  $K_i = 0.0014$ . The performance analysis of the controller is shown in Figure 8, the sensitivity  $S$  and the controller sensitivity  $U$ . The sensitivity shows a good damping for low frequencies which results in an offset free control. No static error remains after any disturbance. The controller sensitivity shows a good roll-off for high frequencies which means that higher frequency movement of the wake is not controlled. Due to the measurement distance downwind of the wind turbine it is needed to adjust the controller in such a way to prevent it from additional control action at higher frequencies, like wake meandering.

## 4 Example case: 3x3 wind farm

### 4.1 Simulation environment

- 10 The high-fidelity wind farm model Simulator fOr Wind Farm Applications (SOWFA), developed by the National Renewable Energy Laboratory, is used to test the proposed control strategy in a wind farm with a regular  $3 \times 3$  layout. Figure 9 gives an overview on the spacing and the wind farm layout as well as the inflow wind direction.

SOWFA is based on large-eddy scale simulation techniques and solves the three-dimensional, unsteady, incompressible Navier-Stokes equations over a finite temporal and spatial mesh, accounting for the Coriolis forces. In SOWFA, the larger scale dynamics are resolved directly while turbulent structures smaller than the spatial discretization are approximated using a subgrid-scale model Churchfield et al. (2012).

15



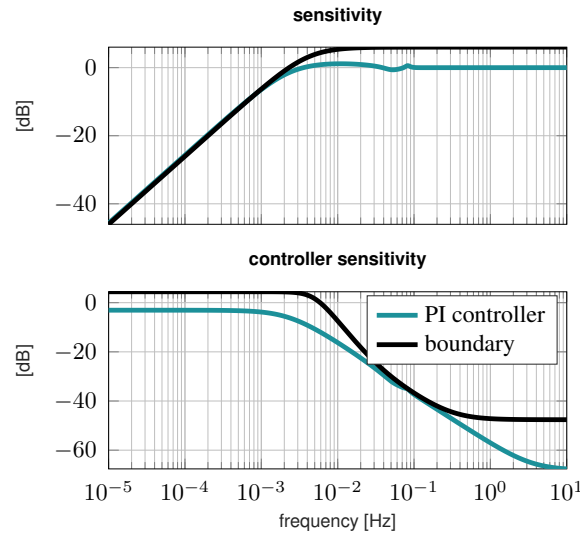


**Figure 8.** Controller analysis: The controller sensitivity and the input sensitivity is analyzed in the two plots. In black, the boundaries of the performance weights are plotted.

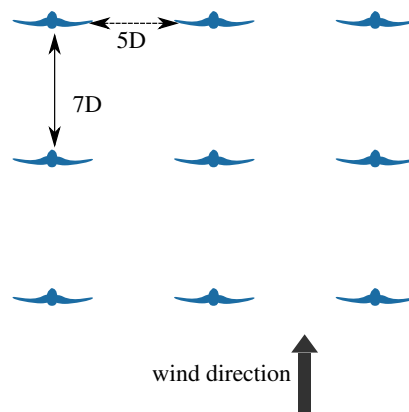


**Figure 9.** The case study wind farm layout, a regular  $3 \times 3$  wind farm layout with a downwind spacing of 7 D and a lateral spacing of 5 D.

The turbine rotor is modeled using an actuator line representation as derived from Sørensen et al. (2002). This model employs a technique in which body forces are distributed along lines representing the blades of the wind turbine. The influence of the rotating blades on the flow field is computed by calculating the local angle of attack and then determining the local forces using tabulated airfoil data. The local forces are then distributed over the blade using a Gaussian filter. Since the ALM is employed, no detailed study regarding fatigue loading can be performed as could be done when employing a turbine model

**Table 1.** SOWFA case study specifications.

Variable	Value	Variable	Value
Domain size	$5 \times 5 \times 1$ km	Turbine spacing	5 D lateral, 7 D downwind
Turbine type	DTU 10 MW	Cell size outer regions	10 m
Ambient wind speed	7.7 m/s	Atmospheric turbulence	6 %
Number of turbines	9		

such as FAST Jonkman and Buhl Jr. (2005). Instead, this work is focused on the control of the flow in a wind farm and thus detailed information on turbines fatigue is not necessary at this stage of the research.

#### 4.2 Demonstration study: atmospheric conditions

In order to cover the turbulent flow for the total domain and the inflow of the SOWFA model a proper precursor needs to be run and used. In this work, a precursor, defined and generated in the CL-Windcon project is used, see CL-Windcon (2019).

The accuracy of the results depend on how realistic the inflow and flow-wind turbine interaction are modeled. Therefore, the inflow and initial flow conditions are generated with the same high-fidelity model. To generate a realistic atmospheric condition, the ground surface is set to a specific roughness length. In our case the roughness is set to  $z_0 = 0.01$  m. The mean wind speed at hub-height is 7.7 m/s with a turbulence intensity  $Ti = 6\%$ . The precursor domain consist of a box of  $l_x \times l_y \times l_z = 5 \times 5 \times 1$  km. All lateral boundaries are set to periodic boundary conditions. This means, the outlet flow is recycled to the inflow. For more details, we refer to the deliverable D1.4 of the CL-Windcon project, which is publicly available, see CL-Windcon Deliverable D1.4 (2018). After a simulation time of 1000 s, a cross-wind of 1 m/s is added at the west boundary to disturb the wake redirection. This modification of the inflow conditions helps to highlight the benefit of the feedback wake redirection controllers.x

The precursor is used as an initial flow field for the 9-turbine case study used throughout this work. Table 1 provides detailed information on the 9-turbine simulation case that is used throughout this work to demonstrate the effectiveness of the proposed control strategy.

##### 4.2.1 Optimal yaw angles for the test scenario

The complete feedforward-feedback solution will be tested on a 9-turbine wind farm in high-fidelity simulation in Section 4.

As the mean atmospheric conditions are constant, the feedforward control signals can be calculated a priori. Specifically, the 9-turbine wind farm is depicted in Fig. 2, in which the freestream wind speed is 8.0 m/s, the freestream turbulence intensity is 6%, and the mean wind direction is along the  $x$ -axis. For simplicity, a brute force approach is leveraged to find the yaw angles

that maximize the power production of the wind farm, leading to

$$\gamma_{\text{FLORIS}} = - \begin{bmatrix} 30^\circ & 25^\circ & 0^\circ \\ 30^\circ & 25^\circ & 0^\circ \\ 30^\circ & 25^\circ & 0^\circ \end{bmatrix}.$$

The yaw angles between the three columns are identical due to symmetry in the wind farm and in the surrogate model. Furthermore, the wake center positions, a quantity directly related to the effectiveness of wake steering, at 3D downstream of

5 each turbine are

$$\Delta y_{\text{wake}} = \begin{bmatrix} -43.2\text{m} & -44.4\text{m} & -11.7\text{m} \\ -43.2\text{m} & -44.4\text{m} & -11.7\text{m} \\ -43.2\text{m} & -44.4\text{m} & -11.7\text{m} \end{bmatrix}.$$

In case of a model mismatch, the predicted wake center locations  $\Delta y_{\text{wake}}$  will deviate from the true locations. In the case that the deflection is too small, then more power may be extracted at the downstream turbine by increasing the yaw angle of the upstream turbine. Similarly, if the wake displacement is larger than necessary, then the upstream turbine may capture more  
 10 power by decreasing the yaw angle at a negligible loss in power of the downstream turbine.

### 4.3 The simulation cases

In the following three different control cases are compared: a baseline case (BL), a feedforward case (FF), and a feedforward+feedback case (FF+FB).

In the baseline case all wind turbines are aligned with the main wind direction and now yaw actuation is assumed. This case  
 15 represents the current operation of a wind farm.

In the feedforward case, optimal yaw angles are computed with FLORIS as described in section 3.1.

In the feedforward+feedback case at each wind turbine the wake position is controlled with the feedback controller and supported by the feedforward controller. A major question in this case is the choice of desired wake position information for each wind turbine. In our case, first, open-loop simulations with the optimized yaw angles using the FLORIS model are  
 20 conducted. The wake positions are analyzed and the steady state was then used as commanded information for the feedback controller. In reality a combination of a pre-study with a steady state model like FLORIS or a high fidelity model like SOWFA may give initial values which will be adapted after in a tuning phase with measurement data.

### 4.4 Results

The simulations are initialized with the evolved precursor flow field and the specified inflow conditions. Figure 10 compares  
 25 the total power output of the wind farm with the three controller cases. Altogether, the improvements of feedforward and feedforward+feedback are visible and a higher power output is reached compared to the baseline case. Due to the adaption

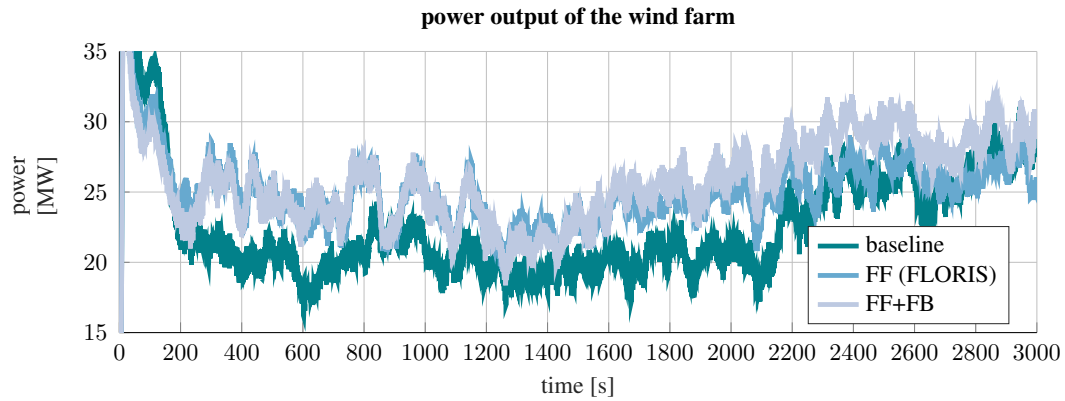


**Figure 10.** Comparison of the total wind farm power output: The baseline case, in which the wind turbines are all aligned with the main wind direction, is compared to the feedforward case, in which the optimized yaw angles of FLORIS are applied, and the feedforward+feedback case, in which additional feedback controllers are controlling the wake position of each wind turbine.

to the changing inflow condition the feedforward+feedback controller over performs the feedforward and baseline cases. The reason for that can be seen in Figure 11 where the yaw angles of turbine 1 and turbine 4 of the different cases are compared. The feedback controllers in case 3 adapt to the changing wind conditions and avoid wind turbine wake interactions. The impact can be seen in Table 2 where the total energy yield with respect to the baseline case is analyzed.

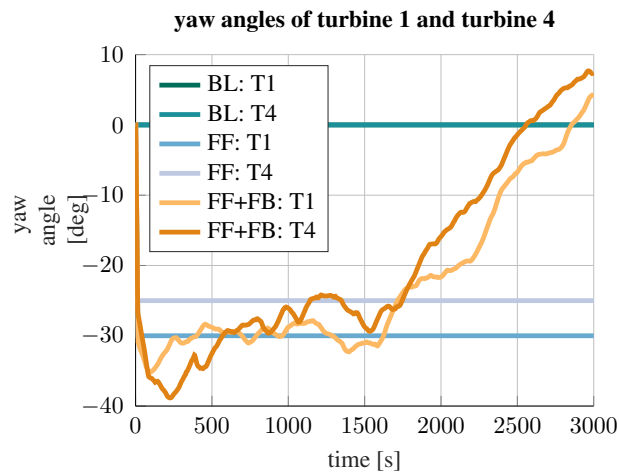


**Figure 11.** Analysis of the yaw angles of wind turbine, which is located in the first row, and wind turbine 4 being in the second row. In the baseline case, the yaw angle is constantly 0 deg, in the feedforward case, a static yaw angle is applied, and in the feedforward+feedback case, the yaw angle is adjusted by the feedback controller.

**Table 2.** A comparison between the total power output of the example case. The table presents the total produced energy of the wind farm with the different control concepts baseline (BL), feedforward (FF), and feedforward+feedback (FF+FB). Furthermore, the power increase with respect to the baseline case is analyzed.

Case	Total Energy [MWh]	Increase [%]
BL	12.4	-
FF	13.8	11.2
FF+FB	14.5	16.9

## 5 Conclusions

This paper has presented a combined feedforward-feedback wake redirection control approach. The framework and control approach has been presented in detail. Afterwards, it was adapted to a demonstration case in which a  $3 \times 3$  wind farm layout is investigated. Three controller cases are compared to each other: a baseline case, a feedforward case, and a feedforward+feedback case. The feedforward yaw angles are computed using the surrogate model based on FLORIS. For the feedback controller a proportional-integral (PI) controller is investigated and designed using a structured  $\mathcal{H}_\infty$  controller synthesis approach.

The control cases are applied to the wind farm using neutral atmospheric conditions and a mean wind speed of 7.7 m/s which is in the partial load region of the wind turbines. Additionally, a cross-wind is imposed to demonstrate the adaptivity of the feedback controller. The combined feedforward+feedback controller adapts to the disturbance. This means the feedback controllers maintain the desired wake and steer the wake to it by adjusting the yaw. Therefore, the enforced wake impingement are mitigated. This results in a higher power output compared to baseline and feedforward only case. Altogether, both controllers, the feedforward and feedforward+feedback, increase the total power yield of the demonstration case compared to the baseline simulation case.

As a next step, changing inflow angles need to be taken into account, as well as changing atmospheric conditions. It further needs to be studied, how these additional changes impact the wake redirection and the feedback controller. Another important question is the choice of wake position set points of the wind turbines in the farm. This point needs further investigation, especially the different calculation methodologies need to be studied.

*Code availability.* The FLORIS model is publicly available at Github<sup>2</sup>.

*Competing interests.* There are no competing interests of the authors.

*Acknowledgements.* The CL-Windcon project is acknowledged which has received funding from the European Union's Horizon 2020 research and innovation programme under grant agreement No 727477.

<sup>2</sup>[https://github.com/TUDELFT-DataDrivenControl/FLORISSE\\_M](https://github.com/TUDELFT-DataDrivenControl/FLORISSE_M)

## References

- Annoni, J., Fleming, P., Scholbrock, A., Roadman, J., Dana, S., Adcock, C., Porte-Agel, F., Raach, S., Haizmann, F., and Schlipf, D.: Analysis of control-oriented wake modeling tools using lidar field results, *Wind Energy Science*, 3, 819–831, <https://doi.org/10.5194/wes-3-819-2018>, <https://www.wind-energ-sci.net/3/819/2018/>, 2018.
- 5 Apkarian, P. and Noll, D.: Nonsmooth  $H_\infty$  Synthesis, *IEEE Transactions on Automatic Control*, 51, 71–86, <https://doi.org/10.1109/TAC.2005.860290>, 2006.
- Bastankhah, M. and Porté-Agel, F.: Experimental and theoretical study of wind turbine wakes in yawed conditions, *Journal of Fluid Mechanics*, 806, 506–541, 2016.
- Boersma, S., Doekemeijer, B. M., Gebraad, P. M. O., Fleming, P. A., Annoni, J., Scholbrock, A. K., Frederik, J. A., and van Wingerden, J.-W.: A tutorial on control-oriented modelling and control of wind farms, in: *Proceedings of the American Control Conference (ACC)*, 2017.
- 10 Campagnolo, F., Petrović, V., Schreiber, J., Nanos, E. M., Croce, A., and Bottasso, C. L.: Wind tunnel testing of a closed-loop wake deflection controller for wind farm power maximization, 753, 032 006, 2016.
- Churchfield, M., Lee, S., and Moriarty, P.: Overview of the Simulator for Offshore Wind Farm Application (SOWFA), 2012.
- 15 Ciri, U., Rotea, M., and Leonardi, S.: Model-free Control of Wind Farms. A comparative study between individual and coordinated extremum seeking, *Renewable Energy*, vol. 113, pp. 1033–45, 2017.
- CL-Windcon, H.: H2020 CL-Windcon project website, [www.clwindcon.eu](http://www.clwindcon.eu), 2019.
- CL-Windcon Deliverable D1.4: Deliverable D1.4 - Classification of control-oriented models for wind farm control applications, Tech. rep., H2020 project CL-Windcon, <http://www.clwindcon.eu/wp-content/uploads/2019/04/CL-Windcon-D1.4-Classification-control-oriented-models.pdf>, 2018.
- 20 Clayton, B. and Filby, P.: Measured effects of oblique flows and change in blade pitch angle on performance and wake development of model wind turbines, *BWEA Wind Energy Conference*, 1982.
- Doekemeijer, B. M., Fleming, P. A., and van Wingerden, J. W.: A tutorial on the synthesis and validation of a closed-loop wind farm controller using a steady-state surrogate model, in: *Proceedings of the American Control Conference (ACC)*, Philadelphia, USA, in review, 2019.
- 25 Fleming, P. A., Gebraad, P. M. O., Lee, S., van Wingerden, J.-W., Johnson, K., Churchfield, M., Michalakes, J., Spalart, P., and Moriarty, P.: Evaluating techniques for redirecting turbine wakes using SOWFA, *Renewable Energy*, 70, 211–218, 2014.
- Fleming, P. A., Annoni, J., Scholbrock, A., Quon, E., Dana, S., Schreck, S., Raach, S., Haizmann, F., and Schlipf, D.: Full-scale field test of wake steering, in: *Journal of Physics: Conference Series*, vol. 854, p. 012013, IOP Publishing, 2017a.
- Fleming, P. A., Annoni, J., Shah, J. J., Wang, L., Ananthan, S., Zhang, Z., Hutchings, K., Wang, P., Chen, W., and Chen, L.: Field test of wake steering at an offshore wind farm, *Wind Energy Science*, 2, 229–239, <https://doi.org/10.5194/wes-2-229-2017>, 2017b.
- 30 Gebraad, P. M. O., Teeuwisse, F. W., van Wingerden, J.-W., Fleming, P. A., Ruben, S. D., Marden, J. R., and Pao, L. Y.: Wind plant power optimization through yaw control using a parametric model for wake effects - a CFD simulation study, *Wind Energy*, 19, 95–114, <https://doi.org/10.1822/we>, 2016.
- Grant, I., Parkin, P., and Wang, X.: Optical vortex tracking studies of a horizontal axis wind turbine in yaw using laser-sheet, flow visualisation, *Experiments in Fluids*, vol. 23, pp. 513–519, 1997.
- 35 Howland, M. F., Bossuyt, J., Martinez-Tossas, L. A., Meyers, J., and Meneveau, C.: Wake structure in actuator disk models of wind turbines in yaw under uniform inflow conditions, *Journal of Renewable Sustainable Energy*, 2016.

- Jiménez, Á., Crespo, A., and Migoya, E.: Application of a LES technique to characterize the wake deflection of a wind turbine in yaw, *Wind Energy*, 13, 559–572, 2010.
- Jonkman, J. and Buhl Jr., M.: FAST User's Guide, Tech. Rep. EL-500-38230, National Renewable Energy Laboratory, Golden (Colorado), USA, 2005.
- 5 Katic, I., Højstrup, J., and Jensen, N. O.: A simple model for cluster efficiency, in: *Proceedings of the European Wind Energy Association Conference and Exhibition*, pp. 407–410, 1986.
- Munters, W. and Meyers, J.: Towards practical dynamic induction control of wind farms: analysis of optimally controlled wind-farm boundary layers and sinusoidal induction control of first-row turbines, *Wind Energy Science*, 2018.
- Quick, J., Annoni, J., King, R., Dykes, K., Fleming, P. A., and Ning, A.: Optimization Under Uncertainty for Wake Steering Strategies, *Journal of Physics: Conference Series*, 19, 95–114, <https://doi.org/10.1822/we>, 2017.
- 10 Raach, S., Schlipf, D., Borisade, F., and Cheng, P. W.: Wake redirecting using feedback control to improve the power output of wind farms, in: *Proceedings of the American Control Conference (ACC)*, Boston, USA, 2016.
- Raach, S., Boersma, S., van Wingerden, J.-W., Schlipf, D., and Cheng, P. W.: Robust lidar-based closed-loop wake redirection for wind farm control, in: *Proceedings of the 20th World Congress of the International Federation of Automatic Control (IFAC)*, Toulouse, France,
- 15 2017a.
- Raach, S., Schlipf, D., and Cheng, P. W.: Lidar-based wake tracking for closed-loop wind farm control, *Wind Energy Science*, 2, 257–267, <https://doi.org/10.5194/wes-2-257-2017>, 2017b.
- Raach, S., van Wingerden, J.-W., Boersma, S., Schlipf, D., and Cheng, P. W.:  $H_\infty$  controller design for closed-loop wake redirection, in: *Proceedings of the American Control Conference (ACC)*, pp. 703–708, Seattle, USA, 2017c.
- 20 Raach, S., Boersma, S., Dockemeijer, B. M., Wingerden, J. W., and Cheng, P. W.: Lidar-based closed-loop wake redirection in high-fidelity simulation, *Journal of Physics: Conference Series*, DOI: 10.1088/1742-6596/1037/3/032016, 2018.
- Skogestad, S. and Postlethwaite, I.: *Multivariable Feedback Control: Analysis and Design*, John Wiley & Sons, 2005.
- Sørensen, P., Hansen, A. D., Andr  , P., and Rosas, C.: Wind Models for Simulation of Power Fluctuations from Wind Farms, *Journal of Wind Engineering and Industrial Aerodynamics*, 90, 1381–1402, 2002.
- 25 Steinbuch, M., de Boer, W. W., Bosgra, O. H., Peters, S. A. W. M., and Ploeg, J.: Optimal control of wind power plants, *Journal of Wind Engineering and Industrial Aerodynamics*, vol 27(1-3), pp. 237-246, 1988.
- Vollmer, L., Steinfeld, G., Heinemann, D., and K  hn, M.: Estimating the wake deflection downstream of a wind turbine in different atmospheric stabilities: An LES study, *Wind Energy Science*, vol. 1, pp. 129-141, 2016.

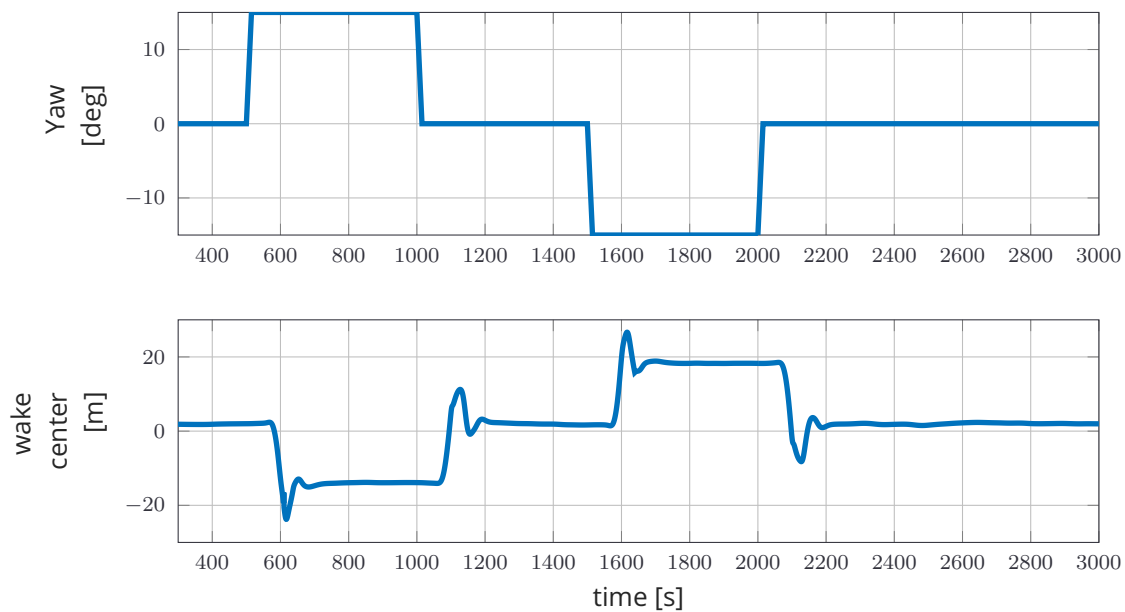


**Figure 14. Model identification steps to obtain a controller design model with SOWFA. The first plot shows the yaw angle, the second plot gives the estimated wake position at a downwind distance of 3 times the rotor diameter (3D).**

### 5.3 Control design

The paper just briefly discusses the controller design procedure of the feedback controller. Here, more details are shown. Especially the challenges of the 2 DOF controller design (combined feedback-feedforward control) are highlighted. The controller design section is structured as following: First, the controller design model is derived. Second, design procedures are stated and compared to each other.

#### 5.3.1 Control design model

For the feedforward part, the FLORIS model is used, which has been used in various feedforward wake redirection investigations, see [32, 3, 13]. It has been tuned to match the DTU 10 MW wind turbine wake and overall flow behavior in SOWFA.

For the feedback controller design a suitable dynamic model that describes the dynamic response of the wake position to a yaw actuation is needed. There has been different approaches how this can be obtained, [51] used model assumptions and an identification technique to obtain single-input single-output models that describe the relationship. In [52, 49] fixed structure model identification techniques are used to obtain the models. Here, the latter is also used. A predefined model structure is used. Step responses are performed in SOWFA to assess the input output behavior of the wind turbine and the resulting wake structure, see Figure 14.

For different setpoints the simulations are performed and the resulting dynamic single-input single-output models are derived. Figure 15 is showing the obtained models in a Bode plot. They mainly



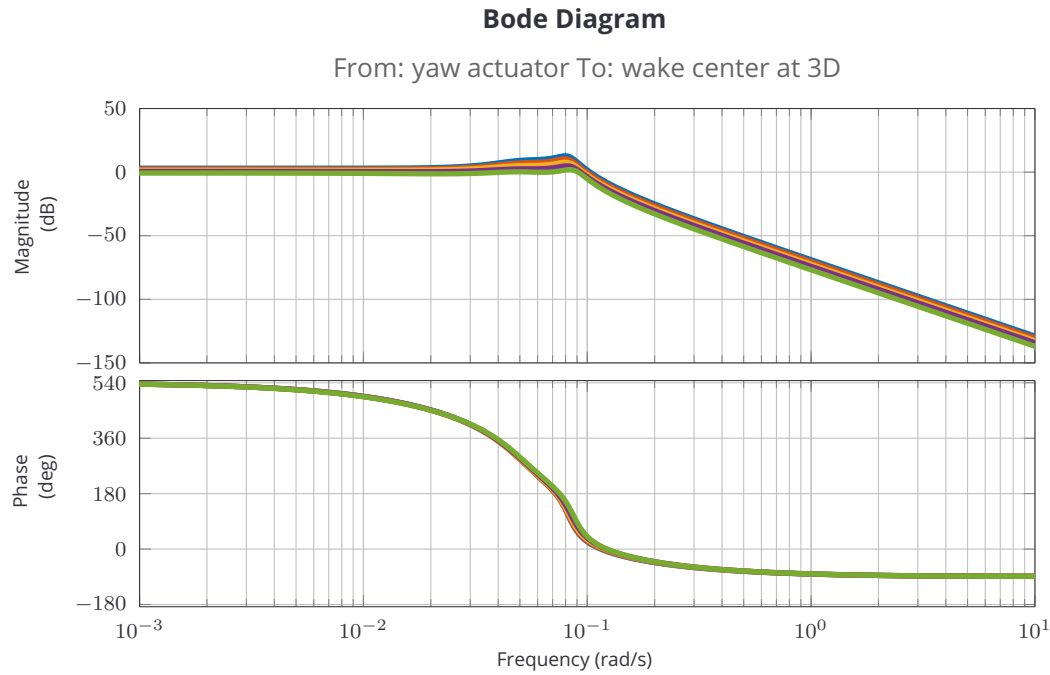


**Figure 15. Bode plot**

differ in dynamics and in static gain which result from the different responses at different yaw set-point. They can be combined into an average model, shown in Figure 16 by using

$$|g(i\omega_j)| = \frac{1}{m} \sum_{l=1}^m |G_l(i\omega_j)|, \quad (5.1)$$

$$\angle g(i\omega_j) = \frac{1}{m} \sum_{l=1}^m \angle G_l(i\omega_j), \quad (5.2)$$

where  $\angle G_l(i\omega_j)$  are the phase of each model and  $\angle g(i\omega_j)$  describes the average phase of  $G(s)$  at frequency  $\omega_j$ . In this analysis  $m = 5$  results from the models of Figure 15 which are considered in the calculation.  $|g(i\omega_j)|$  gives the average amplitude of  $G(s)$  at frequency  $\omega_j$ . Thus, the average model can be written as

$$g(i\omega_j) = |g(i\omega_j)|^{i\angle g(i\omega_j)}. \quad (5.3)$$

### 5.3.2 Control synthesis

The feedforward controller is synthesized by optimizing the yaw angles of the wind farm for specific atmospheric conditions to maximize the total power output of the wind farm. This has yielded a set of yaw angles for the different conditions that are applied in simulation.

For the feedback controller synthesis, there have been exploited several methodologies of deriving controllers for closed-loop wake redirection; an internal model controller in [51], an  $H_\infty$  controller in [52], and a robust controller in [49]. Here, a comparison of  $H_\infty$  and robust controller as well as a

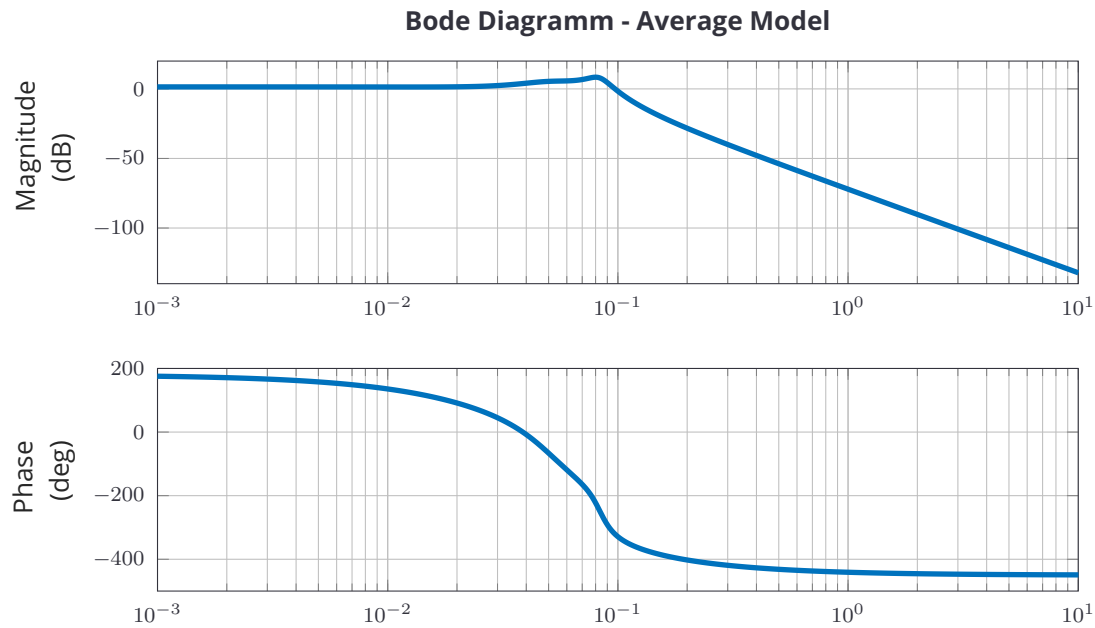


**Figure 16. Averaged model from the model identification.**

different technique, the fixed structure controller synthesis is used. The idea of the fixed structure controller design is to pre-define the controller structure and parametrize the controller with given design bounds. The same design bounds on sensitivity, and controller sensitivity are applied for all three designs and are stated in the paper in Eq. (12) and (13). The resulting controllers are shown in Figure 17. The design bounds are shown in Figure 18 as well as the obtained controller performances are analyzed. The fixed structure PI controller and the robust controller obtain almost the same controller sensitivity whereas the  $H_\infty$  and the fixed structure PI controller reach similar sensitivity results. Altogether, all controller have high damping in the sensitivity to guarantee an offset free control performance (integral behavior) and roll-off at high frequencies in the controller sensitivity.

## 5.4 Controller analysis

The feedforward controller doesn't need a specific performance analysis. However, the combination between feedforward and feedback controller is discussed later in the section.

For the feedback controller, a first analysis of the controllers have been given in Figure 17 and Figure 18. As a next step, the controllers will be compared in time domain with closed-loop step responses. A nominal environment is assumed first, later, an output disturbance is applied. This investigates the controller sensitivity and verifies that the controller is not acting at high frequencies. Figure 19 is presenting the inputs (yaw angle) and the outputs (wake center) of the step responses in the nominal and in the disturbed condition.

A challenge in the design of the combined-feedback-feedforward controller is the selection of the desired wake position for the feedback controller. Due to the model mismatch between high-fidelity simulation, which is considered to represent the reality, and the reduced order wake model FLORIS,

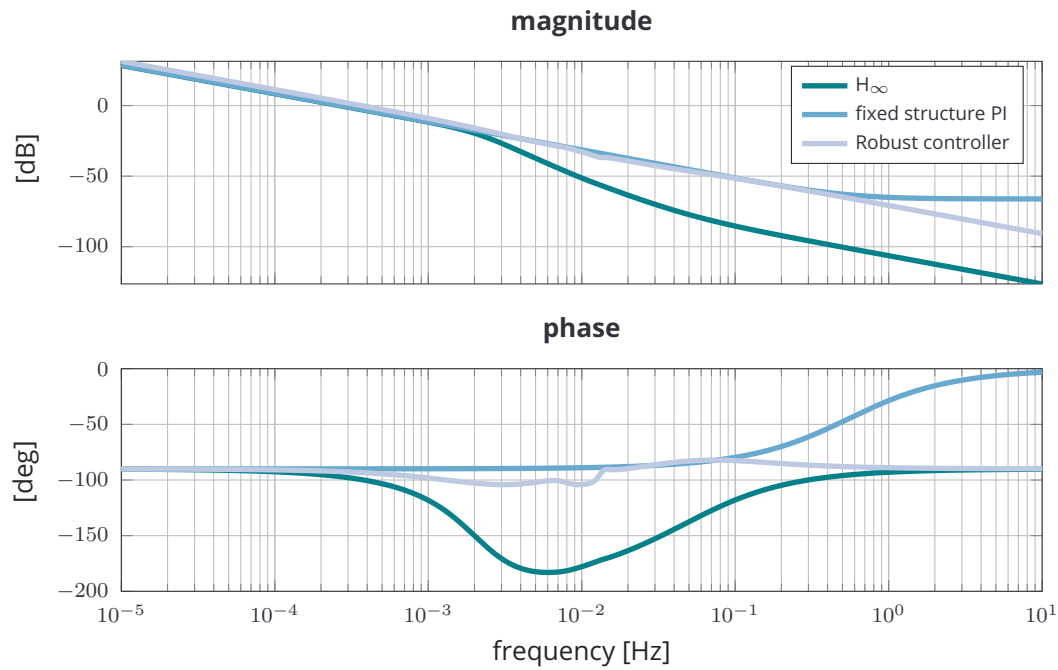


Figure 17. The different controllers synthesized using the obtained controller design models. A  $H_\infty$  controller, a fixed structure PI controller and a robust controller taking all models into account.

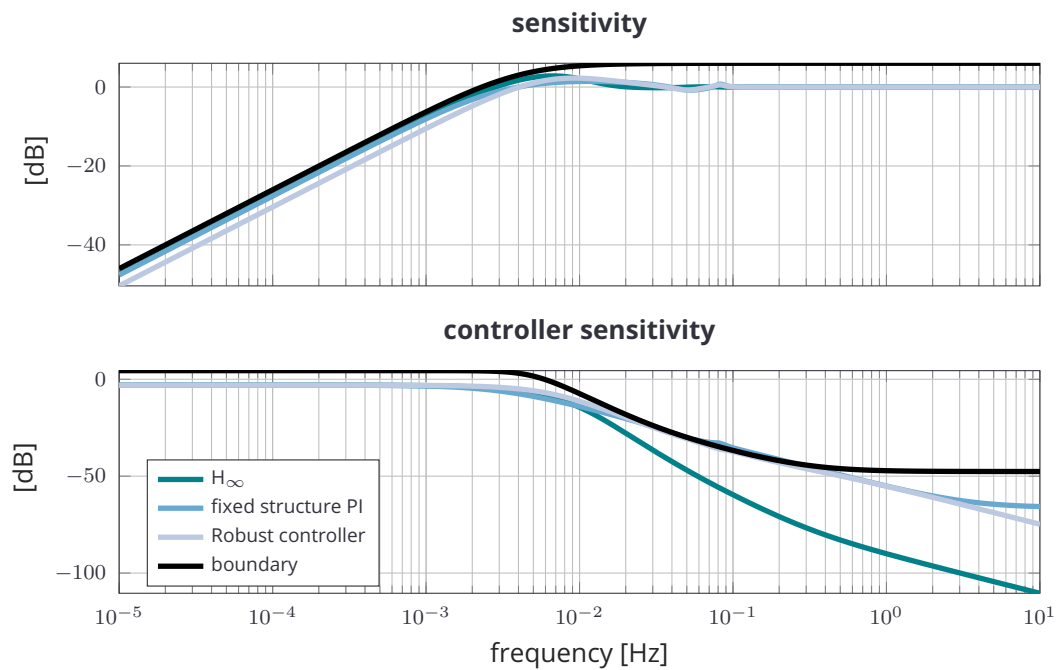
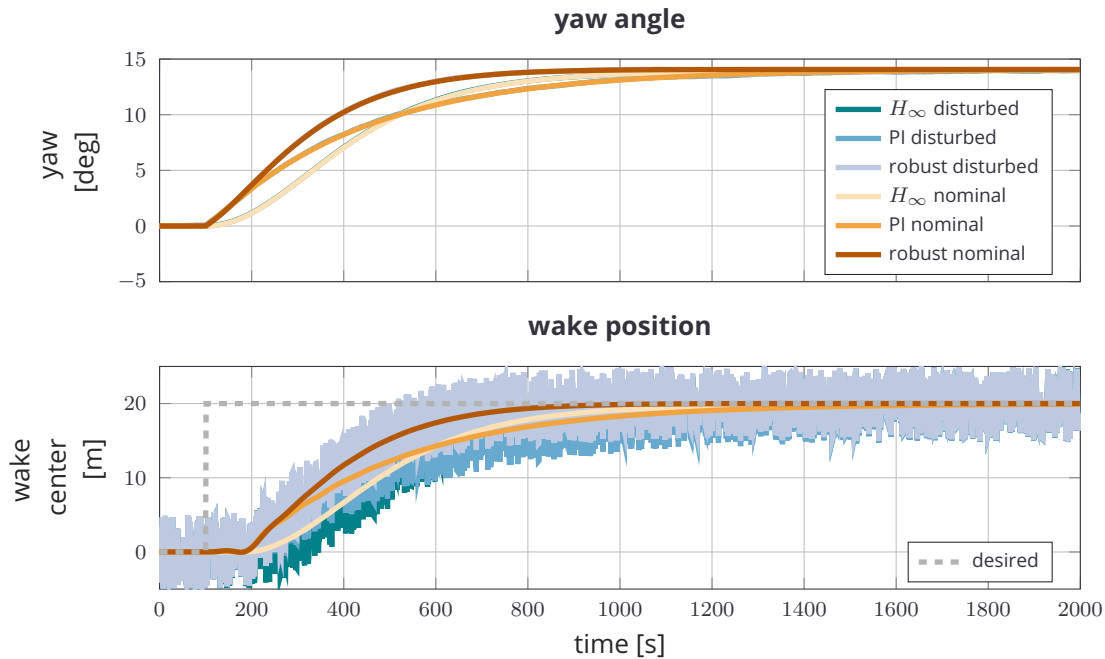


Figure 18. The different controllers synthesized using the obtained controller design models. A  $H_\infty$  controller, a fixed structure PI controller and a robust controller taking all models into account.



**Figure 19. Step responses of the closed-loop controller. In the disturbed case, output disturbances are applied which can be seen in the second plot. All controllers perform well and achieve an error-free final result.**

it is not obvious how setpoints are calculated. The following options are available: 1) take the wake positions predicted by FLORIS, 2) perform steady state simulations with SOWFA and calculate the wake positions from the FLOW field, 3) take FLORIS predicted wake position as initial values and derive an adaption algorithm, that uses the information and adapts the setpoints to the real values. In our case, the second option was chosen since it gives less uncertainty at the beginning and further provided suitable setpoints for the demonstration case in the study.

## 5.5 Conclusions and Discussion

This chapter has described the general concept of combined feedback-feedforward wake redirection control. The concept develops further the idea of using lidar flow measurements in a wind farm to enable a closed-loop wake redirection. The combination with the feedforward action, calculated by the FLORIS model, improves the control performance in such a way that the controller can be designed less aggressive and thus, avoiding too much control action by the feedback. However, the main advantages of the feedback controller remain, which are the adaptivity to model uncertainties and the possibility to react on disturbances.

Details on the overall implementation and the controller design in special are given and different strategies have been discussed. Overall the fixed structure PI controller has been chosen for the combined setup because of its simplicity and the control performance which is comparable to the other controllers.

The setup has been tested in the SOWFA environment and has shown its ability to react on a cross wind disturbance. This is a first verification that the combined setup is feasible and might improve the single concepts. A deeper investigation for multiple conditions is needed to study its overall benefit. Furthermore, as mentioned in the controller analysis section, the setpoint generation procedure might be improved with different techniques. however, it remains a challenge in this methodology.

Combined feedback-feedforward wake redirection control might be the next level in wake redirection control because of using additional information through the lidar sensor(s) the overall performance can be improved. The concept offers new possibilities in controlling the flow in a wind farm because local disturbances still might lead to suboptimal flow conditions. The feedforward controller will steer the main portion and the local control only acts in a defined range around the feedforward value. Overall this can be step towards smarter wind farms and an optimized wind farm operation.

## 6 DYNAMIC INTEGRATION OF FEED-FORWARD INDUCTION CONTROL

This chapter describes the work carried out by CENER related to the integration of wind farm controllers. The progress is based on previous contributions, basically related to wind farm optimization by means of depowering configurations (induction control), taking into account the power of the wind farm (calculated with FLORIS) and the flapwise Damage Equivalent Load (DEL) at the blade root, which is estimated with CENER's methodology developed in [55]. For this dynamic integration, adaption to varying ambient wind conditions is also provided. That is, the optimized wind farm configuration selected by the supercontroller changes in accordance to the free-stream wind conditions, in particular ambient mean wind speed and TI in the present work.

Some additional developments have been necessary at different levels to reach the objective of the dynamic integration of the wind farm controller, in this case, into a medium-fidelity farm simulation code (FAST.Farm):

- Estimation of environmental conditions of the wind farm, based on measurable data from wind turbines
- Calculation of optimum depowering settings depending on the environmental conditions, using FLORIS and taking into account power and loads
- Gain of knowledge on FAST.Farm supercontroller

The final result of this work is the integration of the optimized wind farm solutions based on FLORIS and the estimation of DEL (flapwise bending moment at the blade root) in the FAST.Farm simulations making use of the supercontroller. The current example is focused on the flapwise bending moment at the blade root, but the methodology would be similar for other components and loads using consistent modeling.

The estimator of free-stream ambient conditions requires information from the dynamic results of FAST.Farm in order to get the environmental conditions of the wind farm. Taking into account the inflow, the appropriate derating settings are selected from the database precalculated by the optimizer. The supercontroller implemented in FAST.Farm demands the derating settings to the wind turbines in the next period.

### 6.1 Estimation of environmental conditions

#### 6.1.1 Introduction

The need to develop an estimator of ambient conditions is imposed by the definition of optimization cases, which are based on FLORIS simulations. Apart from the wind farm lay-out and the  $C_p$  and  $C_t$  curves, the wake modelling code needs information of the environmental conditions of the wind farm: wind speed, turbulence intensity (TI) and wind direction.

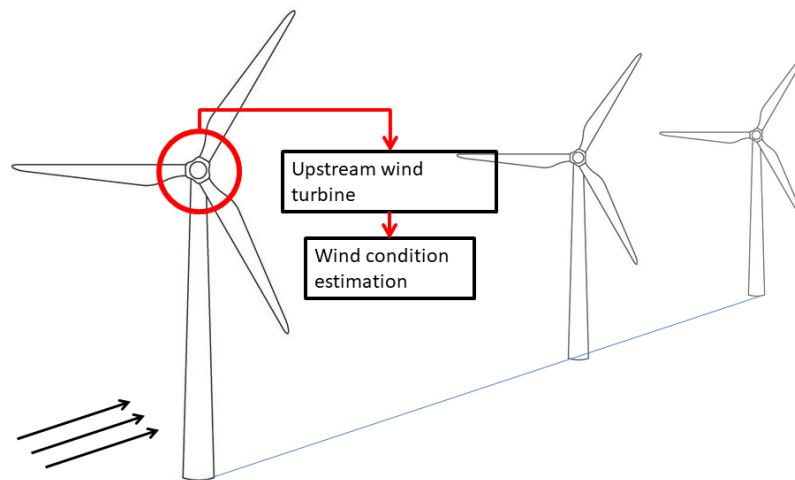


**Figure 20. Methodology of ambient wind conditions estimation**

A tool has been developed in Python to generate the information that is required from measurable data of the wind turbines. This first approach only needs information from the upstream wind turbine (Figure 20), because the rest of the wind turbines are affected by the wake and the estimation of the free-wake conditions from their data would probably provide less accurate results with more complex calculations. In fact, changes in behaviour of the upstream wind turbine related to environmental conditions are observed with a delay in the rest of downstream turbines. Therefore, the fact of using the data of the first turbine where the changes in the wind are observed, allows to act in advance.

The data from the wind turbine used for the estimation of the environmental conditions includes: power, rotor speed, blade pitch angle and torque. Average values and standard deviations are required, which are typically included in SCADA data. In order to carry out the wind farm control, 5-min to 10-min data is enough. Usually in SCADA systems the data is stored in 10-min files. However, in this example 5-min data will be taken in order to reduce the computational time and verify the methodology in a shorter simulation (4000 s) with several actuations of the supercontroller and variations in the wind. The mean values in the selected time frame are necessary for the estimation of the wind speed (Figure 22), while the standard deviations are used for the estimation of the TI (Figure 25).

In addition, a database of average values (power, rotor speed, blade pitch angle and torque) from precalculated simulations will be an input for the estimation tool, including results from different combinations of wind speed, TI, yaw angles and depowering settings. To get this database, numerous simulations were run, covering a range of wind speeds from 4 m/s to 24 m/s, TI from 5% to 20%, yaw angle from  $-30^\circ$  to  $30^\circ$  and depowering configuration from 50% to 100%. All simulations were calculated by CENER for deliverable D2.3 [55]. Now the whole database contains all useful turbine

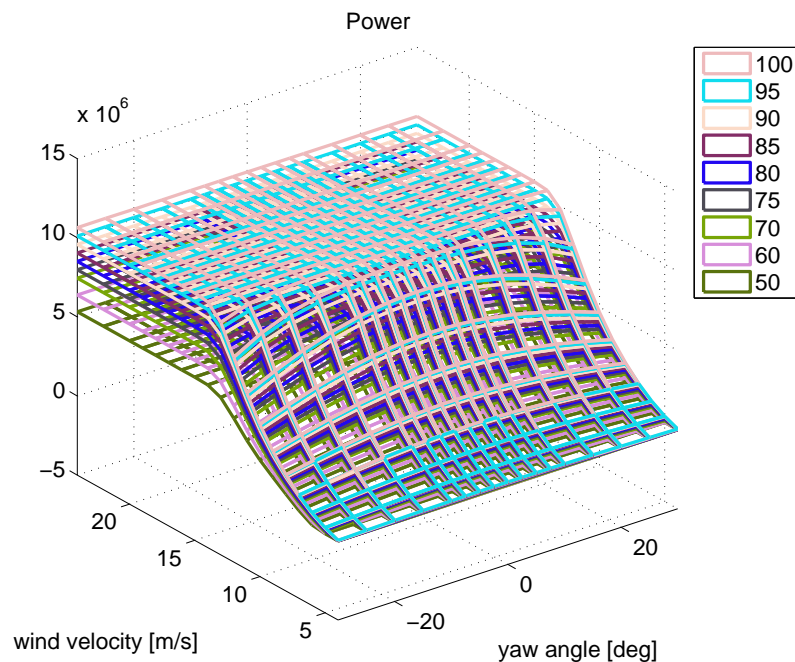


**Figure 21. Power ( $W$ ) distributions for all combinations of wind velocities and yaw angles (for different derating settings,  $TI = 8\%$ )**

values (power, rotor speed, blade pitch angle and torque) for every wind speed/ $TI$ /yaw angle/depowering configuration. A graphic representation of the database for mean power results can be seen in Figure 21, without combination of  $TI$ , presenting only values for  $TI = 8\%$ .

Once the entire database is available, the values for the unknown variables, ambient wind speed and  $TI$ , must be found based on yaw angle and depowering data. To do so, the database must be filtered, that is, all the rows are deleted, except for the ones with the yaw angle and depowering data measured in the current state in the upstream wind turbine. Thus, the resulting reduced database for the estimation contains results of mean values and standard deviations for different combinations of wind speed and  $TI$ . Then, the turbine data is used in order to find the appropriate value for wind speed and  $TI$ . In the following subsections it is explained how this procedure is carried out for each variable of interest.

### 6.1.2 Ambient wind speed estimation

The first step is to find the wind speed (one for every  $TI$  level) for which the simulation mean values are similar to those measured in the SCADA/simulator (Figures 22 and 23). The estimation for each level of  $TI$  (marked with a X in Figure 24) is averaged because in general the results are very approximate, as can be observed in Figures 23 and 24. There are however some regions where there may be abrupt changes and the level of  $TI$  may have a significant influence. In the figures, the value of wind speed averaged among  $TI$ s is presented with a purple dot in the estimation coming from each turbine variable.



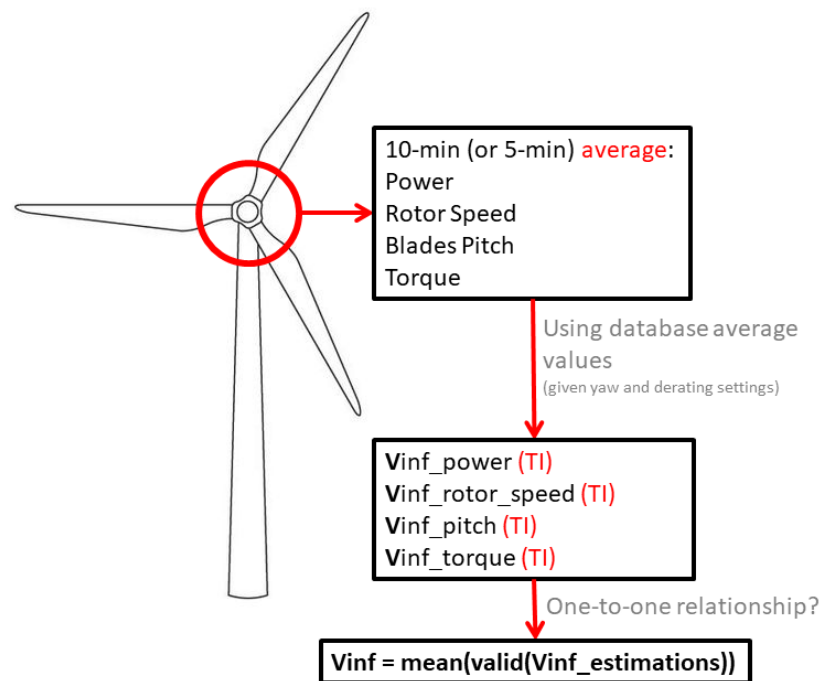


**Figure 22. Methodology of ambient wind speed estimation**

An estimation of the wind speed is obtained from each available variable (power, rotor speed, pitch angle and torque). After the extraction of the estimations for every variable, a quality verification is included in order to only select the valid approaches for the selection of the final wind speed. There are regions where the average values of one variable are not dependent only on the wind speed, so these estimations must be discarded. In the case of wind speed, Figure 23c (pitch angle) estimation is not correct, because for this region there is no one-to-one relationship with the wind speed.

The resulting estimated ambient wind speed is calculated as the average among the valid estimates.

### 6.1.3 TI estimation

At this point, the mean ambient wind speed is known. Hence now the ambient TI must be found. In general, the wind speed estimation value will have some decimals. Nevertheless, in the database there are only integer values for the wind speed. Therefore, the database is filtered again leaving only the next (upper velocity) and previous (lower velocity) integers to the estimated value. For example, if the estimated wind speed is 9.3 m/s, a wind speed of 10 m/s is taken as upper velocity and a wind speed of 9 m/s as lower velocity.

The exercise for the ambient TI is similar to the one carried out in subsection 6.1.2. The first step is to find the TI (one for the upper velocity and one for the lower velocity) for which the simulation standard deviation values are similar to those measured in the SCADA/simulator (Figures 25 and 26). The estimation for both upper and lower wind speeds is interpolated by linear approximation in order to obtain the correspondent value for the estimated wind speed.

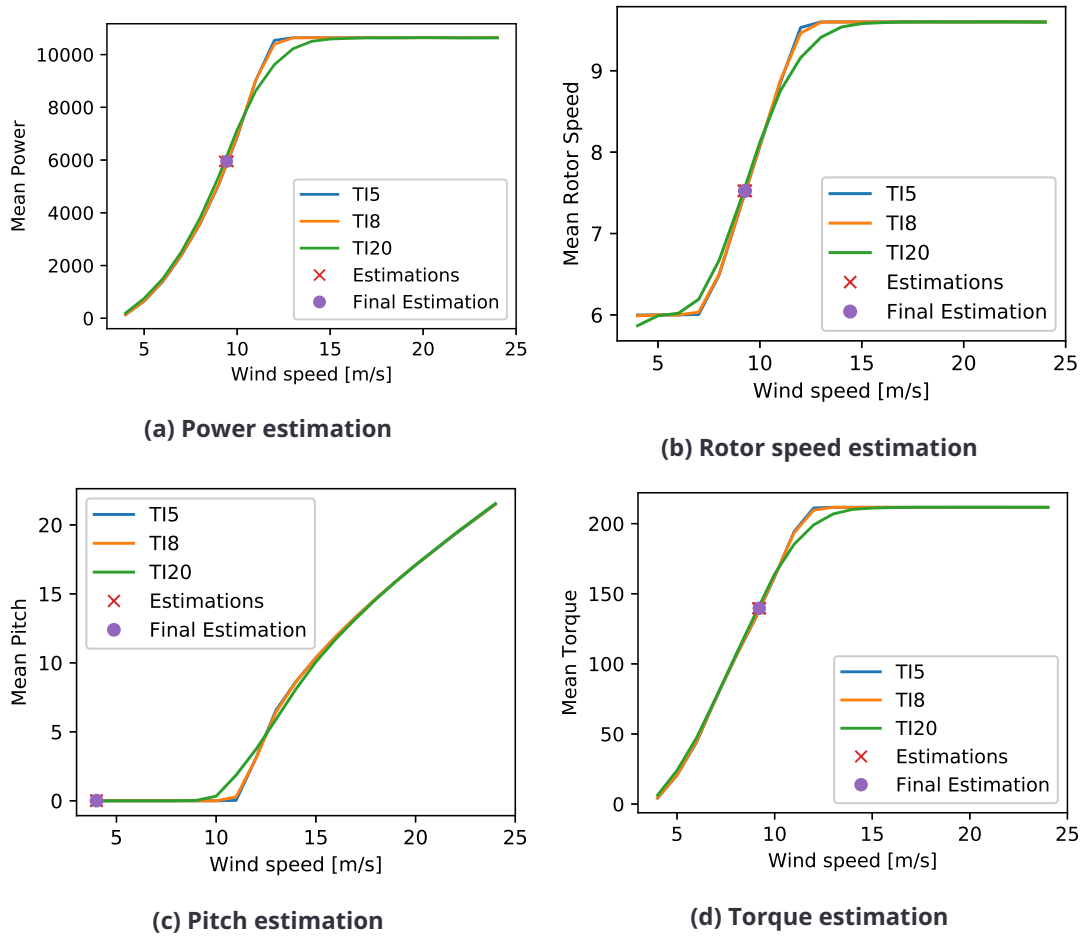


Figure 23. Estimation of mean ambient wind speed

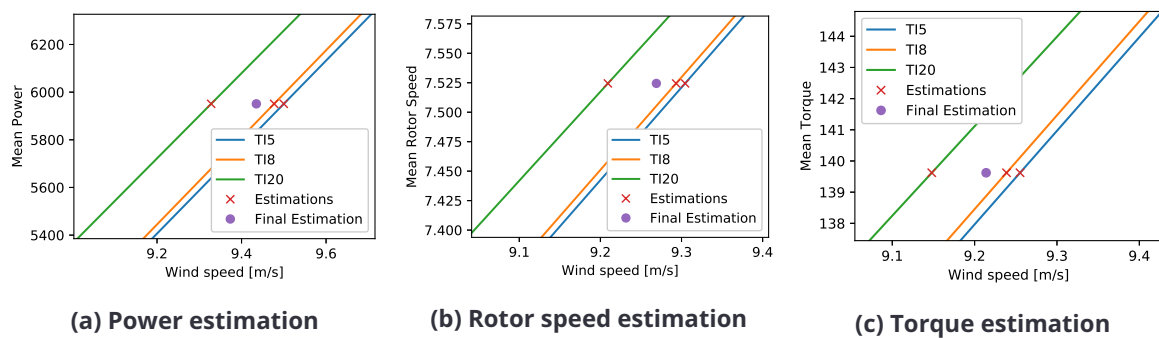
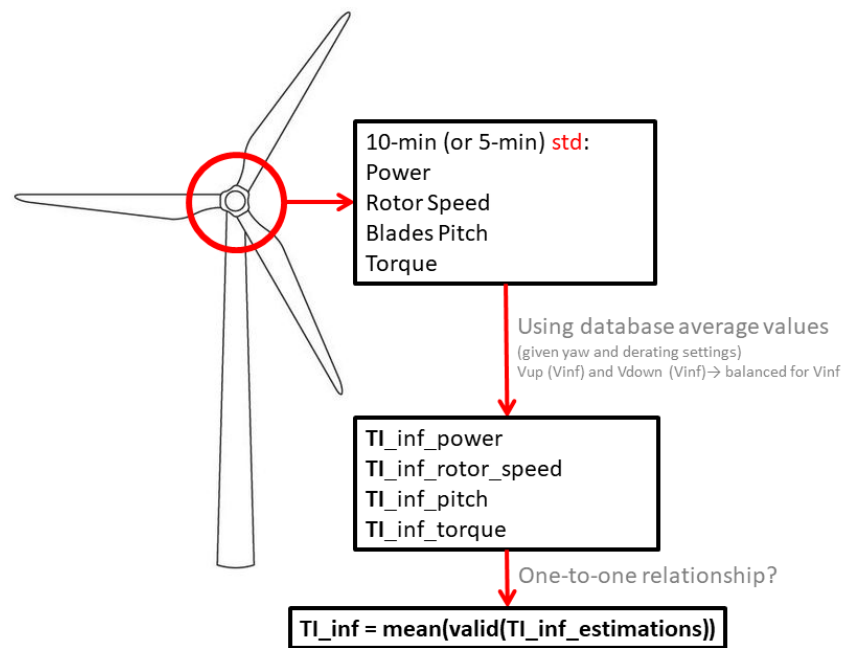


Figure 24. Estimation of mean ambient wind speed (zoom in on variables with valid estimates)



**Figure 25. Methodology of ambient TI estimation**

An estimation of the TI is obtained for every available variable (power, rotor speed, pitch angle and torque). A quality verification is included in order to select only the valid approaches for the selection of the final TI. There are regions where the standard deviations of one variable are dependent not only on the TI at the estimated wind speed, so these estimations must be discarded. In this case, Figure 26c (pitch angle) estimation is not correct, because there is no one-to-one relationship with the TI at the estimated wind speed.

The resulting estimated ambient TI is calculated as the average among the valid estimates.

## 6.2 Calculation of optimum derating configurations

The selection of the optimum configurations for different ambient conditions is calculated off-line, using the optimizer code developed by CENER. This optimizer is based on genetic algorithms and the objective function is a compromise solution between loads and power [55]. It includes estimations of the blade root flapwise bending moment DEL. The wake model is the Porté-Agel [10] implementation in FLORIS, including small improvements developed by CENER, detailed in deliverable D2.3 [55], in terms of power estimation using the new proposed grid, inputs of  $C_p$  and  $C_{t_r}$ , and the estimation of Damage Equivalent Loads.

A database is generated in order to get useful precalculations for the implementation in FAST.Farm. Some optimizations are run for different wind speeds and TIs, while the wind direction is established constant and equal to zero. A more extensive database including the variation of the wind direction could be obtained, however the computational cost increases considerably and for the current study it has been discarded.

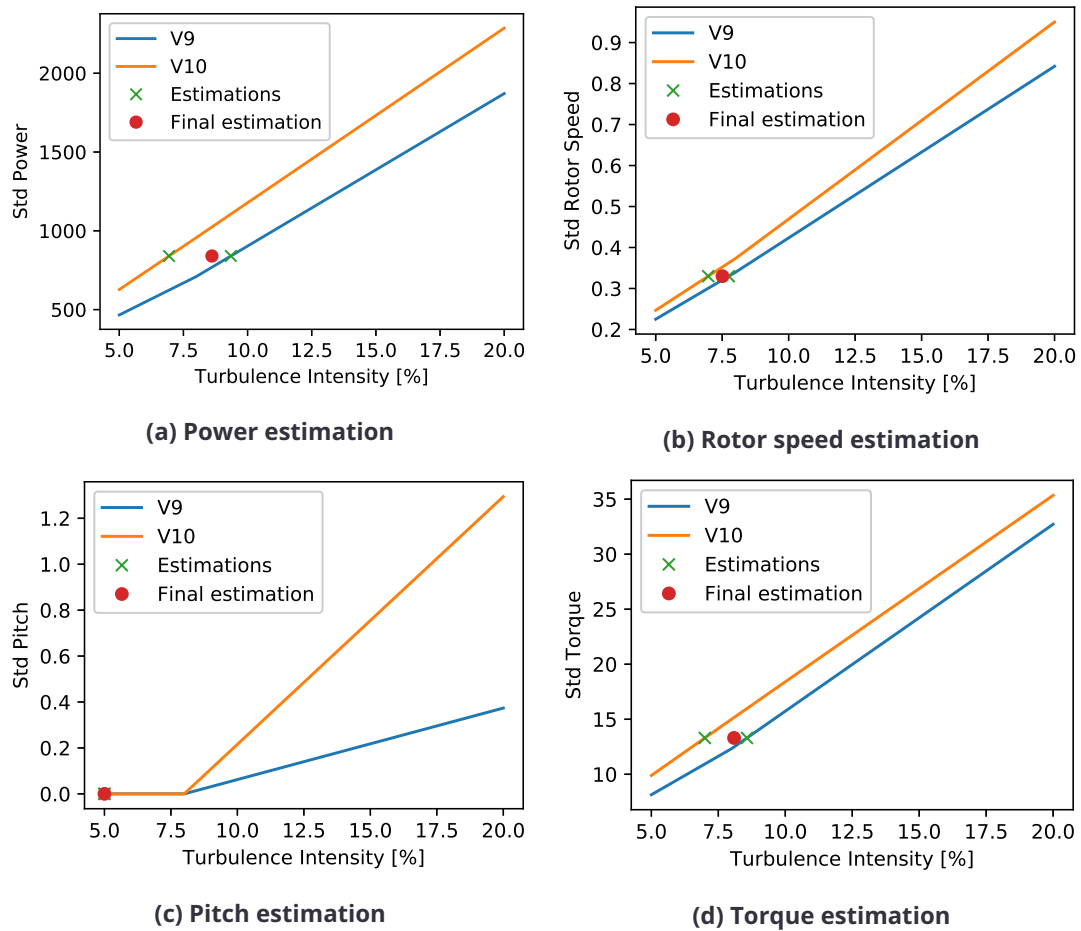


Figure 26. Estimation of ambient TI

### 6.3 Supercontroller interface

Current practice in wind turbines operation is that each turbine has its own controller optimizing its performance in terms of energy capture and loading, based only on the available information of its own measurements. However, turbines interact through their wakes in the flow field they are sharing. For this reason it is important to consider how the whole plant should be controlled when wind farm control algorithms are developed.

In section 6.2, different optimum derating configurations have been chosen for each wind turbine. In order to communicate this operational modes from the wind farm controller to all individual wind turbines controllers within the wind farm, it is necessary to create an interface between both types of commanding elements. In the present work, individual wind turbine controllers are coded in OpenDiscon format [26], which is compatible with OpenFAST turbine simulation model. Different strategies were developed in deliverable D2.1 [26] for axial induction control and wake redirection control. The 'minimal thrust coefficient' is chosen here to depower individual wind turbines (more detail in [8]). In this case, input needed in each wind turbine is the ratio of desired vs available power. This command (one value) is sent from the selector of wind farm optimum derating configurations within the supercontroller to each wind turbine by a supercontroller interface.

Then, each OpenDiscon changes its blade pitch command and generator torque command. Due to the fast response of the electrical system, electrical generator torque gets its set point in milliseconds, while blade pitch angle has a slower dynamics. This fast actuation on torque produces undesirable peaks in loads are seen in Figure 36. In damage equivalent loads calculations and for estimation of ambient wind conditions, these 10-s transients are ignored (subsection 6.5.3). Some proposal to avoid this problem is given in subsection 6.5.5.

### 6.4 Integration

The final objective of the individual developments is their integration into the wind farm supercontroller, specifically the integration of optimized solutions, based on the FLORIS wake model, into dynamic simulations with the FAST.Farm medium-fidelity code (Figure 27).

Broadly speaking, the system can be seen as the block diagram of Figure 28. First, the SCADA data of the first free-stream turbine of each column or row, depending on the wind direction, is taken. This information is introduced into the environmental conditions estimator (script in Python), which estimates the ambient wind speed and the TI that reach the first turbine. These two parameters determine the optimal derating configuration for every wind turbine for the next period of time. Finally, the supercontroller interface (developed in FAST.Farm) applies each depowering to the corresponding wind turbine.

It is worth mentioning here that the wind farm controller would still be a feed-forward open-loop farm controller. The configuration shown in Figure 28 acts dynamically, by adapting to the varying ambient conditions, but it does not strictly close the loop feeding back the effect of the control on the

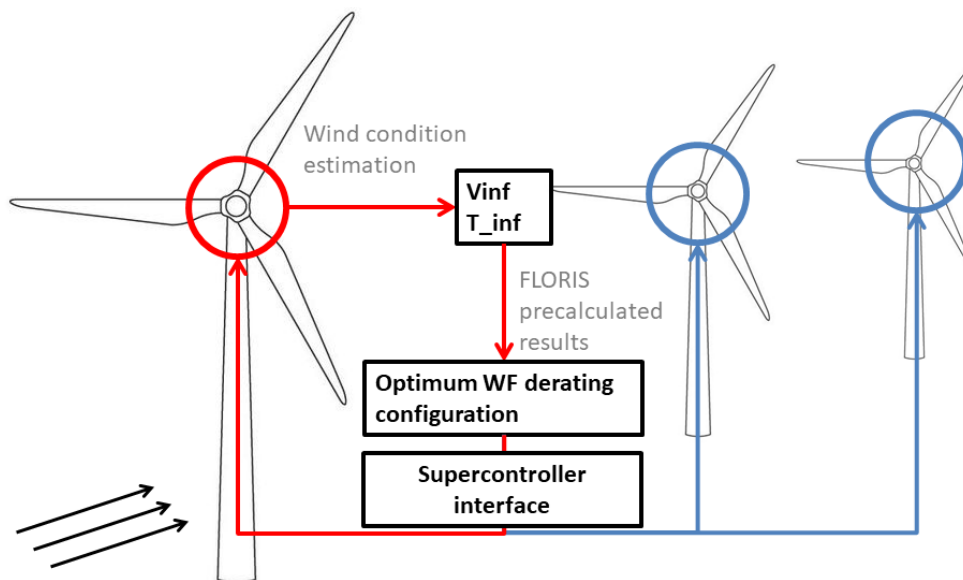


**Figure 27. Methodology for the integration of supercontroller**

controlled variables (power and DEL). This means that the dependence on the farm model accuracy is higher than in a full closed-loop configuration.

An intermediate development has also been included in Section 6.1: the wind condition estimation, developed by CENER. It is necessary, together with the database of precalculated configurations, for the selection of the appropriate configuration when the supercontroller acts.

In the current version of the integration, the solutions are calculated off-line and the selection of the configurations is done by looking for the nearest case in the database of precalculated solutions. However, for future versions of the control integration, the search for the appropriate configuration should be done by launching online the optimization, to ensure that the configuration is optimal for the concrete conditions that are measured. This real-time running optimizer introduces other kind of challenges that are not discussed in this deliverable.

## 6.5 Example

An example of this methodology for the integration of the solutions has been carried out, in order to show it more clearly.

The selected lay-out for this example is the 3x3 lay-out of CL-Windcon, as is shown in Figure 29 [38]. The direction of the wind is fixed to 180° (FLORIS reference system), corresponding to the wind coming from the upper part of the farm, as is shown in Figure 29. The effect of the wakes is relevant for this orientation in terms of loads and power reduction, being the wake recovery is less evident than in the 90° orientation. This case has been reduced to the 3 aligned wind turbines because there is no effect between wind turbines in different columns.

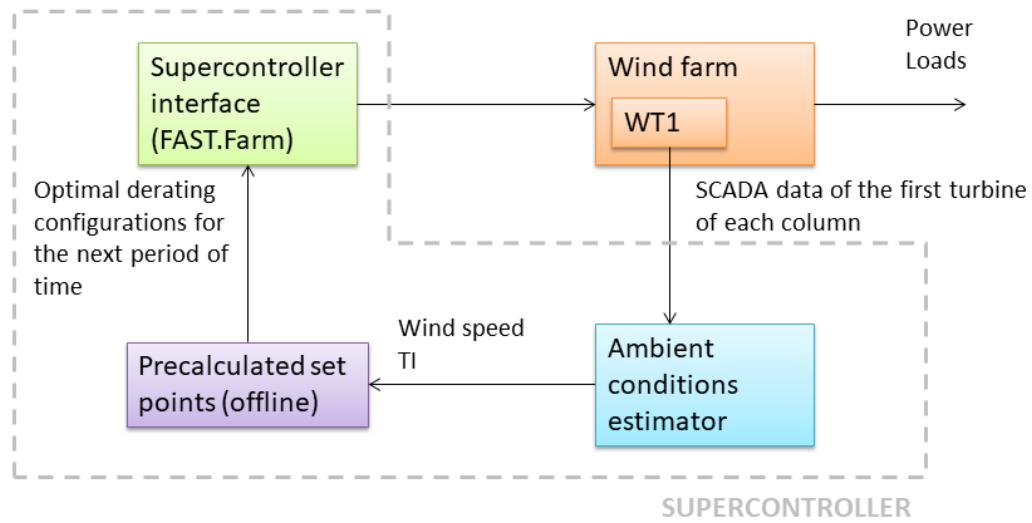


Figure 28. Farm controller block diagram

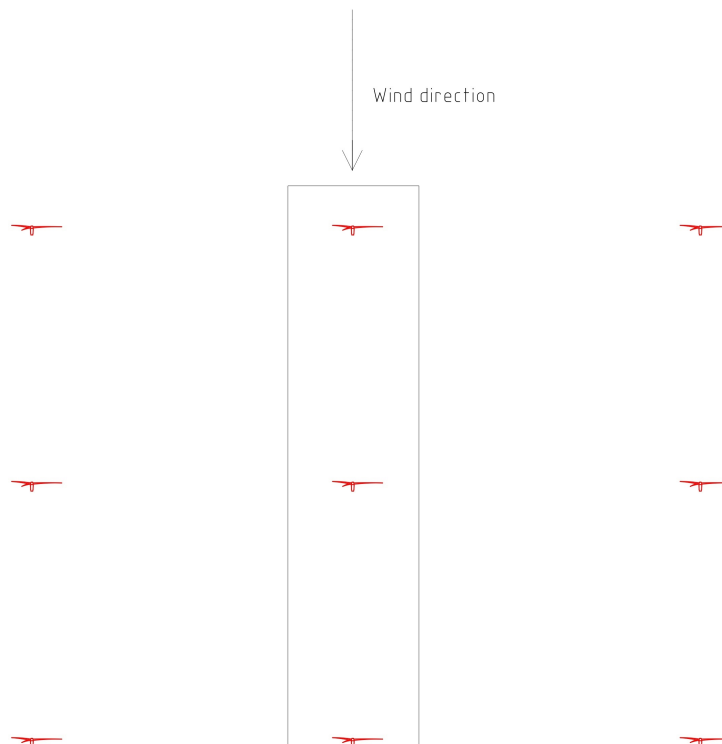
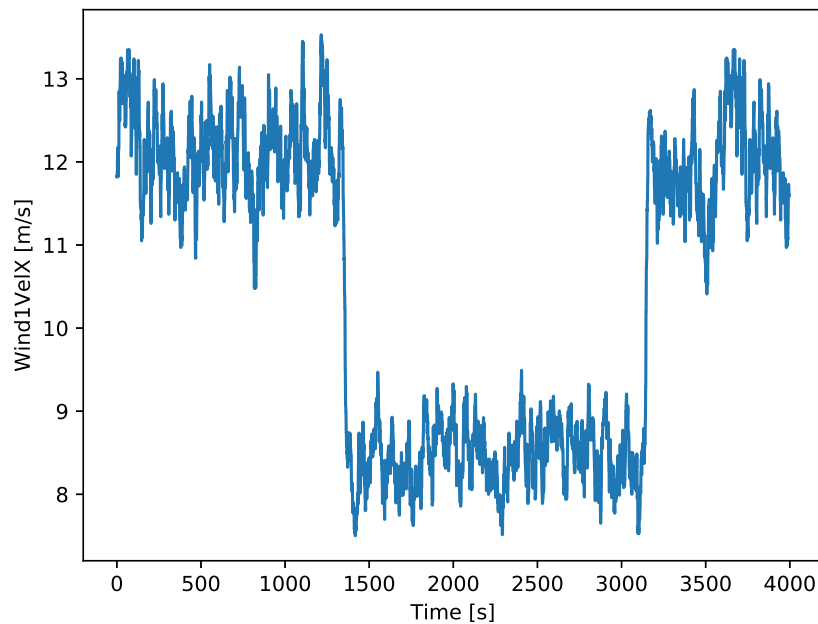


Figure 29. 3x3 CL-Windcon Lay-out



**Figure 30. Wind speed input**

### 6.5.1 Wind input

The wind input (at hub height) for the example case has been created using TurbSim2, and the outputs have been modified in order to get a wind file with a negative pulse (from 12 m/s to 8 m/s) in the mean wind speed. The absolute standard deviation for both wind speeds is kept the same, so the TI also changes, because so does the mean wind speed. The final wind can be observed in Figure 30, where the change of wind speed is evident around 1400 s and 3100 s. Time between 0 s and 1300 s is called Zone A and time between 1500 s and 3000 s is called Zone B.

The objective of this wind input is to verify that the methodology is valid for changes in the wind conditions in a dynamic code (in this case FAST.Farm). The variation of the environmental conditions has been considered necessary to verify that the wind estimator works correctly and the control settings related to the supercontroller are modified according to this. The wind files created using TurbSim2 present approximately constant characteristics with respect to mean wind speed and TI, not allowing changes such as gusts. So, the outputs have been postprocessed. A Matlab script has been developed in order to adapt the TurbSim2 outputs.

### 6.5.2 Baseline result

A FAST.Farm case has been run without supercontroller in order to get the baseline results in the wind farm using the wind input described in subsection 6.5.1. The most important variables for the analysis are the generator power and the blade root flapwise moment, *GenPower* and *RootMyb*, respectively, in FAST.Farm. The analysis of the total power of the wind farm and the maximum DEL will be the reference to check the behaviour of the wind farm controller.



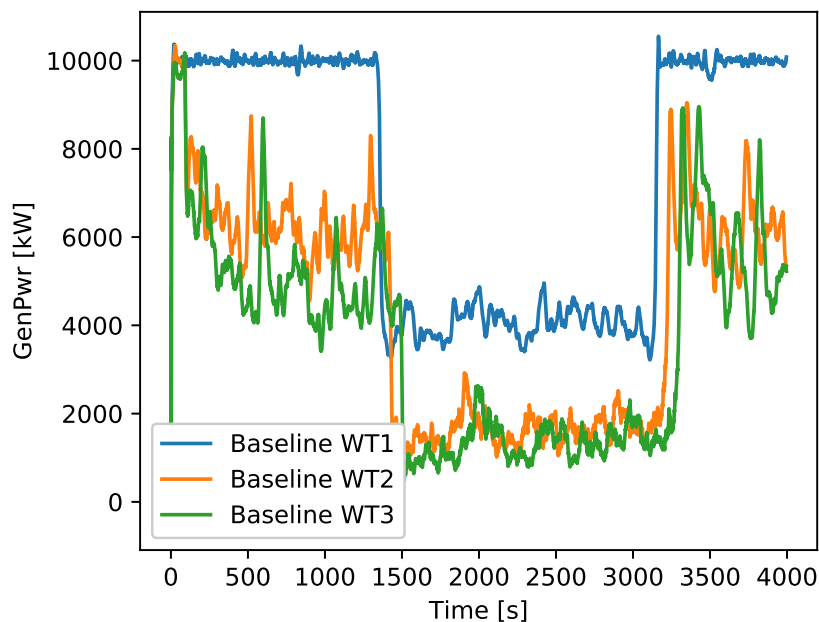


**Figure 31. Power for all wind turbines (baseline)**

In Figures 31 and 32 the results in terms of power and flapwise loads for all wind turbines in the simulation can be seen. It is clear that the upstream wind turbine (WT1) must present a higher level of power than the second (WT2) and third (WT3) wind turbines, as can be seen zoomed in Figures 33a and 33c. It can be observed that the first seconds of simulations, WT2 and WT3 present power similar to the one in WT1, because of the delay of the wake in the dynamic simulation, which has not reached yet the downstream turbines. WT3 shows the lowest level in terms of average value in Zone A, while in Zone B the average values for WT2 and WT3 are very similar. This can be observed in Figure 34a.

The average values observed in terms of flapwise bending moment are coherent with the mean wind speeds for the wind turbines and with the observed power. The highest average moments are observed in WT1, while WT3 presents the lowest values, quite similar to WT2 in Zone B (Figures 33b and 33d).

Finally, the analysis of the DELs for the above-mentioned flapwise bending moment for time windows every 300 s is included in Figure 34b. The average power in these time windows can also be observed in Figure 34a. It is evident that WT3 presents in general the highest DEL values and this is not dependent on the wind speed. This is still consistent with the results for the flapwise bending moment previously mentioned, where WT1 presented the highest average values. These do not necessarily lead to higher DELs, which also depend on the moments oscillation. As expected, the downwind turbine WT3 is experiencing the highest fatigue. WT2 shows a level of DEL close to that of WT3, and WT1 presents the lowest values, except for the region where WT1 receives the gust from 8 m/s to 12 m/s in advance to the rest of the wind turbines, before this effect propagates within the wind farm.

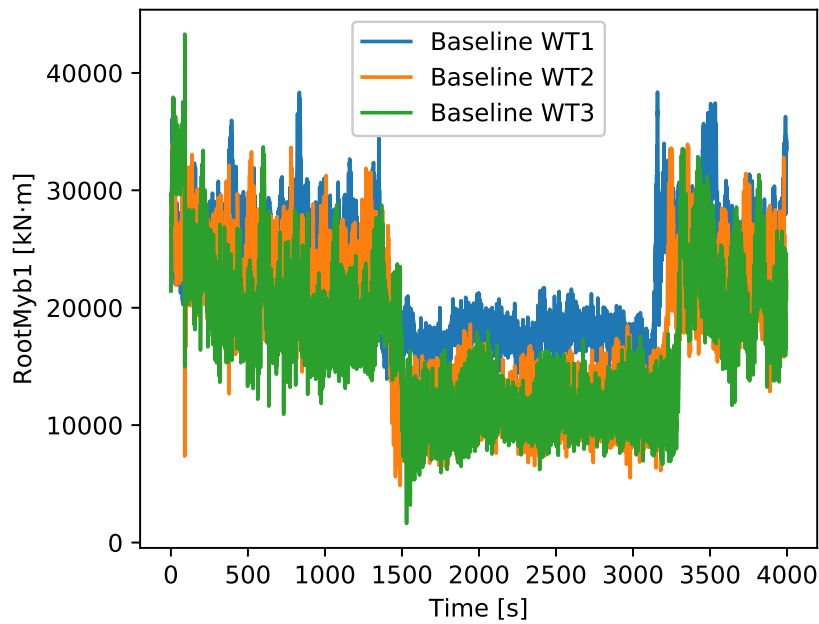


Figure 32.  $RootMyb$  for all wind turbines (baseline)

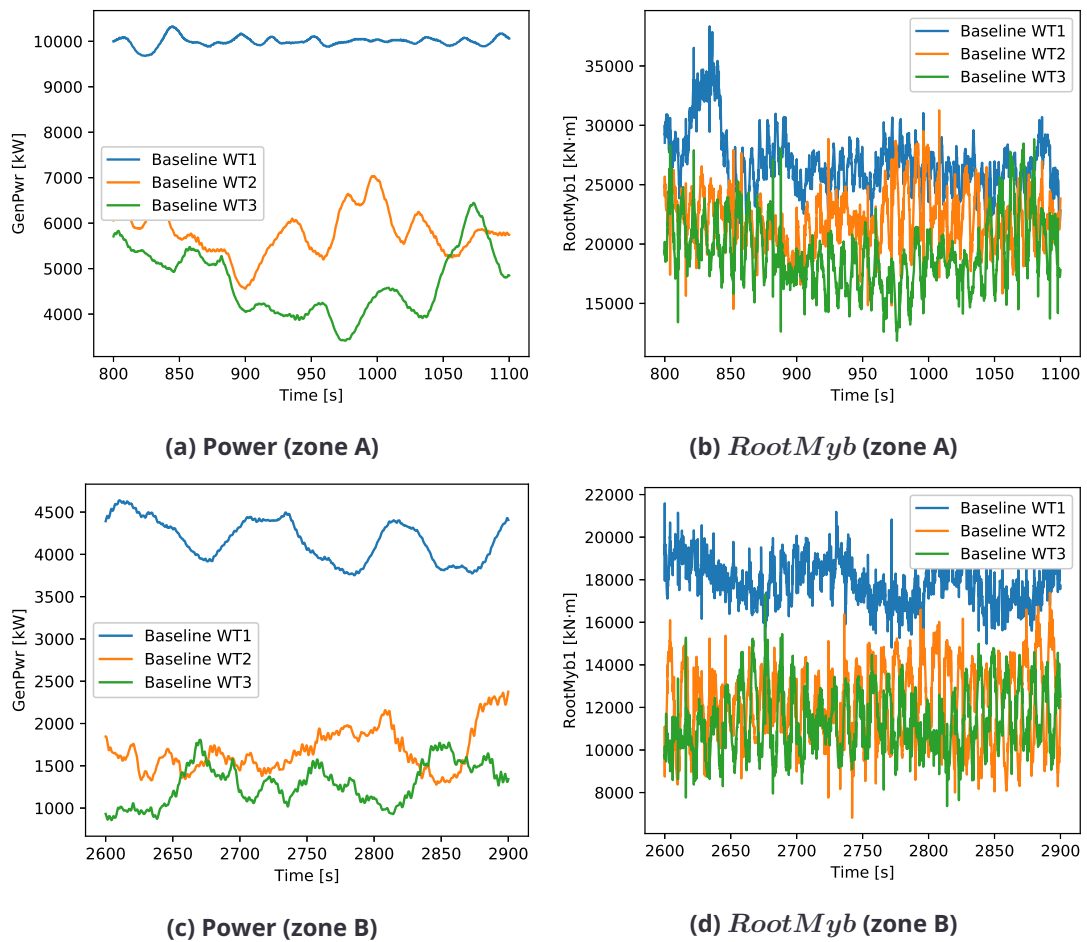


Figure 33. Zoom analysis (baseline)

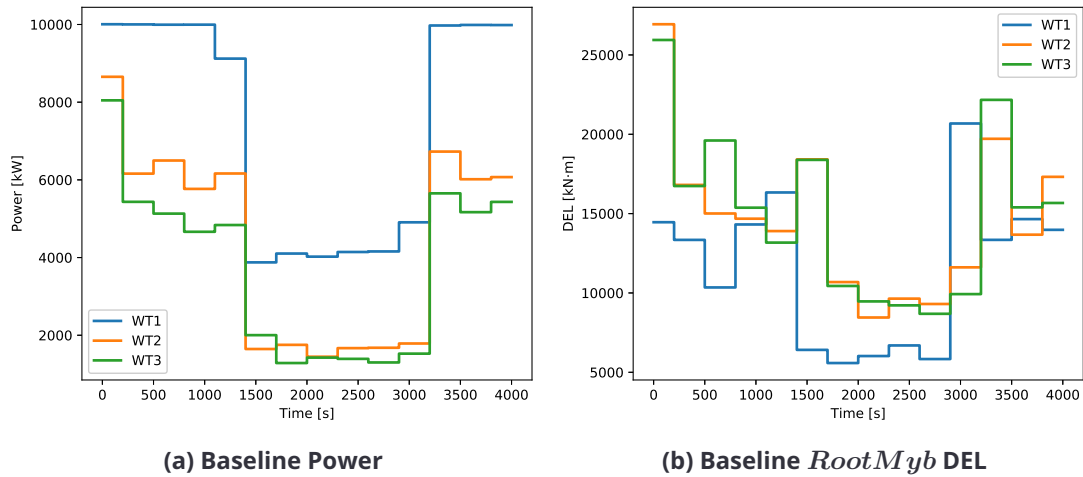


Figure 34. Time window analysis (baseline)

### 6.5.3 Estimation of environmental conditions

As explained in previous sections, a tool has been developed in Python to estimate the environmental conditions using data from FAST.Farm outputs, being also applicable to SCADA data.

This tool has been used with the FAST.Farm case of study in order to extract the environmental conditions without the additional information of the wind input, because this data is not available for the general cases of use of the supercontroller. Transients due to sudden changes of the current supercontroller are not realistic (explained in section 6.3). Therefore the first 10 seconds of each time window have not been taken into account for the average values, standard deviations and later DEL of this example. For future work, it is expected to eliminate these limitations of the supercontroller, therefore it will not be necessary to neglect any transient and it will be possible to work with the complete data, or directly SCADA values. The estimations observed in Table 4 are calculated from the case with supercontroller, which presents similar values to the baseline case for all time windows.

The regions where the gusts from 12 m/s to 8 m/s and from 8 m/s to 12 m/s occur, present a significant value of estimated TI, and the estimated wind velocity is between both wind speeds, which is coherent with the input wind file. The rest of the analyzed regions are also coherent with the inputs and present a slight variation of mean wind speed and TI (Table 4), which in general will not generate abrupt changes in the control settings if the precalculated control settings are robust.

### 6.5.4 Calculation of optimum derating configurations

Various optimizations have been run in order to generate a database for a particular wind farm layout and wind direction. The wind speed has been modified from 8 m/s to 12 m/s and the TI from 4% to 20%, in order to get a matrix that can approximate the solution for all conditions of the wind farm.

The objective function of the optimizer includes the maximization of the total wind farm power and the minimization of the maximum DEL of the wind farm. In general, the obtained solutions lead to

Time [s]	V estimated [m/s]	TI estimated [%]
0-200	12.5	4.5
200-500	12.1	3.9
500-800	12.3	4.0
800-1100	12.1	4.8
1100-1400	11.4	21.8
1400-1700	8.1	4.5
1700-2000	8.2	5.0
2000-2300	8.2	4.0
2300-2600	8.3	4.3
2600-2900	8.3	4.0
2900-3200	9.1	28.0
3200-3500	11.9	7.2
3500-3800	12.2	4.6

**Table 4. Environmental conditions for each time window**

lower loads in the wind turbines but also to a slight reduction of the total wind farm power at high wind speeds, while for lower wind speeds the total power is also increased.

The configurations for different wind conditions can be seen in Tables 5, 6 and 7. These results are included in a solution database that will be used by the supercontroller, in order to select the configuration depending on the estimated environmental conditions. Note that the last downstream turbine WT3 is also depowered in the optimized configurations due to the consideration of DEL in the objective function. On the contrary, if only power was taken into account in the objective function, then it would be intuitive to think that this turbine should take advantage of all the available power in the wind as the last turbine in the row or column.

The configurations for the different wind turbines present a continuing trend for 8 m/s wind speed. For WT1 at 8 m/s, the set point increases with the turbulence. Similar trend is observed for WT2, and WT3 presents negative growth with the turbulence (Table 5). However, this constant increase or decrease in the set points with the TI is not observed in the solutions for wind speed 10 m/s (WT1 and WT2) and for 12 m/s (WT2), where some irregular trends or oscillations between different set points are obtained. The reason for the oscillation, for example in WT2 at 12 m/s between 95/80/85 and 95/85/85, is that the result of the objective function for both results is very close. The table of solutions could be slightly modified in order to increase its robustness, with a similar quality of results. For the current study, the proposed post-process of the database has not been included.

### 6.5.5 Supercontroller operational modes

The created database of configurations is used together with the estimation of the environmental conditions. Taking into account all these data, the derating configurations for the three turbines are obtained, which will be obviously applied in the next period of time. This information is shown in Table 8.

WindSpeed	TI	Direction	WT1	WT2	WT3
8	0.04	180	85	70	95
8	0.05	180	90	70	95
8	0.06	180	90	80	95
8	0.07	180	90	85	95
8	0.08	180	90	90	95
8	0.09	180	90	90	95
8	0.1	180	90	90	95
8	0.15	180	90	90	90
8	0.2	180	90	95	90

Table 5. Depowering settings for wind speed 8 m/s

WindSpeed	TI	Direction	WT1	WT2	WT3
10	0.04	180	90	90	90
10	0.05	180	95	90	90
10	0.06	180	95	95	90
10	0.07	180	90	95	90
10	0.08	180	90	90	80
10	0.09	180	90	90	80
10	0.1	180	90	90	90
10	0.15	180	95	90	85
10	0.2	180	95	90	85

Table 6. Depowering settings for wind speed 10 m/s

WindSpeed	TI	Direction	WT1	WT2	WT3
12	0.04	180	95	85	85
12	0.05	180	95	80	85
12	0.06	180	95	85	85
12	0.07	180	95	80	90
12	0.08	180	95	80	90
12	0.09	180	95	85	90
12	0.1	180	95	90	90
12	0.15	180	95	90	90
12	0.2	180	90	90	90

Table 7. Depowering settings for wind speed 12 m/s

time	V estimated	TI estimated	WT1 der.	WT2 der.	WT3 der.
0-200	12.5	4.5	95	85	85
200-500	12.1	3.9	95	85	85
500-800	12.3	4.0	95	85	85
800-1100	12.1	4.8	95	85	85
1100-1400	11.4	21.8	90	90	90
1400-1700	8.1	4.5	90	70	95
1700-2000	8.2	5.0	90	70	95
2000-2300	8.2	4.0	85	70	95
2300-2600	8.3	4.3	85	70	95
2600-2900	8.3	4.0	85	70	95
2900-3200	9.1	28.0	95	90	85
3200-3500	11.9	7.2	95	80	90
3500-3800	12.2	4.6	95	85	85

**Table 8. Derating solutions for all time windows of the FAST.Farm simulation**

Using the supercontroller interface explained in section 6.3, it is possible to send depowering ratios from wind farm control to all wind turbines. Values are uploaded instantly each certain time interval chosen by the user, 300 s in this analysis. As a consequence of this step in reference signal, together with the fast response in generator torque system, an overreaction detrimental to the life of the turbine components is provoked. To avoid this problem some alternatives could be implemented in future:

- Individual wind turbine control level: Modify each wind turbine controller (OpenDiscon) so that the command to the generator torque actuator has a slower dynamics through appropriate filtering. It seems less practical to perform it at this part of the system in a real implementation, since this might interfere and affect the actuator's expected behaviour in other solicitations required by the turbine control system.
- Supercontroller level: a more straightforward option could be to filter the depowering set point already at the supercontroller level, before sending the command to the individual wind turbines. This option has the advantage that there is no need for changes in wind turbine controllers code, which may reveal more practical in some real wind farm control applications.

### 6.5.6 Comparison of power and DEL

The general results, in terms of power and loads, of the integration of the supercontroller into FAST.Farm can be observed in Figures 35 and 36. As expected, the power in WT1 is the biggest one, followed by WT2 and WT3, which are sometimes quite similar. At this point two particularities should be mentioned:

- As has been said earlier, the obtained derating configurations are applied in the next period of time. It can be clearly seen in WT1, which produces 100% of the power in the first 200 s, but then decreases a little bit, down to 95%. In WT2 and WT3 it also happens, although it is not so well seen in the Figure 35.

- The wake produced by WT1 takes some time to reach the following turbines and that phenomenon can be seen when the pulse in the wind speed happens. The power of WT1 changes almost immediately, but it takes a few seconds to affect WT2 and a few more to affect WT3. It can be also seen in the initial instants for WT2 and WT3.

Regarding the loads, there is not such a big difference between the turbines, as it happened with the power. It is worth mentioning here that quite high peaks in the loads occur when a big change in the derating setting is applied ( $> 10\%$ ). As has been mentioned earlier, this happens because it has not been taken into account in the optimization the difference between two consecutive derating settings.

The actuator command could be appropriately filtered in order to avoid these peaks as explained above in subsection 6.5.5. Additionally, for the sake of global efficiency, restrictions could be integrated to avoid unnecessary modifications of the setting points in the wind turbines that do not generate a significant improvement in the wind farm performance but lead to actuators' energy consumption.

The analysis of these results must include the comparison with respect to the baseline case without supercontroller, in order to evaluate the validity of the integration and the quality of the wind farm controller.

First, a comparison of the power and loads of the upstream wind turbine WT1 can be seen in Figures 37 and 38. It is evident that the power of this first wind turbine in comparison with the baseline case is lower, except for the initial instants without wake affection in downstream turbines, as has already been said. This is also coherent with the depowering solutions obtained using the optimizer. The comparison of the loads shows important peaks in the blade root flapwise bending moment when abrupt changes of the depowering configurations are commanded by the supercontroller. These abrupt changes have been neglected in the wind estimations, as previously explained in subsection 6.5.3.

In any case, the general oscillations of the loads seem to be similar to the baseline case, because the ambient conditions of this first wind turbine are equivalent and its control settings do not present a significant effect on loads. In Zone B, a slight reduction in the mean value of the loads can be seen. However, the DELs depend more on the standard deviation of the load than on the mean value. Hence, this reduction does not seem to have a big impact in the DEL of the turbine.

In Figure 39 a zoom of the previous graphs can be seen. In Figure 39a and 39c a zoom of the power is shown. As has been mentioned in the previous paragraphs, the power of the upstream wind turbine is reduced a little bit when the supercontroller is utilized. In Figure 39b and 39d a zoom of the loads is shown. Again, which has been previously said can be better appreciated. In Zone A the loads with the supercontroller are minimally lower, but in Zone B is clearer that there is notable difference between the mean value of both cases.

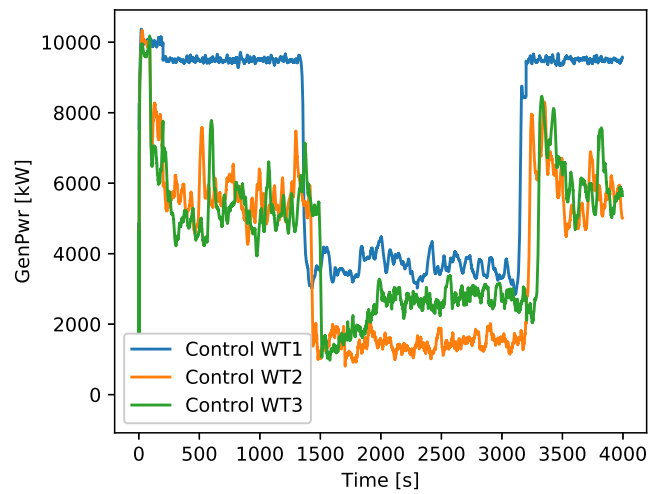


Figure 35. Power for all wind turbines (with supercontroller)

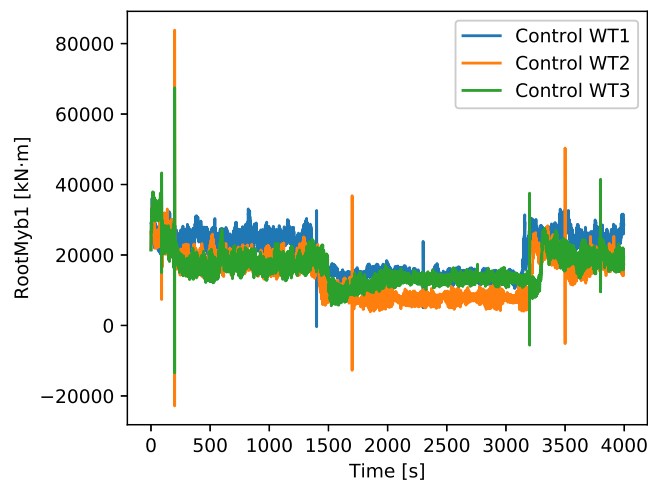


Figure 36. *RootMyb* for all wind turbines (with supercontroller)

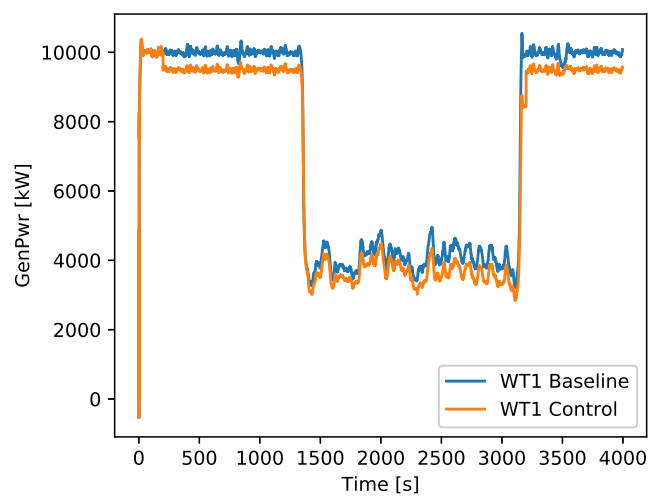


Figure 37. WT1 Power Comparison (baseline and supercontroller)



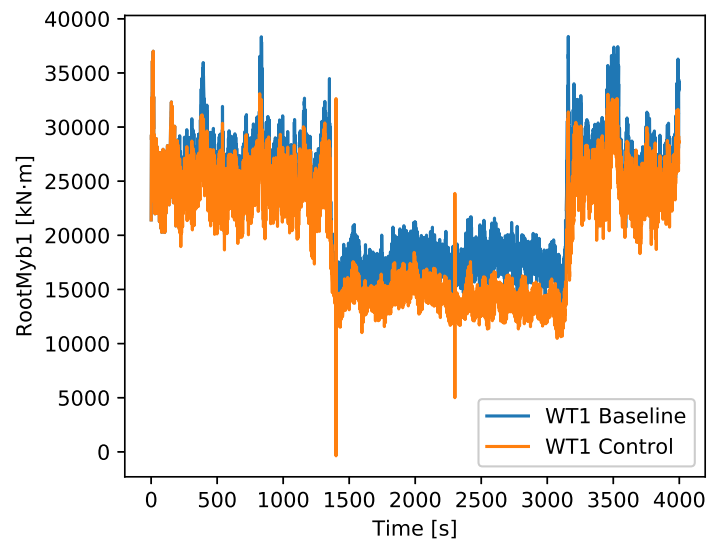


Figure 38. WT1 *RootMyb* Comparison (baseline and supercontroller)

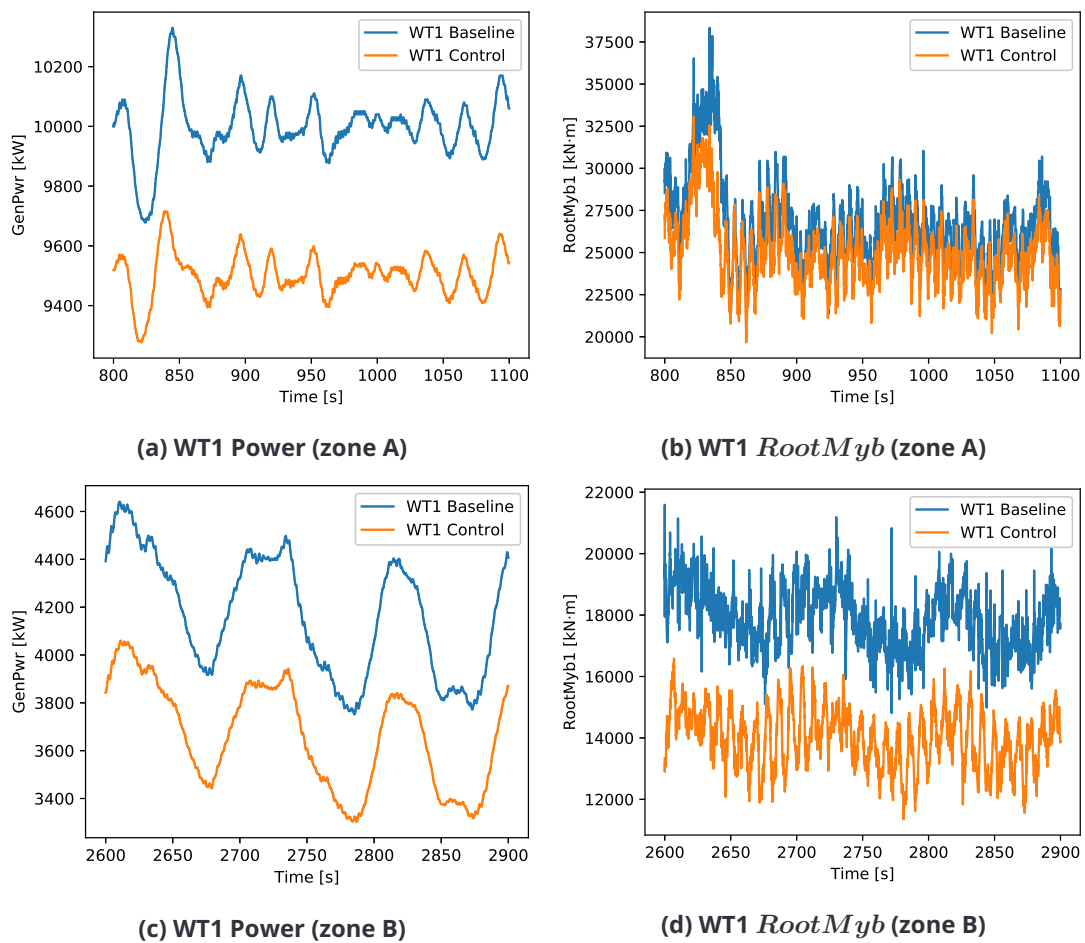
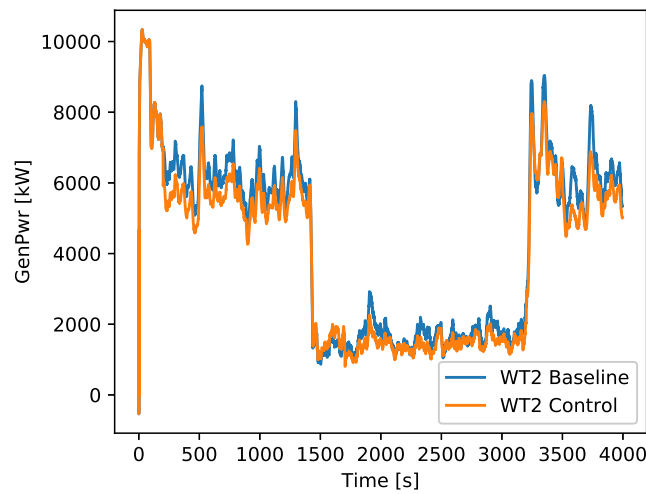
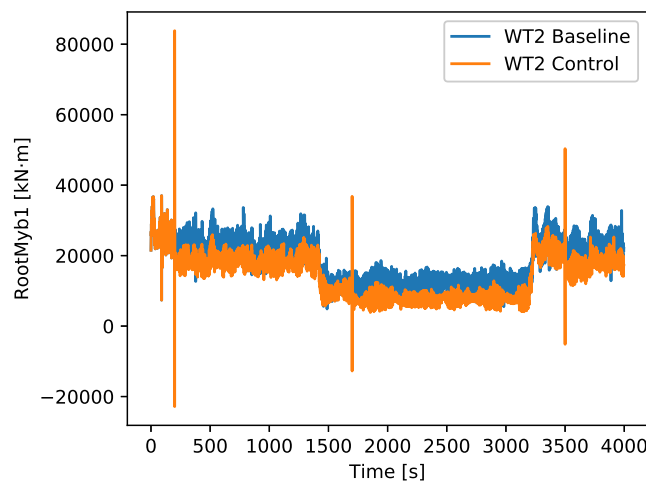


Figure 39. WT1 zoom Comparison (baseline and supercontroller)



**Figure 40. WT2 Power Comparison (baseline and supercontroller)**



**Figure 41. WT2 *RootMyb* Comparison (baseline and supercontroller)**

The general performance of the second wind turbine is analyzed in Figures 40 and 41, comparing the baseline results and the outputs with the supercontroller. A slight reduction of the power is observed during the complete simulation. This power reduction is related to the depowering configuration and the wind condition for this wind turbine. Due to this turbine configuration, the loads in the blade root are also reduced. Apart from the big peaks aforementioned, not only the mean value, but also the standard deviation is lowered using the supercontroller.

In Figure 42 the power and loads can be seen in more detail. The power with the supercontroller is usually lower (Figure 42a and 42c) and so are the blade root flapwise loads, both in mean value and standard deviation (Figure 42b and 42d). This improvement is supposed to minimize the blade root flapwise DELs.

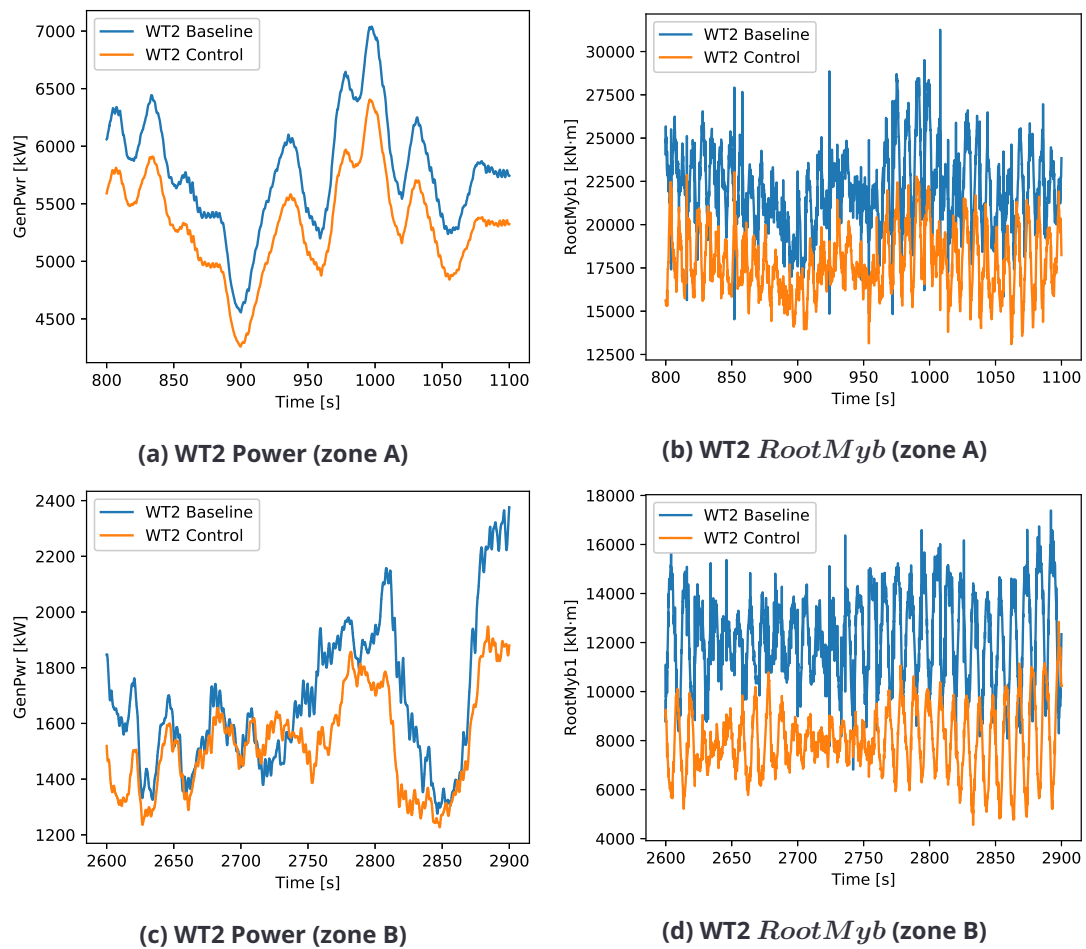


**Figure 42. WT2 zoom Comparison (baseline and supercontroller)**

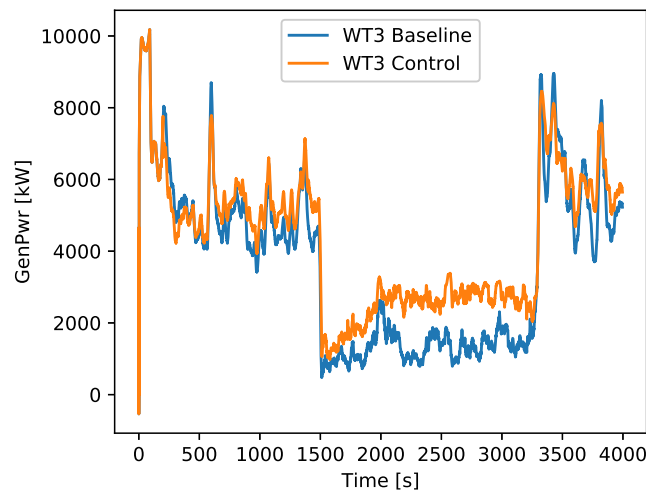


**Figure 43. WT3 Power Comparison (baseline and supercontroller)**

With regard to the third turbine (the most downstream one), its power and blade root flapwise load are shown in Figures 43 and 44 for both cases: baseline and with supercontroller. Its power is, in most cases, bigger with the supercontroller than in the baseline case, as one could expect. This is due to the fact that the upstream turbines are in derating conditions, producing a weaker wake and therefore this wind turbine receives a higher wind. The loads may seem similar, but, as has been stated before, the standard deviation plays a more important role than the mean value. In this case, the mean values are similar, but the deviation is noticeably lower in the case with the supercontroller (ignoring the big peaks).

In Figure 45 a zoom of the power and loads is shown. The power is almost always bigger, but this difference can be really appreciated in Zone B, where the downstream turbine power with supercontroller is close to 200% the baseline case (Figures 45a and 45c). The mean value of the loads is similar, especially in Zone A, but the standard deviation is lower, leading to lower DELs (Figure 45b and 45d).

This standard deviation difference can be better seen if we look at the signals in the frequency domain. A Fast Fourier Transform (FFT) has been applied to both signals in both zones. As can be seen in Figure 46, there are quite important peaks around 0.1 Hz, which are noticeably lower when the supercontroller is applied. As has been stated before, this reduction will have a significant impact on the DELs.

The average power for every time window (each 300 s) can be observed in Figures 47a, 47c and 47e, where the comparison is clearer than in the temporal comparisons, being the conclusions equivalent. In order to claim that the reduction in the standard deviation (or a peak in the frequency domain) of the blade root flapwise loads leads to a reduction in the DELs, now these ones are analyzed. The DELs for all three wind turbines are calculated for all time windows every 300 s (except the initial one, which is calculated taking 200 s) and can be seen in Figures 47b, 47d and 47f.

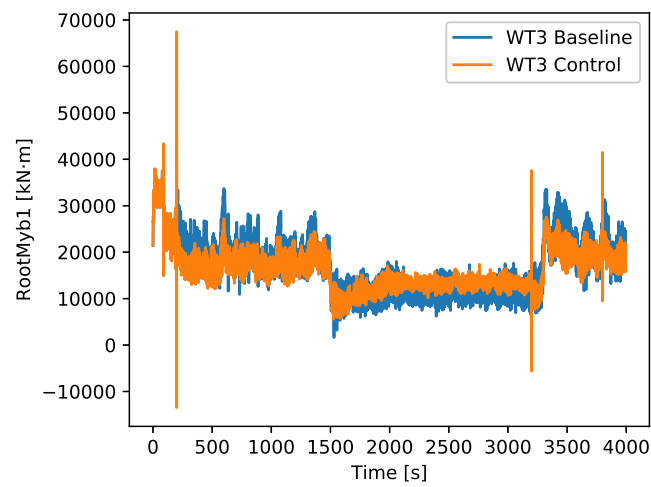


Figure 44. WT3 *RootMyb* Comparison (baseline and supercontroller)

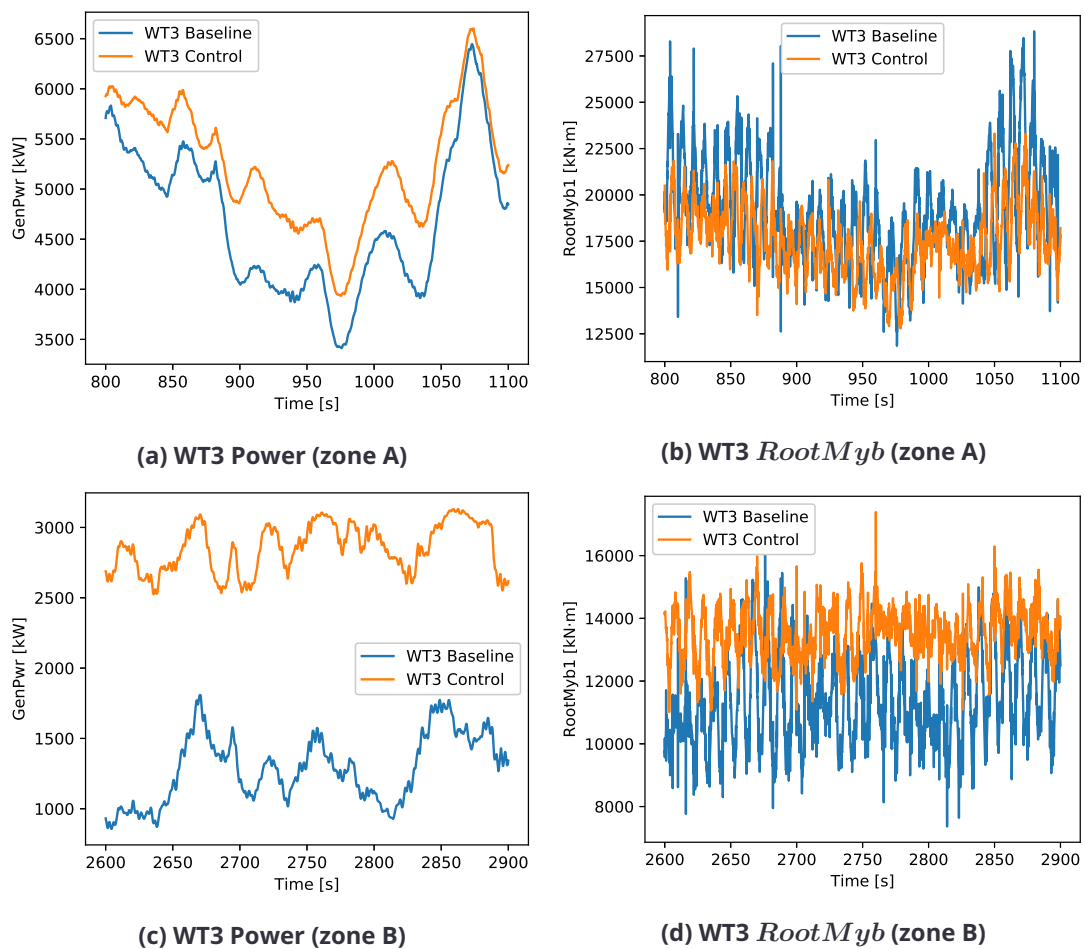
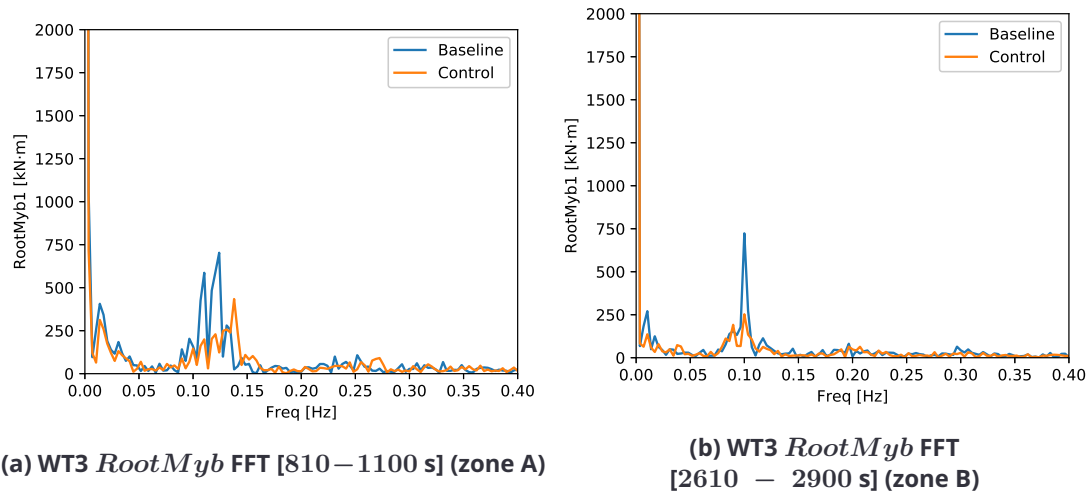


Figure 45. WT3 zoom Comparison (baseline and supercontroller)



**Figure 46. WT3 FFT Comparison (baseline and supercontroller)**

For the upstream wind turbine the power is reduced if the supercontroller is used, but so do the DELs (Figure 47a and 47b). As has been said earlier, there is not such a big difference between both cases, because this turbine does not receive any wake coming from any other turbine and therefore the supercontroller does not improve the baseline case to great extent.

Regarding the second wind turbine (Figure 47c and 47d), the differences are now bigger, specially in the DELs. As it happened in the previous turbine, the power is slightly reduced with the supercontroller, but in this case the DELs are reduced in a more significant manner, due to the standard deviation reduction shown before.

The most downstream turbine WT3 is supposed to be the most promising one to use the supercontroller, and analyzing Figure 47e and 47f these assumptions are confirmed. The power is increased and the DELs are reduced in a significant manner due to the derating combinations carried out in the upstream wind turbines.

Figure 48 shows more clearly how the supercontroller is capable of reducing the damage equivalent loads and increasing the power of the wind farm as a whole, in comparison with the baseline case, where every wind turbine has its own control scheme and act independently from the others. The percentages of the maximum DEL in the wind farm with respect to the baseline show the significant reduction of load for most of the time windows where the supercontroller is active.

## 6.6 Conclusions and Future Work

This chapter has shown the effective dynamic integration of the feed-forward induction scheme for wind farm power and loads optimization, initially introduced in Deliverable D2.3 [55], with adaption of the optimized turbine set points to the variation in ambient conditions. In particular, it was integrated into medium-fidelity simulations in FAST.Farm, although the configuration can also be applied to measurable SCADA data. Different building blocks within the supercontroller were developed for

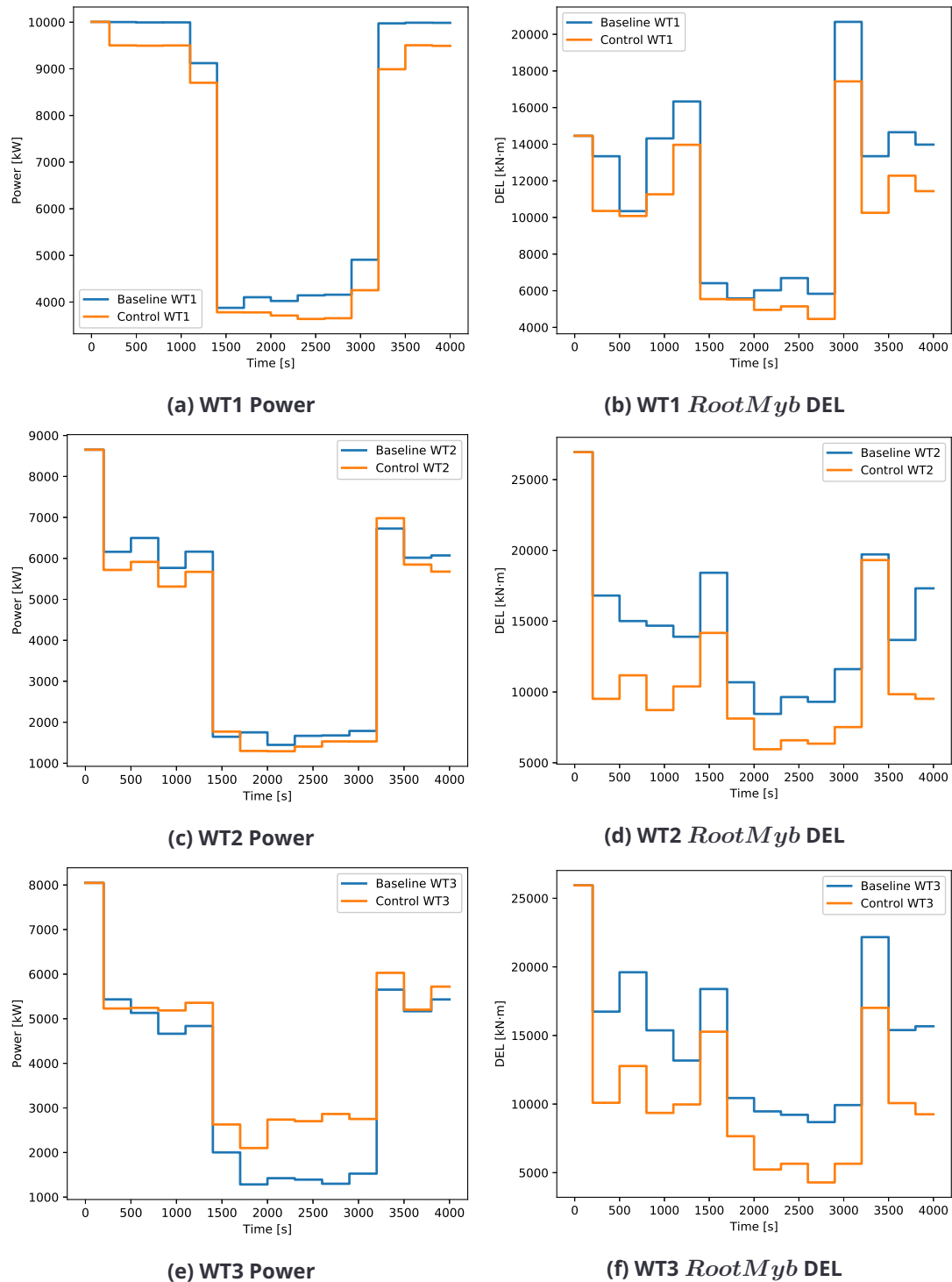
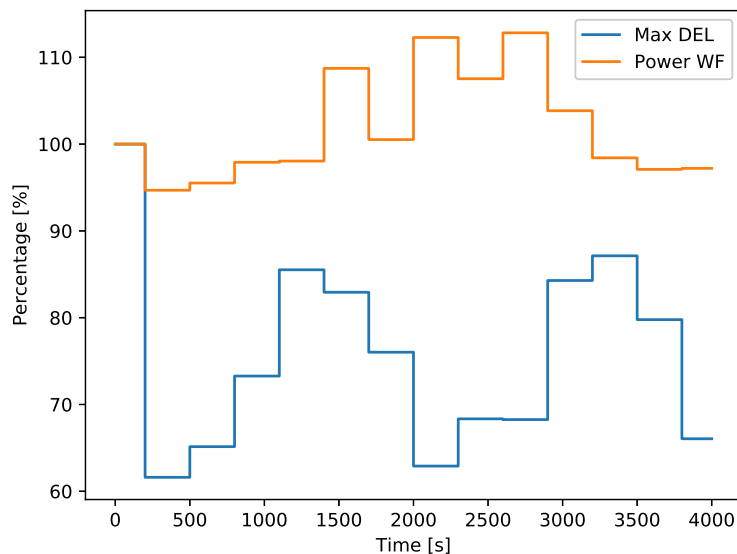


Figure 47. Time window comparison (baseline and supercontroller)



**Figure 48. General results in percentage: Power of the wind farm and Maximum DEL *RootMyb***

such purpose, such as the ambient conditions estimation. The developments represent an incremental step towards full closed-loop application of induction wind farm control.

The simulation results in a 3x3 wind farm, with variation of ambient wind speed and TI, show how wind farm control can lead to better results at farm level than the greedy approach (baseline). Some references call induction control into question when it comes to increase farm power production on static high-fidelity simulations ([7], [18], [36]). By contrast, the promising field of application for this technology seems to be the joint optimization of power and loads. Maximum DEL for flapwise bending moment was reduced in the example while practically maintaining the total power production with slight decreases and increases. This opens up the possibility to also take life management aspects into consideration.

Some improvements to the presented methodology have been selected for future work:

- Modify the abrupt change of derating settings in the supercontroller, in order to avoid the high load peaks in the transition between different configurations
- Post-process or development in the supercontroller to increase the robustness of the solutions, in order to get farm configurations less dependent on the environmental conditions. This improvement would reduce unnecessary modifications of setting points with similar results, therefore reducing the actuators demand and the effect of transients
- Introduce the estimation of variations in ambient wind direction
- Selection of best parameters to get the free-stream conditions for different kind of cases
- Quality improvement of estimation of free-stream conditions



- Optimization taking into account DEL at different components of the wind turbine
- Online calculation of optimum derating with the exact environmental conditions input (online solution)
- Effective feedback of downstream turbines information to get a full closed-loop configuration

## 7 WIND FARM CONTROLLER DESIGN AND TESTING WITH LONGSIM

This chapter presents a wind farm control solution that leverages the simplified surrogate model LongSim from DNV GL. This controller is synthesized for the onshore wind farm in Sedini on the island of Sardinia, Italy for real-world experiments on axial induction control for power maximization. In this chapter, special attention is paid towards the shift from static to dynamic control, which is a topic mostly unexplored in the literature, yet of immense importance when considering real-world wind-farm operation.

The core content of this chapter is presented from the following page onwards.

## 7 Wind farm controller design and testing with LongSim

### 7.1 Introduction

This chapter describes the use of DNV GL's 'LongSim' code for the design and simulation testing of wind farm controllers. The work is based on a part of the Sedini wind farm which was selected to be used for field testing of both induction and wake steering controllers within the CL-Windcon project. Thus, this chapter is an account of the preliminary work done in preparation for those field tests. Eventually, because of time and resource constraints, the additional instrumentation required for the wake steering tests was not installed, and so only the induction control tests could be carried out. The final calculations in preparation for these tests will be reported in Work Package 3.

The calculations used for the actual tests made use of confidential wind turbine data provided by GE which may not be revealed, so where necessary, information from the public-domain WindPACT turbine model [1] has been used in the description provided here, since this model is fairly closely based on a GE 1.5 turbine similar to those used for the Sedini testing.

The LongSim model has been previously described in CL-Windcon Deliverable D1.2 [2]. The workflow described here consists of the following main stages:

- 1) Site and turbine Input data set-up for LongSim.
- 2) Steady-state set-point optimisations using LongSim, to generate look-up tables of optimal set-points for the turbines to be used in the experiment as a function of steady-state wind conditions.
- 3) Repeat optimisations for different wake model variants to evaluate the sensitivity of set-points and wind farm control performance to wake modelling uncertainties.
- 4) Generation of final look-up tables suitable for implementation, aiming at robustness to wake model uncertainty and to uncertainties in the measurement of the wind conditions over the relevant area.
- 5) Implementation of a realisable dynamic control algorithm, including measurement of wind conditions, filtering and choice of sampling interval, set-point table look-up and communication of the set-points to the turbines.
- 6) Dynamic time-domain simulations using LongSim, using realistic time-varying wind conditions derived from historical met mast data at the site, and attempting to model as many real-world effects as possible.

### 7.2 Site layout and experiment design

Details of the Sedini wind farm, planned instrumentation and test campaigns are provided in CL-Windcon Deliverable D3.2 [3]. The farm consists of 43 GE 1.5 turbines laid out as in Figure 7.1. Most of the turbines are of type GE 1.5s (1.5 MW, 70.5m rotor diameter, 65 m hub height), but the seven turbines shown in red are the larger GE 1.5sle (1.5 MW, 77 m rotor diameter, 80 m hub height). The diagonal row of turbines #13 and #31 – #38 are involved in the experiment described here, and since only wind directions blowing along this row from a roughly south-westerly direction are relevant to the experiment, only these nine turbines were modelled in LongSim in the work described here. Terrain complexity has been ignored – with south-westerly wind directions, the effect of the terrain on the wind flow at these nine turbines is likely to be relatively small.

In the experiment as originally designed, both induction and wake steering schemes for wake control were to be tested using these turbines. The two schemes were to be tested separately. Since no loads

instrumentation would be available on these turbines, the wake control in each case is aimed only at increasing the power production from this row. The wake control will be switched on and off at regular intervals so that the performance with and without wake control can be compared. As it is important to compare in similar wind conditions, the upstream turbine, #38, will be used to define the wind condition, and will remain in baseline operation throughout to ensure that the wind condition measurement is unaffected by the wake control. This means that some of the potential wake control gains will not be realised, since some additional gain would be expected if #38 could also be controlled.

For induction control, the power output of turbines #31 – #37 can be modified, and the power output of all nine turbines will be monitored (although the power output of #38 should not be affected). For wake steering control, improved wind vanes are needed, and for cost reasons these were to be installed only on turbines #34 – #38. With #38 used as the ‘wind sensor’, this means that wake steering would be applied to four turbines, #34 – #37, but again the power output of all nine turbines would be monitored.

In the end, time and resource constraints mean that the improved wind vanes were not installed on #34 – #37. As a result, the wake steering tests on this row of turbines had to be abandoned, and only the induction control tests could be carried out. Nevertheless, the preliminary design work for both the wake steering and the induction control tests is presented in this report. The final optimisations and simulations for the induction control tests that were actually carried out will be reported as part of Work Package 3.

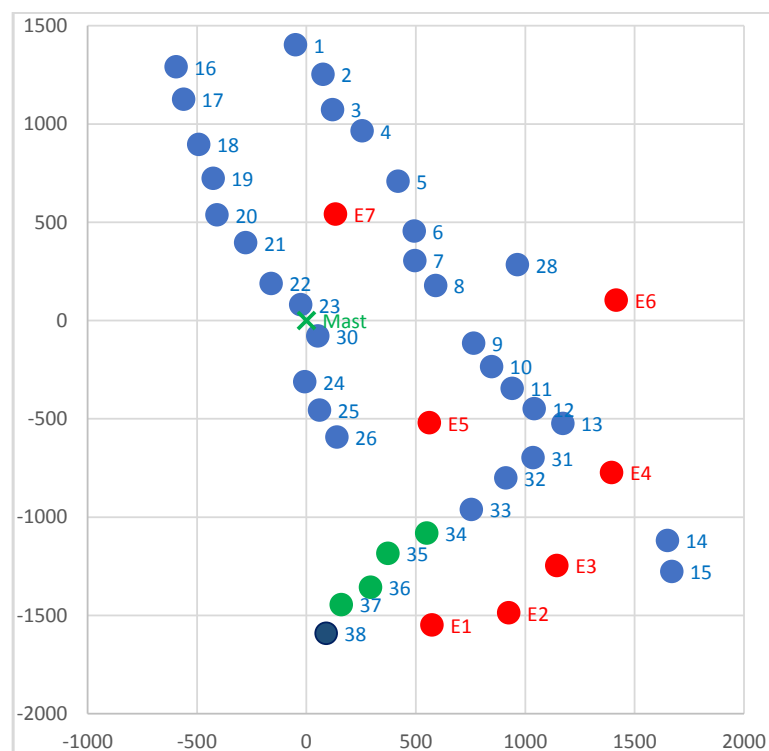


Figure 7.1: Sedini site layout

When running the set-point optimisations with LongSim, the optimiser only modifies the set-points of the turbines which can be controlled. Furthermore, when running the dynamic simulations, only the wind conditions measured at turbine #38 are used as input to the set-point look-up tables. The simulation generates a realistic correlated time-varying wind field covering all the turbines, so each turbine will see different wind conditions at any one time.

### 7.3 Input data for LongSim

#### 7.3.1 Site layout

The positions of turbines #13 and #31-38 were supplied by GE. Although the wake of turbine E1 could have an effect at the more southerly end of the direction range of interest, it was not included in the modelling because the required turbine data for this larger turbine was not available.

#### 7.3.2 Wind turbines

LongSim can model the turbines to different levels of detail. At the simpler end, power and thrust curves can be used to define the turbine power performance and the thrust force which determines the wake. For somewhat greater fidelity, look-up tables of power and thrust coefficients as a function of tip speed ratio, pitch angle and yaw angle can be used, together with basic control gains and other parameters which allow the pitch action and the rotor speed degree of freedom to be simulated. Yaw control logic can also be implemented.

For Sedini, power and thrust curves were provided by GE for different yaw angles, and also for different settings of the power reduction set-point used for induction control, so the pitch and rotor speed degrees of freedom were not simulated explicitly. Turbine yaw control, however, was simulated explicitly, using the yaw hysteresis logic and yaw rate supplied by GE. For reasons of confidentiality, the turbine details cannot be given here.

#### 7.3.3 Wake models

LongSim uses 'engineering' wake models superimposed on an underlying wind field. Although some detailed physical effects may not be captured in such a model, it runs very fast on a single core, making it suitable for iterative optimisations both in steady state and in the time domain. Several alternative wake models are currently available in LongSim, some of which also have empirical parameters which can be varied. Research on the different wake model variants is still ongoing, and it is not yet clear which wake model variants are likely to perform best in which situations. There are different models available to describe the velocity profile in the wake and how it evolves downstream (including effects of wake-added turbulence), the lateral deflection of the wake caused by yaw misalignment, and the superposition of multiple wakes. To obtain a representative range of results, the following specific variants have been used in generating the results which follow:

- A1: Standard Ainslie model [4] using added turbulence, dominant wake superposition and a meandering correction all as described in [2], and the wake deflection model of Jimenez [5] with deflection parameter  $k_d = 0.15$  as in Gebraad [6].
- A2: Same as A1 but without the meandering correction.
- E1: EPFL default model as in [7].
- E2: EPFL model matched to NREL version of Floris [8], which includes a factor 2 on wake deflection.

## 7.4 Steady-state set-point optimisations with LongSim

LongSim was used to perform steady-state optimisation of set-points. It loops through a pre-defined range of wind speeds, directions and turbulence intensities, and for each wind condition, the set-points are varied iteratively to optimise a defined merit function, using an optimisation algorithm based on the simplex method [9]. For each turbine, the optimal set-points are then output as look-up tables dependent on wind speed, direction and turbulence intensity.

Optimisations were performed with different wake models, as described above. Then the optimal setpoints calculated with one wake model were tested against other wake models to see to what extent the power gains obtained with one wake model might be realised if the wake characteristics were actually different. This gives an impression of the robustness of the wake control to variations in wake characteristics. Furthermore, the use of setpoints averaged across different wake models has also been investigated.

In the following graphics, the power increase is presented as a ratio of the power obtained with a given set of optimised setpoints to the power obtained without wake control, using steady-state analysis. The results are presented as a colour map against wind speed and direction, for different turbulence intensities. The actual setpoints for individual turbines are presented in a similar way, to give an impression of how smooth the setpoint lookup tables are. This is especially important for wake steering, because of the need to avoid rapid variation of yaw offsets which could significantly increase yaw actuator duty.

### 7.4.1 Induction control optimisations

For induction control, the power reduction set-points were optimised. The following inputs were defined for these initial optimisations:

- Turbine set-points to optimise: #31 to #37
- Permitted set-point range: 0 (no power reduction) to 10 (giving roughly 300 kW power reduction at 10-12 m/s but tapering off to zero below 6m/s or above 16 m/s)
- Merit function: total energy production from the whole row, i.e. turbines #13 & #31 - #38
- Wind speeds: 6, 7, 8, 9, 10 m/s
- Turbulence intensity: 10%, 13%, 14%, 17%
- Wind directions: 200° to 245° in steps of 2.5°
- Wake models: A1, A2, E1

Figure 7.2 shows the power ratios achieved in the steady state with the different wake models at 10%, 13% and 17% turbulence. Wake model A1 gives the highest ratios, over 1.1 (i.e. 10% increase), in narrow direction sectors between 225 and 240 degrees, and for wind speeds in the upper half of the range. Without the meandering correction (wake model 2), there is almost no benefit anywhere. Wake model E1 shows benefits over a wider range of conditions, but only up to about 5% increase. In all cases, as the turbulence intensity increases, the benefit decreases significantly.

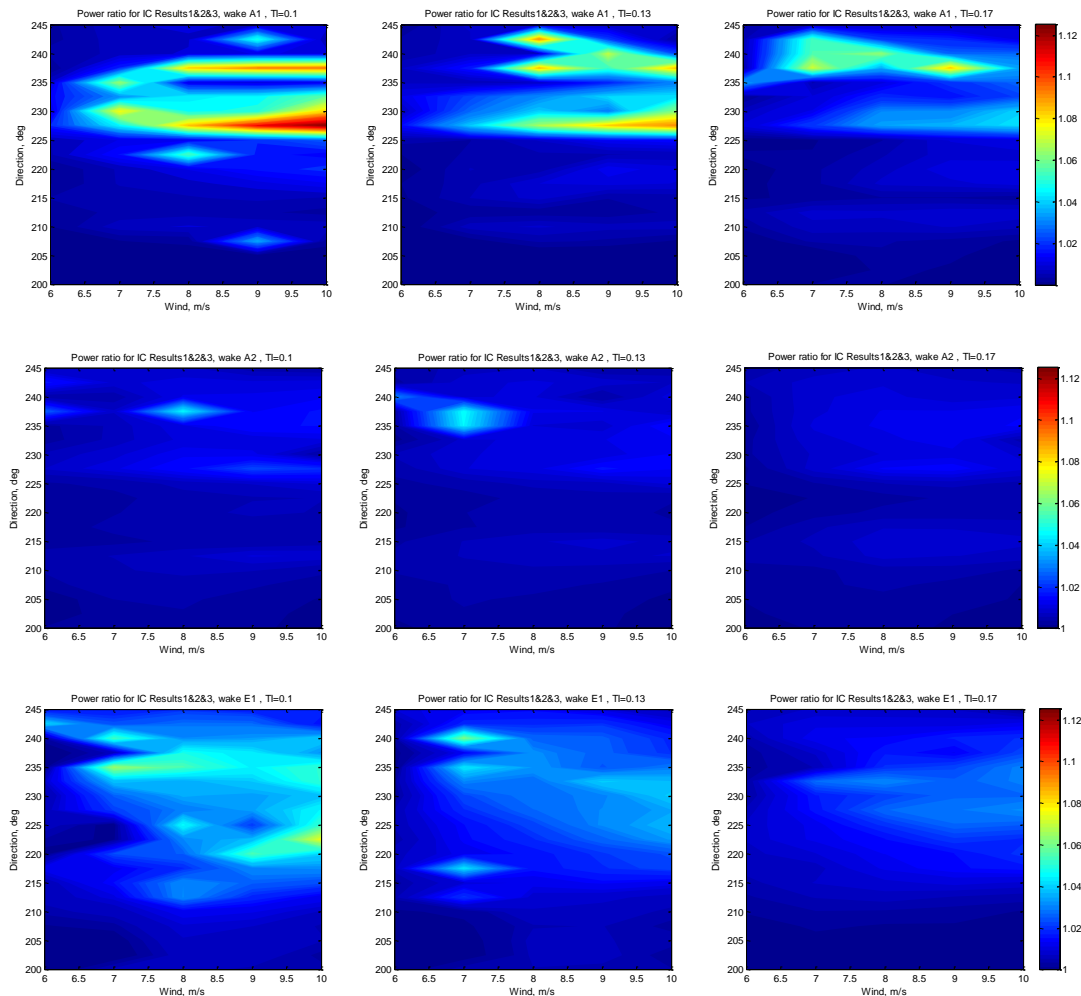


Figure 7.2: Power ratios for induction control at 10%, 13% and 17% turbulence  
Wake model A1 (top), A2 (middle), E1 (bottom)

Figure 7.3 shows the optimized power reduction setpoints for four of the seven controlled turbines, as a function of wind direction. The colours represent different wake models; the thin lines represent different wind conditions: different line styles represent turbulence intensities, with separate lines for each wind speed. Clearly, the optimal setpoints vary widely, but some patterns emerge. The thick coloured lines show the setpoints averaged across all wind speeds and turbulence intensities for each wake model. The black line is an average across all three wake models; using this for the induction control will result in a scheme which is suboptimal, but might perhaps be ‘robust’ to uncertainties in knowing both the wake characteristics and the actual wind speed and turbulence intensity. This is tested in Figure 7.4 (using the same colour scale as in Figure 7.2). Although the setpoints are no longer optimal for each model, nor for the specific wind speed and turbulence intensity, the power gains, although smaller, are still quite similar to the optimal gains in Figure 7.2. This gives some confidence that it may be possible to achieve some of the gain in practice, despite the uncertainties.

At some points in Figure 7.4, the power gain is actually slightly negative, because the averaged setpoints are actually making things worse for a particular wake model in that condition. The colour scaling is limited to 1 or greater for comparison with Figure 7.2, so all areas with power ratio less than or equal to 1 are dark blue. In practice, the lowest value seen in any of these cases was just below 0.99, apart from one or two individual points at 6 m/s (but the induction control should anyway be disabled here because the setpoint reduction feature in the turbine controllers only acts above 7m/s).

At one or two individual points in Figure 7.4, the power gain is actually a bit higher than in Figure 7.2. This is simply an indication that the optimization did not always converge to the global optimum; there is of course no guarantee of reaching the global optimum, given the nature of the merit function and the optimization scheme used.

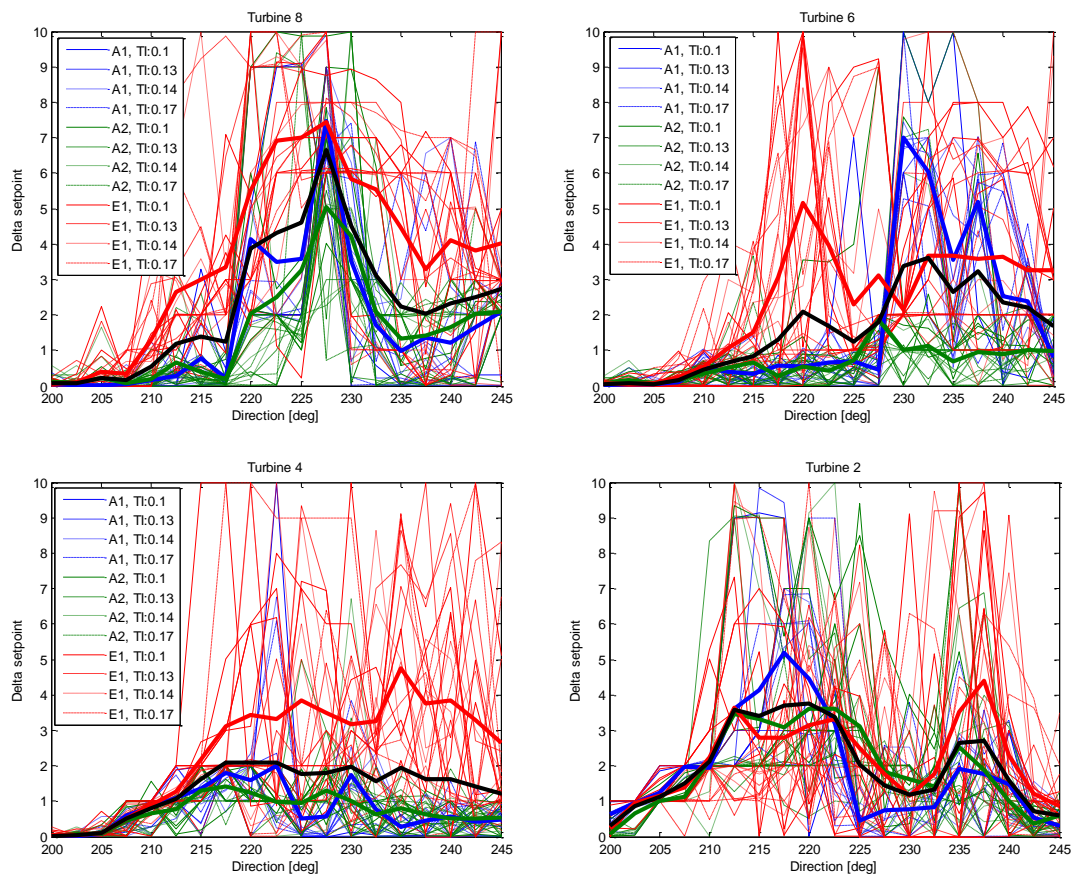


Figure 7.3: Example power reduction setpoints for four of the turbines: #37, #35, #33, #31



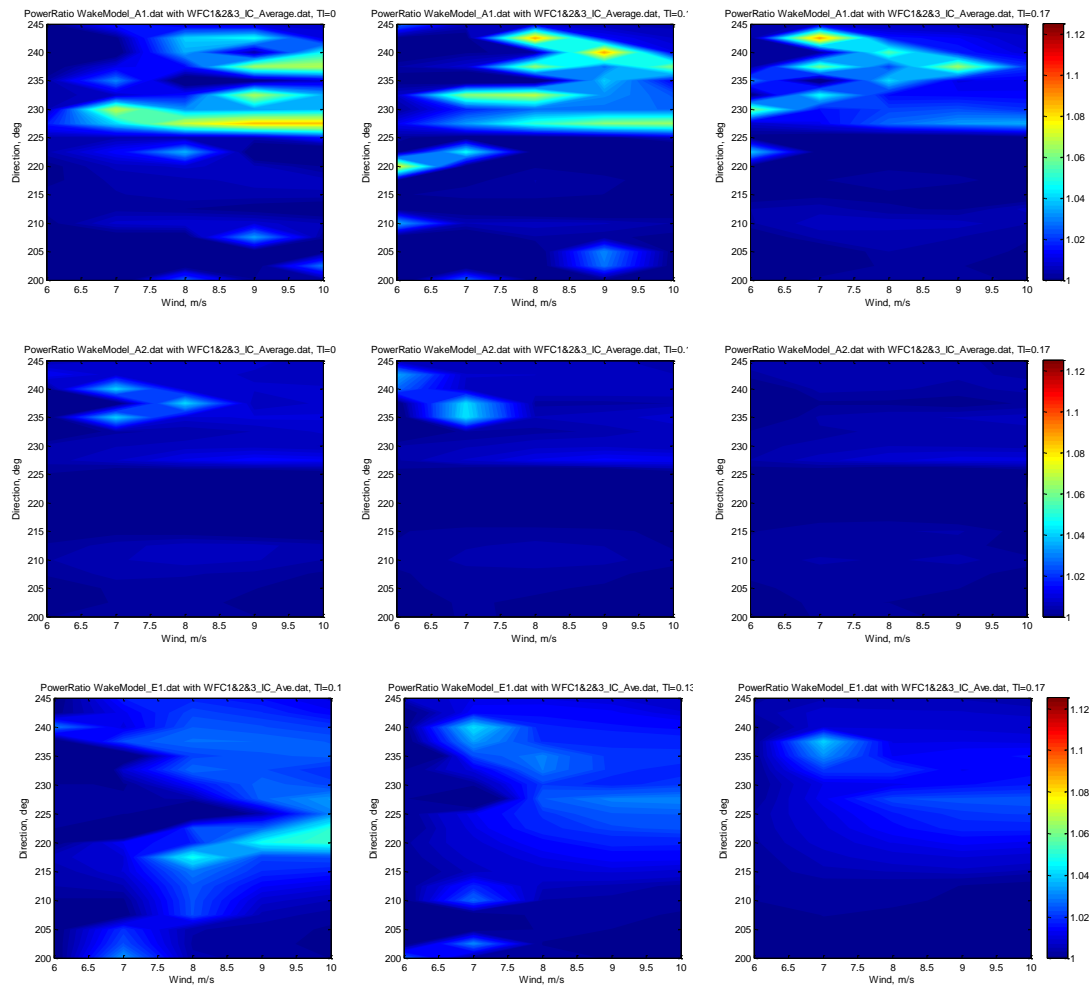


Figure 7.4: Power ratios using ‘robust’ setpoints tested against the different wake models: A1 (top), A2 (middle), E1 (bottom), at turbulence intensities of 10%, 13% and 17%

#### 7.4.2 Wake steering optimisations

For wake steering, the yaw misalignment set-points were optimised. The following inputs were defined for these initial optimisations:

- Turbine set-points to optimise: #34 to #37
- Permitted set-point range:  $\pm 35^\circ$
- Merit function: total energy production from the whole row, i.e. turbines #13 & #31 - #38
- Wind speeds: 6, 7, 8, 9, 10 m/s
- Turbulence intensity: 10%, 13%, 14%, 17%
- Wind directions:  $220^\circ$  to  $260^\circ$  in steps of  $2.5^\circ$
- Wake models: A1, A2, E1, E2

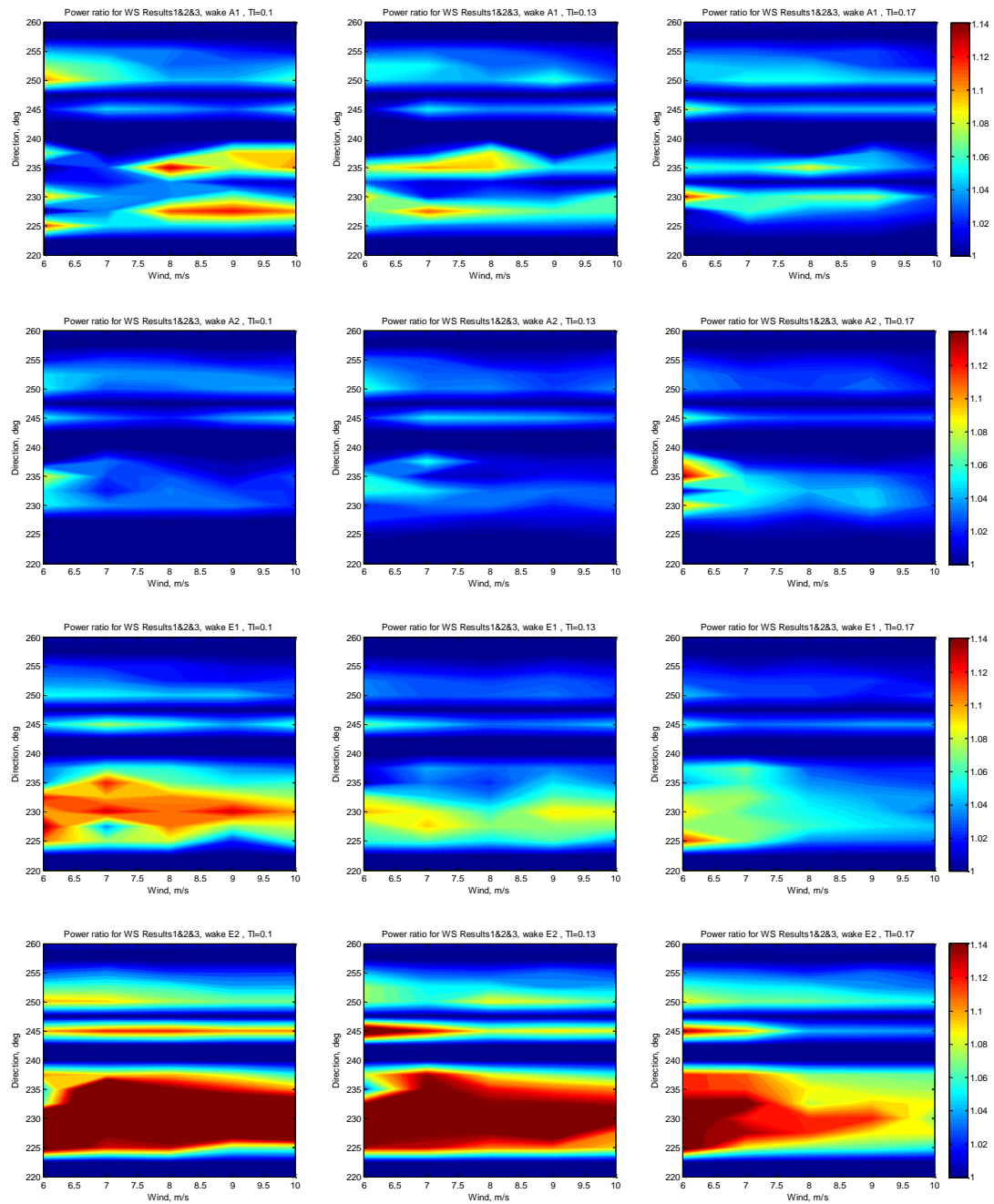


Figure 7.5: Power ratios for wake steering at 10%, 13% and 17% turbulence. Wake model A1 (top), A2, E1 and E2 (bottom). Note that the colour scaling is up to 1.14, appropriate for the first three rows, but in the E2 case, the dark red areas contain power ratios exceeding 1.3.

Figure 7.5 shows the power ratios achieved in the steady state with the different wake models at 10%, 13% and 17% turbulence. Wake model E2 gives by far the greatest power ratios (up to 1.3). The wake deflections are effectively twice as great as in model E1, and this is reflected in more than double the power increase. The wake steering is effective in several direction bands, but especially around  $220^\circ - 240^\circ$ , across the whole wind speed range, and even at the higher turbulence levels.

Yaw setpoints for the four controlled turbines are shown in Figure 7.6. As before, the line styles show turbulence intensity, with all wind speeds plotted, and the colours show the different wake models. The thick coloured lines show averages over wind speeds and turbulence intensities for each wake model, and the thick black line is an average over all wake models. The patterns appear to be rather more consistent than in the induction control case. Note that in some cases, positive and negative yaw setpoints seem almost equivalent, so when averaging, the mean absolute yaw offset is taken, with its sign set to the sign of the mean yaw offset. Furthermore, if the average setpoint for a particular direction has the opposite sign from its two neighbours, its sign is changed. Although these modifications will result in suboptimal steady-state performance, they are likely to perform better in a dynamic situation, avoiding frequent large reversals in yaw offset.

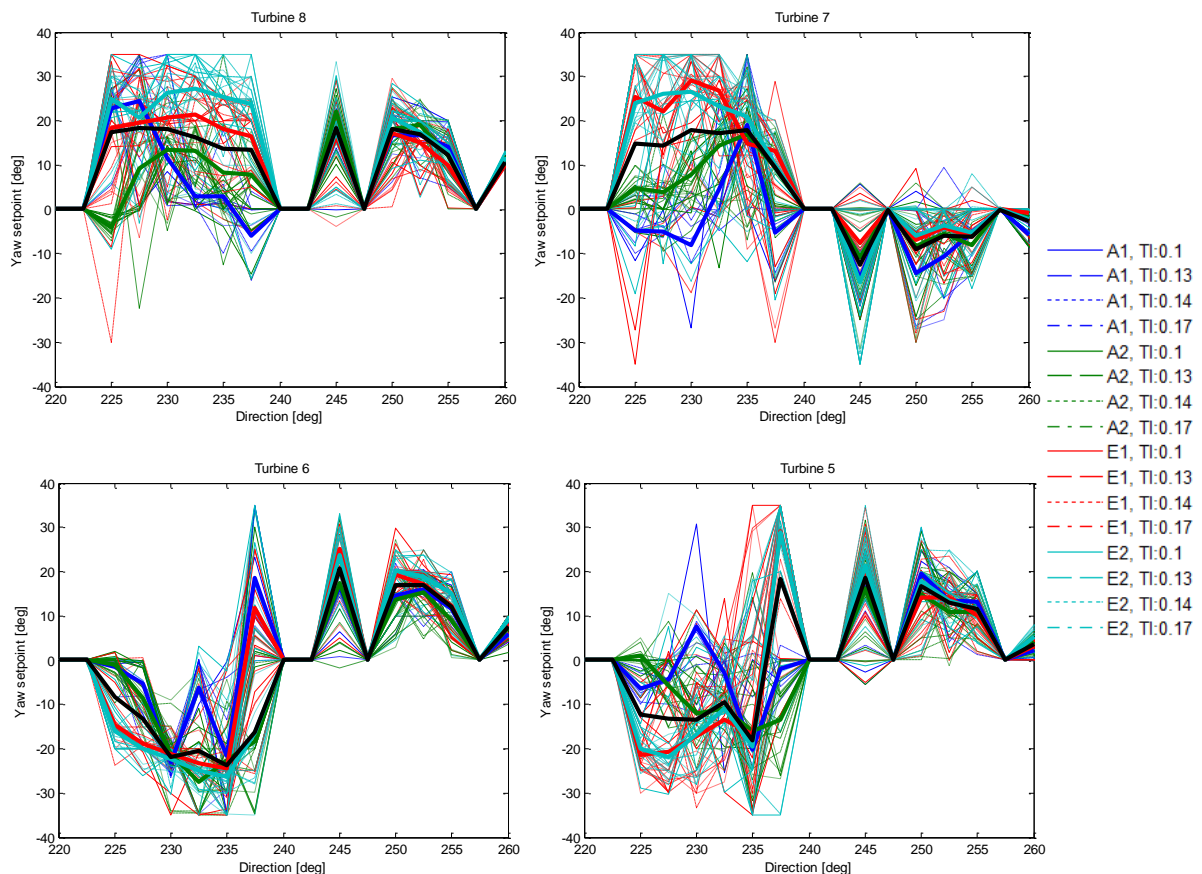


Figure 7.6: Yaw setpoints for the controlled turbines: #37, #36, #35, #34

A further possible modification to the yaw setpoints is to introduce directional smoothing, to allow for the uncertainty in wind direction measurement. (This could also be done for induction control setpoints, but the averaged setpoint curves in that case are already smoother than in the wake steering case.) As an example, Figure 7.7 shows the yaw setpoints as in Figure 7.6 but with directional smoothing applied corresponding approximately to a directional uncertainty with a standard deviation of  $2.12^\circ$ .

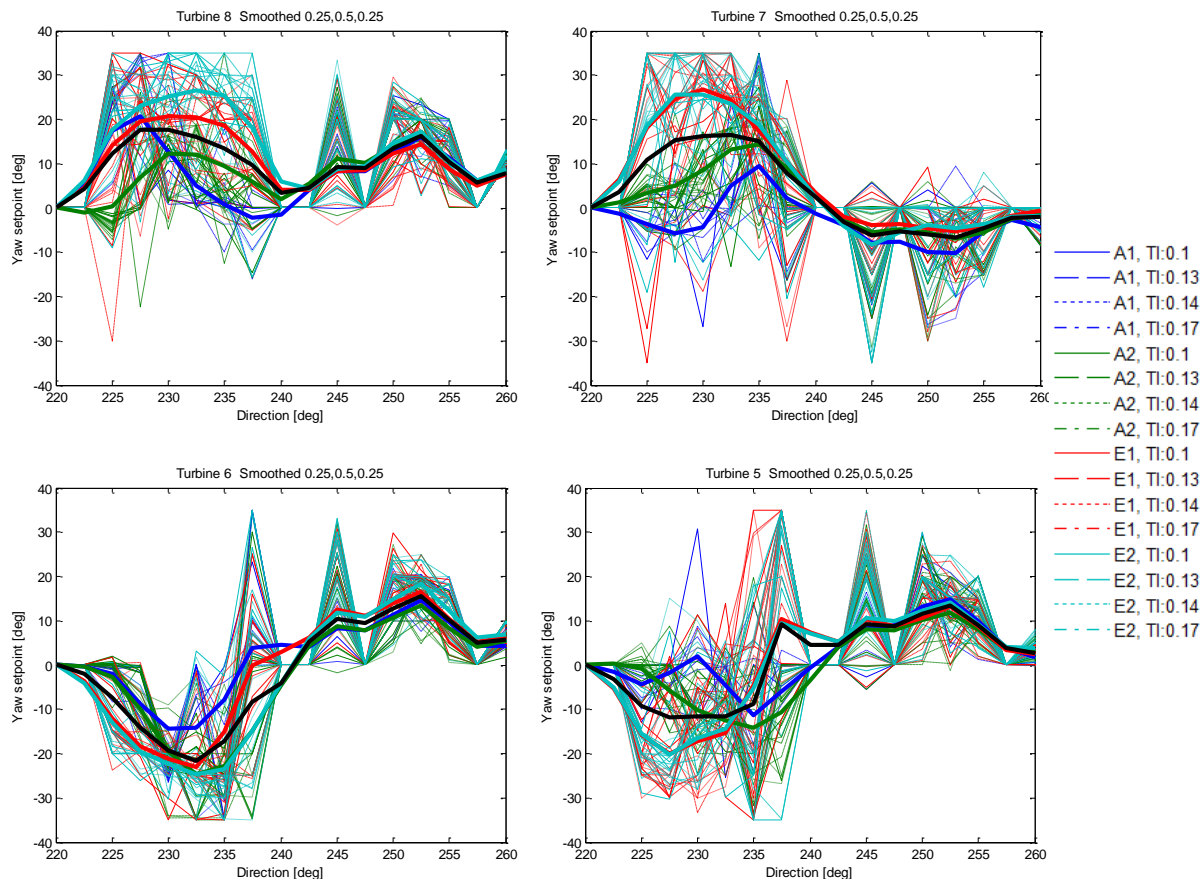


Figure 7.7: Yaw setpoints for the controlled turbines: #37, #36, #35, #34 with directional smoothing applied

An alternative is for the uncertainty in wind conditions to be taken into account as part of the optimisation calculation. This 'robust optimisation' produces setpoints which are optimal for a distribution of wind conditions around the bin centres, rather than for the exact bin centre conditions. The optimisation will be much slower of course, depending on how many samples are taken around the bin centres. Using the bin centre optimisations and then smoothing the setpoints afterwards, as illustrated above, has an advantage in that the degree of smoothing can be varied in real time, as the uncertainty in the wind conditions changes.

#### 7.4.3 Joint setpoint optimisations

In the general case, depending on the layout, there may be conditions in which the optimal performance is obtained with a combination of power reduction setpoints and yaw offsets, in other words using a combination of wake steering and induction control. Simply by including both sets of setpoints in a single setpoint vector for optimisation, *LongSim* is capable of jointly optimising all the setpoints. An example of such joint optimisation was reported in [10]. Such an optimisation has not been carried out for Sedini however, partly because the relevant turbine information was not provided (i.e. the power and thrust curves as a function of both the power reduction setpoint and the yaw misalignment), and because the field test program would not allow for the testing of such a joint control strategy.

#### 7.4.4 Behaviour around cut-in wind speed

During the optimisation of setpoints in low wind speed conditions, it is important to consider the turbine supervisory control behaviour around the cut-in wind speed. Even at ambient wind speeds a little above cut-in, some of the more wake-affected turbines may not be producing any power. If these turbines are effectively idling, they will not produce a significant wake; however, if these turbines are still rotating at significant speed, their thrust coefficients may still be quite large, and they may therefore still have a significant waking effect on other turbines. For the optimisation to work correctly, therefore, it is important to specify what the thrust coefficient will be for turbines which are not producing power. If wind conditions change slowly and turbines producing zero power rapidly feather to idling mode, the optimisation should assume a small thrust coefficient for these turbines. However, if wind conditions are changing more rapidly compared to the time taken for the supervisory controller to decide to switch to idling mode, then the thrust coefficient will be much higher, and the optimisation should take this into account. In the absence of detailed information regarding supervisory control actions for the Sedini turbines, the above optimisations have assumed an intermediate thrust coefficient of 0.3 for turbines producing zero power.

### 7.5 Dynamic control algorithm implementation

The smoothed and 'tolerant' set-point look-up tables calculated as above were incorporated into a dynamic wind farm control algorithm, as described in this section. The resulting wind farm control algorithm was then tested using realistic time-domain simulations as described in Section 7.6.

Firstly, the wind conditions are determined. In this case, turbine #38 is used to define the wind speed, direction and turbulence intensity at any point in time. The wind speed estimation algorithm used in the turbine controller could be implemented in the simulation, but as details of the actual algorithm were not available, the actual rotor-average wind speed has been used directly. In practice a wind speed estimator will have some error and some lag, but since this is then filtered, it is not important to model the estimation errors, as long as any bias error is small. Random estimation errors, including bias, can of course be introduced into the simulation, but this has not been done in this case.

The wind direction estimate is made up of the measured nacelle position plus the measured wind vane signal. Once again, measurement errors could be introduced into the simulation, but this was not done as no sensor accuracy information was provided.

For the turbulence intensity, a perfect estimate has again been assumed. In practice, the variations in estimated wind speed over each period could be used to estimate turbulence intensity, with a correction for higher frequencies based on an assumed turbulence spectrum.

The loss of performance which can be expected due to imperfect estimation of wind conditions are to some extent taken into account in the smoothing of the look-up tables. Uncertainties in wake modelling probably have a much greater effect.

As mentioned, the wind condition indicators (speed, direction and turbulence) are then filtered. A first-order filter with a time constant of 60s has been used. This value was chosen to match the wind farm controller time step to be used at Sedini, and also because the required wind condition is meant to be an average over all the turbines, and it takes time for wind conditions measured at turbine #38 to propagate to the middle of the set of controlled turbines. At 8m/s for example, the 60s time constant corresponds to an averaging distance of 480m – compare with Figure 7.1. Repeat simulations with different filter time constants could be used to tune this value for best performance. The time constant could also be made to vary, so that it corresponds to the same distance at any wind speed.

The filtered wind conditions are used with the look-up tables to find the current set-points for each turbine. The set-points are updated every minute, since this is the update time to be implemented at Sedini for these tests; but as for the filter time constant, repeat simulations could be used to select the best update time.

Power reduction setpoints are then applied at each turbine without significant delay in the case of induction control. For wake steering, yaw offset demands are also sent to each turbine without delay, but then the way in which these offsets interact with the turbine yaw control algorithm has to be modelled correctly, since this could have a significant impact on the effectiveness of the wake steering control. The turbine yaw control is assumed to continue operating as normal, but with the yaw offset simply applied to the wind vane signal before it is processed by the yaw control logic.

A different approach to yaw control, in which the turbine yaw controllers are over-ridden by a nacelle position command calculated centrally by the wind farm controller by adding the offset to the estimated wind direction, has also been simulated. This gives improved performance, but it was not practical to implement this at Sedini in the context of this project.

## 7.6 Dynamic time-domain simulation testing with LongSim

Dynamic simulations were carried out using LongSim, with and without the wind farm controllers for induction control and wake steering described above, so that the benefits could be evaluated. The simulations used a correlated stochastic wind field covering the turbines, generated by LongSim from measured met mast data. The results were evaluated in terms of power output and, in the case of wake steering, the yaw actuator duty.

### 7.6.1 Wind field

The technique for generating the correlated wind field has been described in [2]. The 10-minute average historical met mast data was inspected, and a period selected where the wind speeds and directions were varying over a range suitable for exercising the wind farm control. This time history was assumed to apply at a point in the middle of the row of turbines, and higher-frequency synthetic turbulence was added at that point, and also at a grid of points covering all the turbines, using assumed coherence properties, so that variations across the wind farm are realistically correlated, spatially and in time.

Figure 7.8 illustrates the variations in wind speed, direction and turbulence during the two-hour period selected for the particular set of simulations described here.

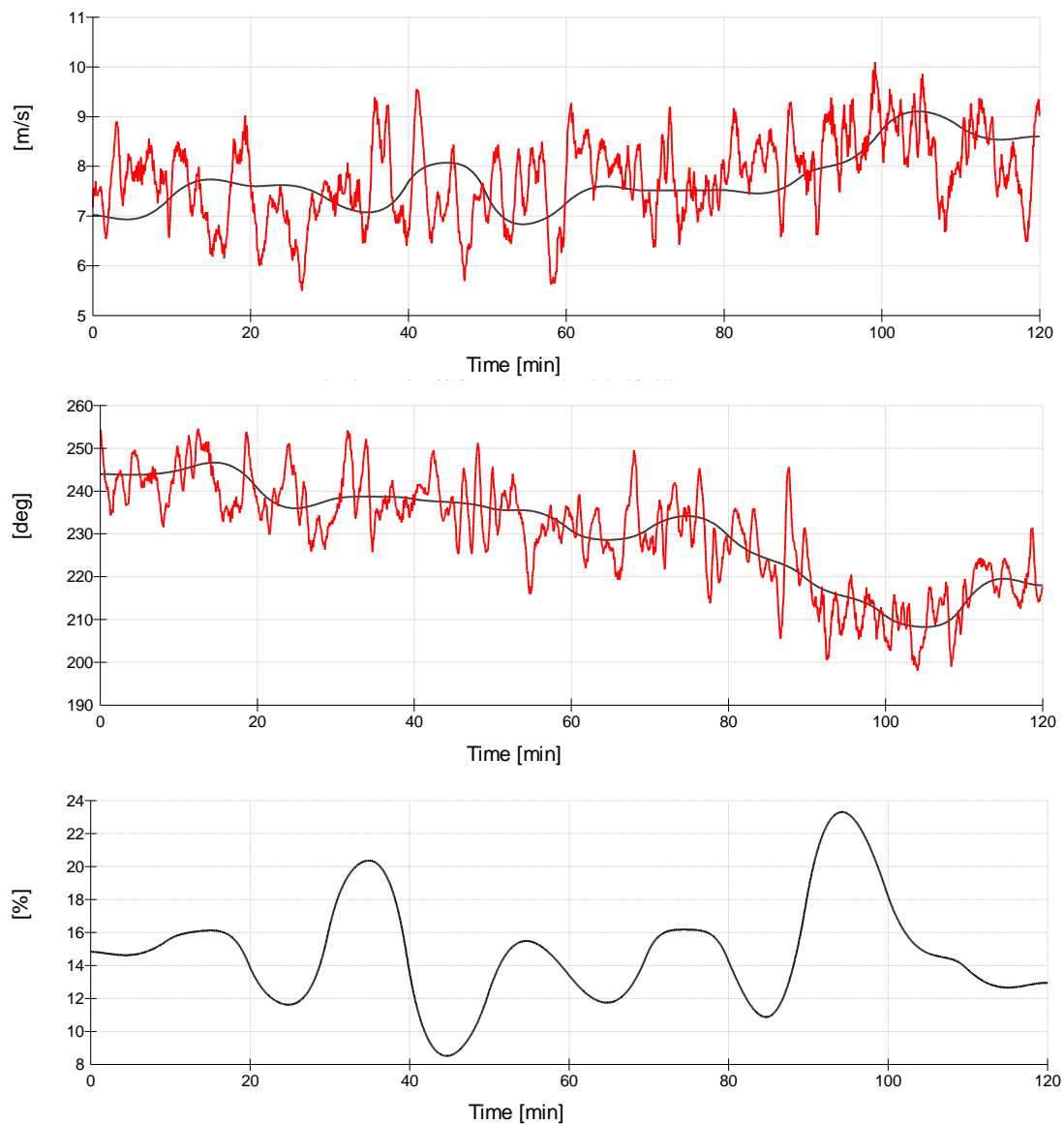


Figure 7.8: Wind conditions for the simulation test. Wind speed (top), direction (middle) and turbulence intensity (bottom). The black lines are smoothed 10-minute met mast data, and the red lines are the rotor average wind speed and direction at turbine #38, showing the synthetic turbulence from that point in the wind field.

#### 7.6.2 Yaw control

One aspect of the turbine supervisory control which it is important to simulate correctly is the yaw control, especially in the case of wake steering since the turbine yaw logic could have a significant impact on the effectiveness of this type of wind farm control.



The yaw logic used by the Sedini turbines is proprietary, but was made available to DNV GL for the purposes of the CL-Windcon project, and was implemented in the turbine description used for the LongSim simulations. A typical example of the simulated yaw control response is shown in Figure 7.9.

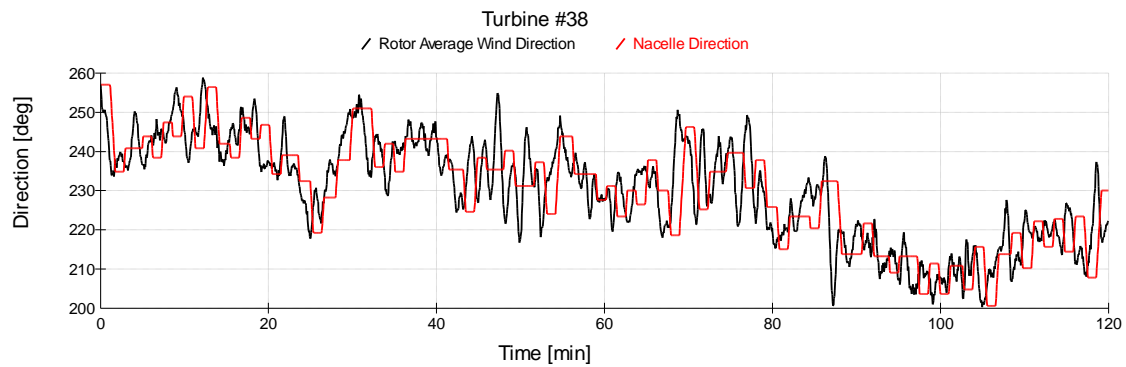


Figure 7.9: Typical simulated yaw control response.

### 7.6.3 Induction control results

The following set of time-domain simulations have been run for illustration:

Wake model used in the simulation	Wake model used for setpoint optimisation	Further processing of setpoints	Run name
A1	-	-	Base_A1
A1	A1	-	IC_A1_A1
A1	Average of A1,A2,E1	Averaged over wind speeds and turbulence intensities	IC_A1_Ave
-	A1	-	QS_IC_A1
A2	-	-	Base_A2
A2	A2	-	IC_A2_A2
A2	Average of A1,A2,E1	Averaged over wind speeds and turbulence intensities	IC_A2_Ave
-	A2	-	QS_IC_A2
E1	-	-	Base_E1
E1	E1	-	IC_E1_E1
E1	Average of A1,A2,E1	Averaged over wind speeds and turbulence intensities	IC_E1_Ave
-	E1	-	QS_IC_E1

Table 7.1: Induction control cases simulated

In each case, the results with induction control are compared to the base case for the same wake model without induction control – see Table 7.2. The run names beginning with QS are not from dynamic simulations – they are ‘quasi-static’ results obtained by interpolating the power increases from the steady-state optimisations using the actual simulation wind conditions (see Figure 7.8), point by point.



Run name	Power increase compared to base case
IC_A1_A1	0.13%
IC_A1_Ave	0.09%
QS_IC_A1	1.41%
IC_A2_A2	0.36%
IC_A2_Ave	0.02%
QS_IC_A2	0.76%
IC_E1_E1	1.23%
IC_E1_Ave	1.59%
QS_IC_E1	0.96%

Table 7.2: Power increases from induction control in dynamic simulations

The results are quite variable. In keeping with the steady-state results of Section 7.4.1, wake model A1 gives the best quasi-static result, but the dynamic simulation gives less than one tenth of the benefit. If the averaged setpoints are used, the result is worse. Wake model A2 produces the worst quasi-static result, but performs significantly better in the dynamic simulations, achieving about half of the quasi-static gain, although if the averaged setpoints are used the gain is virtually zero. Wake model E1 produces the best dynamic simulation results, which even exceed the quasi-static result, and if the averaged setpoints are used, the result is even better.

The variability of these results suggests that longer simulations are probably needed in order to obtain more reliable comparisons, and this is desirable in any case to cover a wider range of wind conditions. Nevertheless, these short sample simulations already indicate that some gains may be expected from induction control even when the dynamic effects are taken into account.

Some sample time-domain results for the best case (IC\_E1\_Ave) are presented for illustration in Figure 7.10. The differences in total wind farm power compared to the base case and the quasi-static result are subtle, sometimes slightly positive and sometimes slightly negative. Setpoint time histories are shown at four of the turbines. The actual power at the most upstream controlled turbine, #37, is reduced because of the power reduction setpoints, but the resulting power increase at the next turbine is quite apparent (this turbine also has some setpoint reductions, but the power increases overall because of the high wind speed).

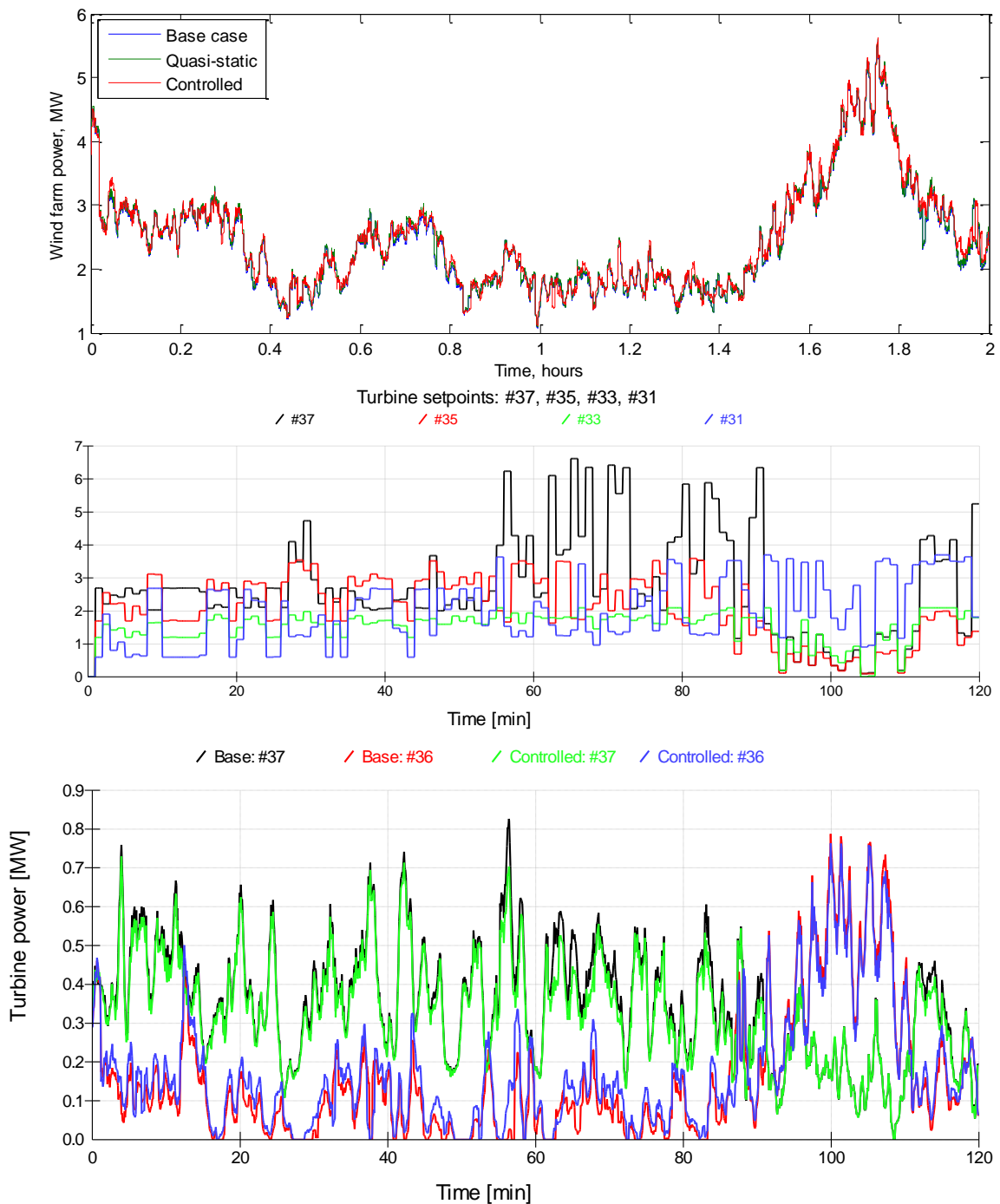


Figure 7.10: Sample dynamic simulation results – case IC\_E1\_Ave.

Top: Wind farm power (red) compared to base case and quasi-static result.

Middle: example power reduction setpoints at four turbines.

Bottom: Turbine power compared to base case, at two turbines

#### 7.6.4 Wake steering control results

Still using the same wind conditions, the following set of time-domain simulations with wake steering have been run for illustration:

Wake model used in the simulation	Wake model used for setpoint optimisation	Further processing of setpoints	Run name
A1	-	-	Base_A1
A1	A1	-	WS_A1_A1
A1	Average of A1,A2,E1,E2	Averaged over wind speeds and turbulence intensities	WS_A1_Ave
-	A1	-	QS_WS_A1
A2	-	-	Base_A2
A2	A2	-	WS_A2_A2
A2	Average of A1,A2,E1,E2	Averaged over wind speeds and turbulence intensities	WS_A2_Ave
-	A2	-	QS_WS_A2
E1	-	-	Base_E1
E1	E1	-	WS_E1_E1
E1	Average of A1,A2,E1,E2	Averaged over wind speeds and turbulence intensities	WS_E1_Ave
-	E1	-	QS_WS_E1
E2	-	-	Base_E2
E2	E2	-	WS_E2_E2
E2	Average of A1,A2,E1,E2	Averaged over wind speeds and turbulence intensities	WS_E2_Ave
E2	Average of A1,A2,E1,E2	Averaged over wind speeds and turbulence intensities, with directional smoothing	WS_E2_AvSm
As WS_E2_E2 but with central yaw control			WS_E2_E2_CY
-	E2	-	QS_WS_E2

Table 7.3: Wake steering control cases simulated

As for the induction control cases, the mean power from each of the wake steering cases is compared to the appropriate base case, and also to the ‘quasi-static’ result obtained by interpolating the power increases from the steady-state optimisations using the actual simulation wind conditions (run names beginning with QS). The power increases are shown in Table 7.4, which also summarises the change in the yaw system duty caused by the wake steering control.

For this row of turbines, the wake steering results show larger and more consistent power increases than the induction control results. The power increases would presumably be even larger if wake steering could be applied to more of the turbines: here only four turbines are controlled compared to seven in the induction control case; and in both cases, the increase would presumably be larger still if control were also applied to the first turbine, #38, rather than keeping it in baseline operation as a way of measuring the incident wind.

Run name	Change compared to base case		
	Power increase	Yaw manoeuvres	Total yaw travel
WS_A1_A1	0.29%	-6.2%	8.4%
WS_A1_Ave	0.38%	-4.1%	10.3%
QS_WS_A1	1.48%	n/a	n/a
WS_A2_A2	0.40%	-5.2%	10.3%
WS_A2_Ave	0.35%	-4.1%	10.3%
QS_WS_A2	1.00%	n/a	n/a
WS_E1_E1	1.38%	-7.1%	11.4%
WS_E1_Ave	1.44%	-4.1%	10.3%
QS_WS_E1	1.35%	n/a	n/a
WS_E2_E2	2.55%	-7.1%	12.4%
WS_E2_Ave	2.25%	-4.1%	10.3%
WS_E2_AveSm	2.31%	-1.4%	8.7%
WS_E2_E2_CY	3.29%	-20.3%	-2.5%
QS_WS_E2	3.02%	n/a	n/a

Table 7.4: Power increases from wake steering in dynamic simulations

Table 7.4 also shows a significantly greater benefit with the wake deflection assumptions of the EPFL model, and particularly if the wake deflection is effectively doubled as in model E2 (not surprisingly).

The results using averaged setpoints are typically similar to using the ‘pure’ setpoints for each wake model, and sometimes actually give a slight improvement, perhaps because of reduced sensitivity to changing wind conditions. Comparing WS\_E2\_Ave against WS\_E2\_AveSm also indicates that directional smoothing can be slightly beneficial.

Finally, comparing WS\_E2\_E2 against WS\_E2\_E2\_CY shows that if it were possible to use centralised yaw control (see Section 7.5), overriding each turbine’s yaw control logic with a nacelle position demand from the wind farm controller, a significant further improvement is possible. In this case, the difference between the nacelle position demand and the actual nacelle position is integrated, and whenever the integrated error in radians reaches  $\pm 5$ s (i.e. 5 radian-seconds, or 4.77 degree-minutes) the turbine yaw drive is switched on until the error returns to zero. An example of how this works is shown in Figure 7.11 for turbine #37. The nacelle position is compared against the demanded position, and also against the nacelle position in the base case, and in the wake steering case using the turbine’s normal control logic.

Looking at the yaw duty, in most cases the wake steering causes an increase in total yaw travel of the order of 10% (averaged across all 9 turbines, of which only four are controlled), although the number of yaw manoeuvres actually decreases. Using the directionally-smoothed setpoints has a beneficial effect on the yaw duty as well as on the power increase. The central yaw control strategy is particularly beneficial: as well as giving the greatest power increase, it reduces yaw manoeuvres by 20%, and the total yaw travel is actually reduced by 2.5% compared to the base case.

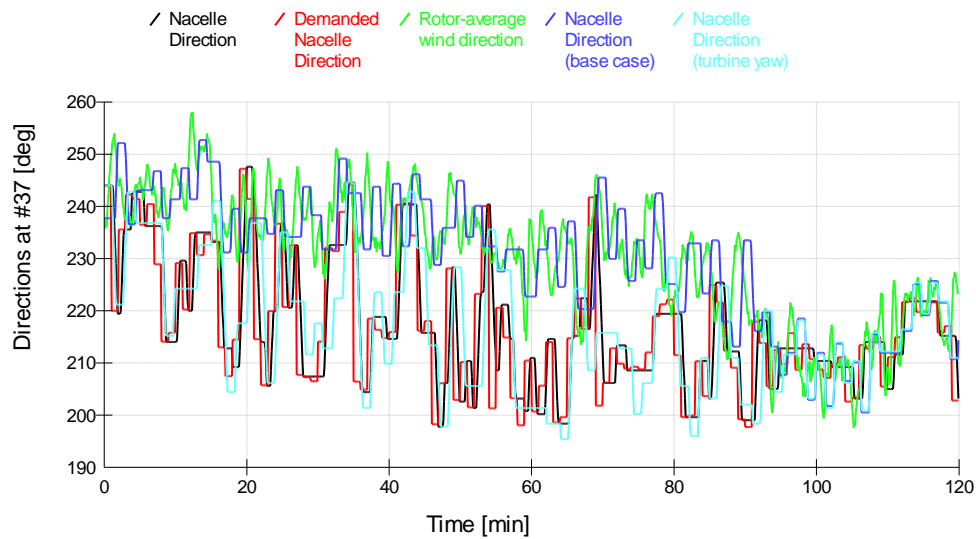


Figure 7.11: Effect of central yaw control – turbine #37.

More sample time-domain results for the best case (WS\_E2\_E2\_CY) are presented for illustration in Figure 7.12. As before, the differences in total wind farm power compared to the base case and the quasi-static result are sometimes slightly positive and sometimes slightly negative. Time histories of the yaw offsets at the four controlled turbines are shown in the middle plot. In the lower plot, the actual power at the most upstream controlled turbine, #37, is reduced because of the yaw offsets, but the effect on the power of the next turbine is generally positive.

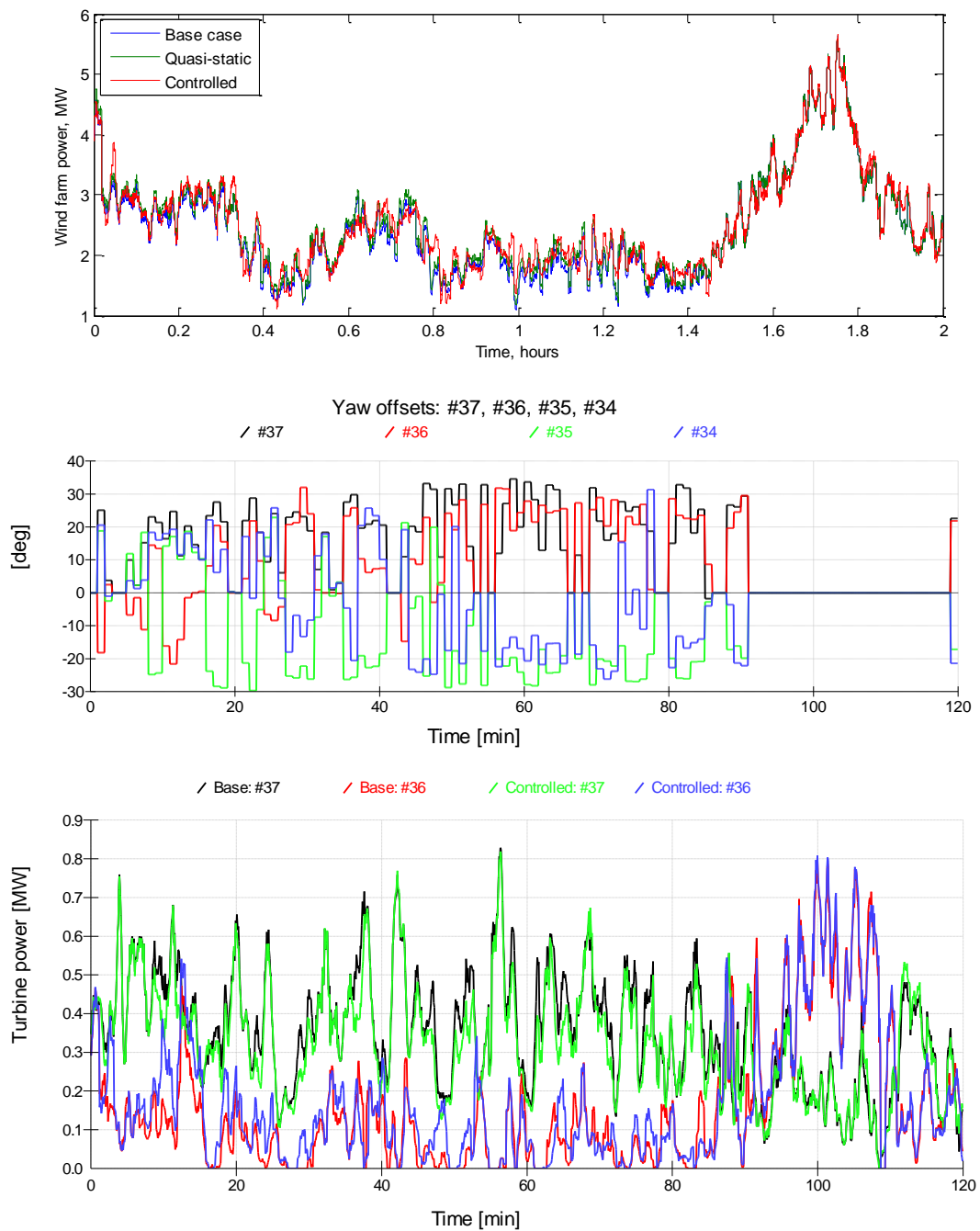


Figure 7.12: Sample dynamic simulation results – case WS\_E2\_E2\_CY.  
 Top: Wind farm power (red) compared to base case and quasi-static result.  
 Middle: yaw offsets at the four controlled turbines.  
 Bottom: Turbine power compared to base case, at two turbines

## 7.7 Conclusions

This chapter has demonstrated the use of the engineering code LongSim for the design and simulation testing of wind farm controllers, both induction control and wake steering control. It has been used to generate complete implementable wind farm controllers, and to test them in realistic dynamic simulations to evaluate performance and build confidence, ready for the field testing to be carried out at Sedini.

LongSim has been used to generate optimal set-point tables in the context of quasi-static open-loop wind farm control. Considerable uncertainties in wake modelling remain, so controllers have been generated with different wake assumptions. Furthermore, controllers generated with some wake assumptions have then been tested against different assumptions, to build confidence that gains can be achieved despite wake modelling uncertainties. Various ways have been investigated for making the setpoint tables more robust to uncertainties in wind conditions and wake effects.

LongSim has further been used to carry out time-domain simulations of these controllers in realistic time-varying conditions, to evaluate their performance in the face of many real-world effects, uncertainties and imperfections which the model is able to simulate. It also allows additional dynamic aspects of the control strategy to be developed and optimised, such as sampling intervals, filter parameters, estimation of wind conditions, and the way in which setpoints are actually implemented, including the effect on yaw actuator duty. For example, the benefits of a centralised yaw control strategy have been clearly demonstrated.

This has provided a new level of confidence in the ability of such controllers to achieve desired performance improvements in real life. Controllers generated and tested in this way can be considered ready for implementation and field testing on the Sedini wind farm.

The actual field tests on this row of turbines at Sedini will now consist only of induction control, since the yaw sensor upgrades required for the originally-planned wake steering tests unfortunately had to be abandoned. Before the start of the tests, LongSim will be used again to carry out final set-point optimisations using the most recent wake modelling improvements based on site SCADA measurements, and to run a final set of dynamic simulation tests. This will be reported in the Work Package 3 deliverables.

## References

- [1] [https://github.com/WISDEM/Ref\\_Turbines/tree/6ee8df1f6d7de0a9841d006c4139d25121bd0e1e/WindPACT](https://github.com/WISDEM/Ref_Turbines/tree/6ee8df1f6d7de0a9841d006c4139d25121bd0e1e/WindPACT)
- [2] Description of the reference and the control-oriented wind farm models, CL-Windcon deliverable D1.2, 30<sup>th</sup> April 2018, [www.clwindcon.eu](http://www.clwindcon.eu).
- [3] Definition of field-testing conditions, CL-Windcon deliverable D3.2, 31<sup>st</sup> October 2017, [www.clwindcon.eu](http://www.clwindcon.eu).
- [4] Ainslie J F 1988 Calculating the flowfield in the wake of wind turbines J. Wind Engineering and Industrial Aerodynamics 27.
- [5] Jiménez A, Crespo A and Migoya E 2010 Application of a LES technique to characterize the wake deflection of a wind turbine in yaw Wind Energy, 13-6:559–572, 2010.
- [6] Gebraad P M O 2014 Data-driven wind plant control PhD Thesis (T U Delft).
- [7] Experimental and theoretical study of wind turbine wakes in yawed conditions”, Majid Bastankhah and Fernando Porté-Agel, J. Fluid Mech. (2016), vol. 806, pp. 506-541.
- [8] <https://floris.readthedocs.io/en/develop/>
- [9] [https://en.wikipedia.org/wiki/Simplex\\_algorithm](https://en.wikipedia.org/wiki/Simplex_algorithm)
- [10] “Combining induction control and wake steering for wind farm energy and fatigue loads optimisation”, E. Bossanyi, Proc. Torque from Wind conference, Milan 2018, (IOP proceedings).



## 8 DATA-DRIVEN EMPC FEEDBACK WIND FARM CONTROL

In [55, Chap. 3] a feedback wind farm control concept based on data driven modeling and economic model predictive control (EMPC) has been developed and it was tested in [56, Part IV].

The objective was to maximize the wind farm power. The measurements used were standard measurements from a wind turbine i.e. power, pitch and generator speed. The actuator was relative derating of the wind turbine as described in [26]. The control model was data driven multi-variable auto regressive model with derating input (MARX). The control method selected was economic model predictive control (EMPC) [27].

The main motivation for the data driven model approach is that wake modeling is complicated and may be less accurate in real terrain perhaps with hills and forest. The idea is that the recursive estimation used for the MARX model potentially can account for all this.

For high excitation of turbine derating in the range between 0 and 0.5 the MARX model estimation worked well. The wind speed and turbine power prediction was promising for horizon up to half an hour. However, for excitation expected from static analysis in the range from 0 to 0.05 the MARX parameter uncertainty was too large. Consequently this particular approach is not suggested for further testing. This does of course not rule out other data driven approaches based on other model structures and/or parameter estimation methods. However, induction control only is probably not the right way to go. It should at least be combined with wake redirection control. This is also supported by other results within CL-Windcon [55, 56, 24].

## 9 LOAD-MINIMIZING ACTIVE POWER CONTROL FOR WIND FARMS

This chapter is concerned with the usage of axial induction control for two objectives, being active power control (electricity grid integration) and structural load mitigation. This chapter stands in contrast with previous chapters which were predominantly focused on power maximization.

### 9.1 Introduction

As the participation of renewable energy sources in the electricity network increases, there is a strong need for these energy sources to provide ancillary services to the electricity grid. Therefore, the field of *active power control* has largely focused on having wind turbines and wind farms produce a prespecified amount of power, or even have them track a reference power signal to deal with fluctuations in the electricity consumption on the grid. In practice, this means that wind turbines purposefully produce less energy than they could in theory extract to follow this prescribed reference signal.

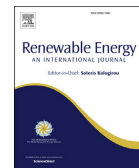
This chapter is concerned with an active power control solution. Moreover, this control algorithm includes a secondary objective being load minimization. Additionally, this work includes techniques of yaw-based wake steering for power maximization, as described earlier throughout this deliverable, to maximize the power production when necessary.

### 9.2 Methodology

When it comes to active power control in wind farms, the question arises which turbines to derate, and by how much. As there are plethora of derating possibilities, this allows the introduction of a secondary objective for active power control in wind farms. The most straight-forward secondary objective is load minimization, explored in this chapter.

Moreover, if the demanded power signal is higher than the available power that *can possibly* be extracted from the wind farm at this moment in time, then yaw-based wake steering can be used to increase the total power produced by the wind farm, and further reduce or eliminate the power tracking error.

A control solution is synthesized combining these components, yielding a load-minimizing active power control solution that additionally leverages yaw-based wake steering for power maximization, when necessary. This work has been published as an open-access article in the Elsevier Renewable Energy journal [15]. This article is presented in the remainder of this chapter.



# A constrained wind farm controller providing secondary frequency regulation: An LES study

S. Boersma<sup>a,\*</sup>, B.M. Doekemeijer<sup>a</sup>, S. Siniscalchi-Minna<sup>b</sup>, J.W. van Wingerden<sup>a</sup>

<sup>a</sup> Delft University of Technology, Delft Center for Systems and Control, Mekelweg 2, 2628 CC Delft, the Netherlands

<sup>b</sup> Catalonia Institute for Energy Research, IREC, Jardins de le Dones de Negre, S/n, Barcelona, Spain



## ARTICLE INFO

### Article history:

Received 1 June 2018

Received in revised form

8 September 2018

Accepted 8 November 2018

Available online 19 November 2018

### Keywords:

Active power control

Closed-loop wind farm control

Model predictive control

Wake redirection control

## ABSTRACT

Active power control for wind farms is needed to provide ancillary services. One of these services is to track a power reference signal with a wind farm by dynamically de- and uprating the turbines. In this paper we present a closed-loop wind farm controller that evaluates 1) thrust coefficients on a seconds-scale that provide power tracking and minimize dynamical loading on a farm level and 2) yaw settings on a minutes-scale that maximize the possible power that can be harvested by the farm. The controller is evaluated in a high-fidelity wind farm model. A six-turbine simulation case study is used to demonstrate the time-efficient controller for different controller settings. The results indicate that, with a power reference signal below the maximal possible power that can be harvested by the farm with non-yawed turbines, both tracking and reduction in dynamical loading can be ensured. In a second case study we illustrate that, when a wind farm power reference signal exceeds the maximal possible power that can be harvested with non-yawed turbines for a time period, it can not be tracked sufficiently. However, when solving for and applying optimized yaw settings, tracking can be ensured for the complete simulation horizon.

© 2018 The Authors. Published by Elsevier Ltd. This is an open access article under the CC BY license (<http://creativecommons.org/licenses/by/4.0/>).

## 1. Introduction

The trend towards clean energy is irreversible [1]. A large part of the clean energy we are currently generating is harvested by wind farms that extract energy from the wind [2]. A wind farm is a collection of wind turbines placed in each other's proximity to, *i.e.*, reduce maintenance and electricity cabling costs. However, a wake develops downstream of each turbine, which is a region that is characterized by a flow velocity deficit and an increased turbulence intensity [3]. Since wind turbines are placed together in a farm, the wakes of upstream turbines influence the performance of downstream turbines. For example, the flow velocity deficit influences the power production of downstream turbines [4] while an increased turbulence intensity will increment the turbine's fatigue loads as suggested in Refs. [5,6], which possibly can reduce the turbine's lifetime. The objective of wind farm control is to reduce the leveled cost of wind energy by intelligently operating the turbines inside the farm. Subgoals may include the increase of the farm-wide power generation, the reduction of turbine fatigue, and

the integration of energy from wind farms with the electricity grid. This integration is related to the provision of ancillary services. One example is secondary frequency regulation (a subclass of active power control) in which the objective is to have the wind farm's power generation track a power reference signal generated by transmission system operators, during a time span of several minutes [7]. We call this power tracking and turbines need to increase and decrease their power output during this time span such that tracking at a farm level is ensured. Since the power reference signal is below the maximum possible power that can be harvested, the tracking problem has multiple solutions. For example, one could uprate the downstream turbines while derating the upstream turbines or the other way around while generating an equal amount of power with the farm. It is therefore possible and necessary to add, besides tracking, another performance measure, such as the decrease of load variations over time (dynamical loading) on the turbines and/or the increase of available power in the farm (see *e.g.*, [8]). Two actuation methods to ensure these objectives are axial induction and wake redirection control. In the former, generator torques and pitch angles or thrust coefficients are utilized as control variables while in the latter, the yaw angles are utilized as control variables [9].

\* Corresponding author.

E-mail address: [s.boersma@tudelft.nl](mailto:s.boersma@tudelft.nl) (S. Boersma).

<https://doi.org/10.1016/j.renene.2018.11.031>

0960-1481/© 2018 The Authors. Published by Elsevier Ltd. This is an open access article under the CC BY license (<http://creativecommons.org/licenses/by/4.0/>).

Results that provide power tracking using axial induction actuation can be found in Refs. [10–14]. More precisely [10], proposes a wind farm tracking solution that additionally reduces the turbine's tower and shaft bending moments. This controller utilizes turbine models to illustrate the controllers effectiveness, but is not tested in a wind farm simulation model. It is therefore uncertain whether the proposed solution works in a wind farm model. Then in Refs. [11,12], the authors each propose a different wind farm power tracking solution while minimizing the axial force exerted by the flow on the turbines. However, as stated in Ref. [6], the dynamical turbine loading is a better measure of fatigue than static turbine loading. In Ref. [13], the authors propose a distributed controller providing tracking while minimizing variation in the axial force that is exerted by the turbine on the flow. In Ref. [14], besides tracking, a power reference distribution among the turbines is also found by the controller that maximizes the available power in the farm. The work presented in Ref. [15] demonstrates an optimization algorithm that provides power tracking while minimizing the added turbulence intensity. However, all the above proposed controllers except for [10] are tested in a simplified wind farm model [16], keeping the question open if similar results can be obtained when a more realistic dynamical wind farm model, such as a Large-Eddy Simulation (LES) based wind farm model, is utilized. The authors in Ref. [17] propose a tracking controller that contains a simplified wind farm model to evaluate control signals and the controller is tested in a simplified wind farm model. In this work, no additional objectives are considered and also, it remains questionable if the proposed controller will give similar results when tested in a more realistic simulation environment. A controller that is tested in an LES based wind farm model and employs axial induction actuation providing power tracking can be found in Ref. [18]. The therein solved optimization problem contains dynamical wake and turbine models, but the only objective is tracking and no constraint regarding, e.g., dynamical loading is included. Additionally, it is questionable if the controller can evaluate control signals within one second, which makes the proposed method not suitable for control on a seconds-scale. The controller presented in Ref. [19] is also tested in an LES, but no wake model nor constraints were taken into account. The controller provides tracking and the wind farm power reference signal is distributed heuristically among the turbines without taking any measure of fatigue into account.

Time-varying yaw actuation has, to the best of our knowledge, yet to be employed in power tracking. However, this wake actuation method is utilized for the maximization of wind farm power generation in LES based simulations [20,21], a wind tunnel [22] and in a field test experiment [23].

From the above, we conclude that results obtained with a closed-loop controller that provides power tracking and dynamical load minimization in an LES based wind farm model and additionally increases the available wind farm power using yaw actuation are not yet available in current literature.

Therefore, in this work, a closed-loop reference power tracking solution is proposed in which 1) thrust coefficients that provide wind farm power tracking while minimizing dynamical turbine loading are evaluated for every second with a constrained model predictive controller (MPC) and 2) yaw settings that increase the available wind farm power can be evaluated every fifteen minutes in the situation where the farm's power generation has to be close to or above its upper limit, in order to increase the range of power reference signals that can be tracked. The MPC employs a dynamical wind farm model that is updated according to optimized yaw settings and rotor-averaged flow velocities, and solves for a constrained optimization problem that finds a distribution of the thrust coefficients among the turbines accordingly. This is different with

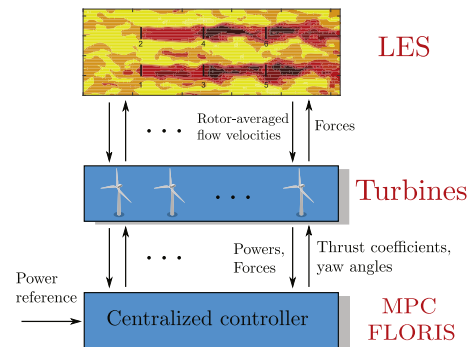


Fig. 1. Flowchart of the proposed control framework.

respect to the previous work presented in Ref. [24] where a control signal distribution is imposed. When doing so, it is not possible to change controller settings to have the controller find a control signal distribution among the turbines that reduces, i.e., dynamical turbine loading. In this work we investigate different controller settings and corresponding control signal distributions that minimize dynamical turbine loading. In addition to the MPC, if a reference will be above the maximum possible power extractable from the wind with zero yaw settings, the FLOW Redirection and Induction in Steady-state (FLORIS) tool [25] is employed to find optimal yaw settings that maximize the power that could be harvested from the wind with zero yaw settings. In addition to the proposed control strategy, another important contribution of this work is the controller evaluation in LES. For this, a software framework referred to as the PALM Supervisory Controller<sup>1</sup> is developed that allows for programming controllers in a controller friendly software environment and their evaluation in the PARallelized Large-eddy simulation Model (PALM) [26], an LES based wind farm model. Hence this work is more focused on controller evaluation in a more realistic wind farm flow model. The following enumeration summarizes the above described contributions:

1. A parameter-varying wind farm model is introduced, which can be employed in a time-efficient controller that provides power tracking.
2. A constrained time efficient closed-loop wind farm control approach is introduced.
3. Power tracking and dynamical loading are performance indices considered by the controller.
4. Axial induction and wake redirection control are employed both to ensure wind farm power tracking.
5. Online available software is developed that allows for advanced controller evaluation in a high-fidelity wind farm model.

The proposed framework is schematically depicted in Fig. 1.

This paper is organised as follows. In Section 2, the developed PALM Supervisory Controller is introduced and a brief explanation of the PALM itself is presented. Then in Section 3, a description of the employed surrogate models is given and in Section 4, the wind farm controller is formally introduced. Simulation results are presented in Section 5. More precisely, in section 5.3, results obtained

<sup>1</sup> The developed software package is available in the public domain: <https://github.com/TUdelft-DataDrivenControl/PALMSuperController>.

with different controller settings are compared and we show that these can influence the control signal distribution among the turbines. Consequences with respect to tracking behaviour and dynamical turbine loading are also presented. Then, in section 5.4, we illustrate the potential of including yaw actuation when power generation has to be close to or above its upper limit. This paper is concluded in Section 6.

## 2. Simulation model

The true wind farm is replaced by the high-fidelity “PARallelized Large-eddy simulation Model (PALM)” [26], because 1) a wind farm is not available and 2) in a high-fidelity model, controller settings can be compared under exactly equivalent atmospheric conditions, which is not possible in a real wind farm. PALM is programmed in FORTRAN, while almost all academic wind farm control algorithms are implemented in MATLAB or Python. One of the contributions of this work is the development of the PALM Supervisory Controller, which provides a communication interface between PALM and wind farm controllers implemented in MATLAB. This allows the straight-forward evaluation of such control algorithms in a high-fidelity simulation environment. In section 2.1, a brief summary of PALM is given. Then in section 2.2, the PALM Supervisory Controller is introduced and in section 2.3, the specific controller implementation used throughout this work is given.

### 2.1. The PARallelized large-eddy simulation model

PALM is a meteorological model for atmospheric and oceanic boundary-layer flows. It has been developed as a turbulence-resolving large-eddy simulation (LES) model and is open source, available in the public domain [27]. In the LES approach, only the large eddies are simulated due to spatially filtering the Navier-Stokes equations. The dynamic influence of the small turbulent scales are consequently not resolved, but their influence is accounted for with a so called subgrid model. PALM is based on the unsteady, filtered, incompressible Navier-Stokes equations and the subgrid-scale turbulent kinetic energy (SGS-TKE) model [28]. PALM can simulate the effect of the Coriolis forces and if non-cyclic boundary conditions are imposed, PALM can generate time-dependent turbulent inflow data by using a turbulence recycling method (see Ref. [26]). The resolved equations are discretized using finite differences on a staggered grid (see Appendix A for a more detailed discussion on employed discretization methods). Examples of embedded models for PALM are a land surface model, canopy model, radiation models and wind turbine models. The latter is employed in this work. Two different turbine models are available in PALM. The actuator disk model (ADM) [29] and the rotating actuator disk model (ADM-R) [30] (see Refs. [31,32] for an overview on generalized ADMs). Both these turbine models can be utilized with the PALM Supervisory Controller that is discussed in the following section.

### 2.2. PALM Supervisory Controller

The Supervisory Controller is a MATLAB/FORTRAN interface that allows for communicating with a wind farm controller implemented in MATLAB. This communication infrastructure is used for evaluating control signals by using measurements from PALM. A schematic representation is depicted in Fig. 2, where  $\mathcal{Y}$  is the set of available measurements and  $\mathcal{U}$  the set of control signals. The content of these sets depend on the employed turbine model, on

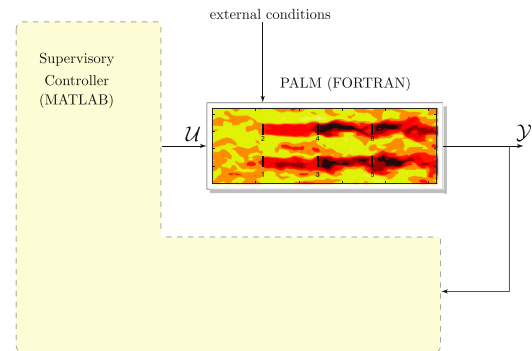


Fig. 2. Schematic representation of the PALM Supervisory Controller. The signals  $\mathcal{Y}$  and  $\mathcal{U}$  are the measurements and control signals, respectively. External conditions are, i.e., boundary conditions.

the assumed measurements, and on the control signals sent from the wind farm controller. Table 1 gives all the possible options.

Note again that the developed framework is suitable for any controller programmed in MATLAB and that the developed software is available in the public domain [33]. Examples where it has already been utilized can be found in Refs. [24,34]. The specific implementation of the Supervisory Controller used in this work is discussed in the following section.

### 2.3. Supervisory Controller implementation proposed in this work

In this work, PALM includes the ADM to determine the turbine's forcing terms acting on the flow and power generation. This turbine model is efficient due its lower requirements of grid resolution and coarser allowed time-stepping as compared to having to resolve detailed flow surrounding rotating blades [35]. A consequence of choosing the ADM is that the control signals for turbine  $i$  are the disk-based thrust coefficient  $C_{Ti}'(t)$  following [35,36] and yaw angle  $\gamma_i(t)$ . Both of these signals can be used to manipulate the turbine thrust force and power generation (see (2)). In this work, the measurements at time  $t$  are 1) the axial force that a turbine exerts on the flow  $F_i(t)$ , 2) the power generated by a turbine  $P_i(t)$  and 3) the rotor-averaged wind velocity  $v_i(t)$  for  $i = 1, 2, \dots, n$  with  $n$  the number of turbines. The rotor-averaged wind velocity is assumed to be known, which could be realized by employing online estimation of the rotor-averaged wind velocity with techniques as presented in Refs. [37–39]. This is however outside the scope of this work. The above defines the sets of measurements and control signals as follows:

$$\mathcal{Y} = \{F_i(t), P_i(t), v_i(t)\}, \quad \mathcal{U} = \{C_{Ti}'(t), \gamma_i(t)\}, \quad (1)$$

for  $i = 1, \dots, n$

Fig. 3 illustrates the specific controller architecture programmed in the Supervisory Controller. The architecture contains two closed loops with in one loop a model predictive controller (MPC) containing a dynamical surrogate model of the wind farm and in the other loop a wind farm controller containing a steady-state surrogate model of the wind farm. The former regulates the thrust coefficients on the seconds-scale to provide power reference tracking, while the latter is utilized when it is desired to increase the

**Table 1**  
Available set of measurements  $\mathcal{Y}$  and control signals  $\mathcal{U}$  for the different turbines models.

PALM + ADM	
$\mathcal{Y}$	wind velocities, generated turbine power, axial force
$\mathcal{U}$	thrust coefficient, yaw angle
PALM + ADM-R	
$\mathcal{Y}$	wind velocities, generated turbine power, axial force,
$\mathcal{U}$	generator speed
	generator torque, pitch angle, yaw angle

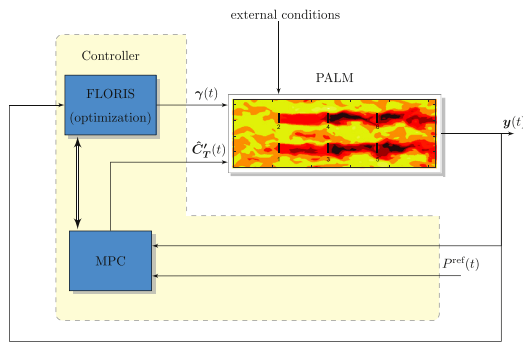


**Fig. 3.** Proposed closed-loop control framework with measurements  $\mathbf{y}(t)$  and power reference signal for the farm  $p^{ref}(t)$ . The control signals are the filtered thrust coefficients  $\hat{C}_T'(t)$  and yaw angles  $\gamma(t)$ . The vertical arrow connecting the MPC and FLORIS represents the information exchange between the different parts of the controller.

available power in the farm. The following section will detail both the dynamical and steady-state surrogate models.

### 3. Controller models

The closed-loop controller proposed in this work contains two different surrogate models. Both are in the feedback loop (see Fig. 3), but work on different time scales, in different situations and with different control signals. The first loop contains an MPC employing a dynamical wind farm model. This controller works on the seconds-scale and its goal is to track a wind farm reference power signal using the filtered thrust coefficients  $\hat{C}_T'(t)$  as control signals (see Fig. 3). The dynamical model used for this control loop is detailed in section 3.1. The objective of the second control loop is to, when there will not be enough energy in the farm, increase the possible power that can be harvested by finding yaw settings  $\gamma(t)$ . This loop is working on the minutes-scale and employs the FLORIS optimization tool, which utilizes a steady-state model that is detailed in section 3.2.

#### 3.1. Dynamical model

An MPC is based on the receding horizon principle in which a constrained optimization problem is solved at each time step using future predictions of the system and it therefore needs a dynamical model. Additionally, we require a computationally efficient model

of the wind farm dynamics because we control on the seconds-scale. Yet, due to nonlinear dynamics, uncertain atmospheric conditions and wind farm model dimensions, it is challenging to obtain such a dynamical wind farm model suitable for control. Examples of computationally expensive dynamical control-oriented wind farm models can be found in Refs. [18,36]. However, axial induction based wind farm power tracking results that are presented in Refs. [19,24] indicate that flow dynamics could be neglected and a wind farm can be modelled as  $n$  uncoupled subsystems, each subsystem consisting of a dynamical turbine model that is based on the actuator disk theory. While wake effects are neglected in the surrogate dynamical model, the turbine dynamics are still affected by the local flow conditions. Hence, the turbine models are updated according to the local rotor-averaged wind velocity, which in reality may or may not be affected by other turbines inside the farm. In this work, the following model for turbine  $i$  is employed

$$\begin{aligned}
 P_i(t) &= \frac{\pi D^2}{8} (v_i(t) \cos[\gamma_i(t)])^3 \hat{C}_{T_i}'(t), \\
 F_i(t) &= \frac{\pi D^2}{8} (v_i(t) \cos[\gamma_i(t)])^2 \hat{C}_{T_i}'(t), \\
 \hat{C}_{T_i}'(t) &= \tau \frac{d\hat{C}_{T_i}'(t)}{dt} + \hat{C}_{T_i}'(t),
 \end{aligned} \tag{2}$$

for  $i = 1, 2, \dots, n$ , with  $P_i(t)$  the generated power,  $F_i(t)$  the axial force that flow exerts on turbine  $i$ ,  $\hat{C}_{T_i}'(t)$  the control signal,  $\hat{C}_{T_i}'(t)$  the first-order filtered control signal,  $\gamma_i(t)$  the yaw angle and  $v_i(t)$  the rotor-averaged wind speed perpendicular to the rotor. Notice that  $v_i(t)$  is, i.e., influenced by the upstream turbine settings through wake propagation. We furthermore have  $\tau \in \mathbb{R}^+$ , the time constant of the filter that acts on the control signal such the applied control signal is smooth. Temporally discretizing (2) at sample period  $\Delta t$  using the zero-order hold method yields the following state-space representation of turbine  $i$

$$\mathbf{x}_{i,k+1} = A_i \mathbf{x}_{i,k} + B_i(v_{i,k}, \gamma_{i,k}) \hat{C}_{T_{i,k}}', \quad \mathbf{y}_{i,k} = \mathbf{x}_{i,k}, \tag{3}$$

with

$$\begin{aligned}
 A_i &\in \mathbb{R}^{3 \times 3}, \quad B_i(v_{i,k}, \gamma_{i,k}) \in \mathbb{R}^3, \quad \mathbf{y}_{i,k} \in \mathbb{R}^3, \\
 \hat{C}_{T_{i,k}}' &\in \mathbb{R}, \quad \mathbf{x}_{i,k}^T = \begin{pmatrix} F_{i,k} & P_{i,k} & \hat{C}_{T_{i,k}}' \end{pmatrix} \in \mathbb{R}^3.
 \end{aligned} \tag{4}$$

Lifting the state variables of the turbines and adding the wind farm power error signal to the state variable results in the following wind farm state-space model:



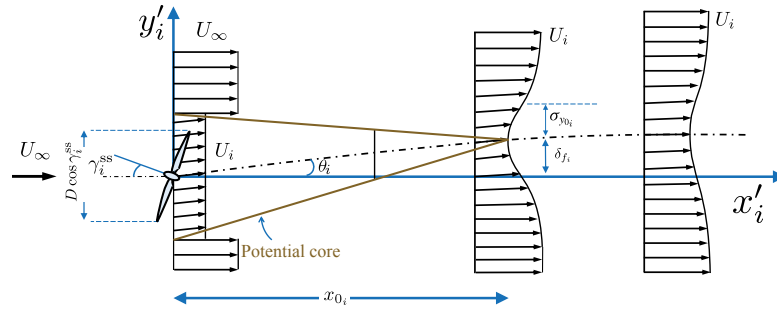


Fig. 4. Schematic representation of a wake evaluated with the steady-state model. The figure is taken from Ref. [40] and adapted.

$$\mathbf{x}_{k+1} = A\mathbf{x}_k + B_u(\mathbf{v}_k, \gamma_k)C'_{T_i,k} + B_r P_k^{\text{ref}}, \quad \mathbf{y}_k = \mathbf{x}_k, \quad (5)$$

which is a linear parameter-varying system due to the varying matrix  $B(\mathbf{v}_k, \gamma_k)$ . Furthermore we have:

$$\begin{aligned} \mathbf{x}_k^T &= (\mathbf{x}_{1,k} \quad \mathbf{x}_{2,k} \quad \dots \quad \mathbf{x}_{N,k} \quad e_k) \in \mathbb{R}^{3N+1}, \\ \mathbf{v}_k^T &= (v_{1,k} \quad v_{2,k} \quad \dots \quad v_{N,k}) \in \mathbb{R}^{3N}, \\ C'_{T_i,k} &= (C'_{T_1,k} \quad C'_{T_2,k} \quad \dots \quad C'_{T_N,k})^T \in \mathbb{R}^N, \\ \hat{C}'_{T_i,k} &= (\hat{C}'_{T_1,k} \quad \hat{C}'_{T_2,k} \quad \dots \quad \hat{C}'_{T_N,k})^T \in \mathbb{R}^N, \\ e_k, P_k^{\text{ref}} &\in \mathbb{R}, \\ \bar{A}_1 &= \text{blkdiag}(A_1, A_2, \dots, A_N) \in \mathbb{R}^{3N \times 3N}, \\ \bar{A}_2 &= (0 \quad -1 \quad 0 \quad \dots \quad 0 \quad -1 \quad 0) \in \mathbb{R}^{1 \times 3N}, \\ A &= \begin{pmatrix} \bar{A}_1 & 0 \\ \bar{A}_2 & 0 \end{pmatrix}, \\ B_u^1(\mathbf{v}_k, \gamma_k) &= \text{blkdiag}(B_1(v_{1,k}, \gamma_{1,k}), \\ B_2(v_{2,k}, \gamma_{2,k}), \dots, B_N(v_{N,k}, \gamma_{N,k})) &\in \mathbb{R}^{3N \times N}, \\ B_u^2 &= (0 \quad 0 \quad \dots \quad 0 \quad 0) \in \mathbb{R}^{1 \times N}, \quad B_u = \begin{pmatrix} B_u^1(\mathbf{v}_k, \gamma_k) \\ B_u^2 \end{pmatrix}, \\ B_r &= (0 \quad 0 \quad \dots \quad 0 \quad 1)^T \in \mathbb{R}^{3N+1 \times 1}, \end{aligned}$$

where  $\text{blkdiag}(\cdot)$  denotes block diagonal concatenation of matrices or vectors. Furthermore we have the wind farm power reference signal  $P_k^{\text{ref}}$  and tracking error signal  $e_k$ . The model described above will be employed in the controller part presented in section 4.1.

### 3.2. Steady-state model

For the evaluation of the steady-state yaw angles that increase the possible power that can be harvested, the FLOW Redirection and Induction in Steady-state (FLORIS) tool is utilized, which is a low-fidelity steady-state wind farm model and it can be used for the purpose of wind farm control, offline analysis and layout optimization. The most recent version is based on the analytical wake model inspired by Bastankhah and Porté-Agel [40] and employed in this work. For brevity, the focus in this section lies on the far-wake model and the following formulation has not yet been published elsewhere.

All single wake equations described here are in the wind-aligned frame, with  $x'_i$  aligned with the wind,  $y'_i$  the lateral component, and  $z'_i$  the vertical component, all centred at the hub of turbine  $i$  (see Fig. 4).

For a single wake, the near-wake region is modelled as a cone

with its base at the rotor plane, and its tip at a distance  $x_{0i}$  downstream of turbine  $i$ . That is

$$x_{0i} = \frac{\frac{\sqrt{2}D}{2} \cdot \cos[\gamma_i^{\text{ss}}] \cdot (1 + \sqrt{1 - \bar{C}_{T_i}})}{\alpha \cdot I_i + \beta (1 - \sqrt{1 - \bar{C}_{T_i}})}, \quad (6)$$

where  $\bar{C}_{T_i}$  is the time-averaged<sup>2</sup> thrust coefficient of turbine  $i$ . The steady-state yaw angle is defined with respect to the wind direction and defined as  $\gamma_i^{\text{ss}}$ . This variable is a decision variable in the optimization to be defined in section 4.2. Note clearly that  $\bar{C}_{T_i}$  is a static value during the optimization. However, tracking a wind farm reference will be achieved when varying the thrust coefficient over time hence this assumption might seem not realistic. However, wake deflection mostly depends on wind direction and yaw settings, and to a much lesser extend on the thrust coefficient and therefore, this is assumed to be constant in the model defined in this section. In (6) we also have two tuning parameters  $\alpha$  and  $\beta$ . A relation between  $\bar{C}_{T_i}$  and  $\bar{C}'_{T_i}$  is defined as

$$\bar{C}_{T_i} = \frac{4(1 - \sqrt{1 - \bar{C}'_{T_i}})}{1 + \sqrt{1 - \bar{C}'_{T_i}}}. \quad (7)$$

The local turbulence intensity in front of turbine  $i$ ,  $I_i$ , is calculated as a squared summation of the atmospheric turbulence intensity  $I_\infty$  and the added turbulence intensities from upstream turbines  $I_j^+$ . Mathematically, this is defined as

$$I_i = \sqrt{\sum_{j=1}^N \left( \frac{A_{w,j}^j}{\frac{1}{4}\pi D^2} I_j^+ \right)^2} + I_\infty^2, \quad (8)$$

with  $A_{w,j}^i$  the relative overlap area between the rotor of turbine  $i$  and wake of turbine  $j$ . Notice that the sum is taken over all turbines since  $A_{w,j}^i$  is zero for turbines downstream of turbine  $i$ . Furthermore,

$$I_j^+ = t_a \cdot \bar{a}_j^{t_b} \cdot I_\infty^{t_c} \cdot \left( \frac{\Delta x_{\text{turb}}^j}{D} \right)^{t_d}, \quad (9)$$

<sup>2</sup> The time over which is averaged is proposed to be the past fifteen minutes, equal to the period that new optimal yaw angles are evaluated and can be applied when necessary.

where  $\Delta x_{\text{turb}}^j$  the stream-wise distance between the turbines  $i$  and  $j$ , and  $\bar{a}_j$  the time-averaged axial induction factor with relation

$$\bar{C}_T = \frac{4\bar{a}_j}{1 - \bar{a}_j} \quad (10)$$

The variables  $t_a$ ,  $t_b$ ,  $t_c$ , and  $t_d$  are considered as tuning parameters.

For  $x'_i \geq x_0$ , the wake is modelled as a two-dimensional Gaussian velocity deficit in  $y'_i$ - and  $z'_i$ -direction, symmetrical around a centreline. This centreline lies in the horizontal plane at hub height, displaced in  $y'_i$ -direction from the  $i^{\text{th}}$  turbine hub by  $\delta_{fi}$ , as

$$\begin{aligned} \delta_{fi} &= \tan[\theta_i]x_0 + \frac{\theta_i}{5.2} \cdot (C_{0i}^2 - 3e^{1/12}C_{0i} + 3e^{1/3}) \times \\ &\quad \sqrt{\frac{\sigma_{y_0}\sigma_{z_0}}{k_y \cdot k_z \cdot \bar{C}_T}} \cdot \ln \left[ \frac{(1.6 + \sqrt{\bar{C}_T})(1.6S_{\sigma_i} - \sqrt{\bar{C}_T})}{(1.6 - \sqrt{\bar{C}_T})(1.6S_{\sigma_i} + \sqrt{\bar{C}_T})} \right] + \delta_{ri}. \end{aligned} \quad (11)$$

In this equation,  $\theta_i$  is the initial deflection angle in radians, calculated as

$$\theta_i \approx \frac{0.3\gamma_i^{\text{ss}}}{\cos[\gamma_i^{\text{ss}}]} \left( 1 - \sqrt{1 - \bar{C}_T \cos[\gamma_i^{\text{ss}}]} \right). \quad (12)$$

Furthermore,  $C_{0i} = 1 - \sqrt{1 - \bar{C}_T}$ ,  $k_y$  and  $k_z$  are linear wake expansion coefficients similar to that in Ref. [41], and  $S_{\sigma_i}$  is defined as  $S_{\sigma_i} = \sqrt{(\sigma_{y_i}\sigma_{z_i})/(\sigma_{y_0}\sigma_{z_0})}$ , with  $\sigma_{y_i}$  and  $\sigma_{z_i}$  the standard deviations of the Gaussian in  $y'_i$ - and  $z'_i$ -direction, respectively, both a linear function of  $x'_i$ . They are calculated as

$$\sigma_{y_i} = \sigma_{y_0} + (x'_i - x'_0)k_y, \quad \text{with } \sigma_{y_0} = \frac{D}{2\sqrt{2}} \cos[\gamma_i^{\text{ss}}], \quad (13)$$

$$\sigma_{z_i} = \sigma_{z_0} + (x'_i - x'_0)k_z, \quad \text{with } \sigma_{z_0} = \frac{D}{2\sqrt{2}}, \quad (14)$$

Further,  $\delta_{ri}$  is the wake deflection induced by the rotation of the blades, approximated using a linear function, by  $\delta_{ri} = a_d \cdot D + b_d \cdot x'_i$ , with  $a_d$  and  $b_d$  tuning parameters. The steady-state wind speed  $U_i$  in the far-wake region at some location  $(x'_i, y'_i, z'_i)$ , with  $x'_i \geq x'_0$ , and with its origin at the hub of turbine  $i$ , is now defined as

$$\begin{aligned} \frac{U_i(x'_i, y'_i, z'_i)}{U_\infty} &= 1 - \left( 1 - \sqrt{1 - \frac{\sigma_{y_0}\sigma_{z_0}\bar{C}_T}{\sigma_{y_i}\sigma_{z_i}}} \right) \cdot \exp \left( \frac{(y'_i - \delta_{fi})^2}{2\sigma_{y_i}^2} \right. \\ &\quad \left. + \frac{(z'_i)^2}{2\sigma_{z_i}^2} \right), \end{aligned}$$

with  $U_\infty$  the free-stream wind speed, which is the mean longitudinal wind speed in front of the wind farm. Furthermore, the power capture in steady-state of turbine  $i$  is calculated as

$$P_i^{\text{ss}} = \left( \frac{\pi D^2}{8} \right) \cdot (v_i^{\text{ss}} \cos[\gamma_i^{\text{ss}}])^3 \cdot \bar{C}_{T_i}, \quad (15)$$

with  $v_i^{\text{ss}}$  the rotor-averaged stream-wise wind speed in steady-state. This quantity is calculated by integrating the effect of multiple wakes over the turbine rotor, as

$$v_i^{\text{ss}} = U_\infty (1 - \bar{a}_i) \left( 1 - \sqrt{\sum_{j=1}^N \left( \frac{Q_j}{\frac{1}{4}\pi D^2} \right)^2} \right), \quad (16)$$

$$Q_j = \int_0^{D/2} \int_0^{2\pi} \left( r_j \left( 1 - \frac{U_j(r_j, \beta_j)}{U_\infty} \right) \right) d\beta_j dr_j, \quad (17)$$

where  $(r_j, \beta_j)$  is the polar coordinate representation of  $(y'_j, z'_j)$  over the rotor of turbine  $j$ . Note that  $Q_j = 0$  for the wakes of downstream turbines since  $U_j(r_j, \beta_j) = U_\infty$  for  $x'_j < 0$ . The above described model will be employed in the controller as described in section 4.2.

#### 4. Control strategy

The proposed closed-loop controller executes two tasks. The first task is executed on the seconds-scale and solves a finite-time constrained predictive optimization problem using the model defined in section 3.1 assuming full knowledge of the powers, axial forces and rotor-averaged wind velocities. The main objective is to provide power tracking on a farm level. The second task is executed on a 15-min scale and consists of an optimization procedure using the steady-state surrogate model defined in section 3.2 assuming full knowledge of the measured wind direction. The main objective is to increase the possible power extractable from the wind by finding optimal yaw settings. However, the second task will only be executed when the future wind farm reference signal will be above the maximal possible extractable wind farm power such that unnecessary yaw actuation and consequently potential additional loading [42] will not occur. If more than the maximal possible extractable wind farm power with zero yaw settings is demanded from the farm, optimal yaw settings can be evaluated and applied with the additional second loop. The first and second task will be detailed in section 4.1 and section 4.2, respectively.

##### 4.1. Axial induction control for power tracking

The aforementioned MPC is stated to solve the following optimization problem from time  $k_0$  until the prediction horizon  $k_0 + N_h$

$$\min_{\mathbf{C}_{T,k}} \sum_{k=k_0}^{k_0+N_h} e_k^T Q e_k + (\mathbf{F}_k - \mathbf{F}_{k-1})^T S (\mathbf{F}_k - \mathbf{F}_{k-1}) \quad (18a)$$

$$\text{s.t. } \mathbf{x}_{k+1} = \mathbf{A}\mathbf{x}_k + \mathbf{B}_u(\mathbf{v}_{k_0}, \gamma_{k_0})\mathbf{C}_{T,k} + \mathbf{B}_r P_k^{\text{ref}}, \quad \mathbf{P}_k \leq \mathbf{P}_{\max}, \quad (18b)$$

$$C'_{T,\min} \leq C'_{T,k} \leq C'_{T,\max}, \quad |C'_{T,k} - C'_{T,k-1}| < dC'_T, \quad (18c)$$

with



$$\mathbf{F}_k = (F_{1,k} \ F_{2,k} \ \dots \ F_{N,k})^T \in \mathbb{R}^N \quad \mathbf{P}_k = (P_{1,k} \ P_{2,k} \ \dots \ P_{N,k})^T \in \mathbb{R}^N,$$

$$\mathbf{P}_{\max} = (P_{1,k_0}^{\text{av}} \ P_{2,k_0}^{\text{av}} \ \dots \ P_{N,k_0}^{\text{av}})^T \in \mathbb{R}^N, \mathbf{e}_k = P_k^{\text{ref}} - \sum_{i=1}^N P_{i,k} \in \mathbb{R},$$

and

$$P_{i,k_0}^{\text{av}} = \frac{\pi D^2}{8} \left( v_{i,k_0} \cos[\gamma_{i,k_0}] \right)^3 C_{T,\max} \in \mathbb{R}. \quad (19)$$

Furthermore,  $C'_{T,\max}$ ,  $C'_{T,\min}$ ,  $dC'_T$  and  $\mathbf{P}_{\max}$  represent the upper and lower bounds on the thrust coefficients, its variation and upper bound on the turbines power generation, respectively, and  $\gamma_{k_0}$  and  $\mathbf{v}_{k_0}$  the yaw angles and measured rotor-averaged wind velocity at time  $k_0$ , respectively. Note that a constraint on the thrust coefficients is already an indirect constraint on the turbine power signals. However, this generalized framework is beneficial, as it will allow us to investigate different constraints on the power generation of each turbine in future work. We furthermore have the weighting matrices

$$\mathbf{Q} = \mathbf{q} \in \mathbb{R}, \quad \mathbf{S} = \mathbf{I}_N \cdot \mathbf{s} \in \mathbb{R}^{N \times N} \quad (20)$$

with  $\mathbf{q}, \mathbf{s} \in \mathbb{R}$  controller tuning variables. In fact, by tuning each weight one can increase or decrease the importance of the corresponding term in the cost function. More specifically, by increase the weight  $\mathbf{s}$  relative to  $\mathbf{q}$ , the controller puts more effort in minimizing the dynamical turbine loading. We would like to stress here that the optimization problem defined in (18) tries to find a distribution of control signals among the turbines, such that the tracking error and dynamical loading are minimized. This is different with respect to the work presented in Ref. [24] in which a distribution is imposed before the optimization routine. Clearly, by not imposing a distribution manually as done in this work, the controller is given relatively more freedom to find control signals that minimize tracking error and dynamical loading.

#### 4.2. Axial induction control for power tracking with optimized yaw settings

The optimization algorithm described in this paragraph relies on the FLORIS tool described in section 3.2. In practice, first it is predicted whether the wind farm reference can be tracked for the upcoming 15 min.<sup>3</sup> A method to do this could be by taking the maximum value among the upcoming reference signal over a 15 min horizon and then estimate the available power using an algorithm such as presented in Ref. [43]. In this work we are not investigating such a method, but if it is possible to track the wind farm reference signal over the upcoming 15 min, then the turbines are yawed in alignment with the mean wind direction (zero yaw settings) so that no unnecessary yaw actuation will occur. However, when it is estimated that tracking will not be ensured, first the steady-state surrogate model should be adjusted to match the present atmospheric conditions inside the farm such as for example demonstrated in Ref. [44]. These atmospheric conditions such as wind direction could be estimated using, e.g., SCADA data and lidar measurements [34]. Subsequently, the following optimization problem is solved following an interior point method to address the nonlinearity and nonconvexity of the problem:

<sup>3</sup> The necessity of using optimized yaw settings or non-yawed turbines to track the future reference is evaluated every 15 min, but this time-span can be adapted according to atmospheric conditions. Additionally, it is assumed that the reference is known for the upcoming 15 min throughout this work.

$$\gamma^* = \underset{\gamma^{\text{ss}}}{\text{argmin}} \left( - \sum_{i=1}^N P_i^{\text{ss}}(\gamma^{\text{ss}}) \right), \quad (21a)$$

$$\text{s.t. } -25^\circ \leq \gamma_i^{\text{ss}} \leq 25^\circ, \quad \text{for } i = 1, \dots, N, \quad \text{and} \quad (15) \quad (21b)$$

where  $\gamma^{\text{ss}} = (\gamma_1^{\text{ss}} \ \gamma_2^{\text{ss}} \ \dots \ \gamma_N^{\text{ss}})^T$ . The yaw angle is constrained to suppress the increase in structural loading for strongly yawed turbines [42]. The optimal yaw settings,  $\gamma^*$ , are then distributed to the turbines and turbine models (see (2)), and maintained for a fifteen minute period, upon which the above described cycle is repeated.

### 5. Simulation results

PALM simulation results are all of a neutral atmospheric boundary layer and will be discussed in this section. In all simulation cases, the controller is applied to a wind farm with specifications as described in Table 2.

See Table C.3 for the variable definitions. The sample period  $\Delta t = 1$  [s] is chosen such that the Courant condition [45] holds. The time constant  $\tau$  is chosen following [46] and as a consequence, no fast dynamics such as structural vibrations are captured with the turbine model. However, it results in smooth control signals that are fed to the turbines in PALM. The prediction horizon  $N_h$  is found after tuning the controller. The influence of  $\tau$ ,  $N_h$  is not further investigated in this work. The value for  $C'_{T,\max}$  corresponds to the Betz-optimal value and hence no overinductive axial induction control is considered. Furthermore,  $C'_{T,\min} = 0.1$  indicating that we do not allow turbines to shut down completely, which is common practice in wind farms. The bound on the thrust coefficient variation  $dC'_T = 0.2$  is set such that turbines can not de- and uprate instantaneously, but it also provides an upper and lower bound on the maximum allowable dynamical loading (see (2)).

The topology under consideration is illustrated in Fig. 5 and contains heavily waked wind turbines due to the fact that turbines are aligned with the mean wind direction. Although farms are designed such that the occurrence of this situation is minimized, it remains an interesting case study to investigate farm dynamics in these worst case scenarios [47]. This section is organised as follows. Firstly in section 5.1, two performance measures are introduced such that controllers with different settings can be evaluated. Secondly, in section 5.2, a brief summary on how PALM is initialized is given. In section 5.3, we investigate the influence of the controller parameter  $\mathbf{s}$  (see (20)) on the tracking performance, the dynamical loading and consequently the differences between the found control signal distributions. Then in section 5.4, we illustrate by example that a wind farm power reference signal that temporarily exceed the maximal possible extractable wind farm power with zero yaw can be tracked when yawing turbines in an optimized way.

#### 5.1. Performance measures

In order to evaluate the controller performance under different settings, two criteria are introduced.

$$dF_i = \sum_{k=1}^N (F_{i,k} - F_{i,k-1})^2, \quad \text{for } i = 1, \dots, N \quad \text{and},$$

$$dF = \sum_{i=1}^N dF_i. \quad (22)$$

The turbine performance index,  $dF_i$ , represents the turbine's

**Table 2**  
Summary of the simulation set-up.

$L_x \times L_y \times L_z$	$15.3 \times 3.8 \times 1.3 \text{ [km}^3\text{]}$	$D, z_h$	120, 90 [m]
$\Delta x \times \Delta y \times \Delta z$	$15 \times 15 \times 10 \text{ [m}_3\text{]}$	Turbine spacing	$5D \times 3D \text{ [m]}$
$\Delta t$	1 [s]	$U_\infty, V_\infty, W_\infty$	8, 0, 0 [m/s]
$N, \tau, N_h$	850, 5, 10 [s]	$Tl_\infty$	6%
$C'_{T,max}, C'_{T,min}, dC'_T$	2, 0.1, 0.2		

force variations and the quantity  $dF$  represents the force variations on a farm level, both evaluated over the complete simulation horizon. Clearly, a lower performance index indicates less force variations over the simulation horizon.

### 5.2. Simulation initialization

Simulations are initialized as follows: a fully developed flow field is generated in the precursor such that the free-stream wind speeds are  $U_\infty = 8 \text{ [m/s]}$  and  $V_\infty = W_\infty = 0 \text{ [m/s]}$  in the longitudinal, lateral and vertical direction, respectively, and a turbulence intensity in front of the farm of approximately 6% at hub-height in front of the wind farm (see Appendix B for definition of turbulence intensity used in this work). Then, for the specific topology considered in this work, the flow is propagated  $N$  seconds in advance with  $C'_{T,i,k} = 2$  (corresponding to the Betz-optimal value) and  $\gamma_{i,k} = 0$  for  $i = 1, \dots, N$  for the complete  $N$  seconds so that the wakes are fully developed. Here, non-cyclic boundary conditions are imposed in the stream-wise direction, i.e., a turbulent inflow boundary and an open outflow boundary on the opposite side are imposed. The turbulent inflow at one boundary is generated by using a turbulence recycling method [26]. For the flow quantities, Dirichlet conditions are used at the inflow and radiation conditions at the outflow. In the cross stream-wise direction, cyclic boundary conditions are imposed and Dirichlet conditions as bottom and top boundary conditions. The flow field obtained after these  $N$  seconds is utilized as initial flow field (see Fig. 5) for the simulation results presented in this work.

The greedy power ( $p^{\text{greedy}}$ ) is defined as the time-averaged wind farm power harvested with  $C'_{T,i,k} = 2$  and  $\gamma_{i,k} = 0$  for  $i = 1, \dots, N$  and  $N$  seconds of simulation starting with the previous described initial flow field. With unyawed turbines, a wind farm can potentially harvest above the  $p^{\text{greedy}}$  threshold for only a relatively short period of time. Clearly, this period is defined by the wake propagation time. In this work,  $p^{\text{greedy}}$  is defined as the maximal possible extractable wind farm power.

### 5.3. Power tracking while minimizing dynamical turbine loading

In this section, the controller parameter  $s$  is varied so that its

influence on the previously defined performance measures and control signal distribution can be studied. The value of controller parameter  $q = 10^4$  is found after tuning such that tracking is ensured. The wind farm power reference signal is defined as:

$$P_k^{\text{ref}} = 0.7p^{\text{greedy}} + 0.2p^{\text{greedy}}\delta P_k, \quad (23)$$

with  $\delta P_k$  a normalized “RegD” type AGC signal [48] coming from an operator and  $p^{\text{greedy}} \approx 7.5 \text{ [MW]}$ . As can be seen in (23), the reference will never exceed  $p^{\text{greedy}}$  during the simulation period and hence turbines are in derate mode for the complete simulation period. Consequently, the problem described in section 4.1 is exclusively solved to provide power tracking, and the problem described in section 4.2 is not due to the fact that it is possible to track the reference signal given in (23) with unyawed turbines over the complete simulation horizon.

In Fig. 6, it can be observed that tracking is ensured for all presented cases and hence we can conclude that, for the presented cases, the controller parameter  $s$  does not have a significant impact on the tracking performance.

However, in Fig. 7, it can be seen that the performance index  $dF$  as defined in (22) reduces when  $s$  increases indicating that dynamical loading can be reduced on a farm level. This is expected since  $dF$  can be found in the controller's objective function as defined in (18). However, Fig. 7 also depicts the turbine's performance indices as defined in (22), and it can be observed that, although dynamical loading on a farm level is reduced, it can increase for specific turbines in the farm (see for example turbine 5). We note, but do not show, that for  $s > 50$  no significant changes in the dynamical loading can be observed.

Furthermore, from Fig. 8 it can be concluded that the control signal distribution significantly changes for a varying controller parameter  $s$ . In fact, an increasing penalty on the dynamical loading results in a decrease of the downstream thrust coefficients, while upstream turbines receive increased thrust coefficients. The latter results in a decreased rotor-averaged flow velocity and its variation, which reduces the fatigue loading (see (2)). In other words, the dynamical loading of the upstream turbines is reduced when increasing the weight  $s$ , while such a simple relation can not be observed for the downstream turbines. This could possibly be due

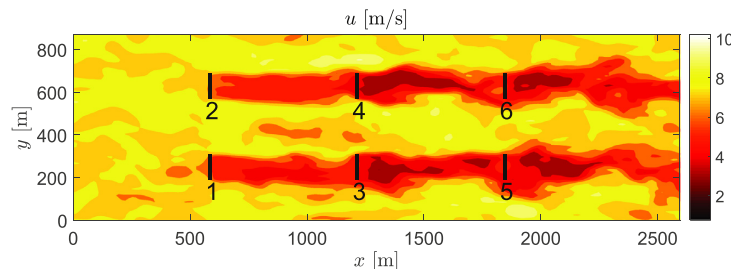


**Fig. 5.** Initial longitudinal flow velocity component at hub-height. The flow is going from west to east and the black vertical lines represent the wind turbines.

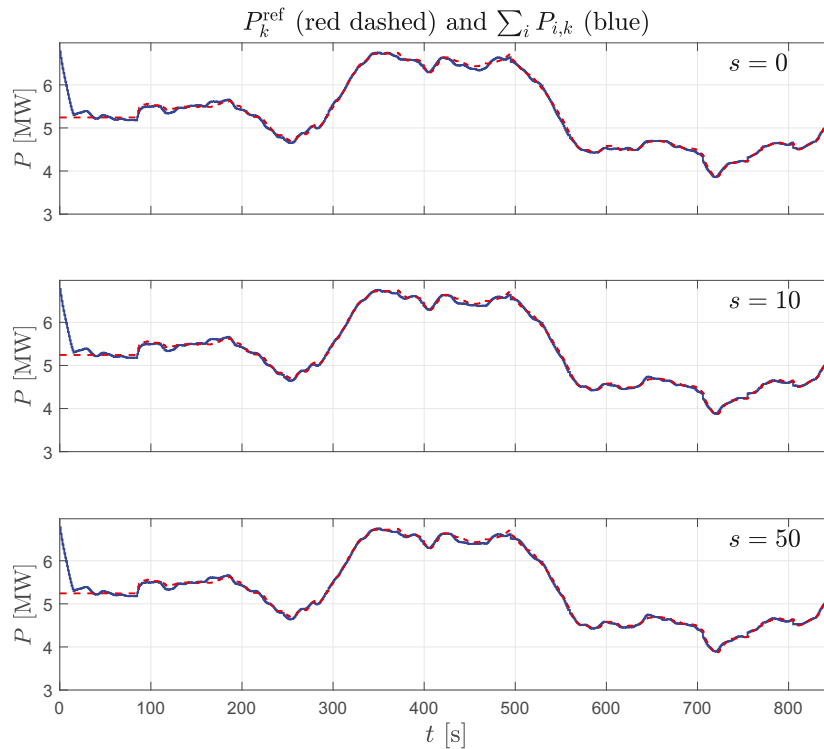


Fig. 6. Wind farm power and reference for different controller settings  $s$ .

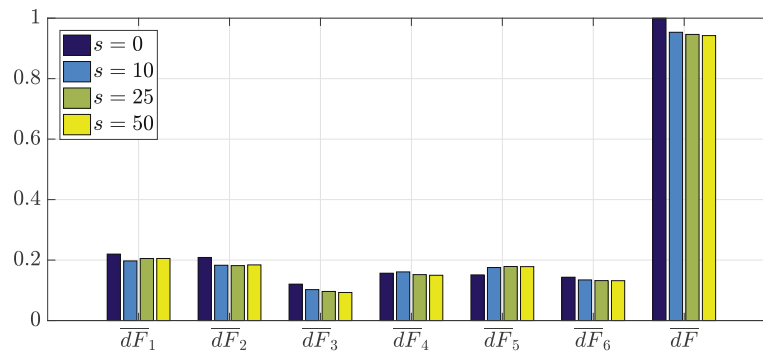


Fig. 7. Normalized performance indices as defined in (22) for different controller settings  $s$ .

to the complex wake dynamics that influence the dynamical loading of the downstream turbines. However, Fig. 7 indicates that, on a farm level, the dynamical loading is reduced when increasing  $s$ , which is expected since the weight  $s$  increases the penalty on the sum of the individual turbine dynamical loading (see Eq. (18)). Fig. 9 additionally depicts the turbine power signals for different controller settings. We observe that in all cases, the upstream turbines produce relatively the most power since the wind speed in

front of these turbines is the highest and that an increase in  $s$  results in incremental power production of the upstream turbines.

#### 5.4. Power tracking with optimized yaw settings

In this section, the controller is evaluated with the following reference signal

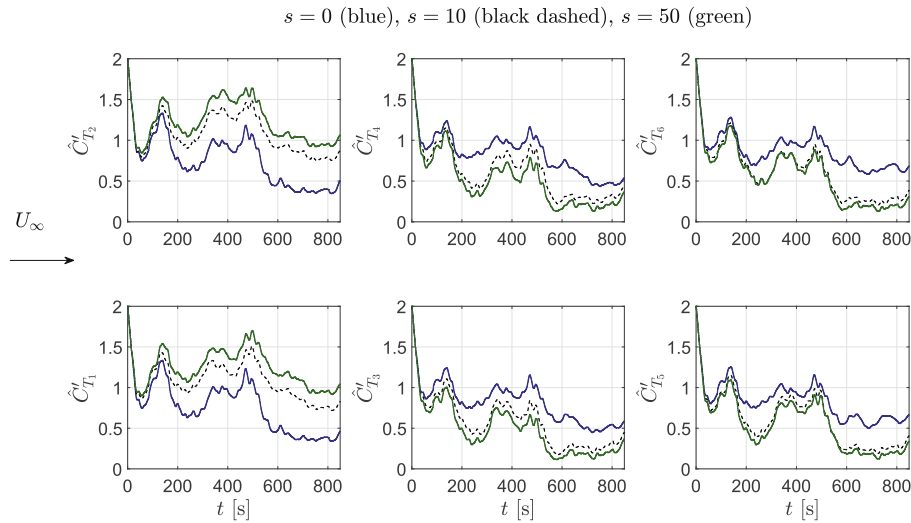


Fig. 8. Wind farm control signals for different controller settings  $s$ . The arrow on the left indicates the wind direction.

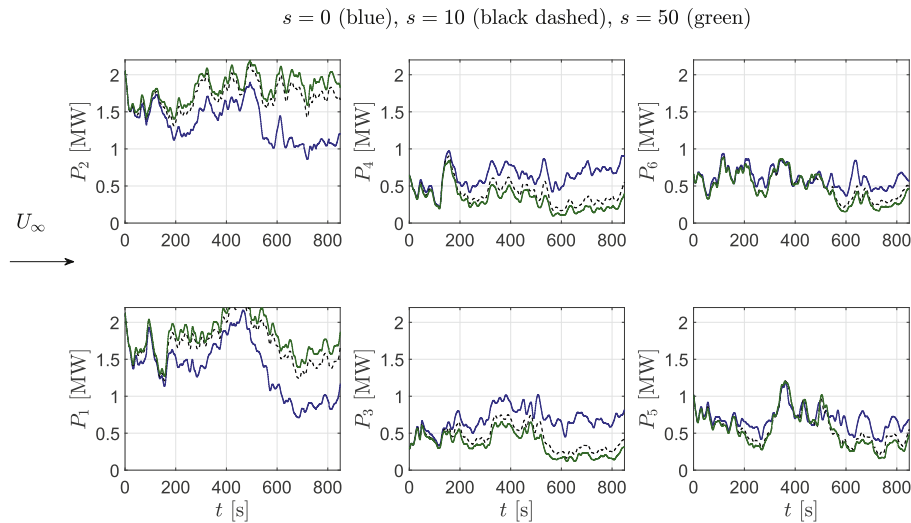


Fig. 9. Turbine power signals for different controller settings  $s$ . The arrow on the left indicates the wind direction.

$$p_k^{\text{ref}} = 0.8p_{\text{greedy}} + 0.5p_{\text{greedy}}\delta p_k. \quad (24)$$

Observe that, for a period, more power is demanded from the farm than the averaged power harvested under greedy control. Consequently, the optimization problem described in section 4.2 is solved firstly for the measured wind direction and topology under consideration to increase the maximum possible power that can be harvested by the farm. Solving the problem given in (21) takes approximately 30 s on a regular notebook and single core. The optimized yaw settings were found to be

$$\gamma_k^* = (-24.3 \ -24.3 \ -16.2 \ -16.2 \ 0 \ 0)^T [\text{deg}]. \quad (25)$$

These yaw settings are kept constant throughout the simulation case presented in this section and applied instantaneously in the initial flow field. See Fig. 10 for instantaneous longitudinal flow velocity components at hub-height. Note that we assume no deviation of the mean wind direction and free-stream wind speed during the simulation period since we update yaw settings every 15 min.

Secondly, the problem described in section 4.1 is solved during the complete simulation horizon and power tracking is provided

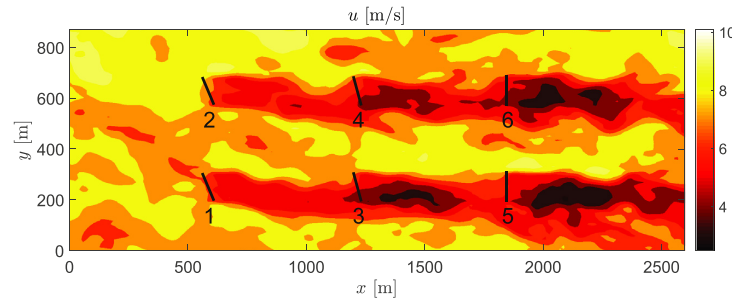


Fig. 10. Instantaneous longitudinal flow velocity component at hub-height at  $t = 600$  [s]. The flow is going from west to east and the black vertical lines represent the wind turbines.

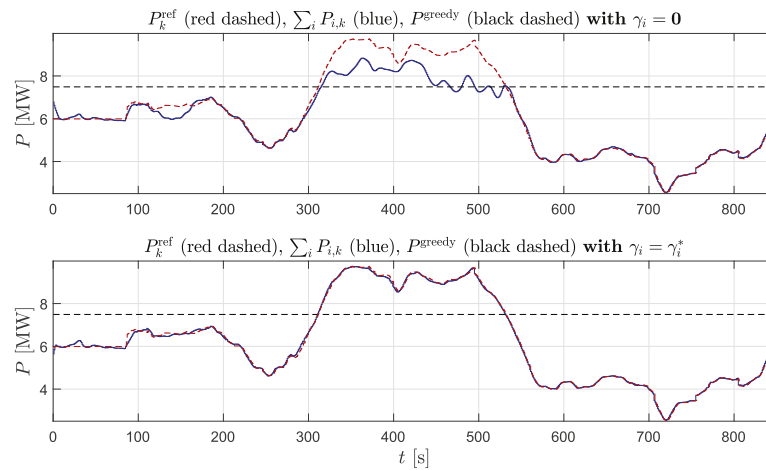


Fig. 11. Wind farm tracking results of the controller with  $\gamma_{i,k} = 0$  (above) and optimized settings  $\gamma_k^*$  (below).

with yawed turbines. On a regular note book and single core, it takes approximately 0.07 s to solve the problem described in section 4.1. Hence, due to the fact that the sample time is chosen to be one second, online power tracking can be achieved. The controller parameters  $q, s$  were found after tuning such that tracking is ensured and set to  $q = 10^4, s = 25$ . Note that during the simulation time, the wake mainly alters due to the changed yaw settings, which makes it extra challenging for the MPC to track the reference signal. Fig. 11 depicts simulation results of two simulations.

In the top plot, tracking results are depicted that are obtained with yawed turbines. Here it can be seen that indeed, the reference can not be tracked sufficiently over the complete simulation horizon, which is due to the absence of sufficient wind power. Interestingly, from  $t = 300$  [s] to  $t = 450$  [s], the wind farm power produces more than  $P_{greedy}$ , which is due to the fact that wakes of upstream turbines are not fully developed yet. However, when the wake changes arrive at downstream turbines, the available wind power decreases and the power production converges to  $P_{greedy}$  from  $t = 450$  [s] to  $t = 520$  [s]. In the below plot, it can be observed that power tracking can be ensured over the complete simulation horizon, which is due to the fact that the yawed turbines increase the possible power that can be harvested by the farm.

Fig. 12 depicts the thrust coefficients that are found by the MPC and it can be seen that in the non-yawed turbine case (i.e.,  $\gamma_{i,k} = 0$ ), the thrust coefficients reach their boundaries from  $t = 300$  [s] to  $t = 450$  [s] and sufficient power tracking can not be ensured during this timespan. However, when the found optimized yaw settings  $\gamma_k^*$  are applied, the wind speed is higher in front of the upstream turbines hence more power can be harvested with these turbines. In order to track the reference, it is therefore possible to reduce the thrust coefficients.

## 6. Conclusions

Ancillary services in wind farms are important to increase the wind power penetration in the energy market. One example is secondary frequency regulation in which the objective is to have the wind farm's power generation track a power reference signal generated by transmission system operators during a time span of several minutes. Due to the uncertain wake dynamics, a closed-loop control solution with a dynamical surrogate model is needed to provide this so called power tracking. Since dynamical wake models are generally complex, approximations are required such that the surrogate model can be employed in a controller that

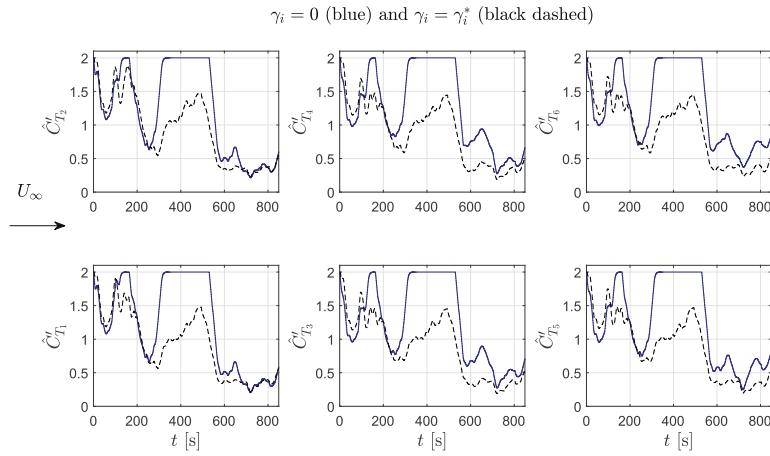


Fig. 12. Control signals with  $\gamma_{i,k} = 0$  and optimized settings  $\gamma_k^*$ .

should work in a real time application. In this paper, we present such a dynamical surrogate wind farm model and utilize it in a model predictive controller that provides power tracking, and additionally is able to reduce the dynamical loading on a farm level by finding for each simulation second new optimized thrust coefficients in approximately 0.07 s. To increase the possible range of traceable power signals, wake steering is used when future reference signals exceed the maximum power that can be harvested with non-yawed turbines. Optimized yaw settings that maximize the possible power that can be harvested are then found by employing a steady-state surrogate model and set for a simulation period of fifteen minutes. The necessity of applying optimized or zero yaw settings to track the future reference can then be re-evaluated. Note that the optimized yaw settings maximize the possible power that can be harvested, which can result in unnecessary turbine yawing. In future work, a more sophisticated method could be incorporated in the controller for determining yaw settings that exactly increase the possible power that can be harvested to the maximal value of the future reference. In this paper, we give an example where the reference can not be tracked sufficiently when turbines are non-yawed, while power tracking is ensured when optimized yaw settings are applied. The controller is evaluated in a high-fidelity simulation environment for which software is developed that allows for programming controllers in MATLAB and evaluating these in a high-fidelity simulation environment. In future work, an analysis on multi-scale dynamics in the high-fidelity simulation environment is necessary to better understand the wind farm flow dynamics under the proposed control strategy. This could possibly lead to a more efficient controller performance.

#### Acknowledgements

The main author would like to thank Sonja Krüger and Gerald Steinfeld from ForWind (Oldenburg) and Will van Geest from the TU-Delft for their valuable input regarding PALM simulations. The authors would like to acknowledge the CL-Windcon project. This project has received funding from the European Union's Horizon

2020 research and innovation programme under grant agreement No 727477.

#### Appendix A. PALM discretization

The model domain in PALM is spatially discretized using finite differences and equidistant horizontal and vertical grid spacing ( $\Delta x$ ,  $\Delta y$ ,  $\Delta z$ ). A staggered grid is used, where scalar quantities are defined at the center of each grid volume, and velocity components are shifted by half a grid width in their respective direction so that they are defined at the edges of the grid volumes. It is therefore possible to calculate the derivatives of the velocity components at the center of the volumes (same location as the scalars). Using a similar argument, derivatives of scalar quantities can be calculated at the edges of the volumes. In this way it is possible to calculate derivatives over only one grid length. The Navier-Stokes equations are discretized using an upwind-biased fifth-order differencing scheme in combination with a third-order RungeKutta time-stepping scheme [26].

#### Appendix B. Turbulence intensity

The turbulence intensity in front of the wind farm  $TI_\infty$  is computed as follows: take the longitudinal flow velocity at hub-height for the area defined by the vertices  $x \in (30, 150)$  [m] and  $y \in (375, 525)$  [m] for  $L$  seconds. Define this local time-varying flow field as  $u_k^l$ . Define:

$$u_k' = u_k^l - \mu_u \quad \text{with} \quad \mu_u = \frac{1}{L} \sum_{k=1}^L u_k^l. \quad (\text{B.1})$$

Using the above to compute the turbulence intensity yields:

$$TI_\infty = \mu_s \left( \text{rms}(u_k') \cdot \mu_u^{-1} \right), \quad (\text{B.2})$$

with  $\text{rms}(u_k')$  the root-mean-square level of  $u_k'$  along the time axis and  $\mu_s(\cdot)$  the spatial average in the  $x$ - and  $y$ -direction.



## Appendix C. Nomenclature

**Table C.3**  
Nomenclature.

$L_x \times L_y \times L_z$	domain wind farm	$D$	turbine rotor diameter
$\Delta x \times \Delta y \times \Delta z$	cell size	$N$	number of turbines
$U_\infty, V_\infty, W_\infty$	free-stream flow velocities	$\Delta t$	sample period flow solver
$z_h$	turbine hub height	$p_k^{\text{ref}}$	wind farm power reference
$N$	simulation time	$Tl_\infty$	turbulence intensity at inflow
$i$	turbine index	$k$	time index
$v_{i,k}$	rotor-averaged flow velocity	$\gamma_i$	yaw angle
$P_{i,k}$	power	$F_{i,k}$	force
$C_{T,i,k}$	thrust coefficient	$\hat{C}_{T,i,k}'$	filtered thrust coefficient
$p_{i,k}^{\text{av}}$	available power	$p_{i,k}^{\text{ref}}$	turbine power reference

## References

- [1] B. Obama, The irreversible momentum of clean energy, *Sci. Pol. Forum* (2017), <https://doi.org/10.1126/science.aam6284>.
- [2] Technical report, WindEurope Business Intelligence 2018: Wind in Power 2017, Annual Combined Onshore and Offshore Wind Energy Statistics, WindEurope Business Intelligence, 2018.
- [3] R. Barthelmie, S. Frandsen, M.N. Nielsen, S.C. Pryor, P.E. Rethore, H.E. Jørgensen, Modelling and measurements of power losses and turbulence intensity in wind turbine wakes at Middelgrunden offshore wind farm, *Wind Energy* 10 (6) (2007) 517–528.
- [4] R. Barthelmie, S.C. Pryor, S. Frandsen, K. Hansen, J. Schepers, K. Rados, W. Schlez, A. Neubert, L. Jensen, S. Neckelmann, Quantifying the impact of wind turbine wakes on power output at offshore wind farms, *J. Atmos. Ocean. Technol.* 27 (8) (2010) 1302–1317.
- [5] A. Rosen, Y. Sheinman, The power fluctuations of a wind turbine, *J. Wind Eng. Ind. Aerod.* 59 (1) (1995) 51–68.
- [6] J. Bossuyt, M.F. Howland, C. Meneveau, J. Meyers, Measurement of unsteady loading and power output variability in a micro wind farm model in a wind tunnel, *Exp. Fluids* 58 (1) (2017).
- [7] E. Ela, V. Gevorgian, P. Fleming, Y.C. Zhang, M. Singh, E. Muljadi, A. Scholbrock, J. Aho, A. Buckspan, L.Y. Pao, V. Singhvi, A. Tuohy, P. Pourbeik, D. Brooks, N. Bhatt, Active Power Controls from Wind Power: Bridging the Gaps, Technical report, National Renewable Energy Laboratory, 2014.
- [8] S. Siniscalchi-Minna, F.D. Bianchi, M. De Prada Gil, C. Ocampo-Martinez, A wind farm control strategy for power reserve maximization, *Renew. Energy* 131 (2018) 37–44.
- [9] S. Boersma, B.M. Doekemeijer, P.M.O. Gebraad, P.A. Fleming, J. Annoni, A.K. Scholbrock, J.A. Frederik, J.W. van Wingerden, A tutorial on control-oriented modelling and control of wind farms, in: *American Control Conference*, 2017, <https://doi.org/10.23919/ACC.2017.7962923>.
- [10] B. Biegel, D.D. Madjidian, V. Spudić, A. Rantzer, J. Stoustrup, Distributed low-complexity controller for wind power plant in derated operation, in: *International Conference on Control Applications*, 2013, <https://doi.org/10.1109/CCA.2013.6662758>.
- [11] V. Spudić, C. Conte, M. Baotić, M. Morari, Cooperative distributed model predictive control for wind farms, *Optim. Contr. Appl. Methods* 36 (3) (2014) 333–352.
- [12] D. Madjidian, Scalable minimum fatigue control of dispatchable wind farms, *Wind Energy* 19 (10) (2016) 1933–1944.
- [13] H. Zhao, Q. Wu, Q. Guo, H. Sun, Y. Xue, Distributed model predictive control of a wind farm for optimal active power control part I: clustering-based wind turbine model linearization, *IEEE Trans. Sustain. Energy* 6 (3) (2015) 831–839.
- [14] S. Siniscalchi-Minna, F.D. Bianchi, C. Ocampo-Martinez, Predictive control of wind farms based on lexicographic minimizers for power reserve maximization, in: *American Control Conference*, 2018, <https://doi.org/10.23919/ACC.2018.8431865>.
- [15] T.N. Jensen, T. Knudsen, T. Bak, Fatigue minimising power reference control of a de-rated wind farm, *J. Phys. Conf.* (2016), <https://doi.org/10.1088/1742-6596/753/5/052022>.
- [16] J.D. Grunnet, M. Soltani, T. Knudsen, M.N. Kragelund, T. Bak, Aeolus Toolbox for Dynamics Wind Farm Model, Simulation and Control, The European Wind Energy Conference & Exhibition, 2010.
- [17] C.J. Bay, J. Annoni, T. Taylor, L.Y. Pao, K. Johnson, Active power control for wind farms used distributed model predictive control and nearest neighbor communication, in: *American Control Conference*, 2018, <https://doi.org/10.23919/ACC.2018.8431764>.
- [18] C.R. Shapiro, P. Bauweraerts, J. Meyers, C. Meneveau, D.F. Gayme, Model-based receding horizon control of wind farms for secondary frequency regulation, *Wind Energy* 20 (7) (2017) 1261–1275.
- [19] J.W. van Wingerden, L.Y. Pao, J. Aho, P.A. Fleming, Active power control of waked wind farms, *Int. Fed. Automat. Contr.* 50 (1) (2017) 4484–4491.
- [20] P.A. Fleming, P.M.O. Gebraad, S. Lee, J.W. van Wingerden, K. Johnson, M. Churchfield, J. Michalakos, P. Spalart, P. Moriarty, Evaluating techniques for redirecting turbine wakes using SOWFA, *Renew. Energy* 70 (2014) 211–218.
- [21] W. Munter, J. Meyers, Dynamic strategies for yaw and induction control of wind farms based on large-eddy simulation and optimization, *Energies* 11 (1) (2018).
- [22] F. Campagnolo, A. Croce, E.M. Nanos, V. Petrovic, J. Schreiber, C.L. Bottasso, Wind tunnel testing of a closed-loop wake deflection controller for wind farm power maximization, *J. Phys. Conf.* (2016), <https://doi.org/10.1088/1742-6596/753/3/032006>.
- [23] P.A. Fleming, J. Annoni, A. Scholbrock, E. Quon, S. Dana, S. Schreck, S. Raach, F. Haizmann, D. Schlupf, Full-scale field test of wake steering, in: *Wake Conference*, 2017, <https://doi.org/10.1088/1742-6596/854/1/012013>.
- [24] S. Boersma, V. Rostampour, B.M. Doekemeijer, W. van Geest, J.W. van Wingerden, A constrained model predictive wind farm controller providing active power control: an LES study, *J. Phys. Conf.* (2018), <https://doi.org/10.1088/1742-6596/1037/3/032023>.
- [25] P.M.O. Gebraad, F.W. Teeuwisse, J.W. van Wingerden, P.A. Fleming, S.D. Ruben, J.R. Marden, L.Y. Pao, Wind plant power optimization through yaw control using a parametric model for wake effects - a CFD simulation study, *Wind Energy* 19 (1) (2014) 95–114.
- [26] B. Maronga, M. Gryschka, R. Heinze, F. Hoffmann, F. Kanani-Sühring, M. Keck, K. Ketelsen, M.O. Letzel, M. Sühring, S. Raach, The Parallelized Large-Eddy Simulation Model (PALM) version 4.0 for atmospheric and oceanic flows: model formulation, recent developments, and future perspectives, *Geosci. Model Dev. (GMD)* 8 (8) (2015) 2515–2551.
- [27] <https://palm.muk.uni-hannover.de/trac>.
- [28] J.W. Deardorff, Stratocumulus-capped mixed layers derived from a three-dimensional model, *Boundary-Layer Meteorol.* 18 (4) (1980) 495–527.
- [29] A. Betz, Wind-Energie und ihre Ausnutzung durch Windmühlen, 1926.
- [30] M. Dörenkämper, B. Witha, G. Steinfeld, D. Heinemann, M. Kühn, The impact of stable atmospheric boundary layers on wind-turbine wakes within offshore wind farms, *J. Wind Eng. Ind. Aerod.* 144 (2015) 146–153.
- [31] L.J. Vermeer, J.N. Sørensen, A. Crespo, Wind turbine wake aerodynamics, *Prog. Aero. Sci.* 39 (6–7) (2003) 467–510.
- [32] M.O.L. Hansen, J.N. Sørensen, S. Voutsinas, N. Sørensen, H.A. Madsen, State of the art in wind turbine aerodynamics and aeroelasticity, *Prog. Aero. Sci.* 42 (4) (2006) 285–330.
- [33] <https://github.com/TUDELFT-DataDrivenControl/PALMSuperController> (2018).
- [34] S. Raach, S. Boersma, B.M. Doekemeijer, J.W. van Wingerden, P.W. Cheng, Lidar-based closed-loop wake redirection in high-fidelity simulation, *J. Phys. Conf.* (2018), <https://doi.org/10.1088/1742-6596/1037/3/032016>.
- [35] J. Meyers, C. Meneveau, Large Eddy Simulations of large wind-turbine arrays in the atmospheric boundary layer, in: *Aerospace Sciences Meeting*, 2010, <https://doi.org/10.2514/6.2010-827>.
- [36] S. Boersma, B.M. Doekemeijer, M. Vali, J. Meyers, J.W. van Wingerden, A control-oriented dynamic wind farm model: WFSim, *Wind Energy Sci.* 3 (2018) 75–95.
- [37] E. Simley, L.Y. Pao, Evaluation of a wind speed estimator for effective hub-height and shear components, *Wind Energy* 19 (1) (2014) 167–184.
- [38] C.R. Shapiro, J. Meyers, C. Meneveau, D.F. Gayme, Dynamic wake modeling and state estimation for improved model-based receding horizon control of wind farms, in: *American Control Conference*, 2017, <https://doi.org/10.23919/ACC.2017.7963036>.
- [39] B.M. Doekemeijer, S. Boersma, L.Y. Pao, T. Knudsen, J.W. van Wingerden, Online model calibration for a simplified LES model in pursuit of real-time closed-loop wind farm control, in: *Wind Energy Science Discussions*, 2018.
- [40] M. Bastankhah, F. Porte-Agél, Experimental and theoretical study of wind turbine wakes in yawed conditions, *J. Fluid Mech.* 806 (10) (2016) 506–541.
- [41] N.O. Jensen, A Note on Wind Generator Interaction, Tech. rep., Risø National Laboratory, 1983.

- [42] R. Damiani, S. Dana, J. Annoni, P.A. Fleming, J. Roadman, J. van Dam, K. Dykes, Assessment of wind turbine component loads under yaw-offset conditions, *Wind Energy Sci.* 3 (2017) 173–189.
- [43] T. Göçmen, G. Giebel, N.K. Poulsen, M. Mahmood, Wind speed estimation and parametrization of wake models for downregulated offshore wind farms within the scope of posspow project, *J. Phys. Conf.* (2014), <https://doi.org/10.1088/1742-6596/524/1/012156>.
- [44] C.L. Bottasso, J. Schreiber, Online model updating by a wake detector for wind farm control, in: American Control Conference, 2018, <https://doi.org/10.23919/ACC.2018.8431626>.
- [45] R. Courant, K. Friedrichs, H. Lewyt, On the partial difference equations of mathematical physics, *IBM J. Res. Dev.* 11 (2) (1928) 215–234.
- [46] W. Munters, J. Meyers, An optimal control framework for dynamic induction control of wind farms and their interaction with the atmospheric boundary layer, *Phil. Trans. Roy. Soc. Lond.: Math., Phys. Eng. Sci.* 375 (2091) (2017).
- [47] P.A. Fleming, J. Aho, P.M.O. Gebraad, L.Y. Pao, Y. Zhang, Computational fluid dynamics simulation study of active power control in wind plants, in: American Control Conference, 2016, <https://doi.org/10.1109/ACC.2016.7525115>.
- [48] C. Pilong, PJM Manual 12: Balancing Operations, Technical report, PJM, 2013.



### 9.3 Conclusion

Fundamentally, the work presented in this literature tackled a very important problem: the integration of electricity from wind with the electricity grid. A closed-loop (feedback) solution was devised to enable power reference tracking at timescales of 1 to 10 seconds, while minimizing the dynamic axial loading on the turbine rotors, which was assumed as a surrogate for fatigue loading. The strength of this feedback control solution was demonstrated in high-fidelity, large-eddy simulation, showing excellent performance.

Additionally, situations may arise where a wind farm cannot provide the energy that is demanded from it by a transmission system operator. To increase the power that the wind farm can extract, yaw-based wake steering is used by leveraging the FLORIS surrogate model, previously described in Chapter 4, among others. The concept of wake steering has not yet been integrated sufficiently for real-time operation, since one would only want to yaw the turbines if the demanded power will exceed the available power in the near future. However, in this article, yaw-based wake steering was applied constantly, rather than toggled.

Future work should focus on the further intergration of these techniques, and dealing with more realistic, time-varying inflow conditions.

## 10 CONCLUSIONS

This document revolved around the synthesis of integrated control solutions to improve the efficiency in wind turbine and wind farm operation. This work continues further on previous work [55] by unifying single-objective and single-method control solutions proposed in an earlier deliverable, moving towards realistic control solutions that attempt to push the envelope of operational efficiency. Several promising solutions were proposed in this document.

In Chapter 3, the effects of axial induction control, wake redirection control, and the combination of both were explored in detail. It became clear that wake redirection control has the highest potential in increasing the energy extraction of wind farms. In some situations, axial induction control may further increase the power production, but this depends on the wind farm layout and the turbine types. Generally, FLORIS predicted gains of up to 15% – 20% using wake redirection and gains of 0% – 5% using axial induction control.

In Chapter 4, a controller combining axial induction control and wake redirection control leveraging FLORIS was further matured and tested. High-fidelity simulation results show that the surrogate model FLORIS does not predict any gains in energy yield for axial induction control, and the controller thereby exclusively employs wake steering for power maximization. Furthermore, the controller was then robustified using a theoretical measure of observability, which ensures that only the parameters that can be estimated, are estimated. Finally, an integrated closed-loop control solution was proposed and tested in high-fidelity simulation using varying inflow conditions, showing an increase of 1% to 9% in energy extraction compared to greedy operation.

In Chapter 5, a lidar-assisted feedforward-feedback wind farm controller was explored. This controller employs FLORIS to optimize the turbine yaw setpoints, and then uses lidar measurements in a feedback setting to correct the yaw angle and thereby achieve the desired wake displacement, effectively accounting for model discrepancies. The controller showed an increase in energy extraction of up to 17% in high-fidelity simulation compared to a baseline wind farm control strategy. In future work, the proposed controller should be tested for changing inflow conditions.

In Chapter 6, a feedforward control solution was presented that integrates turbine derating to balance mechanical loads with energy extraction in the wind farm. To do so, a loads database was constructed through a large number of aero-elastic simulations. This database was integrated in the FLORIS surrogate model to provide predictions on the turbine fatigue loads and power production as a function of the inflow conditions. A solution was also provided for the estimation of such ambient conditions using upstream turbine measurement data, which is an essential component to any model-based wind farm control solution. The supercontroller was tested in the medium-fidelity simulation environment FAST.Farm for a 3x3 wind farm. The results show how the integrated control solution trades off energy extraction and turbine fatigue loading, revealing to be a promising application of this technology.

In Chapter 7, an axial-induction-based wind farm control solution was depicted for an onshore wind farm, to be tested through real-world experimentation. While axial induction control has often appeared impractical for power maximization [13], LongSim does predict increases up to the order of 10% in energy extraction by derating several upstream turbines for conditions with large wake losses (i.e., at a low turbulence intensity and for the right wind direction). Moreover, special attention was paid towards the shift from steady control solutions to a more realistic, dynamic environment, thereby rendering the controller one of the most prominent wind farm control solutions presented in this work.

In Chapter 8, it was concluded that the proposed model-free approach for axial induction control in pursuit of power maximization previously presented [55] was not deemed feasible. This control solution was therefore discontinued.

In Chapter 9, a wind farm control solution for active power control was proposed to track a reference power signal on the 1-to-10 seconds timescale while minimizing the axial force fluctuations on each turbine rotor. This shows to be a very promising application and an absolute necessity as wind energy plays a larger role in national electricity grids. Moreover, this chapter showed initial work on the inclusion of wake steering for power maximization when necessary, though more research must be spent on its efficient integration to avoid turbine yaw misalignment when it is not necessary.

Looking ahead, in workpackage 3 of this project, several of these control algorithms will be tested on various levels of fidelity; in high-fidelity simulation, wind tunnel experiments and/or field campaigns on an onshore wind farm in Sedini, on the island of Sardinia, Italy. This should further verify, validate and increase the trust in these control solutions.

## REFERENCES

- [1] J. Aho, P. Fleming, and L. Y. Pao. "Active power control of wind turbines for ancillary services: A comparison of pitch and torque control methodologies." In: *2016 American Control Conference (ACC)*. IEEE. 2016, pp. 1407–1412.
- [2] V. W. et al. *CL-Windcon 2.3: Control methods for induction-based control and for wake-redirection control*. Tech. rep. CL-Windcon deliverable repository, 2019.
- [3] J. Annoni, P. Fleming, A. Scholbrock, J. Roadman, S. Dana, C. Adcock, F. Porte-Agel, S. Raach, F. Haizmann, and D. Schlipf. "Analysis of control-oriented wake modeling tools using lidar field results." In: *Wind Energy Science* 3.2 (2018), pp. 819–831. URL: <https://www.wind-energ-sci.net/3/819/2018/>.
- [4] J. Annoni, P. M. O. Gebraad, A. K. Scholbrock, P. A. Fleming, and J. W. van Wingerden. "Analysis of axial-induction-based wind plant control using an engineering and a high-order wind plant model." In: *Wind Energy* 19.6 (2016), pp. 1135–1150. ISSN: 1099-1824.
- [5] J. Annoni, P. M. Gebraad, A. K. Scholbrock, P. A. Fleming, and J.-W. v. Wingerden. "Analysis of axial-induction-based wind plant control using an engineering and a high-order wind plant model." In: *Wind Energy* 19.6 (2016), pp. 1135–1150.
- [6] J. Annoni, A. K. Scholbrock, M. J. Churchfield, and P. A. Fleming. "Evaluating Tilt for Wind Plants." In: (July 2017).
- [7] J. Annoni et al. "Analysis of axial induction based wind plant control using an engineering and a high order wind plant model." In: *Wind Energy* 13-1 (2015).
- [8] D. Astrain Juangarcia, I. Eguinoa, and T. Knudsen. "Derating a single wind farm turbine for reducing its wake and fatigue." In: *SCIENCE OF MAKING TORQUE FROM WIND (TORQUE 2018)*. Vol. 1037. Journal of Physics Conference Series. 7th Conference on Science of Making Torque from Wind (TORQUE), Milan, ITALY, JUN 20-22, 2018. Politecnico Milano, Dept Aerosp Sci & Technol. 2018.
- [9] C. Bak et al. "Light Rotor: The 10-MW reference wind turbine." English. In: *Proceedings of EWEA 2012 - European Wind Energy Conference & Exhibition*. European Wind Energy Association (EWEA), 2012.
- [10] M. Bastankhah and F. Porté-Agel. "Experimental and theoretical study of wind turbine wakes in yawed conditions." In: *Journal of Fluid Mechanics* 806 (2016), pp. 506–541.
- [11] M. Bertelè, C. L. Bottasso, S. Cacciola, F. Daher Adegas, and S. Delport. "Wind inflow observation from load harmonics." In: *Wind Energy Science* 2.2 (2017), pp. 615–640.
- [12] S. Boersma, B. M. Doekemeijer, P. M. O. Gebraad, P. A. Fleming, J. Annoni, A. K. Scholbrock, J. A. Frederik, and J. van Wingerden. "A tutorial on control-oriented modeling and control of wind farms." In: *2017 American Control Conference (ACC)*. May 2017, pp. 1–18.
- [13] S. Boersma, B. M. Doekemeijer, P. M. O. Gebraad, P. A. Fleming, J. Annoni, A. K. Scholbrock, J. A. Frederik, and J. W. van Wingerden. "A tutorial on control-oriented modeling and control of wind farms." In: *2017 American Control Conference (ACC)*. May 2017, pp. 1–18.

- [14] S. Boersma, B. M. Doekemeijer, M. Vali, J. Meyers, and J. W. van Wingerden. "A control-oriented dynamic wind farm model: WFSim." In: *Wind Energy Science* 3 (2018), pp. 75–95.
- [15] S. Boersma, B. Doekemeijer, S. Siniscalchi-Minna, and J. van Wingerden. "A constrained wind farm controller providing secondary frequency regulation: An LES study." In: *Renewable Energy* 134 (2019), pp. 639–652. ISSN: 0960-1481. URL: <http://www.sciencedirect.com/science/article/pii/S0960148118313508>.
- [16] E. Bossanyi. "Combining induction control and wake steering for wind farm energy and fatigue loads optimisation." In: *Journal of Physics: Conference Series* 1037 (June 2018), p. 032011. URL: <https://doi.org/10.1088%2F1742-6596%2F1037%2F3%2F032011>.
- [17] F. Campagnolo, V. Petrović, C. L. Bottasso, and A. Croce. "Wind tunnel testing of wake control strategies." In: *Proceedings of the American Control Conference (ACC)* (2016), pp. 513–518.
- [18] F. Campagnolo et al. "Wind tunnel testing of wake control strategies." In: *2016 American Control Conference (ACC)*. IEEE. 2016.
- [19] B. Clayton and P. Filby. "Measured effects of oblique flows and change in blade pitch angle on performance and wake development of model wind turbines." In: *BWEA Wind Energy Conference* (1982).
- [20] Delft University of Technology, DCSC-Data Driven Control Group. *FLORISSE\_M*. 2018. URL: [https://github.com/TUdelft-DataDrivenControl/FLORISSE\\_M](https://github.com/TUdelft-DataDrivenControl/FLORISSE_M).
- [21] B. M. Doekemeijer, P. A. Fleming, and J. W. van Wingerden. "A tutorial on the synthesis and validation of a closed-loop wind farm controller using a steady-state surrogate model." In: *Proceedings of the American Control Conference (ACC)*. In review. Philadelphia, USA, 2019.
- [22] B. M. Doekemeijer, P. A. Fleming, and J. W. van Wingerden. "Model-based closed-loop wind farm control for power maximization: a large eddy simulation study." In: *Conference on Control Technology & Applications*. Hong Kong, China, 2019.
- [23] B. M. Doekemeijer and R Storm. *FLORISSE\_M Github repository*. English. [https://github.com/TUdelft-DataDrivenControl/FLORISSE\\_M](https://github.com/TUdelft-DataDrivenControl/FLORISSE_M). 2018.
- [24] B. M. Doekemeijer, P. A. Fleming, and J. W. van Wingerden. "A tutorial on the synthesis and validation of a closed-loop wind farm controller using a steady-state surrogate model." In: *American Control Conference Philadelphia 10-12 July*. IEEE. 2019.
- [25] B. M. Doekemeijer, P. A. Fleming, and J. van Wingerden. "A tutorial on the synthesis and validation of a closed-loop wind farm controller using a steady-state surrogate model." In: *CoRR* abs/1810.12066 (2018). arXiv: 1810.12066. URL: <http://arxiv.org/abs/1810.12066>.
- [26] I. Eguinoa et. al. *CL-Windcon D2.1: Minimal loading wind turbine de-rating strategy and active yaw controllers*. Tech. rep. CL-Windcon deliverable repository, 2017.
- [27] M. Ellis, H. Durand, and P. D. Christofides. "A tutorial review of economic model predictive control methods." In: *Journal of Process Control* 24 (2014), pp. 1156–1178.
- [28] P. Fleming et al. "Initial results from a field campaign of wake steering applied at a commercial wind farm – Part 1." In: *Wind Energy Science* 4.2 (2019), pp. 273–285. URL: <https://www.wind-energ-sci.net/4/273/2019/>.

- [29] P. A. Fleming, J. Annoni, J. J. Shah, L. Wang, S. Ananthan, Z. Zhang, K. Hutchings, P. Wang, W. Chen, and L. Chen. "Field test of wake steering at an offshore wind farm." In: *Wind Energy Science* 2.1 (2017), pp. 229–239.
- [30] P. A Fleming, J. Annoni, J. J. Shah, L. Wang, S. Ananthan, Z. Zhang, K. Hutchings, P. Wang, W. Chen, and L. Chen. "Field test of wake steering at an offshore wind farm." In: *Wind Energy Science* 2.1 (2017), pp. 229–239.
- [31] P. A. Fleming, P. M. O. Gebraad, S. Lee, J.-W. van Wingerden, K. Johnson, M. Churchfield, J. Michalakes, P. Spalart, and P. Moriarty. "Evaluating techniques for redirecting turbine wakes using SOWFA." In: *Renewable Energy* 70 (2014), pp. 211–218.
- [32] P. M. O. Gebraad. "Data-Driven Wind Plant Control." PhD thesis. Delft University of Technology, 2014.
- [33] P. M. O. Gebraad, F. W. Teeuwisse, J. W. van Wingerden, P. A. Fleming, S. D. Ruben, J. R. Marden, and L. Y. Pao. "Wind plant power optimization through yaw control using a parametric model for wake effects - a CFD simulation study." In: *Wind Energy* 19.1 (2016), pp. 95–114.
- [34] I. Grant, P. Parkin, and X. Wang. "Optical vortex tracking studies of a horizontal axis wind turbine in yaw using laser-sheet, flow visualisation." In: *Experiments in Fluids*, vol. 23, pp. 513–519 (1997).
- [35] D. van der Hoek, S. Kanev, J. Allin, D. Bieniek, and N. Mittelmeier. "Effects of axial induction control on wind farm energy production - A field test." In: *Renewable Energy* 140 (2019), pp. 994 – 1003. ISSN: 0960-1481. URL: <http://www.sciencedirect.com/science/article/pii/S096014811930429X>.
- [36] D. van der Hoek et al. "Effects of axial induction control on wind farm energy production - A field test." In: *Renewable energy* Volume 140 (2019), pp. 994–1003.
- [37] M. F. Howland, J. Bossuyt, L. A. Martinez-Tossas, J. Meyers, and C. Meneveau. "Wake structure in actuator disk models of wind turbines in yaw under uniform inflow conditions." In: *Journal of Renewable Sustainable Energy* (2016).
- [38] U. Irigoyen et al. *CL-Windcon 1.1: Definition of reference wind farms and simulation scenarios*. Tech. rep. CL-Windcon deliverable repository, 2017.
- [39] Á. Jiménez, A. Crespo, and E. Migoya. "Application of a LES technique to characterize the wake deflection of a wind turbine in yaw." In: *Wind Energy* 13.6 (2010), pp. 559–572.
- [40] S. Kanev and T. van Engelen. "Wind turbine extreme gust control." In: *Wind Energy* 13-1 (2010), pp. 122–138.
- [41] S. Kanev, F. Savenije, and W. Engels. "Active wake control: An approach to optimize the lifetime operation of wind farms." In: *Wind Energy* 21.7 (2018), pp. 488–501.
- [42] S. Kanev, F. Savenije, and M. Soleimanzadeh. *Wind farm modeling and control: an inventory*. Tech. rep. ECN-E-13-058. Energy research Center of the Netherlands (ECN), 2014.
- [43] A. C. Kheirabadi and R. Nagamune. "A quantitative review of wind farm control with the objective of wind farm power maximization." In: *Journal of Wind Engineering and Industrial Aerodynamics* 192 (2019), pp. 45 –73. ISSN: 0167-6105. URL: <http://www.sciencedirect.com/science/article/pii/S0167610519305240>.

- [44] T. Knudsen, T. Bak, and M. Svenstrup. "Survey of wind farm control—power and fatigue optimization." In: *Wind Energy* 18.8 (2015), pp. 1333–1351. eprint: <https://onlinelibrary.wiley.com/doi/pdf/10.1002/we.1760>. URL: <https://onlinelibrary.wiley.com/doi/abs/10.1002/we.1760>.
- [45] H. Mendez Reyes, S. Kanev, B. Doekemeijer, and J.-W. van Wingerden. "Validation of a lookup-table approach to modeling turbine fatigue loads in wind farms under active wake control." In: *Wind Energy Science Discussions* 2019 (2019), pp. 1–19. URL: <https://www.wind-energ-sci-discuss.net/wes-2019-34/>.
- [46] L. Y. Pao and K. E. Johnson. "A tutorial on the dynamics and control of wind turbines and wind farms." In: *2009 American Control Conference*. IEEE. 2009, pp. 2076–2089.
- [47] J. Quick, J. Annoni, R. King, K. Dykes, P. A. Fleming, and A. Ning. "Optimization Under Uncertainty for Wake Steering Strategies." In: *Journal of Physics: Conference Series* 19.1 (2017), pp. 95–114.
- [48] S. Raach, S. Boersma, B. M. Doekemeijer, J. W. Wingerden, and P. W. Cheng. "Lidar-based closed-loop wake redirection in high-fidelity simulation." In: *Journal of Physics: Conference Series*, DOI: 10.1088/1742-6596/1037/3/032016 (2018).
- [49] S. Raach, S. Boersma, J.-W. van Wingerden, D. Schlipf, and P. W. Cheng. "Robust lidar-based closed-loop wake redirection for wind farm control." In: *Proceedings of the 20th World Congress of the International Federation of Automatic Control (IFAC)*. Toulouse, France, 2017.
- [50] S. Raach, D. Schlipf, and P. W. Cheng. "Lidar-based wake tracking for closed-loop wind farm control." In: *Wind Energy Science* 2.1 (2017), pp. 257–267.
- [51] S. Raach, D. Schlipf, F. Borisade, and P. W. Cheng. "Wake redirecting using feedback control to improve the power output of wind farms." In: *Proceedings of the American Control Conference (ACC)*. Boston, USA, July 2016.
- [52] S. Raach, J.-W. van Wingerden, S. Boersma, D. Schlipf, and P. W. Cheng. " $H_\infty$  controller design for closed-loop wake redirection." In: *Proceedings of the American Control Conference (ACC)*. Seattle, USA, 2017, pp. 703–708.
- [53] E. Simley, P. Fleming, and J. King. "Design and Analysis of a Wake Steering Controller with Wind Direction Variability." In: *Wind Energy Science Discussions* 2019 (2019), pp. 1–26. URL: <https://www.wind-energ-sci-discuss.net/wes-2019-35/>.
- [54] L. Vollmer, G. Steinfeld, D. Heinemann, and M. Kühn. "Estimating the wake deflection downstream of a wind turbine in different atmospheric stabilities: An LES study." In: *Wind Energy Science*, vol. 1, pp. 129–141 (2016).
- [55] J. W. van Wingerden et al. *CL-Windcon D2.3: Wind farm flow control technologies and algorithms*. Tech. rep. CL-Windcon deliverable repository, 2019.
- [56] J. W. van Wingerden et al. *CL-Windcon D3.5: Demonstration of combined turbine/farm level controls by simulations*. Tech. rep. CL-Windcon deliverable repository, 2019.